

# Exact Nonadiabatic Many-Body Dynamics: Electron-Phonon Coupling in Photoelectron Spectroscopy and Light-Matter Interactions in Quantum Electrodynamical Density-Functional Theory

Dissertation

zur Erlangung des akademischen Grades

doctor rerum naturalium

(Dr. rer. nat.)

im Fach Physik

Spezialisierung: Theoretische Physik

eingereicht an der

Mathematisch-Naturwissenschaftlichen Fakultät

der Humboldt-Universität zu Berlin

von

Dipl. Phys. Johannes Flick

Präsident der Humboldt-Universität zu Berlin

Prof. Dr. Jan-Hendrik Olbertz

Dekan der Mathematisch-Naturwissenschaftlichen Fakultät

Prof. Dr. Elmar Kulke

Gutachter/innen:

1. Prof. Dr. Claudia Draxl
2. Prof. Dr. Angel Rubio
3. Prof. Dr. Dieter Bauer

Tag der mündlichen Prüfung: 30. Mai 2016



## ABSTRACT

---

Many natural and synthetic processes are triggered by the interaction of light and matter. Important examples here include photosynthesis, the vision process, photochemical reactions, solar cells, and nanoplasmonics based on metamaterials. All these complex processes are routinely explained by employing various approximations, e.g. the Born-Oppenheimer approximation, the classical treatment of electromagnetic fields, the rotating-wave approximation, or the reduction of multi-component systems to few-level systems.

In the first part of this work, we assess the validity of the Born-Oppenheimer approximation in the case of equilibrium and time-resolved nonequilibrium photoelectron spectra for a vibronic model system of Trans-Polyacetylene. Using exact diagonalization, we show that spurious peaks appear for the vibronic spectral function in the Born-Oppenheimer approximation, which are not present in the exact spectral function of the system. This effect can be traced back to the factorized nature of the Born-Oppenheimer initial and final photoemission states. Only when correlated initial and final vibronic states are taken into account, the spurious spectral weights of the Born-Oppenheimer approximation are suppressed. In the nonequilibrium case, we illustrate for an initial Franck-Condon excitation and an explicit pump-pulse excitation how the vibronic wave packet motion can be traced in the time-resolved photoelectron spectra as function of the pump-probe delay.

In the second part of this work, we aim at treating both, matter and light, on an equal quantized footing. In the electronic structure community, the quantized nature of electrons and nuclei is usually (approximately) incorporated, whereas the electromagnetic field is mostly treated classically. In contrast, in quantum optics, matter is typically simplified to models with a few levels, while the quantized nature of light is fully explored. To bridge this gap, we apply the recently developed generalized time-dependent density-functional theory, quantum electrodynamical density-functional theory ([QEDFT](#)), which allows to describe electron-photon systems fully quantum mechanically. We present the first numerical calculations in the framework of [QEDFT](#). We show exact solutions for fully quantized prototype systems consisting of atoms or molecules placed in optical high-Q cavities and coupled to quantized electromagnetic modes, both for model systems heavily used in quantum optics, as well as for systems with a real-space description. We focus on the electron-photon exchange-correlation contribution by calculating exact Kohn-Sham potentials in real space using fixed-point inversions and present the performance of the first approximate exchange-correlation potential based on an optimized effective potential approach for a Jaynes-Cummings-Hubbard dimer. In all these examples, we focus on spontaneous emission, atomic revivals, and strong-coupling phenomena, all beyond the rotating-wave approximation.

This work opens new research lines at the interface between materials science and quantum optics with the potential to unravel new physical phenomena (e.g. the mixture of polaritons and polarons) and nonequilibrium effects such as photon or polariton quasi-bound states.





## ZUSAMMENFASSUNG

---

Chemische Reaktionen in der Natur sowie Prozesse in synthetischen Materialien werden oft erst durch die Wechselwirkung von Licht mit Materie ausgelöst. Wichtige Beispiele hierfür sind die Photosynthese, der Sehprozess, photochemische Reaktionen, Solarzellen und Nanoplasmonen auf Metamaterialien. Üblicherweise werden diese komplexen Prozesse mit Hilfe von Näherungen beschrieben, z.B. der Born-Oppenheimer Näherung, der Annahme eines klassischen elektromagnetischen Feldes, der Drehwellennäherung, oder der Reduzierung von Vielkomponentensystemen auf Systeme mit wenigen elektronischen Niveaus. Im ersten Teil der Arbeit wird die Gültigkeit der Born-Oppenheimer Näherung in einem vibronischen Modellsystem (Trans-Polyacetylene) unter Photoelektronenspektroskopie im Gleichgewicht sowie zeitaufgelöster Photoelektronenspektroskopie im Nichtgleichgewicht überprüft. Die mit Hilfe von exakter Diagonalisierung bestimmte vibronische Spektralfunktion zeigt aufgrund des faktorisierten Anfangs- und Endzustandes in der Born-Oppenheimer Näherung zusätzliche Peaks, die in der exakten Spektralfunktion nicht auftreten. Diese falschen Gewichte in der Spektralfunktion verschwinden erst, wenn statt der faktorisierten Zustände die exakten berücksichtigt werden. Im Nichtgleichgewicht zeigen wir für eine Franck-Condon Anregung und eine Anregung mit Pump-Probe Puls, wie die Bewegung des vibronischen Wellenpaketes im zeitabhängigen Photoelektronenspektrum verfolgt werden kann. Im zweiten Teil der Arbeit werden sowohl die Materie als auch das Licht quantisiert behandelt. Normalerweise werden in Elektronenstrukturechnungen die Elektronen quantenmechanisch, die elektromagnetische Felder dagegen in klassischer Näherung berücksichtigt. Hingegen wird in der Quantenoptik die Materie meist auf wenige elektronischen Niveaus reduziert, wohingegen das Licht quantenmechanisch betrachtet wird. Für eine volle quantenmechanische Beschreibung des Elektron-Licht Systems, verwenden wir die kürzlich entwickelte verallgemeinerte zeitabhängige Dichtefunktionaltheorie, die quantenelektrodynamische Dichtefunktionaltheorie (QEDFT), für gekoppelte Elektron-Photon Systeme. Wir zeigen erste numerische QEDFT-Berechnungen voll quantisierter Atome und Moleküle in optischen Kavitäten, die an das quantisierte elektromagnetische Feld gekoppelt sind. Wir konzentrieren uns sowohl auf typische Modellsysteme aus der Quantenoptik, als auch auf Systeme mit voller Ortsauflösung. Mit Hilfe von Fixpunktiterationen berechnen wir das exakte Kohn-Sham Potential im diskreten Ortsraum, wobei unser Hauptaugenmerk auf dem Austausch-Korrelations-Potential liegt. Wir zeigen die erste Näherung des Austausch-Korrelations-Potentials mit Hilfe eines optimierten effektiven Potential Ansatzes angewandt auf einen Jaynes-Cummings-Dimer. In allen Beispielen untersuchen wir spontane Emission, atomare Revivals und stark gekoppelte Phänomene, jeweils ohne Drehwellennäherung. Die dieser Arbeit zugrunde liegenden Erkenntnisse und Näherungen ermöglichen es neuartige Phänomene an der Schnittstelle zwischen den Materialwissenschaften und der Quantenoptik zu beschreiben, wie z.B. die Mischung aus Polaritonen und Polaronen oder Nichtgleichgewichtseffekte wie quasi-gebundene Photon und Polaritonzustände.



# CONTENTS

---

<b>I</b>	<b>INTRODUCTION</b>	<b>1</b>
1	INTRODUCTION	3
<b>II</b>	<b>THEORETICAL BACKGROUND</b>	<b>7</b>
2	THEORETICAL BACKGROUND	9
2.1	The Quantum Many-Body Problem . . . . .	9
2.1.1	Electron-Nuclear Hamiltonian . . . . .	10
2.1.2	Born-Oppenheimer Approximation . . . . .	11
2.1.3	Phonons and the Harmonic Approximation . . . . .	13
2.1.4	Particles in Second Quantization . . . . .	13
2.2	Density-Functional Theory . . . . .	14
2.2.1	Ground-State Density-Functional Theory . . . . .	15
2.2.2	Hohenberg-Kohn Theorem . . . . .	17
2.2.3	Kohn-Sham System in DFT . . . . .	18
2.2.4	Time-Dependent Density-Functional Theory . . . . .	21
2.2.5	Equation of Motion for the Electron Density . . . . .	22
2.2.6	Runge-Gross Theorem . . . . .	22
2.2.7	Kohn-Sham System in TDDFT . . . . .	24
2.2.8	Green's Functions and the Sham-Schlüter Equation . . . . .	25
2.3	Photons and the Electron-Photon Hamiltonian . . . . .	29
2.3.1	Classical Maxwell Field Equations . . . . .	29
2.3.2	Gauge Transformation . . . . .	30
2.3.3	Free Classical Field . . . . .	31
2.3.4	Riemann-Silberstein Vector . . . . .	32
2.3.5	Quantization of the Field in the Schrödinger Picture . . . . .	32
2.3.6	Momentum Gauge and the Minimal-Coupling Hamiltonian . . . . .	33
2.3.7	Pauli-Fierz Hamiltonian and the Maxwell-Schrödinger Propagation . . . . .	34
2.3.8	Quantum Electrodynamics in a Cavity: Zero-Boundary Conditions . . . . .	35
2.3.9	The Length Gauge and the Dipole Approximation . . . . .	35
2.4	Theory of Static and Time-Resolved Photoelectron Spectroscopy . . . . .	37
2.4.1	Equilibrium Spectral Function . . . . .	39
2.4.2	Nonequilibrium Spectral Function . . . . .	40
2.4.3	Approximations for the Electron-Phonon Spectral Function . . . . .	41
<b>III</b>	<b>MODEL SYSTEMS AND NUMERICAL METHODS</b>	<b>43</b>
3	MODEL SYSTEMS AND NUMERICAL METHODS	45
3.1	Model Systems for the Study of the Electron-Boson Interaction . . . . .	45
3.1.1	Su-Schrieffer-Heeger Hamiltonian . . . . .	45
3.1.2	The Jaynes-Cummings-Hubbard Hamiltonian . . . . .	47
3.1.3	GaAs Quantum Dot in an Optical Cavity . . . . .	48
3.2	Methods and Numerical Implementations . . . . .	50

3.2.1	Eigenvalue Problems and Finite-Difference Methods . . . . .	50
3.2.2	Jordan-Wigner Transformation and the Bosonic Operators . .	50
3.2.3	Extension to Photons . . . . .	53
3.2.4	Symmetry and Sparsity . . . . .	53
3.2.5	Exact Diagonalization . . . . .	54
3.2.6	Propagation Methods . . . . .	54
3.2.7	Numerical Integration and Volterra Integral Equations . . . .	55
3.2.8	Fixed-Point Algorithm . . . . .	56
<b>IV</b>	<b>APPLICATIONS</b>	<b>61</b>
<b>4</b>	<b>NONADIABATIC AND TIME-RESOLVED PHOTOEMISSION SPECTROSCOPY</b>	<b>63</b>
4.1	Su-Schrieffer-Heeger Hamiltonian . . . . .	64
4.2	Born-Oppenheimer Approximation for the SSH Hamiltonian . . . .	64
4.3	Numerical Aspects of the Calculation of the Spectral Function . . . .	65
4.4	Comparison of BO and Exact Ground-State Photoelectron Spectra .	67
4.5	Nonadiabaticity in Ground-State Photoelectron Spectroscopy . . . .	68
4.6	Comparison between Propagated Spectra and Sum-over-States . . .	70
4.7	Time-Resolved Pump-Probe Photoelectron Spectra . . . . .	71
4.7.1	Initial Franck-Condon Excitation . . . . .	71
4.7.2	Explicit Pump Pulse . . . . .	73
4.8	Summary . . . . .	75
<b>5</b>	<b>QEDFT IN THE NONRELATIVISTIC LIMIT</b>	<b>77</b>
5.1	Multicomponent Theory . . . . .	78
5.2	Equations of Motion for the Quantized Electromagnetic Field . . . .	80
5.3	Equations of Motion in the Electronic Subsystem . . . . .	81
5.4	Kohn-Sham System in QEDFT . . . . .	82
5.5	Numerical Example for the Model QEDFT . . . . .	84
5.6	Summary . . . . .	90
<b>6</b>	<b>EXACT QEDFT KS POTENTIAL IN REAL SPACE</b>	<b>91</b>
6.1	Kohn-Sham System of the Cavity-GaAs Model . . . . .	91
6.2	Numerical Results in the Ground State . . . . .	92
6.3	Time-Dependent Results Using Different Initial States . . . . .	95
6.4	Interpretation of the Peak and Step Structures in QEDFT . . . . .	99
6.5	Validating the Numerical Fixed-Point Algorithm . . . . .	101
6.6	Interpretation of the Electron-Photon Dynamics in Terms of BO Sur- faces . . . . .	102
6.7	Summary . . . . .	105
<b>7</b>	<b>OPTIMIZED-EFFECTIVE POTENTIALS FOR QEDFT</b>	<b>107</b>
7.1	General Theory of the OEP Approximation for QEDFT . . . . .	107
7.2	Model System: Static Calculation . . . . .	110
7.3	Model System: Time-Dependent Calculation . . . . .	111
7.4	Validation of the Numerical Implementation . . . . .	114
7.5	Summary . . . . .	115
<b>8</b>	<b>THE HYDROGEN-DEUTERIUM DIMER IN AN OPTICAL CAVITY</b>	<b>117</b>
8.1	Introduction . . . . .	117
8.2	Cavity Born-Oppenheimer Approximation . . . . .	117
8.3	Summary . . . . .	123

<b>V CONCLUSION</b>	<b>125</b>
<b>9 SUMMARY, CONCLUSIONS AND OUTLOOK</b>	<b>127</b>
<b>VI APPENDIX</b>	<b>129</b>
<b>A POWER-ZIENAU-WOOLLEY TRANSFORMATION</b>	<b>131</b>
<b>B GAUGE CONDITIONS ON <math>a_{\text{ext}}</math></b>	<b>133</b>
B.1 Coupling of $a_{\text{ext}}^0$ to the Electron Density . . . . .	133
B.2 Coupling of $\mathbf{a}_{\text{ext}}$ to the Electron Current . . . . .	134
<b>C DERIVATION OF JAYNES-CUMMINGS-HUBBARD MODEL FROM THE NON-RELATIVISTIC HAMILTONIAN</b>	<b>135</b>
<b>D DERIVATION OF THE SPECTRAL FUNCTION</b>	<b>137</b>
D.1 Equilibrium Spectral Function . . . . .	137
D.2 Nonequilibrium Spectral Function . . . . .	138
<b>E COORDINATE TRANSFORMATION FOR DIATOMIC MOLECULES</b>	<b>141</b>
<b>F ATOMIC UNITS</b>	<b>143</b>
F.1 Hartree Atomic Units . . . . .	143
F.2 Effective Atomic Units for a GaAs System . . . . .	143
<b>BIBLIOGRAPHY</b>	<b>145</b>
List of Figures	159
List of Tables	161
List of Acronyms	162
List of Publications	165
List of Talks and Posters	167
Acknowledgments	169
Declaration	171



Part I

INTRODUCTION





## INTRODUCTION

---

The advent of quantum mechanics changed the scientific field of physics quite dramatically. Indeed there have been early hints by the famous works of e.g. James Clerk Maxwell [1], Max Planck [2], Albert Einstein [2], Niels Bohr [3], and others that the deterministic and continuous picture of physical processes involving light, molecules or atoms does not hold on the small (atomic) length scale. The combination of all these findings then naturalized in 1925 into the establishment of the Schrödinger Equation [4], named after its founder Erwin Schrödinger. Together with the theory of relativity, this quantum theory is one of the greatest breakthroughs and success stories of the physics community in the 20th century and thus is still a foundation of modern physics. Surely, the Schrödinger equation is also only an approximate description of reality, but well justified in the nonrelativistic limit of slow moving particles and atomic length scales. Since a universal theory (theory of everything) remains unknown, physicists rely on approximate equations, which are justified for certain limits. Besides its formal simplicity, the Schrödinger equation is hard to solve. The exponential wall of many-body problems [5] prevents exact solutions of the Schrödinger equation for more than only a few particles. This is why physicists and chemists invested much time into developing methods to solve the Schrödinger equation only approximately.

One of the first of such methods was Hartree theory, which allows to consider many electrons in the attractive potential generated by their surrounding nuclei. Its generalization to include the Pauli-spin interaction lead to Hartree-Fock theory, which still remains a popular method. In 1964, Pierre Hohenberg and Walter Kohn developed density-functional theory (DFT) [6] by proving the one-to-one correspondence of the electron ground-state density, which is a measure for the probability of finding an electron at a given position in space, to the external potential, which considers e.g. the nuclear attraction. DFT has its origins in Thomas-Fermi theory [7], which was developed in 1927. Thomas-Fermi theory was unable to predict molecular binding, due to the lack of a correct description of the electronic kinetic energy and therefore only applied to specific materials such as metals. However, DFT overcame many limitations of Thomas-Fermi theory. The theory of DFT is formally exact and allows to replace the interacting many-body system by a noninteracting Kohn-Sham system. The hereby emerging exchange-correlation potential requires approximations, but these approximations make DFT practical and applicable for numerical calculations. DFT became popular in the physics community after the development of the local-density approximation (LDA) [8] in 1965 and in the quantum chemistry community after the development of the generalized-gradient approximation (GGA) in the 1980s [9].

Besides its limitation to the ground-state properties of materials, DFT is nowadays one of the most popular methods to calculate quantum properties of materials. The generalization to time-dependent situations was worked out by Erich Runge and Eberhard K. U. Gross in 1983 and termed time-dependent density-functional

theory (TDDFT) [10]. In the last decade, TDDFT has been applied successfully to a wide range of applications, e.g. the calculation of excitation energies [11], the calculation of the dipole moment measured in absorption experiments [12], or to time-dependent photoemission spectroscopy [13, 14].

Originally all the mentioned methods were developed for electronic structure problems and therefore typically treat exclusively the quantum mechanical problem of interacting many-electron systems. However, electrons are not the only quantum particles that drive quantum processes in physics, chemistry, and materials science. In typical situations, the negatively charged electrons are accompanied by positively charged nuclei. Since these nuclei are orders of magnitude heavier than the electrons, most calculations in the electronic structure theory assume the Born-Oppenheimer approximation [15]. In the harmonic Born-Oppenheimer approximation, the nuclear degrees of freedom are typically also termed the phonon modes. For many physical processes, in particular, if the system is in a lowest energy (ground-state) configuration, the assumptions underlying the Born-Oppenheimer approximation are well justified. However, in particular dynamical processes, which include e.g. charge excitations or charge transfer, are typically mediated by quantum interactions. One important interaction here is the electron-nuclear interaction, but also the interaction of particles with the electromagnetic field (photon modes) has to be taken into account. Although the latter interaction is often assumed to be an interaction of the classical electromagnetic field subject to Maxwell's equations with the matter, this assumption breaks down in a quantum limit of few photons. Here, the quantized nature of the electromagnetic field has to be incorporated explicitly. The recently developed theory of QEDFT [16–18] allows to treat photons and electrons on the same quantized footing and is therefore suitable for electron-photon calculations in the quantum limit.

To quantify the effects of these fundamental electron-boson interactions (e.g. electron-phonon and electron-photon), we study in this thesis different situations for which these correlated interactions become important. Therefore, this thesis is divided into nine chapters:

Chapter 2 illustrates the theoretical background applied and developed for this thesis. We briefly discuss the general quantum many-body problem, DFT, the correlated electron-photon interaction, and photoelectron spectroscopy. Chapter 3 discusses the model systems and the numerical methods, which are used throughout this thesis. The applications of the theory are illustrated in the following chapters. In chapter 4, we study the quality of the Born-Oppenheimer approximation in photoelectron spectroscopy for a Su-Schrieffer-Heeger (SSH) model system, which is an electron-phonon problem. In chapter 5, we utilize the recently established framework of QEDFT to treat correlated electron-photon problems on an equal quantized footing in a density-functional framework. We discuss the theoretical framework and as the first application of this recent theory, we apply the framework to a simple yet nontrivial model system, the Jaynes-Cummings-Hubbard (JCH) model. Here, we analyze the quality of a mean-field approximation, which corresponds to a classical Maxwell-Schrödinger propagation scheme and amounts to the neglect of the exchange-correlation (xc) contribution in the Kohn-Sham (KS) potential. In chapter 6, we study the xc contributions for a correlated electron-photon system in a two-dimensional model in real space using fixed-point iterations to

construct the exact [KS](#) potential. In chapter [7](#), we show the first [QEDFT](#) calculations with an approximate [xc](#) potential based on the optimized effective potential ([OEP](#)) method. In the last chapter of the applications section, chapter [8](#), we treat a fully quantized electron-phonon-photon problem and show the implications of strong matter-photon coupling on the chemistry of the system. A summary of all findings of this thesis, a conclusion, and an outlook to future work are given in chapter [9](#).



## Part II

### THEORETICAL BACKGROUND



## THEORETICAL BACKGROUND

---

### 2.1 THE QUANTUM MANY-BODY PROBLEM

The time evolution of a many-body system of (quasi-) particles, e.g. nuclei, electrons, phonons, or photons is described quantum mechanically by the time-dependent Schrödinger equation [4]<sup>1</sup>

$$i\hbar \frac{\partial}{\partial t} |\Psi(t)\rangle = \hat{H}(t) |\Psi(t)\rangle, \text{ with } |\Psi(t=0)\rangle = |\Psi(t_0)\rangle. \quad (1)$$

The time-dependent (normalized) many-body wave function  $|\Psi(t)\rangle$  is a complex function on a Hilbert space  $\mathcal{H}$ . It contains all information about the properties of the system. The self-adjoint quantum-mechanical operator  $\hat{H}(t)$  is the time-dependent Hamiltonian operator of the system. Both, the Hamiltonian and the wave function are defined in a high-dimensional configuration space. The Schrödinger equation is a linear partial differential equation with an initial condition on the wave function (initial state)  $|\Psi(t_0)\rangle$ . This single equation is the only equation, which has to be solved to obtain any desired physical quantity, such as thermal coefficients [20], spectroscopic quantities [13], color [21], or the equilibrium structures [22] of the system of interest by calculating the corresponding observable or expectation value with  $O(t) = \langle \Psi(t) | \hat{O} | \Psi(t) \rangle$ . Here,  $\hat{O}$  is also a quantum mechanical operator defined in  $\mathcal{H}$ . Unfortunately, the Schrödinger equation is very hard to solve exactly for any realistic system. Therefore, in particular theoretical chemists and physicists have developed many different schemes to obtain approximate solutions to the Schrödinger equation.

In equilibrium or static situations, where the Hamiltonian  $\hat{H}(t) = \hat{H}$  is time-independent, the system is typically in the ground state. To obtain the ground state corresponding to the Hamiltonian, Eq. 1 can be restated in terms of an eigenvalue problem. The resulting equation is then called the static Schrödinger equation and is of the following form

$$\hat{H} |\Psi_n\rangle = E_n |\Psi_n\rangle. \quad (2)$$

Here,  $E_n$  are the eigenvalues and  $|\Psi_n\rangle$  the eigenfunctions/eigenstates of the system. If the Hamiltonian  $\hat{H}$  has a lower bound, it satisfies a variational principle. This variational principle is called the Rayleigh-Ritz minimal principle and can be used to obtain the lowest eigenvalue and eigenstate

$$E_0 = \langle \Psi_0 | \hat{H} | \Psi_0 \rangle \leq \langle \Psi | \hat{H} | \Psi \rangle, \quad (3)$$

where the lowest eigenvalue (ground-state energy)  $E_0$  corresponds to the ground-state wave function  $|\Psi_0\rangle$ , while  $|\Psi\rangle$  corresponds to an arbitrary wave function defined in  $\mathcal{H}$ .

---

<sup>1</sup> Throughout this thesis, we use SI units [19], unless stated otherwise.

### 2.1.1 Electron-Nuclear Hamiltonian

In Condensed Matter Physics, Quantum Chemistry, and Electronic Structure Theory, the main targets of numerical simulations are systems containing atoms, molecules, clusters or solids. All these systems contain electrons and nuclei and are therefore described quantum mechanically by the combined electron-nuclear Hamiltonian. To reduce computational complexity, in many numerical simulations only the electrons are considered explicitly, which is justified formally by the Born-Oppenheimer approximation (BOA)<sup>2</sup>. Excellent reviews on these topics can be found, e.g. in Refs. [23, 24].

This section first focuses on the general electron-nuclear Hamiltonian, then we apply the BOA to derive the electronic Born-Oppenheimer (BO) Hamiltonian.

The following electron-nuclear Hamiltonian contains  $n_e$  electrons and  $N_n$  nuclei. The electrons are described by the electronic coordinates  $\mathbf{r}_i$ , they carry electron mass  $m_e$  and negative electric charge ( $-e$ ). In addition, the nuclei in the system are defined by the nuclear coordinates  $\mathbf{R}_I$ , the nuclear mass  $M_I$  and the positive charge ( $Z_I e$ ). The Hamiltonian is then written as follows

$$\hat{H} = \hat{T}_e + \hat{T}_N + \hat{W}_{ee} + \hat{W}_{NN} + \hat{W}_{eN}, \quad (4)$$

with

$$\hat{T}_e = \sum_{i=1}^{n_e} \frac{1}{2m_e} \hat{\mathbf{p}}_i^2, \quad (5)$$

$$\hat{T}_N = \sum_{I=1}^{N_n} \frac{1}{2M_I} \hat{\mathbf{p}}_I^2, \quad (6)$$

$$\hat{W}_{ee} = \frac{1}{4\pi\epsilon_0} \sum_{i=1}^{n_e} \sum_{j>i}^{n_e} \frac{e^2}{|\mathbf{r}_i - \mathbf{r}_j|}, \quad (7)$$

$$\hat{W}_{NN} = \frac{1}{4\pi\epsilon_0} \sum_{I=1}^{N_n} \sum_{J>I}^{N_n} \frac{Z_I Z_J e^2}{|\mathbf{R}_I - \mathbf{R}_J|}, \quad (8)$$

$$\hat{W}_{eN} = -\frac{1}{4\pi\epsilon_0} \sum_{i=1}^{n_e} \sum_{J=1}^{N_n} \frac{Z_J e^2}{|\mathbf{r}_i - \mathbf{R}_J|}. \quad (9)$$

Here,  $\hat{T}_{e(N)}$  corresponds to the electron (nuclear) kinetic energy operator, while  $\hat{W}_{ee(eN/NN)}$  corresponds to the electron-electron (electron-nuclear/nuclear-nuclear) interaction energy operator. In the Hamiltonian, the electron and nuclear momentum operators are defined as  $\hat{\mathbf{p}}_j = \frac{\hbar}{i} \vec{\nabla}_j$  and  $\hat{\mathbf{p}}_J = \frac{\hbar}{i} \vec{\nabla}_J$ , respectively. Throughout this section we refer with small/capital letters to electronic/nuclear quantities. The Heisenberg uncertainty principle [25] dictates the position-momentum commutation relation, thus the following commutation relations are obeyed

$$[\mathbf{r}_i, \hat{\mathbf{p}}_j] = \mathbf{r}_i \hat{\mathbf{p}}_j - \hat{\mathbf{p}}_j \mathbf{r}_i = i\hbar \delta_{ij}, \quad [\mathbf{r}_i, \mathbf{r}_j] = [\hat{\mathbf{p}}_i, \hat{\mathbf{p}}_j] = 0, \quad (10)$$

both for electron and nuclear operators. Furthermore, electrons obey fermionic particle statistics, while nuclei with integer (half-integer) spin obey bosonic (fermionic)

<sup>2</sup> There are many fundamental processes in nonequilibrium-driven phenomena that require a proper treatment of the nuclear degrees of freedom in the system beyond the BOA, e.g. in photoelectron spectroscopy, which is the focus of Sec. 2.4 and Ch. 4.



spin statistics. Although the Hamiltonian in Eq. 4 does not explicitly depend on spin, the correct spin statistics has to be incorporated into the exact many-body wave function.

### 2.1.2 Born-Oppenheimer Approximation

In 1927, Max Born and Julius Robert Oppenheimer [15] proved that the fully correlated<sup>3</sup> electron-nuclear system can be partially decoupled into an electronic and a nuclear problem. In the BOA, the full electron-nuclear many-body wave function is expanded in terms of purely electronic and purely nuclear wave functions. The full expansion is exact in principle, but if the expansion is approximated by only considering the first term, the solution of the Schrödinger equation drastically simplifies. The BOA can be justified physically by the large mass difference between electrons and nuclei, which implies different timescales for each subsystem. Since the electrons have in general much lower masses than nuclei (more than three orders of magnitude), they can adjust much faster to a new charge (nuclei) configuration, than vice versa. Formulated differently, electrons adjust quasi-instantaneously to a modified nuclear configuration, which means effectively that electrons are in a stationary state for each nuclear configuration [26].

Applying the BOA to Eq. 4 has the following consequences: First, the nuclear kinetic energy contribution is neglected by assuming infinite nuclear masses ( $M_I \rightarrow \infty$ ). This assumption effectively reduces all nuclear coordinates  $\{\mathbf{R}\}$  to classical parameters, since the nuclear momentum as the quantum conjugated variable vanishes. Then in a second step, the remaining electronic Hamiltonian

$$\hat{H}_e(\{\mathbf{R}\}) = \hat{T}_e + \hat{W}_{ee} + \hat{W}_{eN}(\{\mathbf{R}\}), \quad (11)$$

with the corresponding (static) eigenvalue problem

$$\hat{H}_e(\{\mathbf{R}\}) |\phi_j(\{\mathbf{R}\})\rangle = E_j(\{\mathbf{R}\}) |\phi_j(\{\mathbf{R}\})\rangle \quad (12)$$

has to be solved for all fixed sets of possible nuclear configurations  $\{\mathbf{R}\}$  to obtain the electronic Born-Oppenheimer states. The eigenvalue  $E_j(\{\mathbf{R}\})$  and the nuclear Hamiltonian  $W_{NN}(\{\mathbf{R}\})$  from Eq. 8 contribute to the  $j$ -th BO potential-energy surface (PES) that is given by

$$U_j(\{\mathbf{R}\}) = W_{NN}(\{\mathbf{R}\}) + E_j(\{\mathbf{R}\}). \quad (13)$$

Thus, every electronic excitation corresponds to an individual potential-energy surface  $U_j$ . For each fixed set of nuclear coordinates  $\{\mathbf{R}\}$ , the electronic eigenstates  $|\phi_j(\{\mathbf{R}\})\rangle$  form a complete set in the electron many-particle Hilbert space. For a given set of nuclear coordinates  $\{\mathbf{R}\}$ , we can expand the exact many-body wave function in terms of the electronic eigenstates  $|\phi_j(\{\mathbf{R}\})\rangle$  and the nuclear eigenstates  $|\chi_{ij}(\{\mathbf{R}\})\rangle$  by the Born-Huang expansion [27]

$$|\Psi_i(\{\mathbf{R}\})\rangle = \sum_{j=0}^{\infty} |\chi_{ij}(\{\mathbf{R}\})\rangle \otimes |\phi_j(\{\mathbf{R}\})\rangle = \sum_{j=0}^{\infty} |\chi_{ij}(\{\mathbf{R}\})\phi_j(\{\mathbf{R}\})\rangle. \quad (14)$$

<sup>3</sup> The term correlated will appear repeatedly at various points of this thesis. By correlated systems, we refer to quantum systems, which are not separable, hence their eigenstates are not factorizable.

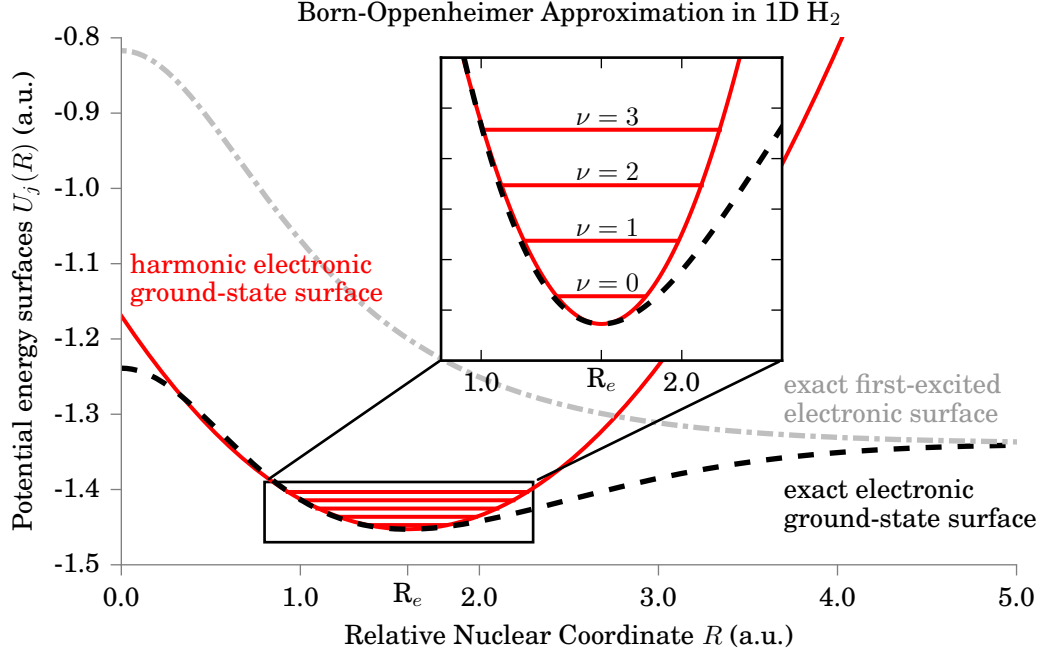


Figure 1: Born-Oppenheimer potential-energy surfaces in a Hydrogen molecule that is confined to one dimension:  $R_e$  corresponds to the equilibrium position of the relative nuclear coordinate, while  $\nu$  refers to nuclear (phonon) excitations.

Both, the electronic eigenstates  $|\phi_i(\{\mathbf{R}\})\rangle$ , as well as the nuclear eigenstates  $\chi_{ij}(\{\mathbf{R}\})$ , depend here parametrically on the set of nuclear coordinates  $\{\mathbf{R}\}$ . The nuclear states  $\chi_{ij}(\{\mathbf{R}\})$  are found by solving the corresponding nuclear Born-Oppenheimer Hamiltonian

$$\hat{H}_j(\{\mathbf{R}\}) = \hat{T}_N + \underbrace{W_{NN}(\{\mathbf{R}\}) + E_j(\{\mathbf{R}\})}_{U_j(\{\mathbf{R}\})} + \sum_{i=0}^{\infty} \langle \phi_j(\{\mathbf{R}\}) | \hat{T}_N | \phi_i(\{\mathbf{R}\}) \rangle, \quad (15)$$

where  $\hat{T}_N$  and  $W_{NN}$  are given by Eq. 6 and Eq. 8, respectively. Eq. 15 has to be solved for each electronic eigenstate  $j$  individually. Here, the matrix elements in the last term in the Hamiltonian are referred to as the nonadiabatic coupling elements that connect different PES. The Born-Oppenheimer approximation now neglects off-diagonal terms in the nonadiabatic coupling elements and only regards the first term in the expansion in Eq. 14, defining the Born-Oppenheimer states as

$$|\Psi_i(\{\mathbf{R}\})\rangle \sim |\chi_{ii}(\{\mathbf{R}\})\phi_i(\{\mathbf{R}\})\rangle. \quad (16)$$

Effectively, the nuclei now move in the electronic potential  $E_j(\{\mathbf{R}\})$ , as if the electrons were in their corresponding ground state. At first glance, this approximation may seem rather drastic, but it has been shown to yield incredibly accurate results for the low-lying states in the Born-Oppenheimer potential-energy surfaces. In particular, the Born-Oppenheimer ground state  $|\Psi_0(\{\mathbf{R}\})\rangle$  is often a remarkably good approximation to the exact ground state with small errors for many systems.

### 2.1.3 Phonons and the Harmonic Approximation

One additional simplification can be achieved by solving Eq. 12 not for every possible nuclear configuration  $\{\mathbf{R}\}$ , but only for the equilibrium positions  $\mathbf{R}_e$  and then Taylor-expand  $U_j(\{\mathbf{R}\})$  around this equilibrium configuration. If the expansion is taken to second order, we arrive at the harmonic Born-Oppenheimer approximation. This approximation is often sufficient for physical situations, where the nuclear positions remain close to their equilibrium positions. The harmonic nuclear Hamiltonian is then written in the following form

$$\hat{H}_j = \hat{T}_N + \sum_{I=1}^{N_p} \frac{1}{2} M_n \omega_{I,j}^2 (\mathbf{R}_I - \mathbf{R}_{I,j,e})^2. \quad (17)$$

Here,  $\mathbf{R}_{I,j,e}$  are the equilibrium positions of the nuclei in the  $j$ -th Born-Oppenheimer potential-energy surface and  $\omega_{I,j}$  are given by the slopes of the  $j$ -th Born-Oppenheimer potential-energy surface of Eq. 15 at the equilibrium positions  $\mathbf{R}_{I,j,e}$ . The Hamiltonian of Eq. 17 has the form of a sum of  $N_p$  independent quantum harmonic oscillators. These harmonic oscillator modes can be interpreted as quasi-particles and are called harmonic phonon modes. The phonon frequencies  $\mathbf{R}_{I,j,e}$  calculated in harmonic approximation turn out to be in excellent agreement with experiment for a vast majority of systems. All effects beyond the harmonic approximation (i.e. anharmonic effects) are important to describe phenomena linked to thermal expansion, phase transitions, and many others.

For a Hydrogen molecule that is confined to one dimension (1D H<sub>2</sub>), Fig. 1 shows two exact PES and the corresponding harmonic approximation as function of the relative nuclear coordinate, i.e. the difference between the two nuclear coordinates. The dashed lines correspond to exact Born-Oppenheimer PES, while the red solid line corresponds to the approximated harmonic potential of the ground-state potential-energy surface. The figure illustrates that the harmonic approximation is relatively close to the exact surface in the case of the ground state ( $\nu = 0$ ). For higher excitations ( $\nu > 0$ ), deviations between the harmonic PES and the exact PES appear, which increase for higher  $\nu$ . The first-excited electronic surface for an one-dimensional Hydrogen molecule has no local minima and hence does not support molecular binding. For large atomic distances, the ground-state and the first-excited state surface both converge towards the limit of the energy of two independent Hydrogen atoms.

### 2.1.4 Particles in Second Quantization

In this section, we briefly introduce the second quantization formalism for fermions and bosons. The Hamiltonian of Eq. 11 is formulated in first quantization, i.e. it is defined for a fixed number of electrons  $n_e$ . Systems for which the number of electrons is not conserved, e.g. open systems, require a reformulation of Eq. 11 in second quantization. All operators present in Eq. 11 can be reformulated alterna-

tively in second quantization. For the one-body operators  $\hat{T}_e$  and  $\hat{W}_{eN}(\{\mathbf{R}\})$ , we find

$$\hat{T}_e = \int d^3\mathbf{r} \hat{\Psi}^\dagger(\mathbf{r}) \frac{1}{2m_e} \hat{\mathbf{p}}^2 \hat{\Psi}(\mathbf{r}), \quad (18)$$

$$\hat{W}_{eN}(\{\mathbf{R}\}) = \int d^3\mathbf{r} w_{eN}(\mathbf{r}, \{\mathbf{R}\}) \hat{\Psi}^\dagger(\mathbf{r}) \hat{\Psi}(\mathbf{r}), \quad (19)$$

while the two-body operator  $\hat{W}_{ee}$  is written in second quantization as follows

$$\hat{W}_{ee} = \frac{1}{2} \int d^3\mathbf{r} \int d^3\mathbf{r}' w_{ee}(\mathbf{r}, \mathbf{r}') \hat{\Psi}^\dagger(\mathbf{r}) \hat{\Psi}^\dagger(\mathbf{r}') \hat{\Psi}(\mathbf{r}') \hat{\Psi}(\mathbf{r}) \quad (20)$$

using the functions

$$w_{ee}(\mathbf{r}, \mathbf{r}') = \frac{e^2}{4\pi\epsilon_0} \frac{1}{|\mathbf{r} - \mathbf{r}'|},$$

$$w_{eN}(\mathbf{r}, \{\mathbf{R}_I\}) = - \sum_{I=1}^{N_h} \frac{Z_I e^2}{4\pi\epsilon_0} \frac{1}{|\mathbf{r} - \mathbf{R}_I|}.$$

In this definition,  $\hat{\Psi}^\dagger(\mathbf{r})$  and  $\hat{\Psi}(\mathbf{r})$  are the electronic creation and annihilation field operators of single-particle states, which create or annihilate an electron at point  $\mathbf{r}$  in space, respectively. These operators have two spin components ( $\sigma = \uparrow / \downarrow$ ) and obey the fermionic anti-commutation (+) relations (we denote now the spin-component explicitly by  $\sigma$ ), which leads to

$$[\hat{\Psi}_\sigma(\mathbf{r}), \hat{\Psi}_{\sigma'}^\dagger(\mathbf{r}')]_+ = \hat{\Psi}_\sigma(\mathbf{r}) \hat{\Psi}_{\sigma'}^\dagger(\mathbf{r}') + \hat{\Psi}_{\sigma'}^\dagger(\mathbf{r}') \hat{\Psi}_\sigma(\mathbf{r}) = \delta(\mathbf{r} - \mathbf{r}') \delta_{\sigma\sigma'}, \quad (21)$$

$$[\hat{\Psi}_\sigma(\mathbf{r}), \hat{\Psi}_{\sigma'}(\mathbf{r}')]_+ = [\hat{\Psi}_\sigma^\dagger(\mathbf{r}), \hat{\Psi}_{\sigma'}^\dagger(\mathbf{r}')]_+ = 0. \quad (22)$$

The commutation relations assure that by interchanging two indistinguishable particles the many-body wave function acquires an additional minus sign as prefactor, i.e.

$$\Psi(\mathbf{r}_1, \mathbf{r}_2, \mathbf{r}_3, \mathbf{r}_4, \dots, \mathbf{r}_{n_e}) = -\Psi(\mathbf{r}_1, \mathbf{r}_4, \mathbf{r}_3, \mathbf{r}_2, \dots, \mathbf{r}_{n_e}).$$

In contrast to fermionic field operators, bosonic creation and annihilation field operators  $\hat{\Phi}^\dagger(\mathbf{r})$  and  $\hat{\Phi}(\mathbf{r})$  obey the boson commutation relations

$$[\hat{\Phi}(\mathbf{r}), \hat{\Phi}^\dagger(\mathbf{r}')] = \hat{\Phi}(\mathbf{r}) \hat{\Phi}^\dagger(\mathbf{r}') - \hat{\Phi}^\dagger(\mathbf{r}') \hat{\Phi}(\mathbf{r}) = \delta(\mathbf{r} - \mathbf{r}'), \quad (23)$$

$$[\hat{\Phi}(\mathbf{r}), \hat{\Phi}(\mathbf{r}')] = [\hat{\Phi}^\dagger(\mathbf{r}), \hat{\Phi}^\dagger(\mathbf{r}')] = 0, \quad (24)$$

which leads to

$$\Phi(\mathbf{r}_1, \mathbf{r}_2, \mathbf{r}_3, \mathbf{r}_4, \dots, \mathbf{r}_{n_e}) = \Phi(\mathbf{r}_1, \mathbf{r}_4, \mathbf{r}_3, \mathbf{r}_2, \dots, \mathbf{r}_{n_e}).$$

## 2.2 DENSITY-FUNCTIONAL THEORY

In the previous sections, we have briefly presented solutions to quantum many-body problems in terms of wave functions. In many-body systems, these wave

functions provide a natural path to obtain observables in and out of equilibrium by taking the expectation value of hermitian operators. In practice, this is often not realizable, due to the large parameter space span by the wave function<sup>4</sup>. For a  $n_e$  electron system, the wave function depends on the spatial coordinates of each electron, i.e.  $3n_e$  independent coordinates. All these coordinates imply a total parameter space of  $10^{3n_e}$ , if for example each coordinate is just sampled on 10 points. For large systems, which here already refers to  $n_e > 10$ , even if the wave function as solution was found, it would be impossible to store the total wave function on an ordinary hard disk. In literature, this exponential scaling is often referred to as the exponential wall of many-body problems [5]. However in most practical applications of quantum mechanics, we are not interested in knowing the full many-body wave function, but instead we would like to arrive at predictions for physical observables. These observables are usually reduced quantities, such as the ground-state energy, excitation energies, or binding energies which are all single real numbers, or the electric charge distribution, or magnetization which are three-dimensional functions. This observation suggests a change of perspective: Is it possible without loosing generality to reformulate the Schrödinger equation such that instead of the wave function a reduced variable becomes the central quantity? In this way, we could avoid the many-body wave function and only consider reduced quantities that provide us access to the relevant observables. It turns out that this is possible by DFT. In literature, there exist many different flavors of density-functional theories. All share that they are based on a specific one-to-one correspondence between conjugated variables. Typically the name density-functional theory refers to the ground-state density-functional theory. It is also the most popular density-functional theory and the conjugated variables are the ground-state density  $n_0(\mathbf{r})$  and the static external potential  $v_0(\mathbf{r})$ . Other flavors are, e.g. the generalization to time-dependent situations, which is named TDDFT. Here, the density and the external potential become time-dependent. Besides these two density-functional theories, which share the electron density as basic variable, there exist also other density-functional theories, such as time-dependent current density-functional theory (TDCDFT), where the conjugated variables are the electronic current density  $\mathbf{J}(\mathbf{r}, t)$  and the external vector potential  $\mathbf{A}(\mathbf{r}, t)$  [28]. TDCDFT allows the treatment of magnetic fields, but is much less developed than DFT or TDDFT. The generalization to quantum fields, QEDFT [18], where sets of conjugated variables appear is discussed in more detail in Ch. 5 and following.

### 2.2.1 Ground-State Density-Functional Theory

This section is dedicated to ground-state DFT and we focus on aspects, which become important in the following chapters. Comprehensive reviews on DFT can be found, e.g. in Refs. [5, 29–32]. In ground-state DFT, the fundamental (basic) quantity is the (ground-state) electron density  $n_0(\mathbf{r})$ , which is an one-body quantity and only depends on three spatial coordinates. It is defined to yield the probability of

<sup>4</sup> In fact, quantum systems for which the exact wave functions are computationally accessible are the exception rather than the rule.

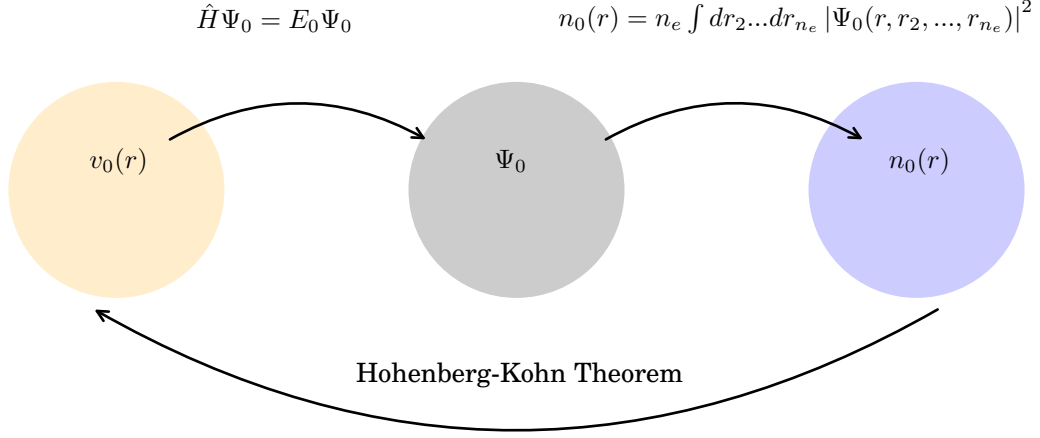


Figure 2: Graphical schematics of the Hohenberg-Kohn theorem: One-to-one correspondence between the external potential  $v_0(\mathbf{r})$  and the ground-state density  $n_0(\mathbf{r})$ .

finding an electron at a given point  $\mathbf{r}$  in space and can be calculated in terms of the ground-state wave function  $\Psi_0$  as follows

$$n_0(\mathbf{r}) = n_e \int d^3\mathbf{r}_2 \dots d^3\mathbf{r}_{n_e} |\Psi_0(\mathbf{r}, \mathbf{r}_2, \dots, \mathbf{r}_{n_e})|^2. \quad (25)$$

The integration variables include all electron coordinates  $\{\mathbf{r}\}$  excluding one. Additionally, the electron density is normalized to the number of electrons  $n_e = \int d^3\mathbf{r} n_0(\mathbf{r})$ . Alternatively, we can define  $n_0(\mathbf{r})$  in second quantization

$$n_0(\mathbf{r}) = \langle \Psi_0 | \hat{n}(\mathbf{r}) | \Psi_0 \rangle = \langle \Psi_0 | \hat{\Psi}^\dagger(\mathbf{r}) \hat{\Psi}(\mathbf{r}) | \Psi_0 \rangle. \quad (26)$$

$|\Psi_0\rangle$  is the ground state of the following time-independent Hamiltonian in agreement with Eq. 11

$$\hat{H}_e = \hat{T}_e + \hat{W}_{ee} + \hat{V}_0, \quad (27)$$

where the external potential operator  $\hat{V}_0$  includes the electron-nuclear interaction operator  $\hat{W}_{eN}$  from Eq. 9 and can be written explicitly as a sum of single-particle potentials  $\hat{V}_0 = \sum_{i=1}^{n_e} v_0(\mathbf{r}_i)$ . The question, whether any arbitrary electron density  $n_0(\mathbf{r})$  can be constructed by an antisymmetric wave function  $\Psi_0$  as in Eq. 25 is termed the  $n$ -representability problem [31]. It has been shown [33, 34] that any finite nonnegative differentiable function is a  $n$ -representable electron density.

In 1964, Hohenberg and Kohn proved in their ground-breaking paper [6] the one-to-one correspondence (bijective mapping) between the ground-state density  $n_0(\mathbf{r})$  and the external potential  $v_0(\mathbf{r})$ . This means that the external potential determines the ground-state density uniquely and vice versa. By connecting both quantities to the ground-state wave function, Hohenberg and Kohn show that knowing the ground-state electron density is sufficient to calculate all observables in the system, at least in principle. All observables are functionals of the ground-state density. However, in many cases, this functional dependence may not be known explicitly [5]. In Fig. 2, we schematically depict the Hohenberg-Kohn theorem.

### 2.2.2 Hohenberg-Kohn Theorem

The Hohenberg-Kohn theorem states explicitly the following [6]: “The ground-state density  $n_0(\mathbf{r})$  in some external potential  $v_0(\mathbf{r})$  determines this potential uniquely.”

This theorem was proved as follows: Let  $n_0(\mathbf{r})$  be a nondegenerate ground-state density of  $n_e$  electrons in the potential  $v_0(\mathbf{r})$  corresponding to the ground state  $|\Psi_0\rangle$  and the ground-state energy  $E_0$ .  $E_0$  is defined as

$$E_0 = \langle \Psi_0 | \hat{H}_e | \Psi_0 \rangle = \int d^3\mathbf{r} v_0(\mathbf{r}) n_0(\mathbf{r}) + \langle \Psi_0 | \hat{T}_e + \hat{W}_{ee} | \Psi_0 \rangle.$$

Now, we assume that there exists a second potential  $v_1(\mathbf{r})$ , with a ground state  $|\Psi_1\rangle$ , different to  $v_0(\mathbf{r})$  and  $|\Psi_0\rangle$ , but leading to the same density  $n_0(\mathbf{r})$ . It follows that

$$E_1 = \int d^3\mathbf{r} v_1(\mathbf{r}) n_0(\mathbf{r}) + \langle \Psi_1 | \hat{T}_e + \hat{W}_{ee} | \Psi_1 \rangle.$$

By applying the minimal principle (Eq. 3), we get

$$E_0 < \int d^3\mathbf{r} v_0(\mathbf{r}) n_0(\mathbf{r}) + \langle \Psi_1 | \hat{T}_e + \hat{W}_{ee} | \Psi_1 \rangle = E_1 + \int d^3\mathbf{r} (v_0(\mathbf{r}) - v_1(\mathbf{r})) n_0(\mathbf{r})$$

and

$$E_1 < \int d^3\mathbf{r} v_1(\mathbf{r}) n_0(\mathbf{r}) + \langle \Psi_0 | \hat{T}_e + \hat{W}_{ee} | \Psi_0 \rangle = E_0 + \int d^3\mathbf{r} (v_1(\mathbf{r}) - v_0(\mathbf{r})) n_0(\mathbf{r}).$$

Adding both inequalities leads to the contradiction  $E_0 + E_1 < E_0 + E_1$  and we can conclude by *reductio ad absurdum* that the assumption of the existence of  $v_1(\mathbf{r})$  is wrong. The generalization of this theorem to degenerate ground states has been worked out by Lieb [35]. Note, that the Hohenberg-Kohn theorem requires a fixed number of particles  $n_e$ , a fixed kinetic energy operator  $\hat{T}_e$ , and a fixed electron-electron interaction operator  $\hat{W}_{ee}$ . If one of these three variables is changed, it may be possible to generate the same density  $n_0$  by a *different* external potential. This feature is exploited later in the Kohn-Sham approach.

The total ground-state energy  $E_0[n_0]$  can be found by a variational principle

$$E_0[n_0] = \min_{\Psi \rightarrow n_0} \langle \Psi | \hat{H}_e | \Psi \rangle = \min_{\Psi \rightarrow n_0} \underbrace{\langle \Psi | \hat{T}_e + \hat{W}_{ee} | \Psi \rangle}_{F[n_0]} + \int d^3\mathbf{r} v_0(\mathbf{r}) n_0(\mathbf{r}). \quad (28)$$

In the above equation, we define the functional  $F[n_0]$ , which does not depend explicitly on the applied external potential  $v_0(\mathbf{r})$ . This is why,  $F[n_0]$  is also called the *universal* Hohenberg-Kohn functional. For three-dimensional Coulomb systems, the explicit form of  $F[n_0]$  is unknown and needs to be approximated for practical applications.

From the static Schrödinger equation in Eq. 2 with the Hamiltonian defined in Eq. 27, we find that we can label all ground-state wave functions  $|\Psi_0\rangle$  by their generating external potential, thus the ground-state densities can also be seen as having a functional dependence on  $v_0$ , such that

$$|\Psi_0\rangle \longrightarrow |\Psi_0[v_0]\rangle \longrightarrow |\Psi_0[n_0]\rangle. \quad (29)$$

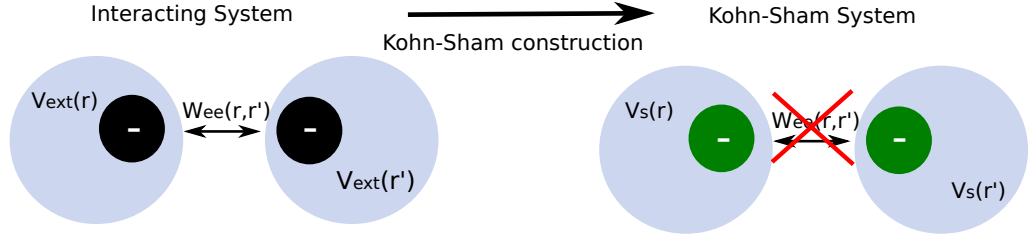


Figure 3: Kohn-Sham construction: Many-body density in external potential  $v_{\text{ext}}(\mathbf{r})$  is reproduced by auxiliary Kohn-Sham system in Kohn-Sham potential  $v_s(\mathbf{r})$ .

In the last step, we already used the one-to-one correspondence proved by Hohenberg and Kohn to replace the functional dependence on  $v_0$  by  $n_0$ . Through the ground-state wave function this functional dependence is inherited by all observables  $O[n_0] = \langle \Psi_0[n_0] | \hat{O} | \Psi_0[n_0] \rangle$ , which therefore become functionals of the ground-state density. This equation yields a strong statement, which leads to the following consequences: In principle, it is sufficient to know the ground-state density, from which then any desired ground-state observable, but also excited-state observables [36] can be obtained, at least in principle. Thus, the explicit knowledge of the exact ground-state wave function becomes obsolete.

The question, whether a given density  $n$ , which can be constructed as in Eq. 25, is a ground-state density of a local potential  $v_0(\mathbf{r})$ , is the  $v$ -representability problem [31, 37]. Here, the Hohenberg-Kohn theorem only guarantees that the mapping of the electron density  $n_0$  to the external potential  $v_0$  is unique, but not that it exists. While there are examples for non- $v$ -representable densities [38, 39], there exist proofs for ensemble  $v$ -representability on lattice systems [31, 37].

### 2.2.3 Kohn-Sham System in DFT

The one-to-one correspondence between the density and the external potential has an appealing consequence: The ground-state proof states that for a given interaction  $\hat{W}_{ee}$ , a density  $n_0(\mathbf{r})$  determines the corresponding external potential  $v_0(\mathbf{r})$  uniquely. But, if we change  $\hat{W}_{ee}$ , it is possible to reproduce the same  $n_0(\mathbf{r})$  with a different (effective) potential  $v_s(\mathbf{r})$ . This approach allows to replace a system of  $n_e$  interacting electrons, obeying the many-body Hamiltonian of Eq. 27, by an artificial (auxiliary) system of  $n_e$  noninteracting Kohn-Sham particles [8]. At first glance, the Kohn-Sham approach overcomes the exponential barrier, since in the Kohn-Sham system we are left with  $n_e$  single-particle equations, instead of the full interacting  $n_e$ -body problem. However, in the end of this section, we will see that the exponential wall is hidden in the effective Kohn-Sham potential  $v_s(\mathbf{r})$ . This potential mimics the electron-electron interaction such that the electron density in the Kohn-Sham system of artificial particles is equal to the electron density of the interacting many-body system.



The noninteracting Kohn-Sham system of  $n_e$  Kohn-Sham particles is described by the Kohn-Sham equation

$$\left( \frac{1}{2m_e} \hat{\mathbf{p}}^2 + \underbrace{v_{\text{ext}}(\mathbf{r}) + v_{\text{H}}(\mathbf{r}) + v_{\text{xc}}(\mathbf{r})}_{v_{\text{s}}(\mathbf{r})} \right) \phi_i(\mathbf{r}) = \epsilon_i \phi_i(\mathbf{r}), \quad (30)$$

where  $\phi_i(\mathbf{r})$  are the Kohn-Sham orbitals. The Kohn-Sham potential  $v_{\text{s}}(\mathbf{r})$ <sup>5</sup> includes the external potential  $v_{\text{ext}}(\mathbf{r})$ , the classical Hartree potential

$$v_{\text{H}}(\mathbf{r}) = \frac{e^2}{4\pi\epsilon_0} \int d^3\mathbf{r}' \frac{n_0(\mathbf{r}')}{|\mathbf{r} - \mathbf{r}'|} \quad (31)$$

and the exchange-correlation potential  $v_{\text{xc}}(\mathbf{r})$ . From the single-particle orbitals  $\phi_i(\mathbf{r})$ , the density can then be constructed using

$$n_0(\mathbf{r}) = \sum_{i=1}^{n_e} |\phi_i(\mathbf{r})|^2. \quad (32)$$

The noninteracting Kohn-Sham wave function  $\Phi(\mathbf{r}_1, \mathbf{r}_2, \dots, \mathbf{r}_{n_e})$  in its properly antisymmetric form can also be constructed explicitly using the Kohn-Sham orbitals  $\phi(\mathbf{r})$ . Due to the fermionic nature of the electrons, it consists of a single Slater determinant

$$\Phi(\mathbf{r}_1, \mathbf{r}_2, \dots, \mathbf{r}_{n_e}) = \frac{1}{\sqrt{n_e!}} \begin{vmatrix} \phi_1(\mathbf{r}_1) & \phi_1(\mathbf{r}_2) & \dots & \phi_1(\mathbf{r}_{n_e}) \\ \phi_2(\mathbf{r}_1) & \phi_2(\mathbf{r}_2) & \dots & \phi_2(\mathbf{r}_{n_e}) \\ \dots & \dots & \dots & \dots \\ \phi_{n_e}(\mathbf{r}_1) & \phi_{n_e}(\mathbf{r}_2) & \dots & \phi_{n_e}(\mathbf{r}_{n_e}) \end{vmatrix}. \quad (33)$$

The total (many-body ground-state) energy  $E_0$  is defined as

$$E_0[n_0] = T_s[n_0] + U[n_0] + E_{\text{xc}}[n_0] + \int d^3\mathbf{r} v_{\text{ext}}(\mathbf{r}) n_0(\mathbf{r}), \quad (34)$$

with the noninteracting kinetic energy  $T_s[n_0] = \langle \Phi | \hat{T}_e | \Phi \rangle$ , the Hartree energy

$$U[n_0] = \frac{e^2}{8\pi\epsilon_0} \int d^3\mathbf{r} \int d^3\mathbf{r}' \frac{n_0(\mathbf{r}') n_0(\mathbf{r})}{|\mathbf{r} - \mathbf{r}'|},$$

and the exchange-correlation energy

$$E_{\text{xc}}[n_0] = \int d^3\mathbf{r} \epsilon_{\text{xc}}([n_0], \mathbf{r}) n_0(\mathbf{r}) \quad (35)$$

with the exchange-correlation energy density  $\epsilon_{\text{xc}}([n_0], \mathbf{r})$  and

$$v_{\text{xc}}(\mathbf{r}) = \frac{\delta E_{\text{xc}}[n_0]}{\delta n_0}. \quad (36)$$

<sup>5</sup> The question of existence of  $v_{\text{s}}(\mathbf{r})$  is called the noninteracting  $v$ -representability problem. For details on this topic, see e.g. Ref. [31].

The total energy  $E_0$  in Eq. 34 can also be reformulated in terms of the Kohn-Sham eigenenergies  $\epsilon_i$  of Eq. 30

$$E_0[n_0] = \sum_{i=1}^{n_e} \epsilon_i - U[n_0] - \int d^3\mathbf{r} v_{\text{xc}}(\mathbf{r}) n_0(\mathbf{r}) + E_{\text{xc}}[n_0]. \quad (37)$$

The exchange-correlation potential  $v_{\text{xc}}(\mathbf{r})$  is responsible to correctly account for all quantum many-body effects, e.g. electron spin-dependent effects, van-der Waals interactions [40], or electron-hole pair creation. From Eq. 28, we can directly connect the universal Hohenberg-Kohn functional  $F[n_0]$  to  $E_{\text{xc}}[n_0]$ :

$$E_{\text{xc}}[n_0] = F[n_0] - T_s[n_0] - U[n_0]. \quad (38)$$

Typically the exchange correlation potential is split further into  $v_{\text{xc}} = v_x + v_c$ , where the first part is responsible for all exchange effects due to the electron spin, while the second part accounts for all correlation effects, which are caused by the Coulombic electron-electron repulsion.

#### 2.2.3.1 Exact Kohn-Sham Potential Construction

In small systems, where it is possible to obtain the exact solution in terms of the wave function, we can construct the Kohn-Sham potential  $v_s$  explicitly [41]. This procedure can give important insight and may help to improve existing approximations. For single electron or the two electrons-singlet problem, we can reformulate the definition of the density in Eq. 32 as  $\phi(\mathbf{r}) = \sqrt{n_0(\mathbf{r})}$  or  $\phi(\mathbf{r}) = \sqrt{n_0(\mathbf{r})/2}$ , because we can choose the ground state to be real and insert it in Eq. 30 to obtain [42]

$$v_s(\mathbf{r}) = \frac{\hbar^2}{2m_e} \frac{\vec{\nabla}^2 \sqrt{n_0(\mathbf{r})}}{\sqrt{n_0(\mathbf{r})}} + E_0. \quad (39)$$

In the Kohn-Sham equation of Eq. 30, only the exchange-correlation potential  $v_{\text{xc}}(\mathbf{r})$  remains unknown. Since this potential is not known in general, we need to rely on approximations in actual calculations. Thus, the exponential wall in quantum many-body problems is hidden in this potential. We will briefly discuss common (ground-state) approximations in the following section.

#### 2.2.3.2 Approximations to the Exchange-Correlation Potential

There exist many different ways to find approximations for  $v_{\text{xc}}$ . For instance, see e.g. Ref. [43] and references therein for a complete overview on existing and commonly used approximate functionals.

#### 2.2.3.3 Local-Density Approximation

The LDA [8] is the most prominent approximation, which is widely used for different applications, ranging from solids, molecular clusters, atoms and molecules. Initially, LDA was used to describe solids, where the electronic structure is considered to be highly homogeneous and thus comparable to the one of the homogeneous electron gas. However, the LDA is now also extensively used for atoms and molecules, where it often yields remarkably accurate bond lengths [44]. The

general idea behind [LDA](#) is the following: In general, the exchange-correlation potential at point  $\mathbf{r}$  in space depends not only on the value of the density at the same point  $n_0(\mathbf{r})$ , but on the whole spatial-resolution of the density  $n_0$ . However, it may be possible to expand the potential in terms of the derivatives of the density as

$$v_{xc}([n_0], \mathbf{r}) = v_{xc}([n_0, \vec{\nabla} n_0, \vec{\nabla}^2 n_0, \dots], \mathbf{r}).$$

The [LDA](#) neglects any derivative of the electron density in  $v_{xc}$  and only considers the density *locally*. Furthermore, one uses the exchange-correlation energy density  $\epsilon_{xc}([n_0], \mathbf{r})$  of a homogeneous electron gas.  $\epsilon_{xc}$  is connected to  $v_{xc}$  by Eqns. [35-36](#). For the homogeneous electron gas, the exchange contribution  $\epsilon_x$  can be calculated analytically, while the correlation contribution  $\epsilon_c$  can be obtained to high accuracy by Monte-Carlo methods [\[45\]](#).

#### 2.2.3.4 Beyond the Local-density Approximation

A natural extension to the [LDA](#) are approximations, in which spatial-derivatives of the density are also considered. This procedure is called *semi-local*. Popular functionals here are the [GGA](#) [\[9, 46\]](#) such as the Perdew-Burke-Ernzerhof ([PBE](#)) [\[47\]](#) approximation including its extension to solids [PBEsol](#) [\[48\]](#). With the development of the first semi-local functionals, [DFT](#) became also popular for quantum chemistry applications [\[49\]](#). In the last years, new developments, such as the hybrid functionals [\[50\]](#), which treat the spin-interaction partly exact or the  $C_6$ -approximations [\[40\]](#), which are able to describe van-der Waals interactions became very successful and are now the state-of-the-art for large-scale [DFT](#) calculations.

#### 2.2.4 Time-Dependent Density-Functional Theory

In this section, we introduce [TDDFT](#). Comprehensive reviews on [TDDFT](#) can be found e.g. in Refs. [\[26, 51, 52\]](#). In [TDDFT](#), the fundamental variable is the time-dependent electron density  $n(\mathbf{r}, t)$ , which is defined in analogy to Eq. [25](#) as

$$n(\mathbf{r}, t) = n_e \int d^3\mathbf{r}_2 \dots d^3\mathbf{r}_{n_e} |\Psi(\mathbf{r}, \mathbf{r}_2, \dots, \mathbf{r}_{n_e}, t)|^2, \quad (40)$$

where the many-body wave function  $\Psi(\mathbf{r}, \mathbf{r}_2, \dots, \mathbf{r}_{n_e}, t)$  is now a time-dependent wave function evolving from the initial state  $\Psi(t_0)$  and subject to the time-dependent Hamiltonian

$$\hat{H}(t) = \hat{T}_e + \hat{W}_{ee} + \hat{V}(t). \quad (41)$$

The external potential operator  $\hat{V}(t)$  includes the electron-nuclear interaction operator  $\hat{W}_{eN}$  of Eq. [9](#), but also an additional, possibly time-dependent, external potential acting solely on the electrons, e.g. the potential of an external laser field applied to the system.  $\hat{V}(t)$  can also be written explicitly as a sum of single-particle potentials  $\hat{V}(t) = \sum_{i=1}^{n_e} v(\mathbf{r}_i, t)$ .

### 2.2.5 Equation of Motion for the Electron Density

The equation of motion (EOM) for the time-dependent density in Eq. 40 can be derived in the second-quantization framework (Eq. 26). The EOM is then derived by applying the Heisenberg equation of motion, which provides a connection between the time derivative of an expectation value  $A(t) = \langle \Psi(t) | \hat{A}(t) | \Psi(t) \rangle$  to the commutator of the corresponding operator  $\hat{A}(t)$  with the Hamiltonian  $\hat{H}(t)$  here written in the Schrödinger picture as

$$\frac{d}{dt}A(t) = \frac{i}{\hbar} \langle \Psi(t) | [\hat{H}(t), \hat{A}(t)] | \Psi(t) \rangle + \langle \Psi(t) | \frac{\partial \hat{A}(t)}{\partial t} | \Psi(t) \rangle. \quad (42)$$

If the operator  $\hat{A}(t) = \hat{A}$  is not explicitly time-dependent, which is typically the case in the Schrödinger picture, we find for the  $k$ -th derivative

$$\frac{\partial^k}{\partial t^k}A(t) = \left(\frac{i}{\hbar}\right)^k \langle \Psi(t) | \underbrace{[\hat{H}(t), [\hat{H}(t), [\hat{H}(t), \dots [\hat{H}(t), \hat{A}]]]]}_{k\text{-times}} | \Psi(t) \rangle. \quad (43)$$

Applying Eq. 42 for the electron density leads to the first time-derivative of the density, which is the continuity equation

$$\frac{\partial}{\partial t}n(\mathbf{r}, t) = -\vec{\nabla} \cdot \mathbf{J}(\mathbf{r}, t), \quad (44)$$

where we define the electron current density operator as

$$\hat{\mathbf{J}}(\mathbf{r}) = \frac{\hbar}{2im_e} \left( \hat{\Psi}^\dagger(\mathbf{r}) \left( \vec{\nabla} \hat{\Psi}(\mathbf{r}) \right) - \left( \vec{\nabla} \hat{\Psi}^\dagger(\mathbf{r}) \right) \hat{\Psi}(\mathbf{r}) \right). \quad (45)$$

For the second time-derivative on the density, we use Eq. 42 twice and obtain

$$\begin{aligned} \frac{\partial^2}{\partial t^2}n(\mathbf{r}, t) &= -\vec{\nabla} \cdot \left( \frac{\partial}{\partial t} \mathbf{J}(\mathbf{r}, t) \right) = -\frac{i}{\hbar} \vec{\nabla} \cdot \langle \Psi(t) | [\hat{H}, \hat{\mathbf{J}}(\mathbf{r})] | \Psi(t) \rangle \\ &= -\vec{\nabla} \cdot \mathbf{Q}(\mathbf{r}, t) + \frac{1}{m_e} \vec{\nabla} \cdot \left[ n(\mathbf{r}, t) \vec{\nabla} v(\mathbf{r}, t) \right], \end{aligned} \quad (46)$$

with the electronic stress force [17]

$$\mathbf{Q}(\mathbf{r}, t) = -\frac{i}{\hbar} \langle \Psi(t) | [\hat{\mathbf{J}}, \hat{T}_e + \hat{W}_{ee}] | \Psi(t) \rangle. \quad (47)$$

### 2.2.6 Runge-Gross Theorem

In 1984, Erich Runge and Eberhard K.U. Gross proved [10] that for fixed initial state  $\Psi(t_0)$  there exists an one-to-one correspondence between the time-dependent density  $n(\mathbf{r}, t)$  and the time-dependent external potential  $v_{\text{ext}}(\mathbf{r}, t)$ . The Runge-Gross theorem forms the basis of TDDFT and proves that TDDFT is an exact reformulation<sup>6</sup> of the time-dependent Schrödinger equation in Eq. 1. Fig. 4 schematically illustrates the proof, which we briefly sketch in the following. The proof concludes

<sup>6</sup> The question of the time-dependent  $v$ -representability was treated in Ref. [53].

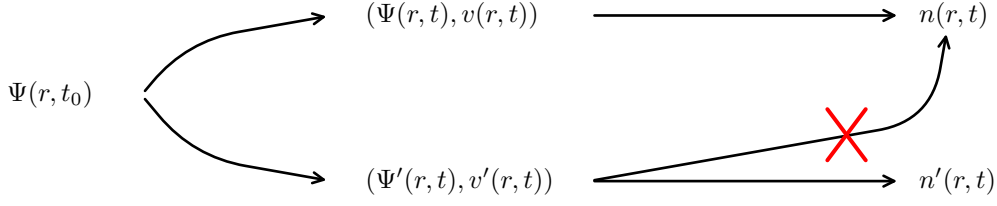


Figure 4: Schematic Runge-Gross proof: Evolving from the same initial state  $\Psi(r, t_0)$ , two different wave functions  $\Psi(r, t)$  and  $\Psi'(r, t)$  will always lead to different densities  $n(r, t)$  and  $n'(r, t)$ , if the potentials  $v(r, t)$  and  $v'(r, t)$  differ by more than a trivial time-dependent constant.

that two solutions  $\Psi(t)$  and  $\Psi'(t)$  to the time-dependent Schrödinger equation governed by the time-dependent Hamiltonians  $\hat{H}(t)$  and  $\hat{H}'(t)$  of Eq. 41 with external potentials  $v(\mathbf{r}, t)$  and  $v'(\mathbf{r}, t)$ , but common initial state  $\Psi(t_0)$ , never lead to the same evolution of the electron density  $n(\mathbf{r}, t)$ , if the two potentials are different such that  $v(\mathbf{r}, t) \neq v'(\mathbf{r}, t) + c(t)$ . Here, the time-dependent constant function  $c(t)$  has no spatial dependence. This restriction however does not assume that e.g. at initial time  $t_0$   $v(\mathbf{r}, t_0) \neq v'(\mathbf{r}, t_0) + c(t_0)$ . The original proof assumes time analyticity in the external potentials, such that a Taylor-expansion in  $t$  around the initial time  $t = t_0$  is possible<sup>7</sup>. Assuming time analyticity, we can expand the external potentials in Taylor series such that

$$v(\mathbf{r}, t) = \sum_{k=0}^{\infty} \frac{1}{k!} v_k(\mathbf{r}, t_0) (t - t_0)^k, \text{ and } v'(\mathbf{r}, t) = \sum_{k=0}^{\infty} \frac{1}{k!} v'_k(\mathbf{r}, t_0) (t - t_0)^k, \quad (48)$$

where we used the Taylor-coefficients  $v_k(\mathbf{r}, t_0) = \frac{\partial^k}{\partial t^k} v(\mathbf{r}, t)|_{t=t_0}$ . The inequality  $v(\mathbf{r}, t) \neq v'(\mathbf{r}, t) + c(t)$  requires that a minimal integer  $k_{\min}$  exists for which

$$\frac{\partial^k}{\partial t^k} (v(\mathbf{r}, t) - v'(\mathbf{r}, t))|_{t=t_0} \neq \text{const.} \quad (49)$$

Let us first focus on the current densities  $\mathbf{J}(\mathbf{r}, t)$  and  $\mathbf{J}'(\mathbf{r}, t)$  that are defined in Eq. 45 and are connected to  $n(\mathbf{r}, t)$  and  $n'(\mathbf{r}, t)$  by Eq. 44. The difference in their time-derivative at  $t_0$  can be calculated as

$$\begin{aligned} \frac{\partial}{\partial t} [\mathbf{J}(\mathbf{r}, t) - \mathbf{J}'(\mathbf{r}, t)]|_{t=t_0} &= \frac{i}{\hbar} \langle \Psi(t_0) | [\hat{H}(t_0) - \hat{H}'(t_0), \hat{\mathbf{J}}(\mathbf{r})] | \Psi(t_0) \rangle \\ &= -\frac{n(\mathbf{r}, t_0)}{m_e} \vec{\nabla} [v(\mathbf{r}, t_0) - v'(\mathbf{r}, t_0)]. \end{aligned} \quad (50)$$

If the potentials  $v$  and  $v'$  differ at initial time by more than a time-dependent constant, i.e.  $v(\mathbf{r}, t_0) \neq v'(\mathbf{r}, t_0) + c(t_0)$ , we find  $k_{\min} = 0$ . This leads in the above equation to a nonvanishing right-hand side implying a nonvanishing  $\mathbf{J}(\mathbf{r}, t_0 + \Delta t) - \mathbf{J}'(\mathbf{r}, t_0 + \Delta t)$  for infinitesimally small  $\Delta t$ . From Eq. 50, we also find that the potential is only defined up to a constant, since  $\vec{\nabla} c(t) = 0$ .

<sup>7</sup> The restriction on time-analytic external potentials has been lifted later [53–55].

If  $k_{\min} = k > 0$ , the potentials are equal (up to a constant) at initial time  $t_0$  but differ for  $t > t_0$ . We apply the Heisenberg equation of motion  $k$ -times (Eq. 43) to find

$$\left. \frac{\partial^{k+1}}{\partial t^{k+1}} [\mathbf{J}(\mathbf{r}, t) - \mathbf{J}'(\mathbf{r}, t)] \right|_{t=t_0} = -\frac{n(\mathbf{r}, t_0)}{m_e} \vec{\nabla} \left( \frac{\partial^k}{\partial t^k} [v(\mathbf{r}, t) - v'(\mathbf{r}, t)] \right) \Big|_{t=t_0}. \quad (51)$$

The right-hand side always vanishes for  $l < k$ , hence we need to go to the order  $k$ . For  $l = k$ , we find also a nonvanishing right-hand side, which leads to a nonvanishing  $\mathbf{J}(\mathbf{r}, t_0 + \Delta t) - \mathbf{J}'(\mathbf{r}, t_0 + \Delta t)$  for infinitesimally small  $\Delta t$ . For the current density, we conclude that two solutions  $|\Psi(t)\rangle$  and  $|\Psi'(t)\rangle$  of the time-dependent Schrödinger equation with external potentials  $v(\mathbf{r}, t)$  and  $v'(\mathbf{r}, t)$ , but common initial state  $|\Psi_0\rangle$  never lead to the same electron current density evolution  $\mathbf{J}(\mathbf{r}, t)$ .

Making use of Eq. 44, we find for the electron densities

$$\left. \frac{\partial^{k+2}}{\partial t^{k+2}} [n(\mathbf{r}, t) - n'(\mathbf{r}, t)] \right|_{t=t_0} = \frac{1}{m_e} \vec{\nabla} \cdot \left[ n(\mathbf{r}, t_0) \vec{\nabla} \left( \frac{\partial^k}{\partial t^k} [v(\mathbf{r}, t) - v'(\mathbf{r}, t)] \right) \right] \Big|_{t=t_0}. \quad (52)$$

Provided the initial density  $n(\mathbf{r}, t_0)$  is reasonably well behaved [10], we can show by *reductio ad absurdum* that also here the right-hand side is nonvanishing for  $k_{\min} = k$ , which leads to a nonvanishing  $n(\mathbf{r}, t_0 + \Delta t) - n'(\mathbf{r}, t_0 + \Delta t)$  for infinitesimally small  $\Delta t$ . This concludes the proof of one-to-one correspondence:  $v(\mathbf{r}, t) \neq v'(\mathbf{r}, t) + c(t)$  automatically leads to  $n(\mathbf{r}, t) \neq n'(\mathbf{r}, t)$  for a given initial state. Thus in this case  $v(\mathbf{r}, t)$  uniquely defines  $n(\mathbf{r}, t)$ .

In TDDFT, all observables have an additional dependence on the initial state  $\Psi(t_0)$ , the so-called initial-state dependence

$$O([n, \Psi(t_0)], t) = \langle \Psi([n, \Psi(t_0)], t) | \hat{O} | \Psi([n, \Psi(t_0)], t) \rangle.$$

### 2.2.7 Kohn-Sham System in TDDFT

Similar to ground-state DFT, introduced in Sec. 2.2.3, the interacting many-body problem can be replaced by a noninteracting Kohn-Sham problem. In the time-dependent Kohn-Sham system, all observables accumulate an additional dependence on the Kohn-Sham initial state  $\Phi(t_0)$ . For all observables, we find

$$O([n, \Psi(t_0), \Phi(t_0)], t) = \langle \Psi([n, \Psi(t_0), \Phi(t_0)], t) | \hat{O} | \Psi([n, \Psi(t_0), \Phi(t_0)], t) \rangle, \quad (53)$$

where  $|\Psi(t_0)\rangle$  is the many-body initial state and  $|\Phi(t_0)\rangle$  is the Kohn-Sham initial state. In general,  $|\Phi(t_0)\rangle$  can be different to  $|\Psi(t_0)\rangle$ , but  $|\Phi(t_0)\rangle$  has to be chosen such that  $n(\mathbf{r}, t_0)$  and  $\frac{\partial}{\partial t} n(\mathbf{r}, t)|_{t=t_0}$  are equal in the many-body and Kohn-Sham system. The time-dependent Kohn-Sham equations for single-particle orbitals  $|\phi_i(t)\rangle$  can be set up as follows

$$i\hbar \frac{\partial}{\partial t} |\phi_i(t)\rangle = \left( \frac{1}{2m_e} \hat{\mathbf{p}}^2 + \underbrace{v_{\text{ext}}(\mathbf{r}, t) + v_{\text{H}}(\mathbf{r}, t) + v_{\text{xc}}(\mathbf{r}, t)}_{v_{\text{s}}(\mathbf{r}, t)} \right) |\phi_i(t)\rangle, \quad (54)$$

where the Kohn-Sham potential  $v_s(\mathbf{r}, t)$  includes the external potential  $v_{\text{ext}}(\mathbf{r}, t)$ , the classical time-dependent Hartree potential

$$v_H(\mathbf{r}, t) = \frac{e^2}{4\pi\epsilon_0} \int d^3\mathbf{r}' \frac{n(\mathbf{r}', t)}{|\mathbf{r} - \mathbf{r}'|}, \quad (55)$$

and the **xc** potential  $v_{\text{xc}}(\mathbf{r}, t)$ . By construction, the time evolution of the electron density in the Kohn-Sham system is equal to the time evolution of the electron density in the many-body system. This equality can be used to define the Hartree-exchange-correlation (**Hxc**) potential  $v_{\text{Hxc}} = v_H + v_{\text{xc}}$  using the equation of motion for the electron density of Eq. 46 and is then given as follows

$$\frac{1}{m_e} \vec{\nabla} \cdot \left( n(\mathbf{r}, t) \vec{\nabla} v_{\text{Hxc}}(\mathbf{r}, t) \right) = \vec{\nabla} \cdot \left( \mathbf{Q}^{(s)}(\mathbf{r}, t) - \mathbf{Q}(\mathbf{r}, t) \right), \quad (56)$$

where  $\mathbf{Q}$  is the electronic stress force of the interacting system as defined in Eq. 47 and  $\mathbf{Q}^{(s)}$  is the electronic stress force of the Kohn-Sham system.

#### 2.2.7.1 Adiabatic approximations

To calculate properties of real systems, we rely on approximations for  $v_{\text{xc}}(\mathbf{r}, t)$ . The simplest and most widely used approximation to describe time-dependent systems is the adiabatic approximation. In the adiabatic approximation, we assume that the system follows adiabatically the external perturbation. Under this assumption, we can apply the ground-state potentials presented in Sec. 2.2.3.2

$$v_{\text{xc}}^{\text{adiabatic}}([n, \Psi_0, \Phi_0], t) = v_{\text{xc}}([n_0], t) \big|_{n_0=n}. \quad (57)$$

Meaning, we use the ground-state functionals in Sec. 2.2.3 developed for the ground-state density  $n_0(\mathbf{r})$ , but insert the time-dependent density  $n(\mathbf{r}, t)$  at each time step. The adiabatic approximation is justified for systems, where the time-dependent density does not change rapidly. One of the most common approximations in **TDDFT** is the adiabatic local-density approximation (**ALDA**), where the functional of the homogeneous electron gas is used. The **ALDA** has no initial-state dependence and only depends on time locally. Locality in time means that the potential at time  $t$  only depends on the density at time  $t$  and is independent on the previous density evolution, hence does not contain memory effects. One way to overcome this limitations is to connect **TDDFT** to many-body perturbation theory, which is the topic in the next section.

#### 2.2.8 Green's Functions and the Sham-Schlüter Equation

In this section, we introduce the basic concepts of many-body perturbation theory using the Green's function formalism that we need in the next chapter to construct approximate **xc** potentials. Comprehensive reviews on the topic of many-body perturbation theory can be found e.g. in Refs. [56–59].

The central object in many-body perturbation theory is the Green's function [58]. The single-particle Green's function is defined in terms of the electron field operators (Eq. 21) in the Heisenberg picture. In the Heisenberg picture, all quantum mechanical operators acquire a time-dependence, but states remain time-independent,

while in the Schrödinger picture, the states are time-dependent, but the operators are time-independent<sup>8</sup>. Operators can be transformed from the Schrödinger picture to the Heisenberg picture by the following transformation

$$\hat{\psi}(\mathbf{r}, t) = \hat{U}(t, t_0) \hat{\psi}(\mathbf{r}) \hat{U}(t_0, t). \quad (58)$$

Here, we make use of the time-evolution operator, which is defined as [60]

$$\hat{U}(t, t_0) = \mathbb{1} + \sum_{n=1}^{\infty} \left( -\frac{i}{\hbar} \right)^n \int_{t_0}^t dt_1 \int_{t_0}^{t_1} dt_2 \dots \int_{t_0}^{t_{n-1}} dt_n \hat{H}(t_1) \dots \hat{H}(t_n), \quad (59)$$

$$= \mathbb{1} + \sum_{n=1}^{\infty} \frac{1}{n!} \left( -\frac{i}{\hbar} \right)^n \int_{t_0}^t dt_1 \int_{t_0}^{t_1} dt_2 \dots \int_{t_0}^{t_n} dt_n \hat{T} [\hat{H}(t_1) \dots \hat{H}(t_n)], \quad (60)$$

$$= \hat{T} \exp \left( -\frac{i}{\hbar} \int_{t_0}^t \hat{H}(t') dt' \right). \quad (61)$$

In Eq. 60, we have introduced the operator  $\hat{T}$ , which is the Wick's time-ordering operator. This operator orders operators with different time arguments such that later times are shifted to the left. Next, we can define the one-particle Green's function

$$i\hbar G(1, 1') = \langle \Psi_0 | \hat{T} [\hat{\Psi}(1) \hat{\Psi}^\dagger(1')] | \Psi_0 \rangle, \quad (62)$$

where  $1 = \{\mathbf{r}, t, \sigma\}$  is the collective index for the space-time-spin variable. The time-ordering operator gives

$$\hat{T} [\hat{\Psi}(1) \hat{\Psi}^\dagger(1')] = \begin{cases} \hat{\Psi}(1) \hat{\Psi}^\dagger(1') & \text{if } t > t', \\ \mp \hat{\Psi}^\dagger(1') \hat{\Psi}(1) & \text{if } t < t'. \end{cases} \quad (63)$$

applied to fermionic (−) or bosonic (+) operators. The many-body wave function  $|\Psi_0\rangle$  is the correlated ground-state of the  $N$ -electron system. Furthermore, we can define a more general Green's function, namely the  $N$ -particle Green's function

$$(i\hbar)^N G_N(1, \dots, N, 1', \dots, N') = \langle \Psi_0 | \hat{T} [\hat{\Psi}(1) \dots \hat{\Psi}(N) \hat{\Psi}^\dagger(N') \dots \hat{\Psi}^\dagger(1')] | \Psi_0 \rangle. \quad (64)$$

The equation of motion of the interacting Green's function gives the Dyson equation in differential form

$$\left[ i\hbar \frac{\partial}{\partial t_1} - h_0(1) \right] G(1, 1') + i\hbar \int d3 w(1, 2) G_2(1, 2^+, 1', 2^{++}) = \delta(1, 1'), \quad (65)$$

where  $2^+$  implies that the time argument in 2 is shifted by a positive infinitesimal. We assume that the electrons in the system obey the electronic Hamiltonian of Eq. 41. In Eq. 65,  $h_0(1)$  is the single-particle Hamiltonian (including  $\hat{T}_e$  and  $\hat{V}$ ) and  $w(1, 2)$  the electron-electron interaction. In the Dyson equation, we find that the equation of motion connects the single-particle Green's function  $G(1, 1')$  with the two-particle Green's function  $G_2(1, 2, 1', 2)$ . By calculating the equation of motion

<sup>8</sup> Also operators in the Schrödinger picture can have an explicit time-dependence, e.g. the Hamiltonian  $\hat{H}(t)$  through a time-dependent external potential, which describes an external laser field.



of the two-particle Green's function, we find a connection to the three-particle Green's function. This procedure gives us a hierarchy of equations of motion such that the  $N$ -particle Green's function is connected to the  $N + 1$ -particle Green's function. This hierarchy is also called Martin-Schwinger hierarchy and can be reformulated formally by introducing the self-energy  $\Sigma(1,2)$  into Eq. 65. This equation then reads

$$\left[ i\hbar \frac{\partial}{\partial t_1} - h_0(1) \right] G(1,1') - \int d3 \Sigma(1,2) G(2,1') = \delta(1,1'). \quad (66)$$

The Dyson equation in Eq. 66 can also be rewritten in terms of the noninteracting Green's function,

$$G(1,1') = G_0(1,1') + \int d2 \int d3 G_0(1,2) \Sigma(2,3) G(3,1'), \quad (67)$$

where  $G_0(1,1')$  is the noninteracting Green's function that obeys

$$\left[ i\hbar \frac{\partial}{\partial t_1} - h_0(1) \right] G_0(1,1') = \delta(1,1'). \quad (68)$$

The noninteracting Green's function is often the starting point in numerical calculations. An example for a noninteracting Green's function is the Kohn-Sham Green's function  $G_s(1,1')$ , which is constructed using Kohn-Sham orbitals. In general, the self-energy  $\Sigma(1,2)$  includes all many-body effects for the evolution of the system. In a similar spirit as in DFT, the self-energy  $\Sigma(1,2)$  can be divided into

$$\Sigma(1,2) = v_H(1)\delta(1,2) + \Sigma_{xc}(1,2)$$

by using the Hartree potential  $v_H$ . In numerical calculations  $\Sigma_{xc}$  is approximated. In many-body perturbation theory the self-energy is routinely expanded using Feynman diagrams [61].

#### 2.2.8.1 Lehmann representation of the Green's function

We derive the Green's function in Lehmann representation by inserting a full set of eigenfunctions  $\mathbb{1} = \sum_n |\Psi_n^N\rangle \langle \Psi_n^N|$ . Here, the label  $(N)$  refers to a  $N$ -particle state. The Green's function can then be expressed as

$$\begin{aligned} i\hbar G(1,1') = & \Theta(t - t') \sum_n \langle \Psi_0 | \hat{\psi}(1) | \Psi_n^{N+1} \rangle \langle \Psi_n^{N+1} | \hat{\psi}^\dagger(1') | \Psi_0 \rangle \\ & - \Theta(t' - t) \sum_n \langle \Psi_0 | \hat{\psi}^\dagger(1') | \Psi_n^{N-1} \rangle \langle \Psi_n^{N-1} | \hat{\psi}(1) | \Psi_0 \rangle, \end{aligned} \quad (69)$$

where the step-function  $\Theta(t - t')$  assures the time-ordering. Using a Fourier transformation and applying the substitution  $\hbar\omega' = \hbar\omega + E_n^{N+1} - E_0$  and  $\hbar\omega' = \hbar\omega - E_n^{N-1} + E_0$ , we find

$$\begin{aligned} G(\mathbf{r}, \mathbf{r}', \omega) = & \lim_{\delta \rightarrow 0^+} \sum_n \frac{\langle \Psi_0 | \hat{\psi}(\mathbf{r}) | \Psi_n^{N+1} \rangle \langle \Psi_n^{N+1} | \hat{\psi}^\dagger(\mathbf{r}') | \Psi_0 \rangle}{\hbar\omega - E_n^{N+1} + E_0 + i\delta} \\ & + \lim_{\delta \rightarrow 0^+} \sum_n \frac{\langle \Psi_0 | \hat{\psi}^\dagger(\mathbf{r}') | \Psi_n^{N-1} \rangle \langle \Psi_n^{N-1} | \hat{\psi}(\mathbf{r}) | \Psi_0 \rangle}{\hbar\omega - E_0 + E_n^{N-1} - i\delta}. \end{aligned} \quad (70)$$

If the many-body wave functions  $\Psi$  are single Slater determinants, e.g. consisting of Kohn-Sham orbitals  $\phi_i$ , we arrive at the Lehmann representation of the noninteracting Green's function [59]

$$G_0(\mathbf{r}, \mathbf{r}', \omega) = \lim_{\delta \rightarrow 0^+} \sum_i \frac{\phi_i(\mathbf{r}) \phi_i^*(\mathbf{r}')}{\hbar\omega - (\epsilon_i - \mu) - i\delta \text{sgn}(\epsilon_i - \mu)}, \quad (71)$$

where  $\mu$  is the Fermi energy.

#### 2.2.8.2 Sham-Schlüter Equation

The gap between many-body perturbation theory and density-functional theory [62, 63] was bridged by the Sham-Schlüter equation. In this equation the exchange-correlation part in the self-energy  $\Sigma_{xc}(1, 1')$  can be used to calculate the corresponding Kohn-Sham potential  $v_{xc}(\mathbf{r}, t)$ .

By construction, the density of the Kohn-Sham system is equal to the density of the interacting system. Therefore, the Kohn-Sham Green's function  $G_s(1, 1')$  and the many-body Green's function  $G(1, 1')$  are connected by

$$n(\mathbf{r}, t) = -\frac{i}{\hbar} \lim_{t' \rightarrow t} G(\mathbf{r}, t, \mathbf{r}, t') = -\frac{i}{\hbar} \lim_{t' \rightarrow t} G_s(\mathbf{r}, t, \mathbf{r}, t'). \quad (72)$$

This direct connection already leads via the Dyson equation of Eq. 66 for the many-body and the Kohn-Sham system directly to the time-dependent Sham-Schlüter equation

$$\begin{aligned} & \int_{-\infty}^{\infty} d\tau_2 \int d^3\mathbf{r}_2 t'(\tau_2) G(\mathbf{r}_1, \tau_1, \mathbf{r}_2, \tau_2) G_s(\mathbf{r}_2, \tau_2, \mathbf{r}_1, \tau_1) v_{xc}(\mathbf{r}_2, \tau_2) \\ &= \int_{-\infty}^{\infty} d\tau_3 \int_{-\infty}^{\infty} d\tau_4 \int d^3\mathbf{r}_3 \int d^3\mathbf{r}_4 t'(\tau_3) t'(\tau_4) G(\mathbf{r}_1, \tau_1, \mathbf{r}_3, \tau_3) \Sigma_{xc}(\mathbf{r}_3, \tau_3, \mathbf{r}_4, \tau_4) \\ & \quad \times G_s(\mathbf{r}_4, \tau_4, \mathbf{r}_1, \tau_1). \end{aligned} \quad (73)$$

Here, the nonphysical pseudo-times  $\tau$  are defined on the complex Keldysh-contour [58]. Typically, the linearized form of the Sham-Schlüter equation is used, where the many-body Green's function  $G(\mathbf{r}, \tau_1, \mathbf{r}, \tau_2)$  is approximated by the Kohn-Sham Green's function  $G_s(\mathbf{r}, \tau_1, \mathbf{r}, \tau_2)$ . Although Eq. 72 allows to connect the diagonals of  $G$  and  $G_s$ , in general their off-diagonals are different. The Sham-Schlüter equation in Eq. 73 allows to calculate approximations for the Kohn-Sham potential  $v_{xc}(\mathbf{r}, t)$  by approximating the self-energy  $\Sigma_{xc}$ . In principle, approximations of the self-energy  $\Sigma_{xc}$  can be improved in a systematic way by including more diagrams into  $\Sigma_{xc}$ . For instance, if the Hartree-Fock approximation is used for  $\Sigma_{xc}$ , we obtain the local exact-exchange potential for  $v_{xc}$ .

#### 2.2.8.3 Optimized Effective Potential

The term optimized effective potential (OEP) refers to a wide class of approximations to obtain the Kohn-Sham potential  $v_{xc}$  [64]. All these approximations use the Kohn-Sham orbitals  $|\phi_i\rangle$  to construct the effective Kohn-Sham potential. Thus,

the Kohn-Sham potential  $v_{\text{xc}}$  has an explicit dependence on these orbitals. The attribute *optimized* is justified by the constraint that the Kohn-Sham potential remains local, while the total energy is minimized. One way to obtain these approximations is by applying the chain rule for functional derivatives and using [64]

$$v_{\text{xc},\sigma}(\mathbf{r}) = \frac{\delta E_{\text{xc}}(\{\phi_i\})}{\delta n_{\sigma}(\mathbf{r})}, \quad (74)$$

where  $n_{\sigma}(\mathbf{r})$  is the spin-resolved electron density and  $E_{\text{xc}}$  the exchange-correlation energy of Eq. 35 depending on the Kohn-Sham orbitals  $\phi_i$ . Another way is by directly using the Sham-Schlüter equation as given by Eq. 73. For the ground state, efficient algorithms are available to directly solve the OEP equation without invoking further approximations [65]. Whereas in the time-dependent case, the OEP equations are rarely solved directly [66], but usually approximately, e.g. by applying the Krieger-Li-Iafrate (KLI) approximation [67] to approximate the OEP equation.

## 2.3 PHOTONS AND THE ELECTRON-PHOTON HAMILTONIAN

In this section, we introduce the framework to study quantized electromagnetic fields. Reviews on this topic can be found e.g. in Refs. [68–71]. So far, we restricted ourselves to the treatment of quantum systems, which contain electrons and nuclei. This restriction is lifted now and to this end, we first briefly introduce how to quantize the classical theory of electromagnetic fields in vacuum based on Maxwell’s equations. In the end of this section, we deal with the coupling of quantum-mechanical electrons to quantized electromagnetic fields.

### 2.3.1 Classical Maxwell Field Equations

The electromagnetic field can be quantized by first considering the classical Maxwell field equations, and then in a second step promoting the field amplitudes to quantum operators. Throughout this section, the field quantities are written in SI units [19].

We start with the classical Maxwell equations [72] for the electric field  $\mathbf{E}(\mathbf{r}, t)$  and magnetic field  $\mathbf{B}(\mathbf{r}, t)$  in their differential form

$$\vec{\nabla} \cdot \mathbf{E}(\mathbf{r}, t) = \rho(\mathbf{r}, t)/\epsilon_0, \quad (75)$$

$$\vec{\nabla} \cdot \mathbf{B}(\mathbf{r}, t) = 0, \quad (76)$$

$$\vec{\nabla} \times \mathbf{E}(\mathbf{r}, t) = -\frac{\partial \mathbf{B}(\mathbf{r}, t)}{\partial t}, \quad (77)$$

$$\vec{\nabla} \times \mathbf{B}(\mathbf{r}, t) = \epsilon_0 \mu_0 \frac{\partial \mathbf{E}(\mathbf{r}, t)}{\partial t} + \mu_0 \mathbf{J}(\mathbf{r}, t), \quad (78)$$

where  $\mathbf{r}$  denotes a three-dimensional position vector,  $t$  the time,  $\rho(\mathbf{r}, t)$  refers to the electron charge density,  $\mathbf{J}(\mathbf{r}, t)$  is the electron current density and  $\epsilon_0$  and  $\mu_0$  are the vacuum permittivity and the magnetic permeability that are connected to the speed of light  $c$  by  $\epsilon_0 \mu_0 = 1/c^2$ . To quantize the fields, it is useful to cast Maxwell’s equations in terms of scalar and vector potentials. Therefore, we introduce the

scalar field  $\phi(\mathbf{r}, t)$  and the vector field  $\mathbf{A}(\mathbf{r}, t)$ . By using Eq. 76 and Eq. 77, we can define these potentials as follows

$$\mathbf{E}(\mathbf{r}, t) = -\vec{\nabla}\phi(\mathbf{r}, t) - \left(\frac{\partial\mathbf{A}(\mathbf{r}, t)}{\partial t}\right), \quad (79)$$

$$\mathbf{B}(\mathbf{r}, t) = \vec{\nabla} \times \mathbf{A}(\mathbf{r}, t). \quad (80)$$

The remaining two Maxwell equations Eq. 75 and Eq. 78 lead to the following field equations

$$\vec{\nabla} \left( \vec{\nabla} \cdot \vec{A}(\mathbf{r}, t) \right) - \vec{\nabla}^2 \vec{A}(\mathbf{r}, t) + \frac{1}{c^2} \frac{\partial \left( \vec{\nabla} \phi(\mathbf{r}, t) \right)}{\partial t} + \frac{1}{c^2} \frac{\partial^2 \mathbf{A}(\mathbf{r}, t)}{\partial t^2} = \mu_0 \mathbf{J}(\mathbf{r}, t), \quad (81)$$

$$-\vec{\nabla}^2 \phi(\mathbf{r}, t) - \vec{\nabla} \cdot \left( \frac{\partial \mathbf{A}(\mathbf{r}, t)}{\partial t} \right) = \rho(\mathbf{r}, t) / \epsilon_0. \quad (82)$$

### 2.3.2 Gauge Transformation

There exist pairs of potentials  $(\mathbf{A}(\mathbf{r}, t), \phi(\mathbf{r}, t))$  and  $(\mathbf{A}'(\mathbf{r}, t), \phi'(\mathbf{r}, t))$ , for which the field quantities  $\mathbf{E}$  and  $\mathbf{B}$  derived from Eq. 79 and Eq. 80 are identical. Therefore  $\mathbf{A}(\mathbf{r}, t)$  and  $\phi(\mathbf{r}, t)$  are often considered nonphysical quantities. In contrast to  $\mathbf{E}(\mathbf{r}, t)$  and  $\mathbf{B}(\mathbf{r}, t)$ ,  $\mathbf{A}(\mathbf{r}, t)$  and  $\phi(\mathbf{r}, t)$  are not directly measurable in experiment. This nonphysical degree of freedom is called the gauge freedom. Performing a gauge transformation does not affect any of the physical quantities, such as  $\mathbf{E}(\mathbf{r}, t)$  or  $\mathbf{B}(\mathbf{r}, t)$ , but instead affects  $\mathbf{A}(\mathbf{r}, t)$  and  $\phi(\mathbf{r}, t)$ . Gauge transformations are used to simplify the equations for the scalar and vector potential in a given setup and are typically defined by using an arbitrary scalar gauge function  $G(\mathbf{r}, t)$

$$\mathbf{A}(\mathbf{r}, t) = \mathbf{A}'(\mathbf{r}, t) - \vec{\nabla} G(\mathbf{r}, t), \quad (83)$$

$$\phi(\mathbf{r}, t) = \phi'(\mathbf{r}, t) + \frac{\partial G(\mathbf{r}, t)}{\partial t}. \quad (84)$$

Throughout this thesis, all fields are written in the Coulomb gauge. This particular gauge is convenient for calculations in the nonrelativistic limit, where electrons and nuclei move considerably slower than the speed of light. The Coulomb gauge is defined by  $\vec{\nabla} \cdot \mathbf{A}(\mathbf{r}, t) = 0$ , or alternatively as a condition for the gauge function,  $\vec{\nabla}^2 G(\mathbf{r}, t) = \vec{\nabla} \cdot \mathbf{A}'(\mathbf{r}, t)$ . Applying the Coulomb gauge has direct consequences: Due to the Helmholtz decomposition [18], it is possible to divide a vector potential into its transverse ( $T$ ) and longitudinal ( $L$ ) part,  $\mathbf{A}(\mathbf{r}, t) = \mathbf{A}_T(\mathbf{r}, t) + \mathbf{A}_L(\mathbf{r}, t)$ , which can be easily defined using the transverse/longitudinal delta-functions [70]:  $\mathbf{V}_{T/L}(\mathbf{r}, t) = \int d^3\mathbf{r}' \mathbf{V}(\mathbf{r}', t) \delta_{T,L}(\mathbf{r} - \mathbf{r}')$ . Applying this partitioning, we find in Coulomb gauge that the vector field  $\mathbf{A}(\mathbf{r}, t)$  is purely transverse and is defined by the transversal part of the electronic current  $\mathbf{J}_T(\mathbf{r}, t)$  alone. In Coulomb gauge, the field equations of Eqns. 81-82 take the following form

$$\vec{\nabla}^2 \mathbf{A}(\mathbf{r}, t) - \frac{1}{c^2} \frac{\partial^2 \mathbf{A}(\mathbf{r}, t)}{\partial t^2} = -\mu_0 \mathbf{J}_T(\mathbf{r}, t), \quad (85)$$

$$-\vec{\nabla}^2 \phi(\mathbf{r}, t) = \rho(\mathbf{r}, t) / \epsilon_0. \quad (86)$$

For a fixed gauge, all vector field potentials are unique and nonphysical degrees of freedom vanish.

## 2.3.3 Free Classical Field

In the absence of charges (sources) and currents in the system meaning  $\rho(\mathbf{r}, t) = 0$  and  $\mathbf{J}(\mathbf{r}, t) = 0$ , the field is considered to be free or in vacuum and Eq. 85 and Eq. 86 simplify to

$$\vec{\nabla}^2 \mathbf{A}(\mathbf{r}, t) + \frac{1}{c^2} \frac{\partial^2 \mathbf{A}(\mathbf{r}, t)}{\partial t^2} = 0, \quad (87)$$

$$\phi(\mathbf{r}, t) = 0. \quad (88)$$

Eq. 87 and Eq. 88 are the starting point in the field quantization procedure. We introduce a cubic quantization cavity of length  $L$ , volume  $V = L^3$  and periodic boundary conditions. We further expand the vector potential  $\mathbf{A}(\mathbf{r}, t)$ , the transverse part of the electric field  $\mathbf{E}_T(\mathbf{r}, t)$  (in Coulomb gauge:  $\mathbf{E}_L(\mathbf{r}, t) = 0$ ) and the magnetic field  $\mathbf{B}(\mathbf{r}, t)$  in terms of plane waves. We solve Eq. 87 for  $\mathbf{A}(\mathbf{r}, t)$  and calculate  $\mathbf{B}(\mathbf{r}, t)$  by Eq. 80 and  $\mathbf{E}(\mathbf{r}, t)$  by Eq. 79, which yields

$$\mathbf{A}(\mathbf{r}, t) = \sum_{\mathbf{k}} \sum_{\lambda=1,2} \mathbf{e}_{\mathbf{k}\lambda} (\mathbf{A}_{\mathbf{k}\lambda} \exp(-i\omega_k t + i\mathbf{k} \cdot \mathbf{r}) + \mathbf{A}_{\mathbf{k}\lambda}^* \exp(i\omega_k t - i\mathbf{k} \cdot \mathbf{r})), \quad (89)$$

$$\mathbf{E}_T(\mathbf{r}, t) = \sum_{\mathbf{k}} \sum_{\lambda=1,2} \mathbf{e}_{\mathbf{k}\lambda} i\omega_k (\mathbf{A}_{\mathbf{k}\lambda} \exp(-i\omega_k t + i\mathbf{k} \cdot \mathbf{r}) - \mathbf{A}_{\mathbf{k}\lambda}^* \exp(i\omega_k t - i\mathbf{k} \cdot \mathbf{r})), \quad (90)$$

$$\mathbf{B}(\mathbf{r}, t) = \sum_{\mathbf{k}} \sum_{\lambda=1,2} \frac{\mathbf{k} \times \mathbf{e}_{\mathbf{k}\lambda}}{|\mathbf{k}|} ik (\mathbf{A}_{\mathbf{k}\lambda} \exp(-i\omega_k t + i\mathbf{k} \cdot \mathbf{r}) - \mathbf{A}_{\mathbf{k}\lambda}^* \exp(i\omega_k t - i\mathbf{k} \cdot \mathbf{r})). \quad (91)$$

Here,  $\mathbf{e}_{\mathbf{k}\lambda}$  is a (unit) polarization vector with two polarization directions  $\lambda$ , both orthogonal to  $\mathbf{k}$ , since there is no propagation along the longitudinal direction in the Coulomb gauge possible. This means that  $\mathbf{e}_{\mathbf{k}1}$ ,  $\mathbf{e}_{\mathbf{k}2}$ , and  $\mathbf{k}$  form a right-handed triad [70]. For periodic boundary conditions, the wave vector  $\mathbf{k}$  takes the following values

$$k_i = 2\pi v_i / L, \quad (92)$$

with  $v_i = 0, \pm 1, \pm 2, \dots$  and  $i = (x, y, z)$ . The relation between the angular frequency  $\omega$  and the wave vector  $\mathbf{k}$  is called the dispersion relation, for which we obtain  $\omega_k = ck$ . The total energy in the cavity is given by the expression

$$E_R = \frac{1}{2} \int d^3\mathbf{r} [\epsilon_0 \mathbf{E}_T \cdot \mathbf{E}_T + \mu_0^{-1} \mathbf{B} \cdot \mathbf{B}]. \quad (93)$$

If we insert the electric field  $\mathbf{E}$  and the magnetic field  $\mathbf{B}$  into Eq. 93, we find that the time dependence vanishes and the total radiative energy  $E_R$  reduces to the sum of time-independent contributions of the individual modes

$$E_R = \sum_{\mathbf{k}} \sum_{\lambda} \epsilon_0 V \omega_k^2 (A_{\mathbf{k}\lambda} A_{\mathbf{k}\lambda}^* + A_{\mathbf{k}\lambda}^* A_{\mathbf{k}\lambda}). \quad (94)$$

### 2.3.4 Riemann-Silberstein Vector

There exists a different way of performing electrodynamical calculations without relying on the gauge-dependent quantities  $\phi$  and  $\mathbf{A}$ . For this purpose, the Riemann-Silberstein vector can be used, which consists of the electric field  $\mathbf{E}$  and the magnetic field  $\mathbf{B}$  that are gauge-invariant quantities. The Riemann-Silberstein vector is a complex vector and is defined as [73, 74]

$$\mathbf{F}(\mathbf{r}, t) = \sqrt{\frac{\epsilon_0}{2}} \mathbf{E}(\mathbf{r}, t) + i \sqrt{\frac{1}{2\mu_0}} \mathbf{B}(\mathbf{r}, t). \quad (95)$$

In the absence of charges and currents, the four Maxwell equations in Eqns. 75-78 can be summarized into two equations by using  $\mathbf{F}(\mathbf{r}, t)$

$$\vec{\nabla} \cdot \mathbf{F}(\mathbf{r}, t) = 0, \quad (96)$$

$$i \frac{\partial}{\partial t} \mathbf{F}(\mathbf{r}, t) = c \vec{\nabla} \times \mathbf{F}(\mathbf{r}, t). \quad (97)$$

Eq. 97 resembles the form of the time-dependent Schrödinger equation in Eq. 1. Thus, the equation can be solved numerically by the same algorithms, which also solve the time-dependent Schrödinger equation.

### 2.3.5 Quantization of the Field in the Schrödinger Picture

The electromagnetic field can be quantized by associating a quantum mechanical harmonic oscillator with each mode  $\mathbf{k}\lambda$  of the radiation field [75]. We can use the creation operator  $\hat{a}_{\mathbf{k}\lambda}^\dagger$  and destruction operator  $\hat{a}_{\mathbf{k}\lambda}$  for a quantized treatment of the electromagnetic field. The creation and annihilation operators obey the usual bosonic commutation relations, i.e.  $[\hat{a}_{\mathbf{k}\lambda}, \hat{a}_{\mathbf{k}'\lambda'}^\dagger] = \delta_{\mathbf{k}\lambda, \mathbf{k}'\lambda'}$  and  $[\hat{a}_{\mathbf{k}\lambda}, \hat{a}_{\mathbf{k}'\lambda'}] = [\hat{a}_{\mathbf{k}\lambda}^\dagger, \hat{a}_{\mathbf{k}'\lambda'}^\dagger] = 0$ .

The quantization of the electromagnetic field is realized by promoting (associating) the vector field amplitude  $\mathbf{A}_{\mathbf{k}\lambda}$  to a quantum operator  $\hat{\mathbf{A}}_{\mathbf{k}\lambda}$  [70]

$$\mathbf{A}_{\mathbf{k}\lambda}^{(*)} \xrightarrow{\wedge} \hat{\mathbf{A}}_{\mathbf{k}\lambda}^{(+)} = \sqrt{\frac{\hbar}{2\epsilon_0 V \omega_k}} \hat{a}_{\mathbf{k}\lambda}^{(+)} \quad (98)$$

Using Eq. 98, we obtain the quantized field operators in analogy to Eqns. 89-91

$$\hat{\mathbf{A}}(\mathbf{r}) = \sum_{\mathbf{k}} \sum_{\lambda=1,2} \left( \frac{\hbar}{2\epsilon_0 c k V} \right)^{1/2} \mathbf{e}_{\mathbf{k}\lambda} \left( \hat{\mathbf{a}}_{\mathbf{k}\lambda} \exp(i\mathbf{k} \cdot \mathbf{r}) + \hat{\mathbf{a}}_{\mathbf{k}\lambda}^\dagger \exp(-i\mathbf{k} \cdot \mathbf{r}) \right), \quad (99)$$

$$\hat{\mathbf{E}}_T(\mathbf{r}) = \sum_{\mathbf{k}} \sum_{\lambda=1,2} i \left( \frac{\hbar c k}{2\epsilon_0 V} \right)^{1/2} \mathbf{e}_{\mathbf{k}\lambda} \left( \hat{\mathbf{a}}_{\mathbf{k}\lambda} \exp(i\mathbf{k} \cdot \mathbf{r}) - \hat{\mathbf{a}}_{\mathbf{k}\lambda}^\dagger \exp(-i\mathbf{k} \cdot \mathbf{r}) \right), \quad (100)$$

$$\hat{\mathbf{B}}(\mathbf{r}) = \sum_{\mathbf{k}} \sum_{\lambda=1,2} i \left( \frac{\hbar k}{2\epsilon_0 c V} \right)^{1/2} \tilde{\mathbf{k}} \times \mathbf{e}_{\mathbf{k}\lambda} \left( \hat{\mathbf{a}}_{\mathbf{k}\lambda} \exp(i\mathbf{k} \cdot \mathbf{r}) - \hat{\mathbf{a}}_{\mathbf{k}\lambda}^\dagger \exp(-i\mathbf{k} \cdot \mathbf{r}) \right). \quad (101)$$

The quantization procedure is motivated by the canonical commutation relation between the conjugated variables, i.e. the vector potential  $\hat{\mathbf{A}}(\mathbf{r})$  and the transversal

electric field  $\hat{\mathbf{E}}_T(\mathbf{r})$ . These two operators have to obey a commutation relation similar to the position-momentum relation for massive particles (see Eq. 10)

$$[\hat{A}_i(\mathbf{r}), \hat{E}_{Tj}(\mathbf{r}')] = -\frac{i\hbar}{\epsilon_0} \delta_{Tij}(\mathbf{r} - \mathbf{r}'). \quad (102)$$

In the vacuum state, we obtain a zero-point or vacuum energy

$$E_0 = \frac{1}{2} \sum_{\mathbf{k}} \sum_{\lambda} \hbar \omega_{\mathbf{k}}. \quad (103)$$

In principle, the frequencies  $\omega_{\mathbf{k}}$  have no upper bound leading to infinite vacuum energy, if all possible  $\omega_{\mathbf{k}}$  are considered. Fortunately, physical observables, i.e. expectation values, only contain energy differences and are therefore independent of the zero-point energy. Note that the zero-point energy has no classical analogue and is a real quantum property of the electromagnetic field.

### 2.3.6 Momentum Gauge and the Minimal-Coupling Hamiltonian

In the Coulomb gauge, the electrodynamics of an electronic system interacting with electromagnetic field modes can be described by the minimal-coupling Hamiltonian [70]. Here, the electron-field coupling is introduced into the Hamiltonian from Eq. 11 by the substitution  $\hat{\mathbf{p}}_i \rightarrow \hat{\mathbf{p}}_i - e\hat{\mathbf{A}}(\mathbf{r}_i)$ . This leads us to the following minimal-coupling Hamiltonian

$$\hat{H}_{\min} = \sum_{i=1}^{n_e} \frac{1}{2m_e} [\hat{\mathbf{p}}_i - e\hat{\mathbf{A}}(\mathbf{r}_i)]^2 + \hat{W}_{ee} + \hat{W}_{eN}(\{\mathbf{R}\}) + \underbrace{\frac{\epsilon_0}{2} \int d^3\mathbf{r} [\hat{\mathbf{E}}_T^2(\mathbf{r}) + c^2 \hat{\mathbf{B}}^2(\mathbf{r})]}_{\hat{H}_{\text{pt}}}, \quad (104)$$

where the last term in the Hamiltonian denotes the field Hamiltonian  $\hat{H}_{\text{pt}}$ . This term can also be rewritten in terms of the photon creation and annihilation operators

$$\hat{H}_{\text{pt}} = \sum_{\mathbf{k}} \sum_{\lambda=1,2} \hbar \omega_{\mathbf{k}} \left( \hat{\mathbf{a}}_{\mathbf{k}\lambda}^\dagger \hat{\mathbf{a}}_{\mathbf{k}\lambda} + \frac{1}{2} \right) = \frac{1}{2} \sum_{\mathbf{k}} \sum_{\lambda=1,2} (\hat{p}_{\mathbf{k}\lambda}^2 + \omega_{\mathbf{k}}^2 \hat{q}_{\mathbf{k}\lambda}^2), \quad (105)$$

where we made use of the photon displacement operator  $\hat{q}_{\mathbf{k}\lambda}$  and photon momentum operator  $\hat{p}_{\mathbf{k}\lambda}$ , which are defined as

$$\hat{q}_{\mathbf{k}\lambda} = \sqrt{\frac{\hbar}{2\omega_{\mathbf{k}}}} (\hat{\mathbf{a}}_{\mathbf{k}\lambda}^\dagger + \hat{\mathbf{a}}_{\mathbf{k}\lambda}), \quad (106)$$

$$\hat{p}_{\mathbf{k}\lambda} = i\sqrt{\frac{\hbar\omega_{\mathbf{k}}}{2}} (\hat{\mathbf{a}}_{\mathbf{k}\lambda}^\dagger - \hat{\mathbf{a}}_{\mathbf{k}\lambda}). \quad (107)$$

The operators  $\hat{q}_{\mathbf{k}\lambda}$  and  $\hat{p}_{\mathbf{k}\lambda}$  are the displacement and momentum operators of the quantum harmonic oscillator that is connected to the photon field mode  $\mathbf{k}\lambda$ .

### 2.3.7 Pauli-Fierz Hamiltonian and the Maxwell-Schrödinger Propagation

For classical external fields, the Hamiltonian of Eq. 104 can be conveniently reformulated to the Pauli-Fierz Hamiltonian. The nonrelativistic Pauli-Fierz Hamiltonian  $\hat{H}_{\text{PF}}$  written in Coulomb gauge is defined as in Ref. [18] and is a reformulation of the minimal-coupling Hamiltonian (see Sec. 2.3.6 and appendix B). To define the Hamiltonian, we use four-component vectors with the notation  $b = (b^0, \mathbf{b})$ .<sup>9</sup> The Hamiltonian is then given by

$$\hat{H}_{\text{PF}}(t) = \hat{T}_e + \hat{W}_{ee} + \hat{H}_{pt} + \hat{H}_{\text{int}} + \hat{H}_{\text{cov}} + \hat{H}_{\text{ext}}, \quad (108)$$

containing the nonrelativistic kinetic energy operator  $\hat{T}_e$  of Eq. 18 and the Coulomb energy operator  $\hat{W}_{ee}$  of Eq. 20, both written in the second quantization framework containing the electron field operators  $\hat{\Psi}^\dagger(\mathbf{r})$ , and  $\hat{\Psi}(\mathbf{r})$ . The next term in the Hamiltonian, the energy of the electromagnetic field, is given by

$$\hat{H}_{pt} = \frac{\epsilon_0}{2} \int d^3\mathbf{r} : \left( \hat{\mathbf{E}}^2(\mathbf{r}) + c^2 \hat{\mathbf{B}}^2(\mathbf{r}) \right) :,$$

where  $\{:\}$  refers to the normal-ordering of the operators to eliminate the infinite vacuum energy. Furthermore, the Pauli-Fierz Hamiltonian contains the electron-photon interaction operator  $\hat{H}_{\text{int}}$ . The interaction is formulated in minimal coupling by a bilinear coupling between the nonrelativistic (electron) internal current operator  $\hat{\mathbf{J}}(\mathbf{r})$  and the electromagnetic Maxwell field operator  $\hat{\mathbf{A}}(\mathbf{r})$

$$\hat{H}_{\text{int}} = - \int d^3\mathbf{r} \hat{\mathbf{J}}(\mathbf{r}, t) \cdot \hat{\mathbf{A}}(\mathbf{r}). \quad (109)$$

The covariant Hamiltonian operator reads as

$$\hat{H}_{\text{cov}} = \frac{1}{c} \int d^3\mathbf{r} \hat{j}_0(\mathbf{r}) \left( A_{\text{tot}}^0(\mathbf{r}, t) - \frac{e}{2m_e} \hat{\mathbf{A}}_{\text{tot}}^2(\mathbf{r}, t) \right), \quad (110)$$

where

$$\begin{aligned} \hat{\mathbf{A}}_{\text{tot}}(\mathbf{r}, t) &= \hat{\mathbf{A}}(\mathbf{r}) + \mathbf{a}_{\text{ext}}(\mathbf{r}, t), \\ A_{\text{tot}}^0(\mathbf{r}, t) &= a_{\text{ext}}^0(\mathbf{r}, t) + \frac{1}{c} \int d^3\mathbf{r}' \frac{j_{\text{ext}}^0(\mathbf{r}', t')}{4\pi\epsilon_0|\mathbf{r} - \mathbf{r}'|}. \end{aligned}$$

The nonrelativistic current is defined by

$$\mathbf{J}(\mathbf{r}, t) = \hat{\mathbf{J}}_p(\mathbf{r}) + \vec{\nabla} \times \hat{\mathbf{M}}(\mathbf{r}) - \frac{e}{m_e c} \hat{j}_0(\mathbf{r}) \hat{\mathbf{A}}_{\text{tot}}(\mathbf{r}, t), \quad (111)$$

with the magnetization-density operator  $\hat{\mathbf{M}}(\mathbf{r})$  [18]. The term  $\frac{e}{m_e c} \hat{j}_0(\mathbf{r}) \hat{\mathbf{A}}_{\text{tot}}(\mathbf{r}, t)$  is the diamagnetic current, while the operator  $\hat{\mathbf{J}}_p(\mathbf{r})$  is the paramagnetic current operator and is defined by

$$\hat{\mathbf{J}}_p(\mathbf{r}) = \frac{e\hbar}{2m_e i} \left[ \hat{\Psi}^\dagger(\mathbf{r}) \vec{\nabla} \hat{\Psi}(\mathbf{r}) - \left( \vec{\nabla} \hat{\Psi}^\dagger(\mathbf{r}) \right) \hat{\Psi}(\mathbf{r}) \right], \quad (112)$$

<sup>9</sup> We note here, that in Ref. [18] the magnetic field operator  $\hat{\mathbf{B}}(\mathbf{r})$  is defined as  $\hat{\mathbf{B}}(\mathbf{r}) = \frac{1}{c} \vec{\nabla} \times \hat{\mathbf{A}}(\mathbf{r})$ , while in this thesis we use the definition  $\hat{\mathbf{B}}(\mathbf{r}) = \vec{\nabla} \times \hat{\mathbf{A}}(\mathbf{r})$  to be consistent with Sec. 2.3 and Ref. [70].



where we add an electronic charge compared to Eq. 45. The paramagnetic current operator has the corresponding zero-component  $\hat{j}_0(\mathbf{r}) = ec\hat{\Psi}^\dagger(\mathbf{r})\hat{\Psi}(\mathbf{r}) = ec\hat{n}(\mathbf{r})$ , which is directly proportional to the electron density operator  $\hat{n}(\mathbf{r})$ .

The covariant Hamiltonian  $\hat{H}_{\text{cov}}$  and the external Hamiltonian  $\hat{H}_{\text{ext}}$  contain the two (classical) external vector potentials, i.e.  $\mathbf{a}_{\text{ext}}$  ( $a_{\text{ext}}^0$ ) that couple to the electron current and  $\mathbf{j}_{\text{ext}}$  ( $j_{\text{ext}}^0$ ) that couples to the Maxwell field operator. The external Hamiltonian is given by

$$\hat{H}_{\text{ext}} = - \int d^3\mathbf{r} (\hat{\mathbf{J}}(\mathbf{r}, t) \cdot \mathbf{a}_{\text{ext}}(\mathbf{r}, t) + \hat{\mathbf{A}}(\mathbf{r}) \cdot \mathbf{j}_{\text{ext}}(\mathbf{r}, t)). \quad (113)$$

We now define as a classical approximation for the electromagnetic field the Maxwell-Schrödinger propagation [76]. In the Maxwell-Schrödinger formalism, we neglect the quantized nature of the electromagnetic field in the Pauli-Fierz Hamiltonian of Eq. 108, hence  $\hat{\mathbf{A}} = 0$ , while the classical vector field  $\mathbf{a}_{\text{ext}}$  satisfies the classical Maxwell wave equation of Eq. 85. If we propagate the Schrödinger equation of Eq. 1 with the Pauli-Fierz Hamiltonian together with the Maxwell wave equation of Eq. 85, we get a set of two equations, which can be solved self-consistently.

### 2.3.8 Quantum Electrodynamics in a Cavity: Zero-Boundary Conditions

Besides periodic boundary conditions, we also study the case of zero-boundary conditions for the electrodynamic field. For zero-boundary conditions, the allowed wave vectors  $k$  are  $k_i = \pi v_i/L$  and we find for the vector potential,

$$\hat{\mathbf{A}}(\mathbf{r}) = \sum_{\mathbf{k}} \sum_{\lambda=1,2} \left( \frac{\hbar}{2\epsilon_0 c k} \right)^{1/2} \mathbf{e}_{\mathbf{k}\lambda} \left( \hat{\mathbf{a}}_{\mathbf{k}\lambda} + \hat{\mathbf{a}}_{\mathbf{k}\lambda}^\dagger \right) \mathcal{S}(\mathbf{k} \cdot \mathbf{r}), \quad (114)$$

where we introduced the normalized mode function

$$\mathcal{S}(\mathbf{k} \cdot \mathbf{r}) = \left( \frac{2}{L} \right)^{3/2} \prod_{i=1}^3 \sin(k_i r_i). \quad (115)$$

For convenience, we introduce the following abbreviations

$$\hat{\mathbf{A}}(\mathbf{r}) = \frac{1}{\sqrt{\epsilon_0}} \sum_{\mathbf{k}\lambda} \mathcal{A}_{\mathbf{k}\lambda}(\mathbf{r}) \hat{q}_{\lambda\mathbf{k}}, \quad (116)$$

$$\hat{\mathbf{E}}_T(\mathbf{r}) = -\frac{1}{\sqrt{\epsilon_0}} \sum_{\mathbf{k}\lambda} \mathcal{A}_{\mathbf{k}\lambda}(\mathbf{r}) \hat{p}_{\lambda\mathbf{k}}, \quad (117)$$

$$\hat{\mathbf{B}}(\mathbf{r}) = \frac{1}{\sqrt{\epsilon_0}} \sum_{\mathbf{k}\lambda} \left( \vec{\nabla} \times \mathcal{A}_{\mathbf{k}\lambda}(\mathbf{r}) \right) \hat{q}_{\lambda\mathbf{k}}, \quad (118)$$

with  $\mathcal{A}_{\mathbf{k}\lambda}(\mathbf{r}) = \mathbf{e}_{\mathbf{k}\lambda} \mathcal{S}(\mathbf{k} \cdot \mathbf{r})$ .

### 2.3.9 The Length Gauge and the Dipole Approximation

The minimal-coupling Hamiltonian is inconvenient from different perspectives: The field variables enter through the vector potential, rather than the electric field. Hence, the electron-field interaction is not explicitly gauge-independent. A gauge-independent electron-field coupling can be found in the so-called length-gauge.

Here, the dielectric displacement operator  $\hat{\mathbf{D}}_T(\mathbf{r})$ , which consists of the transversal electric field operator  $\hat{\mathbf{E}}_T(\mathbf{r})$  and the electric polarization operator  $\hat{\mathbf{P}}(\mathbf{r})$ , couples bilinearly to the electric polarization operator  $\hat{\mathbf{P}}(\mathbf{r})$ . The coupling via  $\hat{\mathbf{D}}_T(\mathbf{r})$  is directly related to optical measurements. In the momentum gauge, the interaction between the particles and the field is nonlinear in the radiation degrees of freedom due to the  $\hat{\mathbf{A}}^2(\mathbf{r})$  term. The change from the momentum gauge to the length gauge, can be achieved by performing the Power-Zienau-Woolley transformation [77, 78]. This transformation is general and independent of the dipole approximation [70]. However, assuming the dipole approximation [68], the Power-Zienau-Woolley transformation has a particularly simple form. For a detailed derivation, we refer the reader to appendix A. The length-gauge Hamiltonian can be written as

$$\begin{aligned} \hat{H}_{\text{dipole}} = & \hat{T}_e + \hat{W}_{ee} + \hat{W}_{eN}(\{\mathbf{R}\}) + \frac{1}{2} \int d^3\mathbf{r} \left[ \frac{\hat{\mathbf{D}}_T^2(\mathbf{r})}{\epsilon_0} + \epsilon_0 c^2 \hat{\mathbf{B}}^2(\mathbf{r}) \right] \\ & - \frac{1}{\epsilon_0} \int d^3\mathbf{r} \hat{\mathbf{P}}_T(\mathbf{r}) \cdot \hat{\mathbf{D}}_T(\mathbf{r}) + \frac{1}{2\epsilon_0} \int d^3\mathbf{r} \hat{\mathbf{P}}_T^2(\mathbf{r}), \end{aligned} \quad (119)$$

with the electric displacement operator  $\hat{\mathbf{D}}(\mathbf{r}) = \epsilon_0 \hat{\mathbf{E}}(\mathbf{r}) + \hat{\mathbf{P}}(\mathbf{r})$  and the polarization operator in dipole approximation

$$\hat{\mathbf{P}}(\mathbf{r}, \{\mathbf{R}\}) = -e \sum_{i=1}^{n_e} \mathbf{r}_i \delta(\mathbf{r} - \mathbf{r}_i) + e \sum_{I=1}^{N_n} Z_I \mathbf{R}_I \delta(\mathbf{r} - \mathbf{R}_I), \quad (120)$$

where  $\mathbf{r}_i$  is the electron position operator and  $\mathbf{R}_I$  the nuclear position. By performing the unitary transformation  $\hat{p}_{\mathbf{k}\lambda} \rightarrow -\omega \hat{q}_{\mathbf{k}\lambda}$  and  $\hat{q}_{\mathbf{k}\lambda} \rightarrow \frac{1}{\omega} \hat{p}_{\mathbf{k}\lambda}$  in Eqns. 116-118, the Hamiltonian in Eq. 119 has a similar form as the free-photon Hamiltonian in Eq. 105 and reads as

$$\hat{H}_{\text{dipole}} = \hat{T}_e + \hat{W}_{ee} + \hat{W}_{eN}(\{\mathbf{R}\}) + \frac{1}{2} \sum_{\mathbf{k}\lambda} \hat{p}_{\mathbf{k}\lambda}^2 + \omega_{\mathbf{k}\lambda}^2 \left( \hat{q}_{\mathbf{k}\lambda} - \frac{e \mathcal{A}_{\mathbf{k}\lambda}(\mathbf{R}_c)}{\omega_{\mathbf{k}\lambda} \sqrt{\epsilon_0}} \hat{\mathbf{R}} \right)^2, \quad (121)$$

with the total electronic dipole moment operator  $\hat{\mathbf{R}} = \sum_{i=1}^{n_e} \mathbf{r}_i$  and

$$\hat{\mathbf{A}}(\mathbf{r}) = \frac{1}{\sqrt{\epsilon_0}} \sum_{\mathbf{k}\lambda} \frac{\mathcal{A}_{\mathbf{k}\lambda}(\mathbf{r})}{\omega_{\mathbf{k}\lambda}} \hat{p}_{\lambda\mathbf{k}}, \quad (122)$$

$$\hat{\mathbf{D}}_T(\mathbf{r}) = \sqrt{\epsilon_0} \sum_{\mathbf{k}\lambda} \omega_{\mathbf{k}\lambda} \mathcal{A}_{\mathbf{k}\lambda}(\mathbf{r}) \hat{q}_{\lambda\mathbf{k}}, \quad (123)$$

$$\hat{\mathbf{B}}(\mathbf{r}) = \frac{1}{\sqrt{\epsilon_0}} \sum_{\mathbf{k}\lambda} \frac{(\vec{\nabla} \times \mathcal{A}_{\mathbf{k}\lambda}(\mathbf{r}))}{\omega_{\mathbf{k}\lambda}} \hat{p}_{\lambda\mathbf{k}}, \quad (124)$$

$$\hat{\mathbf{P}}(\mathbf{r}) = -e \sum_{\mathbf{k}\lambda} (\mathcal{A}_{\mathbf{k}\lambda}(\mathbf{R}_c) \cdot \hat{\mathbf{R}}) \mathcal{A}_{\mathbf{k}\lambda}(\mathbf{r}), \quad (125)$$

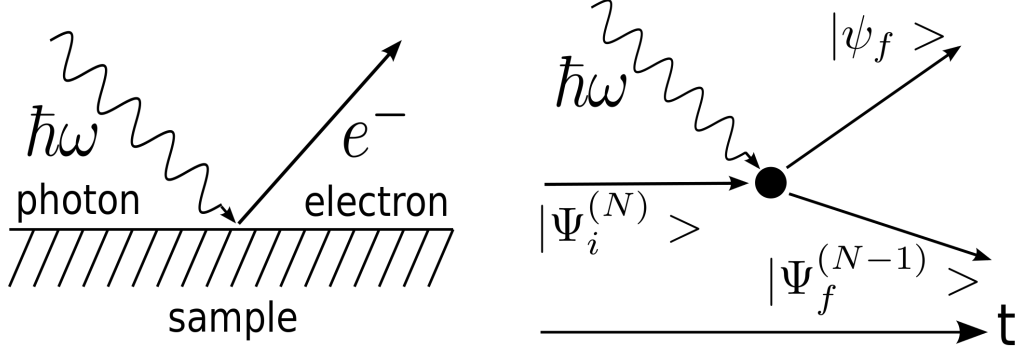


Figure 5: Left: Schematic view on the photoemission process, right: description of the sudden approximation to photoemission.

with the position of the charge center of the system  $\mathbf{R}_c$ . Throughout this thesis, unless stated otherwise, we use SI units [19]. To transfer the field operators defined in SI units in Eqns. 122-124 to Gaussian (G) units [19], we can use

$$\hat{\mathbf{A}}^{(G)}(\mathbf{r}) = \sqrt{\frac{4\pi}{\mu_0}} \hat{\mathbf{A}}(\mathbf{r}) = \sqrt{4\pi} \sum_{\alpha} \frac{c \mathcal{A}_{\alpha}(\mathbf{r})}{\omega_{\alpha}} \hat{p}_{\lambda \mathbf{k}}, \quad (126)$$

$$\hat{\mathbf{D}}_T^{(G)}(\mathbf{r}) = \sqrt{\frac{4\pi}{\epsilon_0}} \hat{\mathbf{D}}_T(\mathbf{r}) = \sqrt{4\pi} \sum_{\alpha} \omega_{\alpha} \mathcal{A}_{\alpha}(\mathbf{r}) \hat{q}_{\lambda \mathbf{k}}, \quad (127)$$

$$\hat{\mathbf{B}}^{(G)}(\mathbf{r}) = \sqrt{\frac{4\pi}{\mu_0}} \hat{\mathbf{B}}(\mathbf{r}) = \sqrt{4\pi} \sum_{\alpha} \frac{c (\vec{\nabla} \times \mathcal{A}_{\alpha}(\mathbf{r}))}{\omega_{\alpha}} \hat{p}_{\lambda \mathbf{k}}. \quad (128)$$

## 2.4 THEORY OF STATIC AND TIME-RESOLVED PHOTOELECTRON SPECTROSCOPY

In this section, we discuss the theory necessary to calculate photoelectron spectra. Therefore, we introduce Fermi's golden rule, discuss the equilibrium and nonequilibrium spectral function, and study the spectral functions in the Born-Oppenheimer approximation.

The light-matter interaction is essential in the field of spectroscopy. One particular spectroscopic method is photoelectron spectroscopy, which is used to investigate the structure of atoms, molecules and solids [79, 80]. Since photoelectron spectroscopy is based on nonneutral transitions between many-body states, it complements other spectroscopic methods such as optical-absorption spectroscopy [12] that access charge neutral transitions, e.g. dipole or quadrupole transitions.

The left-hand side of Fig. 5 depicts schematically a typical photoelectron experiment. In photoelectron experiments, high-energy photons with energy  $\hbar\omega$  are used to probe the sample. The sample absorbs these high-energy photons with the removal of an electron from the system. The emerging photoelectron is then detected by experiment and allows to get insight about the sample structure.

In theory, photoelectron spectra can be obtained by calculating the one-body spec-

tral function [81–84]. While in the literature, the complex photoemission process is explained illustratively by the absorption of photons, which is a quantum process, the one-body spectral function only depends on electronic operators. The quantum nature of the electromagnetic field is implied only implicitly by the usage of Fermi’s golden rule. From Fermi’s golden rule, the expression for the photocurrent  $J_{\mathbf{k}}(\omega)$  that emerges in photoelectron experiments is given by first-order perturbation theory [80, 81, 83] as

$$J_{\mathbf{k}}(\omega) = \frac{2\pi}{\hbar} \sum_j \left| \langle \Psi_{j,\mathbf{k}}^{(N)} | \hat{\Delta} | \Psi_i^{(N)} \rangle \right|^2 \delta(E_{\mathbf{k}} - E_j - \hbar\omega). \quad (129)$$

We denote the final state of the photoemission process by  $\Psi_{j,\mathbf{k}}^{(N)}$ . Typically, these final states contain two contributions: (i) the photoelectron with momentum  $\mathbf{k}$  and energy  $E_{\mathbf{k}}$  is in a scattering state (e.g. a distorted plane wave, or time-inverted scattering/low-energy electron diffraction (LEED) state [79]). (ii) the remaining part of the system is in an excited state  $j$  that contains  $N - 1$  electrons with energy  $E_j^{(N-1)}$ . After the photoemission process, the emitted electron and the remaining photo fragment are in general still correlated. Both parts contribute to the combined state  $\Psi_{j,\mathbf{k}}^{(N)}$ . We denote the  $N$ -body initial state in the photoemission process by  $\Psi_i^{(N)}$  with energy  $E_i^{(N)}$ . From this state, the photoelectron will be emitted during the photoemission process. In Eq. 129,  $E_j$  is given by  $E_j = E_i^{(N)} - E_j^{(N-1)}$ . Throughout this section, we denote by the superscript  $(N)$  the number of electrons in the state.

Fermi’s golden rule as defined in Eq. 129 is strictly valid only for pure states as initial and final states. This is justified for situations, where the system is in the  $N$ -electron ground state before the photoemission process, but also excited eigenstates are allowed in principle. However, in many experimental setups such as pump-probe photoelectron spectroscopy, it is not justified to assume the ground state as initial state in the photoemission process. Instead, an excited state or a superposition of excited states are a better description for the initial state. If the initial state is not an eigenstate, the photoemission process can be described by the nonequilibrium spectral function, which is discussed in Sec. 2.4.2.

The coupling operator  $\hat{\Delta}$  in Eq. 129 between initial and final states is usually considered in dipole approximation either in length gauge ( $\sim \mathbf{r} \cdot \mathbf{E}$ ) or momentum gauge ( $\sim \mathbf{p} \cdot \mathbf{A}$ ), where the electric field  $\mathbf{E}$  and the vector potential  $\mathbf{A}$  are classical fields subject to the classical Maxwell’s equations. The quantum nature of the electromagnetic field, which allows for the absorption and emission of single photons, is incorporated by Fermi’s golden rule by the delta function  $\delta(E_{\mathbf{k}} - E_j - \hbar\omega)$ . The delta function assures energy conservation at  $t \rightarrow \infty$  between the energy of the absorbed photon  $\hbar\omega$  and the energy difference of the electronic transition  $E_{\mathbf{k}} - E_j$ , thus  $0 = \hbar\omega + E_i^{(N)} - (E_{\mathbf{k}} + E_j^{(N-1)})$ .

The widely used sudden approximation (SA) [82, 85] simplifies the problem of calculating Eq. 129 drastically. This approximation assumes the decoupling in the final states by setting

$$|\Psi_{j,\mathbf{k}}^{(N)}\rangle \sim \hat{c}_{\mathbf{k}}^\dagger |\Psi_j^{(N-1)}\rangle, \quad (130)$$

Here, the operator  $\hat{c}_{\mathbf{k}}^\dagger$  is an electronic creation operator, which creates an electron with momentum  $\mathbf{k}$ . We illustrate schematically the SA in Fig. 5 on the right. The SA implies effectively that the final state in the photoemission process  $|\Psi_{j,\mathbf{k}}^{(N)}\rangle$  is a product state between a plane-wave like state for the emitted photoelectron and the remaining  $N - 1$  electron many-body state  $|\Psi_j^{(N-1)}\rangle$ . Formulated differently, after the sample was hit by the high-energy photon, the electron and the remaining photofragment evolve independently, hence both are uncorrelated. Neglecting multi-photon processes, applying the SA and assuming a high-energy limit (X-ray spectroscopy), we can reformulate Eq. 129 in terms of the one-body spectral function  $A_{lm,\sigma}^{SA}(E_{\mathbf{k}} - \hbar\omega)$

$$J_{\mathbf{k}}^{SA}(\omega) \approx \frac{2\pi}{\hbar} \sum_{lm,\sigma} \Delta_{\mathbf{k}l,\sigma} A_{lm,\sigma}^{SA}(E_{\mathbf{k}} - \hbar\omega) \Delta_{m,\sigma\mathbf{k}}, \quad (131)$$

In the high-energy limit, the matrix elements  $\Delta_{\mathbf{k}l,\sigma}$  and  $\Delta_{m,\sigma\mathbf{k}}$  are often approximated by constant values [79, 80].

In the next two section, we discuss the equilibrium and the nonequilibrium spectral function. For a detailed derivation of the equilibrium and nonequilibrium spectral function, we refer the reader to the appendix D.

#### 2.4.1 Equilibrium Spectral Function

Eq. 129 applies for equilibrium situations, where the initial state of the photoemission process  $|\Psi_i^{(N)}\rangle$  is an eigenstate of the Hamiltonian. This assumption is justified for photoelectron experiments, where the sample is in the ground state before the photoemission process. The equilibrium spectral function is defined as

$$A_{lm,\sigma}^{SA}(\omega) = \sum_j \langle \Psi_0^{(N)} | \hat{c}_{l,\sigma}^\dagger | \Psi_j^{(N-1)} \rangle \langle \Psi_j^{(N-1)} | \hat{c}_{m,\sigma} | \Psi_0^{(N)} \rangle \delta(\hbar\omega - E_j). \quad (132)$$

We furthermore assume that the diagonal elements of  $A_{lm,\sigma}^{SA}$  are dominant, hence ( $l = m$ ), which is exact for independent electrons [83]. The spectral function is directly connected to the Lehmann representation of the single-particle Green's function in Eq. 70 [80, 83]

$$A(\omega) = \frac{1}{\pi} \left| \int d^3\mathbf{r} \lim_{\mathbf{r}' \rightarrow \mathbf{r}} G(\mathbf{r}, \mathbf{r}', \omega) \right| = \frac{1}{\pi} |\text{Tr} [\text{Im } G(\omega)]|. \quad (133)$$

The spectral function as in Eq. 132 contains a sum-over-states expression, where all correlated eigenstates have to be known explicitly. Alternatively, the spectral function can be calculated in the time domain by the overlap of the time-evolved initial state with the time-evolved kicked initial state

$$A_{lm,\sigma}^{SA}(t) = \langle \tilde{\Psi}_{-l}^{(N-1)}(t) | \hat{c}_{m,\sigma}^\dagger | \Psi_0^{(N)}(t) \rangle. \quad (134)$$

In the kicked initial state  $|\tilde{\Psi}_{-l}^{(N-1)}(t_0)\rangle = \hat{c}_l |\Psi_0^{(N)}(t_0)\rangle$  an electron has been removed from the system at initial time  $t_0$ . Eq. 134 can also be calculated for systems, where it is not possible to calculate all eigenstates explicitly.

Convergence and completeness of the employed basis set can be tested by evaluating the sum rule

$$N = \sum_l \int d\omega A_{ll,\sigma}(\omega) = \sum_l \langle \Psi_0^{(N)} | \hat{c}_{l,\sigma}^\dagger \hat{c}_{l,\sigma} | \Psi_0^{(N)} \rangle. \quad (135)$$

The spectral function obeys this sum rule, which yields the total number of electrons  $N$  present in the initial state [86].

#### 2.4.2 Nonequilibrium Spectral Function

The expression for the photocurrent in Eq. 131 depends explicitly on the initial state of the photoemission process  $|\Psi_0^{(N)}\rangle$ . In equilibrium experiments, the system is approximately in the ground state before the photoemission process takes place. For nonequilibrium experiments, such as pump-probe experiments, this assumption is not justified and therefore Fermi's golden rule has to be extended to include arbitrary initial states for photoemission. This can be done by replacing the state  $\Psi_0^{(N)}$  in Eq. 132 by the time-dependent state  $\Psi_0^{(N)}(t)$  such that

$$A_{lm,\sigma}^{SA}(t, \omega) = \sum_j \langle \Psi_0^{(N)}(t) | \hat{c}_{l,\sigma}^\dagger | \Psi_j^{(N-1)} \rangle \langle \Psi_j^{(N-1)} | \hat{c}_{m,\sigma} | \Psi_0^{(N)}(t) \rangle \delta(\hbar\omega - E_j). \quad (136)$$

This expression for the spectral function now depends explicitly on the time  $t$  and the frequency  $\omega$  and is further not time invariant in  $t$ . The time  $t$  can be interpreted as the delay time between the pump and the probe pulse. We allow for time-dependent initial-states  $|\Psi_0^{(N)}(t)\rangle = \sum_n d_n(t) |\Psi_n^{(N)}\rangle$ , which can be expanded in terms of the eigenstates  $\Psi_n^{(N)}$  with corresponding eigenenergy  $E_n$  and the coefficients  $d_n(t_0) = \langle \Psi_0^{(N)}(t_0) | \Psi_n^{(N)} \rangle$ . As discussed in more detail in the appendix D, the transition energies  $E_j$  in Eq. 136 depend on the eigenenergies  $E_n$  that correspond to the according eigenstate  $\Psi_n^{(N)}$  and emerge by the expansion of the initial state. For practical purposes, we neglect the  $n$ -dependence in the  $\delta$ -function of the spectral function in Eq. 136 and replace it by the energy of the initial state  $E_0 = \langle \Psi_0^{(N)}(t) | \hat{H} | \Psi_0^{(N)}(t) \rangle$ , i.e.  $E_j = E_0 - E_j^{(N-1)}$ . This approximation allows us to fix peak positions to  $N - 1$  electron states and does not affect the spectral amplitudes. Further, the approximation gives the  $\delta$ -peak position a clear interpretation, rather than the usage of relative energies. Considering the full  $n$ -dependence in the delta function shifts high energy peaks to lower energy. For many situations, e.g. general many-body problems, the exact many-body eigenstates and eigenenergies are not available. In these cases, this approximation allows a practical way to obtain photoelectron spectra.

One way beyond this approximation is to cast the nonequilibrium spectral function directly in the time domain

$$A_{lm,\sigma}^{SA}(t, \tau) = \langle \tilde{\Psi}_{-l}^{(N-1)}(t + \tau) | \hat{c}_{m,\sigma}^\dagger | \Psi_0^{(N)}(t + \tau, t) \rangle, \quad (137)$$

with the kicked initial state  $|\tilde{\Psi}_{-l}^{(N-1)}(t)\rangle = \hat{c}_l |\Psi_0^{(N)}(t)\rangle$ , where the operator  $\hat{c}_l$  acts at time  $t$  on the state  $|\Psi_0(t)\rangle$ . The sum rule of Eq. 135 is also applicable in nonequilibrium

rium situations. For pump-probe photoelectron experiments, we can also calculate the time averages of the spectra, which can be calculated as follows

$$A_{lm,\sigma}^{SA}(\omega) = \frac{1}{t_f - t_1} \int_{t_1}^{t_f} A_{lm,\sigma}^{SA}(\tau, \omega) d\tau. \quad (138)$$

#### 2.4.3 Approximations for the Electron-Phonon Spectral Function

The one-body spectral function as defined in Eq. 132 is formulated in terms of correlated energy eigenstates of the full electron-phonon Hamiltonian. In practice, for most systems the direct evaluation of this expression is not possible, since the eigenstates are not accessible. For electron-phonon systems, a straightforward approximation is the replacement of the correlated electron-phonon initial and final states by factorized Born-Oppenheimer states.

For the following discussion, we define as single-harmonic approximation (SHA) the case where only the initial state is replaced by the corresponding factorized Born-Oppenheimer state in harmonic approximation  $|\chi_{00}\phi_0^{(N)}\rangle$ , while all final states are kept as correlated electron-phonon  $N - 1$  electron states. In the SHA the spectral function takes the form

$$A_{lm,\sigma}^{SA,SHA}(\omega) = \sum_j \langle \chi_{00}\phi_0^{(N)} | \hat{c}_{l,\sigma}^\dagger | \Psi_j^{(N-1)} \rangle \langle \Psi_j^{(N-1)} | \hat{c}_{m,\sigma} | \chi_{00}\phi_0^{(N)} \rangle \delta(\hbar\omega - E_j). \quad (139)$$

Interestingly, since the Born-Oppenheimer ground state is by construction not an eigenstate of the full many-body Hamiltonian, already at the level of the SHA we find a nonequilibrium situation, where in principle the nonequilibrium spectral function applies. If the Born-Oppenheimer ground state is propagated using the exact Hamiltonian, we find (small) oscillations in the observables during the time propagation. This is in contrast to the exact ground state that has time-constant observables by construction.

An additional simplification can be achieved, if the harmonic approximation is assumed for both, the involved initial and final potential-energy surfaces. This approximation replaces the remaining  $N - 1$  electron states by Born-Oppenheimer states in harmonic approximation and leads to the double-harmonic approximation (DHA) for the spectral function

$$A_{lm,\sigma}^{SA,DHA}(\omega) = \sum_{n,j} |\langle \chi_{nj} | \chi_{00} \rangle|^2 \langle \phi_j^{(N-1)} | \hat{c}_{l,\sigma}^\dagger | \phi_0^{(N)} \rangle \langle \phi_0^{(N)} | \hat{c}_{m,\sigma}^\dagger | \phi_j^{(N-1)} \rangle \times \delta(\hbar\omega - \epsilon_j). \quad (140)$$

In the DHA, peak heights in the photoelectron-spectrum are modulated by the Franck-Condon factors  $\langle \chi_{nj} | \chi_{00} \rangle$ , i.e. the overlaps of nuclear wave functions.





### Part III

## MODEL SYSTEMS AND NUMERICAL METHODS



## MODEL SYSTEMS AND NUMERICAL METHODS

In this chapter, we first introduce the model Hamiltonians, which are employed in this thesis. In the second part, we discuss the numerical methods, which are used for practical calculations.

### 3.1 MODEL SYSTEMS FOR THE STUDY OF THE ELECTRON-BOSON INTERACTION

#### 3.1.1 *Su-Schrieffer-Heeger Hamiltonian*

The Su-Schrieffer-Heeger (SSH) model [87, 88] is commonly used to model Trans-Polyacetylene oligomers chains (Fig. 6 (a)) by describing  $\pi$ -electrons in the polymer chain. In literature, the SSH Hamiltonian is employed, among others, to describe soliton propagation in conjugated polymers [88], or long-lived oscillatory incoherent electron dynamics [89]. The SSH Hamiltonian is defined as follows

$$\begin{aligned}\hat{H}_{ssh} &= \hat{H}_\pi + \hat{H}_{ph} + \hat{H}_{\pi-ph}, \\ \hat{H}_\pi &= -T \sum_{n,\sigma} \hat{c}_{n+1,\sigma}^\dagger \hat{c}_{n,\sigma} + \hat{c}_{n,\sigma}^\dagger \hat{c}_{n+1,\sigma}, \\ \hat{H}_{ph} &= \sum_n \frac{\hat{p}_n^2}{2M} + \frac{K}{2} (\hat{u}_{n+1} - \hat{u}_n)^2, \\ \hat{H}_{\pi-ph} &= \sum_{n,\sigma} \alpha (\hat{u}_{n+1} - \hat{u}_n) \left( \hat{c}_{n+1,\sigma}^\dagger \hat{c}_{n,\sigma} + \hat{c}_{n,\sigma}^\dagger \hat{c}_{n+1,\sigma} \right),\end{aligned}\tag{141}$$

where  $\hat{c}_{n,\sigma}^\dagger$ , and  $\hat{c}_{n,\sigma}$  denote the fermionic creation and annihilation operators that create or destroy  $\pi$ -electrons with spin  $\sigma$  on site  $n$  of the chain, respectively. The nuclear Hamiltonian  $H_{ph}$  is described by the nuclear displacement operators  $\hat{u}_n$ , whose expectation values measure the displacement of the nuclear positions on site  $n$  to the equidistant arrangement of the oligomers in the chain. The nuclear displacement operators  $\hat{u}_n$  and the nuclear momentum operators  $\hat{p}_n$  obey the usual commutation relations as stated in Eq. 10. The Hamiltonian then naturally separates into three parts: (i) the electronic Hamiltonian  $\hat{H}_\pi$  describes electron hopping of  $\pi$ -electrons within a tight-binding scheme [90]. (ii) The nuclear Hamiltonian  $\hat{H}_{ph}$  treats nuclei as a chain of coupled quantum harmonic oscillators, and (iii) the electron-nuclear interaction part in the Hamiltonian  $\hat{H}_{\pi-ph}$  considers electron-nuclear coupling up to first-order in the nuclear displacement. Formally, the electron-phonon coupling  $\hat{H}_{\pi-ph}$  can also be combined with the kinetic term  $\hat{H}_\pi$ . The hopping parameter  $T$  is then replaced by  $T - \alpha (\hat{u}_{n+1} - \hat{u}_n)$ . This formal rearrangement has a clear physical interpretation: For electrons it is more favorable to hop when two nuclei are closer to each other or formulated differently the effective hopping parameter is reduced when the nuclei are moving apart. In all numerical calculations, we use the standard set of parameters for the SSH-Hamiltonian [88],  $\alpha = 4.1 \text{ eV/\AA}$ ,  $T = 2.5 \text{ eV}$ ,  $K = 21 \text{ eV/\AA}^2$ ,  $M = 1349.14 \text{ eVfs}^2/\text{\AA}^2$ , which leads

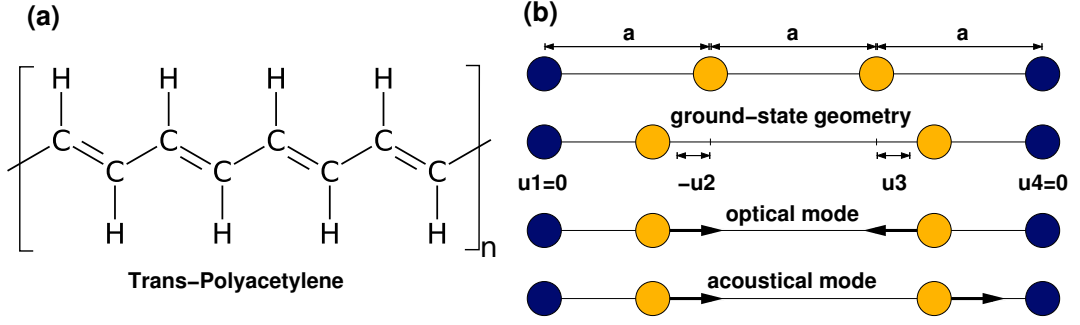


Figure 6: (a) Chemical formula of a Trans-Polyacetylene chain. (b) Four Trans-Polyacetylene oligomers containing two dynamic and two fixed nuclei. The coordinates  $u_j$  describe the oligomer displacement with respect to an equidistant arrangement with lattice spacing  $a$ . In the ground state, the chain favors a dimerized arrangement. This setup gives rise to one optical and one acoustical phonon mode in the chain.

to a lattice spacing of  $a = 1.22 \text{ \AA}$  in the chain. Using this set of parameters, the chain energetically favors a dimerized arrangement in the ground state, leading to a nonvanishing displacement coordinate  $u_i \neq 0$ , which is illustrated in Fig. 6 (b). The many-body Su-Schrieffer-Heeger Hamiltonian of Eq. 141 can be rewritten in terms of the BOA such that

$$\begin{aligned} \hat{H}_{ssh,el} &= \hat{H}_{\pi,el} + \hat{H}_{\pi-ph,el}, \\ \hat{H}_{\pi,el} &= -T \sum_{n,\sigma} \hat{c}_{n+1,\sigma}^\dagger \hat{c}_{n,\sigma} + \hat{c}_{n,\sigma}^\dagger \hat{c}_{n+1,\sigma}, \\ \hat{H}_{\pi-ph,el} &= \sum_{n,\sigma} \alpha (u_{n+1} - u_n) \left( \hat{c}_{n+1,\sigma}^\dagger \hat{c}_{n,\sigma} + \hat{c}_{n,\sigma}^\dagger \hat{c}_{n+1,\sigma} \right), \end{aligned} \quad (142)$$

which leads to an electronic Schrödinger equation of the following form

$$\hat{H}_{ssh,el}(\{u_n\}) |\phi_j^{(N)}(\{u_n\})\rangle = \epsilon_{el,j}(\{u_n\}) |\phi_j^{(N)}(\{u_n\})\rangle. \quad (143)$$

This Hamiltonian considers the electronic degrees of freedom quantum mechanically, while the nuclear component is reduced to classical coordinates  $\{u_n\}$ . Furthermore, the eigenvalues  $\epsilon_{el,j}(\{u_n\})$  as function of  $\{u_n\}$  contribute to the Born-Oppenheimer surfaces of the system as given by Eq. 13. Besides the surfaces, the Hessian of the electronic energies with respect to the displacements can be computed to obtain the harmonic frequencies  $\omega$ , which are fundamental frequencies in the harmonic approximation of the BOA.

If external laser fields are applied to the system, we need to extend the Hamiltonian of Eq. 141. In dipole coupling, the correlated many-body Hamiltonian can be modified to

$$\begin{aligned} \hat{H}_{ssh}(t) &= \hat{H}_{\pi} + \hat{H}_{ph} + \hat{H}_{\pi-ph} + \hat{H}_{\pi,E}(t) + \hat{H}_{ph,E}(t), \\ \hat{H}_{\pi,E}(t) &= -e \sum_{n,\sigma} x_n \hat{c}_{n,\sigma}^\dagger \hat{c}_{n,\sigma} \cdot E(t), \\ \hat{H}_{ph,E}(t) &= \sum_n q_n \hat{u}_n \cdot E(t), \\ E(t) &= E_0 \exp\left(-(t-t_0)^2/\sigma^2\right) \sin \omega_l t, \end{aligned} \quad (144)$$

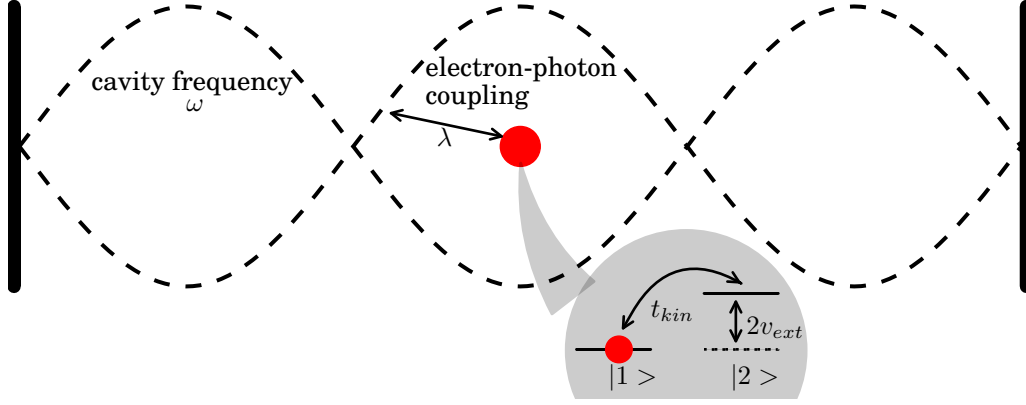


Figure 7: The two-site Jaynes-Cummings-Hubbard model is defined by the electron hopping element  $t_{kin}$ , the on-site potential difference  $v_{ext}$ , the electron-photon interaction strength  $\lambda$  and the photon mode frequency  $\omega$ .

where  $x_n$  corresponds to the position of site  $n$ ,  $e$  to the electric charge constant and  $q_n$  to the charge of the nuclei  $n$ . The electric field  $E(t)$  describes the amplitude of the laser pulse. In the Hamiltonian of Eq. 144, the external laser pulse couples linearly to both, the electric dipole moment, and the nuclear dipole moment.

### 3.1.2 The Jaynes-Cummings-Hubbard Hamiltonian

The general nonrelativistic light-matter Hamiltonian of Eq. 108 can be directly connected to the Jaynes-Cummings-Hubbard (JCH) Hamiltonian, the Rabi Hamiltonian, and spin-boson models, which all have been intensively investigated in the quantum optics literature [75, 91–94]. All these Hamiltonians have been applied in the context of Rabi oscillations, field fluctuations, oscillation collapses, revivals, coherences, entanglement, and the dynamics of dissipative systems (see e.g. Ref. [93] and references therein). The direct connection between the Hamiltonian in Eq. 108 and the Jaynes-Cummings-Hubbard Hamiltonian is discussed in appendix C.

The JCH Hamiltonian contains one single electron on two sites in space with hopping constant  $t_{kin}$ . This two-site model is coupled to a single photon-field mode of frequency  $\omega$  with the coupling strength  $\lambda$ . Fig. 7 shows a schematic view of the model system. Furthermore, in the Hamiltonian two external variables are present, i.e.  $v_{ext}(t)$  and  $j_{ext}(t)$ , which couple only to the photon field and the electron, respectively. We define the Hamiltonian in the electron site basis as

$$\hat{H}(t) = -t_{kin}\hat{\sigma}_x + \omega\hat{a}^\dagger\hat{a} + \lambda(\hat{a} + \hat{a}^\dagger)\hat{\sigma}_z + j_{ext}(t)(\hat{a} + \hat{a}^\dagger) + v_{ext}(t)\hat{\sigma}_z. \quad (145)$$

where  $\sigma_x$  and  $\sigma_z$  are Pauli-matrices and fulfill the commutation relation  $[\hat{\sigma}_i, \hat{\sigma}_j] = 2i\epsilon_{ijk}\hat{\sigma}_k$  with  $(ijk = xyz)$ . The photon creation and annihilation operators  $\hat{a}^\dagger$  and  $\hat{a}$  create or destroy a photon in the photon mode. The JCH Hamiltonian can be transformed to the electron energy basis by the unitary transformation  $\hat{U} = \frac{1}{\sqrt{2}}(\hat{\sigma}_x + \hat{\sigma}_z)$ ,

which effectively interchanges  $\hat{\sigma}_x \leftrightarrow \hat{\sigma}_z$ . In the energy basis the Hamiltonian in Eq. 145 is commonly referred to as the Rabi Hamiltonian and reads

$$\hat{H}_{\text{rabi}}(t) = -t_{\text{kin}}\hat{\sigma}_z + \omega\hat{a}^\dagger\hat{a} + \lambda(\hat{a} + \hat{a}^\dagger)\hat{\sigma}_x + j_{\text{ext}}(t)(\hat{a} + \hat{a}^\dagger) + v_{\text{ext}}(t)\hat{\sigma}_x. \quad (146)$$

A popular approximation for the Rabi Hamiltonian and the JCH Hamiltonian is the rotating-wave approximation (RWA). The RWA divides the Pauli matrix  $\hat{\sigma}_x$  in the interaction term into  $\hat{\sigma}_x = \hat{\sigma}_+ + \hat{\sigma}_-$  where  $\hat{\sigma}_+ = \frac{1}{2}(\hat{\sigma}_x + i\hat{\sigma}_y)$ ,  $\hat{\sigma}_- = \frac{1}{2}(\hat{\sigma}_x - i\hat{\sigma}_y)$  and then neglects the energy nonconserving terms  $\hat{\sigma}_+\hat{a}^\dagger$  and  $\hat{\sigma}_-\hat{a}$ , respectively<sup>1</sup>. In the RWA, the Rabi Hamiltonian is analytically solvable [93]. However, the RWA is only valid in the weak-coupling regime ( $\lambda \sim 0.01$ ), while in the strong-coupling limit ( $\lambda \geq 0.1$ ), the RWA breaks down [95]. Recently, analytical results without invoking the RWA have been published [94].

The electron density  $n$  has for a two-site model two components  $n = (n_1, n_2)$  that describe the probability of finding an electron on the individual site. However, since the number of electrons is fixed, i.e.  $n_1 + n_2 = 1$  in the case of the JCH model, only one nontrivial degree of freedom remains. This is why in the following, we refer to the on-site density difference  $\sigma_z = \langle \hat{\sigma}_z \rangle = n_1 - n_2$  as the electron density for the JCH model. We emphasize that  $\sigma_z$  is in a physical sense not an electron density as defined by Eq. 25, since it can also have negative values. We will define here the photon displacement coordinate  $q$  as in Eq. 106. The Heisenberg equations of motion for  $q$  and  $\sigma_z$  are given as follows

$$\dot{\sigma}_z(t) = -i\langle [\hat{\sigma}_z, \hat{H}(t)] \rangle = -2t_{\text{kin}}\hat{\sigma}_y(t), \quad (147)$$

$$\ddot{\sigma}_z(t) = -i\langle [\dot{\hat{\sigma}}_z, \hat{H}(t)] \rangle = -4t_{\text{kin}}\left(t_{\text{kin}}\sigma_z(t) + v_{\text{ext}}(t)\sigma_x(t) + \lambda\langle (\hat{a}^\dagger + \hat{a})\hat{\sigma}_x \rangle\right), \quad (148)$$

$$\dot{q}(t) = -i\langle [\hat{q}, \hat{H}(t)] \rangle = i\sqrt{\frac{\omega}{2}}(a^\dagger(t) - a(t)) = p(t), \quad (149)$$

$$\ddot{q}(t) = -i\langle [\dot{\hat{q}}, \hat{H}(t)] \rangle = -\omega^2 q(t) - \sqrt{2\omega}(\lambda\sigma_z(t) + j_{\text{ext}}(t)). \quad (150)$$

The last equation can be solved directly

$$q(t) = \int_0^t dt' \frac{1}{\omega} \sin(\omega(t-t')) f(t') + q_0 \cos(\omega t) + \frac{\dot{q}_0}{\omega} \sin(\omega t), \quad (151)$$

$$f(t') = -\sqrt{2\omega}(\lambda\sigma_z(t') + j(t')). \quad (152)$$

with the initial conditions  $q(t_0) = q_0$  and  $\dot{q}(t_0) = \dot{q}_0$ . This integral equation will be important later for the calculation of Kohn-Sham mean-field potentials.

### 3.1.3 GaAs Quantum Dot in an Optical Cavity

The model system consisting of a single electron coupled to a single photon-field mode is schematically depicted in Fig. 8. To describe the electron in the gallium arsenide (GaAs) semiconductor medium, we use an effective atomic mass system [96]

<sup>1</sup> Some papers in the literature, e.g. Ref. [93], refer to the Rabi Hamiltonian in Eq. 146 after applying the RWA to the Jaynes-Cummings Hamiltonian. In this thesis, we refer to the case, where the electronic Hamiltonian is written in energy eigenbasis to the Rabi Hamiltonian, whereas the case, where the electronic Hamiltonian is written in the site basis to the JCH Hamiltonian.

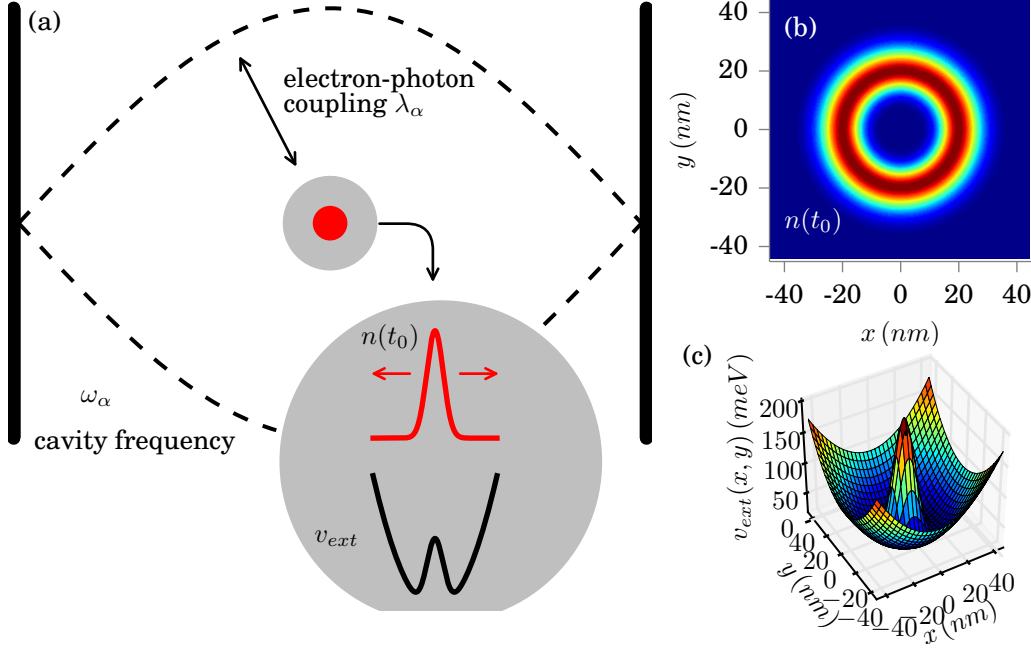


Figure 8: Model system for a GaAs quantum dot in an optical cavity: (a) the single electron confined to two dimensions is coupled to a resonant photon field mode and subject to the external potential  $v_{\text{ext}}(\mathbf{r})$ . The field mode with frequency  $\omega_\alpha$  influences the time evolution of the electron density  $n(\mathbf{r}, t)$  through the electron-photon interaction strength  $\lambda_\alpha$ . (b) shows the two-dimensional electronic ground-state density  $n_0(\mathbf{r})$  and (c) illustrates the external potential  $v_{\text{ext}}(\mathbf{r})$ .

(see appendix. F.2). The electron is confined in two dimensions in space and the model Hamiltonian is given as follows

$$\hat{H}(t) = \left( -\frac{\hbar^2}{2m} \vec{\nabla}^2 + v_{\text{ext}}(\mathbf{r}, t) \right) + \frac{1}{2} \left[ \hat{p}_\alpha^2 + \omega_\alpha^2 \left( \hat{q}_\alpha - \frac{\lambda_\alpha}{\omega_\alpha} \cdot \mathbf{r} \right)^2 \right] + \frac{j_{\text{ext}}^\alpha(t)}{\omega_\alpha} \hat{q}_\alpha, \quad (153)$$

where  $\mathbf{r} = x\mathbf{e}_x + y\mathbf{e}_y$ . The electron has an effective mass of  $m = 0.067m_e$  and is subject to the following external potential  $v_{\text{ext}}(\mathbf{r}) = \frac{1}{2}m\omega_0^2\mathbf{r}^2 + V_0e^{-\mathbf{r}^2/d^2}$ . The external potential is a harmonic trap with a Gaussian peak in its center. The parameters are chosen according to experimental values:  $\hbar\omega_0 = 10$  meV,  $V_0 = 200$  meV,  $d = 10$  nm, and the effective dielectric constant  $\kappa = 12.7\epsilon_0$ . While the electronic ground state is nondegenerate, the first excited state has a two-fold degeneracy [96]. We choose the frequency of the photon field mode  $\omega_\alpha$  in resonance to the excitation from the ground state to the first-excited state with  $\hbar\omega_\alpha = 1.41$  meV. We assume  $\lambda_\alpha = \lambda_\alpha(\mathbf{e}_x + \mathbf{e}_y)$ , hence the photon field mode is polarized in  $\mathbf{e}_x + \mathbf{e}_y$  direction, without loss of generality. To connect to experiments in the field of cavity quantum electrodynamics (QED), we will tune the values for  $\lambda_\alpha$  in the calculations. Using the introduced parameters, we employ in the weak-coupling limit values for  $\lambda \sim 10^{-3}\sqrt{\text{meV}}/\text{nm}$  and in the (ultra) strong-coupling limit [97, 98]  $\lambda \sim 10^{-1}\sqrt{\text{meV}}/\text{nm}$ . Furthermore for all numerical calculations using the cavity-GaAs model system, we apply a  $127 \times 127$  two-dimensional real-space grid to rep-

represent the electronic subsystem and we include up to 40 photon number states. The correlated problem has then a total dimensionality of 645160 ( $127 \times 127 \times 40$ ) basis functions, which is still numerically solvable.

### 3.2 METHODS AND NUMERICAL IMPLEMENTATIONS

#### 3.2.1 Eigenvalue Problems and Finite-Difference Methods

To solve the Schrödinger equations in Eqns. 1 and 2 numerically, we need to discretize the equations in space and time. Therefore, we expand the equations that were originally defined in the continuum in a finite basis set. In principle, many basis sets are possible. In practice however, most basis sets are physically motivated. In the literature, many different basis sets are used, each of them have their individual advantages and disadvantages. Popular choices of basis sets are the Gaussian basis set [99], augmented plane waves [100], centered atomic orbitals [101], and the real-space grid [102]. An arbitrary wave function can be expanded into  $n_b$  arbitrary basis functions  $|\phi_i\rangle$  such that

$$|\Psi_n\rangle = \sum_{i=1}^{n_b} c_i^{(n)} |\phi_i\rangle. \quad (154)$$

Using the basis set expansion, we reformulate Eq. 2 in terms of a generalized eigenvalue equation

$$\sum_{i=1}^{n_b} \langle \phi_j | \hat{H} | \phi_i \rangle c_i^{(n)} = E_n \sum_{i=1}^{n_b} S_{ji} c_i^{(n)}, \quad (155)$$

where we multiplied Eq. 2 from the left with  $\langle \phi_j |$  and defined the overlap matrix  $S_{ji} = \langle \phi_j | \phi_i \rangle$ . Eq. 155 is a generalized matrix eigenvalue problem of the form  $h\mathbf{v} = \lambda s\mathbf{v}$  with the matrix  $h = h_{ij}$ , the eigenvectors  $\mathbf{v} = c_i^{(n)}$ , the eigenvalues  $\lambda = E_n$  and the overlap matrix  $s = S_{ji}$ . For an orthogonal basis set such as the real-space grid,  $S_{ij}$  corresponds to the unit matrix  $\mathbb{1}$  and the generalized eigenvalue problem reduces to a normal eigenvalue problem. The matrix elements of the Hamiltonian matrix  $h$  can be calculated explicitly, if the basis functions are known explicitly. For instance, for a uniform real-space grid first-order derivatives and the Laplacian in the Hamiltonian can be discretized with the finite-difference scheme. Throughout this thesis, we use a uniform real-space grid.

#### 3.2.2 Jordan-Wigner Transformation and the Bosonic Operators

The matrix representation of the electronic creation and annihilation operators in Fock space can be constructed in terms of a Jordan-Wigner transformation [103]. Using the Jordan-Wigner transformation, we construct the electronic creation and annihilation operators using the Pauli-Matrices  $\sigma_i$  with  $i = (x, y, z)$ ,  $\sigma_+$ , and  $\sigma_-$ .



The electronic creation (annihilation) operator  $\hat{c}_{n\downarrow}^{(\dagger)}$  creates (destroys) an electron with down ( $\downarrow$ ) spin at site  $n$  on the real-space grid. These operators are defined as

$$\begin{aligned}
 \mathcal{H}_{\text{fm}} &= \mathcal{H}_{n\uparrow}^{2 \times 2} \otimes \mathcal{H}_{n\downarrow}^{2 \times 2} \otimes \cdots \otimes \mathcal{H}_{2\downarrow}^{2 \times 2} \otimes \mathcal{H}_{1\uparrow}^{2 \times 2} \otimes \mathcal{H}_{1\downarrow}^{2 \times 2} \\
 \hat{c}_{1\downarrow} &= \mathbb{1} \otimes \mathbb{1} \otimes \cdots \otimes \mathbb{1} \otimes \mathbb{1} \otimes \sigma_+ \\
 \hat{c}_{1\uparrow} &= \mathbb{1} \otimes \mathbb{1} \otimes \cdots \otimes \mathbb{1} \otimes \sigma_+ \otimes \sigma_z \\
 \hat{c}_{2\downarrow} &= \mathbb{1} \otimes \mathbb{1} \otimes \cdots \otimes \sigma_+ \otimes \sigma_z \otimes \sigma_z \\
 &\vdots \\
 \hat{c}_{n\uparrow} &= \sigma_+ \otimes \sigma_z \otimes \cdots \otimes \sigma_z \otimes \sigma_z \otimes \sigma_z
 \end{aligned} \tag{156}$$

where the operation  $\otimes$  corresponds to a tensor product of two Hilbert-spaces. The electron creation operators are constructed accordingly, by replacing  $\sigma_+$  by  $\sigma_-$ .  $\mathcal{H}_{\text{fm}}$  denotes the total Fock space of the system. The discretized electron creation and annihilation operators anticommute as their real-space analogue in the continuum (Eq. 21) and fulfill the anticommutation relations  $[\hat{c}_i, \hat{c}_j]_+ = [\hat{c}_i^\dagger, \hat{c}_j^\dagger]_+ = 0$  and  $[\hat{c}_i, \hat{c}_j^\dagger]_+ = \delta_{i,j}$ , exactly. The total size of the Fock space is  $2^{2n_s}$ , where  $n_s$  is the number of sites.

The corresponding bosonic operators can be constructed as

$$\hat{a} = \begin{pmatrix} 0 & 1 & 0 & \cdots & 0 \\ 0 & 0 & \sqrt{2} & \cdots & 0 \\ \vdots & \vdots & \vdots & \ddots & \vdots \\ 0 & 0 & 0 & \cdots & \sqrt{n} \\ 0 & 0 & 0 & \cdots & 0 \end{pmatrix} \quad \text{and} \quad \hat{a}^\dagger = \begin{pmatrix} 0 & 0 & \cdots & 0 & 0 \\ 1 & 0 & \cdots & 0 & 0 \\ 0 & \sqrt{2} & \cdots & 0 & 0 \\ \vdots & \vdots & \ddots & \vdots & \vdots \\ 0 & 0 & \cdots & \sqrt{n} & 0 \end{pmatrix}. \tag{157}$$

The bosonic annihilation (creation) operator  $a_n^{(\dagger)}$  destroys (creates) a boson on site  $n$ . Furthermore these operators are routinely used in the calculation of the quantum harmonic oscillator. Interestingly, in case of bosons it is not possible to satisfy their real-space commutation relations correctly with the truncated form in Eq. 157. These operators commute as follows

$$[\hat{a}, \hat{a}^\dagger] = \begin{pmatrix} 1 & 0 & 0 & \cdots & 0 & 0 \\ 0 & 1 & 0 & \cdots & 0 & 0 \\ 0 & 0 & 1 & \cdots & 0 & 0 \\ \vdots & \vdots & \vdots & \ddots & \vdots & \vdots \\ 0 & 0 & \cdots & 0 & 1 & 0 \\ 0 & 0 & \cdots & 0 & 0 & -n \end{pmatrix} \neq \mathbb{1}. \tag{158}$$

The value  $n$  in the last row even increases with increasing basis size  $n_b$ . This illustrates the need of choosing a sufficiently large basis size such that the dynamics in the system is not influenced by the highest basis function. In practical calculations this can be directly tested by increasing the basis size until convergence is found.

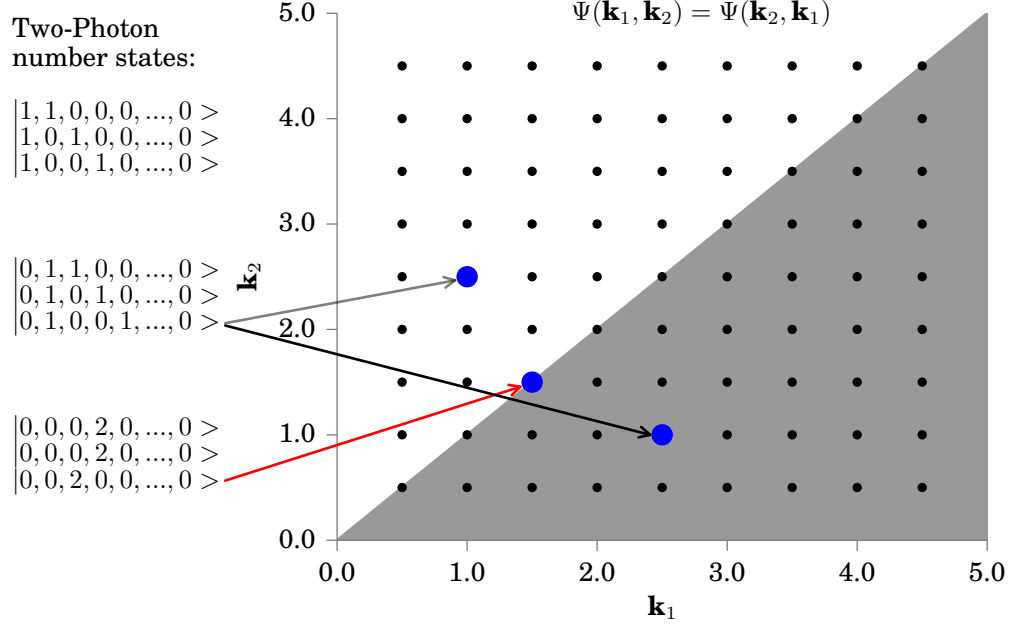


Figure 9: The mapping of the two-photon number states onto a two-dimensional two-photon wave function in momentum representation.

For many bosonic sites, we can construct the total operators operating in the total bosonic Fock space  $\mathcal{H}_{\text{ph}}$  in analogy to Eq. 156 as

$$\begin{aligned}
 \mathcal{H}_{\text{ph}} &= \mathcal{H}^{n \times n} \otimes \mathcal{H}^{n \times n} \otimes \dots \otimes \mathcal{H}^{n \times n} \otimes \mathcal{H}^{n \times n} \otimes \mathcal{H}^{n \times n} \\
 \hat{a}_1 &= \mathbb{1} \otimes \mathbb{1} \otimes \dots \otimes \mathbb{1} \otimes \mathbb{1} \otimes \hat{a} \\
 \hat{a}_2 &= \mathbb{1} \otimes \mathbb{1} \otimes \dots \otimes \mathbb{1} \otimes \hat{a} \otimes \mathbb{1} \\
 \hat{a}_3 &= \mathbb{1} \otimes \mathbb{1} \otimes \dots \otimes \hat{a} \otimes \mathbb{1} \otimes \mathbb{1} \\
 &\vdots \\
 \hat{a}_n &= \hat{a} \otimes \mathbb{1} \otimes \dots \otimes \mathbb{1} \otimes \mathbb{1} \otimes \mathbb{1}
 \end{aligned} \tag{159}$$

The creation operators  $\hat{a}_n^\dagger$  follow by replacing  $\hat{a}$  with  $\hat{a}^\dagger$ . The combined Fock space containing electrons and phonons is constructed by using the tensor products

$$\begin{aligned}
 \mathcal{H}_{\text{ph-fm}} &= \mathcal{H}_{\text{ph}} \otimes \mathcal{H}_{\text{fm}} \\
 \hat{c}_n &= \mathbb{1} \otimes \hat{c}_n \\
 \hat{a}_n &= \hat{a}_n \otimes \mathbb{1} \\
 &\vdots
 \end{aligned} \tag{160}$$

While the unit matrix  $\mathbb{1}$  in Eq. 156 has the size  $2 \times 2$ , in Eq. 159 the size  $n \times n$ , the matrix  $\mathbb{1}$  has in Eq. 160 the size of the total fermionic subsystem or bosonic subsystem, respectively.

### 3.2.3 Extension to Photons

To include photons into numerical calculations, we perform a wave function expansion in terms of photon number states

$$\begin{aligned}
 |\Psi(t)\rangle &= \sum_j \alpha_{j,0}(t) |\phi_j\rangle \otimes |0\rangle && \text{(zero-photon state)} \\
 &+ \sum_j \sum_n \alpha_{j,n}(t) |\phi_j\rangle \otimes \hat{a}_n^\dagger |0\rangle && \text{(one-photon states)} \\
 &+ \sum_j \sum_{n,n'} \alpha_{j,n,n'}(t) |\phi_j\rangle \otimes \hat{a}_n^\dagger \hat{a}_{n'}^\dagger |0\rangle && \text{(two-photon states)} \\
 &+ \dots && (161)
 \end{aligned}$$

Here,  $|\phi_j\rangle$  are the atomic or molecular basis functions, while  $|0\rangle$ ,  $\hat{a}_n^\dagger |0\rangle$ , and  $\hat{a}_n^\dagger \hat{a}_{n'}^\dagger |0\rangle$  denote the photonic Fock number states. The tensor product connects the two Hilbert spaces. If we create the individual basis function applying the photon creation operator  $\hat{a}_n^\dagger$  on the vacuum state, we obtain already properly symmetrized wave functions, which fulfill the boson commutation relation.

In Fig. 9, we show the mapping from the flat number index of all wave functions that contain two photons to the two-dimensional photon wave function. Due to the symmetric behavior of the photons, we only need to consider the lower half of all possible combinations of states (gray-shaded area). This leaves  $(N^2 - N)/2 + N$  basis functions in the two-photon subspace.

### 3.2.4 Symmetry and Sparsity

In many cases, the Hamiltonian obeys different symmetries, which can be exploited to simplify the computational problem. If a Hamiltonian commutes with a quantum mechanical operator, i.e.

$$[\hat{H}, \hat{O}] = 0, \quad (162)$$

its expectation value is conserved in time. This time-conservation of expectation values is a classical analogue of conserved quantities. Possible conserved quantities of the Hamiltonian are the spin operators  $\hat{S}_z$ ,  $\hat{S}^2$ , the particle number  $\hat{N}$ , or the parity  $\hat{P}$ , among others. By ordering basis states according to sets of eigenvalues of all symmetry operators that commute with the Hamiltonian, we first block diagonalize the Hamiltonian. Then in a second step, we can perform exact diagonalization in the emerging subblocks, which is computationally much more favorable than the full problem.

In Tab. 1, we show the Pascal's triangle. By calculating the triangle, we can calculate how many one-, two-, three-,... particle states exist for a given number of electronic sites. The last row in the table represents the case of four electronic sites both with spin  $\uparrow$  and spin  $\downarrow$ . Here, we find 9 different values for the electron number (0 – 8). In particular, we find 8 different one-particle states, and 70 four-particle states. The corresponding block structure of the Hamiltonian is shown in Fig. 10 for the case of the electron number operator  $\hat{N}$ , where the size of the individual blocks correspond to the value of the Pascal's triangle and the number of blocks corresponds to the different values of the electron particle number operator.

																																																																																																																																																																																																																																																																																																																																																																																																																																																																																																																																																																																																																																																																																																																																																																																																																																																																																																																																																																																																																																																																																																																																																																																																																																																																																																																																																																																																																																																																																																																																						</
--	--	--	--	--	--	--	--	--	--	--	--	--	--	--	--	--	--	--	--	--	--	--	--	--	--	--	--	--	--	--	--	--	--	--	--	--	--	--	--	--	--	--	--	--	--	--	--	--	--	--	--	--	--	--	--	--	--	--	--	--	--	--	--	--	--	--	--	--	--	--	--	--	--	--	--	--	--	--	--	--	--	--	--	--	--	--	--	--	--	--	--	--	--	--	--	--	--	--	--	--	--	--	--	--	--	--	--	--	--	--	--	--	--	--	--	--	--	--	--	--	--	--	--	--	--	--	--	--	--	--	--	--	--	--	--	--	--	--	--	--	--	--	--	--	--	--	--	--	--	--	--	--	--	--	--	--	--	--	--	--	--	--	--	--	--	--	--	--	--	--	--	--	--	--	--	--	--	--	--	--	--	--	--	--	--	--	--	--	--	--	--	--	--	--	--	--	--	--	--	--	--	--	--	--	--	--	--	--	--	--	--	--	--	--	--	--	--	--	--	--	--	--	--	--	--	--	--	--	--	--	--	--	--	--	--	--	--	--	--	--	--	--	--	--	--	--	--	--	--	--	--	--	--	--	--	--	--	--	--	--	--	--	--	--	--	--	--	--	--	--	--	--	--	--	--	--	--	--	--	--	--	--	--	--	--	--	--	--	--	--	--	--	--	--	--	--	--	--	--	--	--	--	--	--	--	--	--	--	--	--	--	--	--	--	--	--	--	--	--	--	--	--	--	--	--	--	--	--	--	--	--	--	--	--	--	--	--	--	--	--	--	--	--	--	--	--	--	--	--	--	--	--	--	--	--	--	--	--	--	--	--	--	--	--	--	--	--	--	--	--	--	--	--	--	--	--	--	--	--	--	--	--	--	--	--	--	--	--	--	--	--	--	--	--	--	--	--	--	--	--	--	--	--	--	--	--	--	--	--	--	--	--	--	--	--	--	--	--	--	--	--	--	--	--	--	--	--	--	--	--	--	--	--	--	--	--	--	--	--	--	--	--	--	--	--	--	--	--	--	--	--	--	--	--	--	--	--	--	--	--	--	--	--	--	--	--	--	--	--	--	--	--	--	--	--	--	--	--	--	--	--	--	--	--	--	--	--	--	--	--	--	--	--	--	--	--	--	--	--	--	--	--	--	--	--	--	--	--	--	--	--	--	--	--	--	--	--	--	--	--	--	--	--	--	--	--	--	--	--	--	--	--	--	--	--	--	--	--	--	--	--	--	--	--	--	--	--	--	--	--	--	--	--	--	--	--	--	--	--	--	--	--	--	--	--	--	--	--	--	--	--	--	--	--	--	--	--	--	--	--	--	--	--	--	--	--	--	--	--	--	--	--	--	--	--	--	--	--	--	--	--	--	--	--	--	--	--	--	--	--	--	--	--	--	--	--	--	--	--	--	--	--	--	--	--	--	--	--	--	--	--	--	--	--	--	--	--	--	--	--	--	--	--	--	--	--	--	--	--	--	--	--	--	--	--	--	--	--	--	--	--	--	--	--	--	--	--	--	--	--	--	--	--	--	--	--	--	--	--	--	--	--	--	--	--	--	--	--	--	--	--	--	--	--	--	--	--	--	--	--	--	--	--	--	--	--	--	--	--	--	--	--	--	--	--	--	--	--	--	--	--	--	--	--	--	--	--	--	--	--	--	--	--	--	--	--	--	--	--	--	--	--	--	--	--	--	--	--	--	--	--	--	--	--	--	--	--	--	--	--	--	--	--	--	--	--	--	--	--	--	--	--	--	--	--	--	--	--	--	--	--	--	--	--	--	--	--	--	--	--	--	--	--	--	--	--	--	--	--	--	--	--	--	--	--	--	--	--	--	--	--	--	--	--	--	--	--	--	--	--	--	--	--	--	--	--	--	--	--	--	--	--	--	--	--	--	--	--	--	--	--	--	--	--	--	--	--	--	--	--	--	--	--	--	--	--	--	--	--	--	--	--	--	--	--	--	--	--	--	--	--	--	--	--	--	--	--	--	--	--	--	--	--	--	--	--	--	--	--	--	--	--	--	--	--	--	--	--	--	--	--	--	--	--	--	--	--	--	--	--	--	--	--	--	--	--	--	--	--	--	--	--	--	--	--	--	--	--	--	--	--	--	--	--	--	--	--	--	--	--	--	--	--	--	--	--	--	--	--	--	--	--	--	--	--	--	--	--	--	--	--	--	--	--	--	--	--	--	--	--	--	--	--	--	--	--	--	--	--	--	--	--	--	--	--	--	--	--	--	--	--	--	--	--	--	--	--	--	--	--	--	--	--	--	--	--	--	--	--	--	--	--	--	--	--	--	--	--	--	--	--	--	--	--	--	--	--	--	--	--	--	--	--	--	--	--	--	--	--	--	--	--	--	--	--	--	--	--	--	--	--	--	--	--	--	--	--	--	--	--	--	--	--	--	--	--	--	--	--	--	--	--	--	--	--	--	--	--	--	--	--	--	--	--	--	--	--	--	--	--	--	--	--	--	--	--	--	--	--	--	--	--	--	--	--	--	--	--	--	--	--	--	--	--	--	--	--	--	--	--	--	--	--	--	--	--	--	--	--	--	--	--	--	--	--	--	--	--	--	--	--	--	--	--	--	--	--	--	--	--	--	--	--	--	--	--	--	--	--	--	--	--	--	--	--	--	--	--	--	--	--	--	--	--	--	--	--	--	--	--	--	--	--	--	--	--	--	--	--	--	--	--	--	--	--	--	--	--	--	--	--	--	--	--	--	--	--	--	--	--	--	--	--	--	--	--	--	--	--	--	--	--	--	--	--	--	--	--	--	--	--	--	--	--	--	--	--	--	--	--	--	--	--	--	--	--	--	--	--	--	--	--	--	--	--	--	--	--	--	--	--	--	--	--	--	--	--	--	--	--	--	--	--	--	--	--	--	--	--	--	--	--	--	--	--	--	--	--	--	--	--	--	--	--	--	--	--	--	--	--	--	--	--	--	--	--	--	--	--	--	--	--	--	--	--	--	--	--	--	--	--	--	--	--	--	--	--	--	--	--	--	--	--	--	--	--	--	--	--	--	--	--	--	--	--	--	--	--	--	--	--	--	--	--	--	--	--	--	--	--	--	--	--	--	--	--	--	--	--	--	--	--	--	--	--	--	--	--	--	--	--	--	--	--	--	--	--	--	--	--	--	--	--	--	--	--	--	--	--	--	--	--	--	--	--	--	--	--	--	--	--	--	--	--	--	--	--	--	--	--	--	--	--	--	--	--	--	--	--	--	--	--	--	--	--	--	--	--	--	--	--	--	--	--	--	--	--	--	--	--	--	--	--	--	--	--	--	--	--	--	--	--	--	--	--	--	--	--	--	--	--	--	--	--	--	--	--	----

Table 1: Pascal's triangle with rows zero to eight.

### 3.2.5 Exact Diagonalization

To get access to all eigenvalues and eigenstates of the system, we employ the exact diagonalization technique [104]. To this end, we explicitly construct all operators in the combined electron-nuclear Fock space  $\mathcal{H}_{\text{ph-fm}}$  present in the Hamiltonian by using their matrix representation in the chosen basis set. In Fock space, states with different electron number  $n_e$  are directly accessible, which is convenient in situations, where the particle number changes, e.g. for the calculation of photoelectron spectra. All remaining blocks of the blockdiagonal Hamiltonian can be diagonalized with either a dense or a sparse eigenvalue solver. Standard sparse diagonalization approaches for exact diagonalization are usually much faster, but only give access to a few (usually the lowest) eigenvalues and eigenvectors, whereas dense eigenvalue solvers return the full spectrum of all eigenvalues and eigenvectors of the static Schrödinger equation, but are limited to small systems.

### 3.2.6 Propagation Methods

If we know all eigenvectors  $\Psi_n$  and  $E_n$  eigenvalues of Eq. 2 explicitly and the Hamiltonian  $\hat{H}$  is time-independent, we can expand the wave function  $\Psi(t)$  formally into the energy eigenbasis of the Hamiltonian  $\hat{H}$  and solve the time-dependent Schrödinger equation in Eq. 1 with the initial state  $\Psi(t_0)$  in principle exactly by

$$|\Psi(t)\rangle = \sum_{i=1}^{n_b} e^{-\frac{i}{\hbar} E_n t} c_n(t_0) |\Psi_n\rangle. \quad (163)$$

with  $c_n(t_0) = \langle \Psi(t_0) | \Psi_n \rangle$ . However for most systems, exact diagonalization is numerically impossible and even if the exact eigenstates are known, it is usually more convenient to directly approximate the time-evolution operator, due to performance and stability conditions. Here, time is discretized on a time-grid with spacing  $\Delta t$ . Formally, Eq. 1 can then be solved for time-dependent Hamiltonians

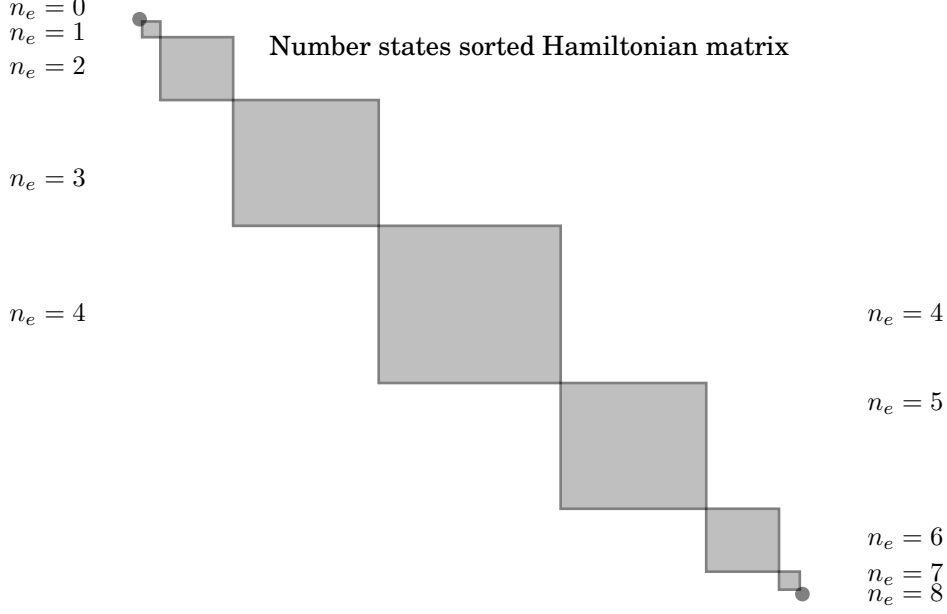


Figure 10: Block structure of the Hamiltonian imposed by the conserved number operator  $\hat{N}$  for four electronic sites. Each block corresponds to a fixed particle number.  $n_e = 4$  corresponds to the largest block in this setup.

$\hat{H}(t)$  by using the group property of the time-evolution operator from Eq. 59 as follows

$$\begin{aligned} |\Psi(t)\rangle &= \hat{U}(t, t_0) |\Psi(t_0)\rangle \\ &= \hat{U}(t, t - \Delta t) \hat{U}(t - \Delta t, t - 2\Delta t) \cdots \hat{U}(t_0 + \Delta t, t_0) |\Psi(t_0)\rangle. \end{aligned} \quad (164)$$

The time-evolution operator  $\hat{U}(t', t)$  has to be approximated. Popular choices are the Lanczos propagation scheme [105, 106], Crank-Nicolson propagators or the Runge-Kutta propagator. For a comprehensive analysis of the different possible propagation schemes used in time-dependent many-body calculations, we refer the reader to Ref. [107]. In this thesis, we employ the Lanczos propagation scheme, unless otherwise stated.

### 3.2.7 Numerical Integration and Volterra Integral Equations

Throughout this thesis we perform numerical integrations of arbitrary functions  $f(x)$  defined on a grid with  $N + 1$  grid points using the trapezoidal rule [108]

$$\int_a^b dx f(x) \sim \frac{b-a}{2N} (f(x_1) + 2f(x_2) + 2f(x_3) + \dots + 2f(x_N) + f(x_{N+1})). \quad (165)$$

The error of the trapezoidal rule scales quadratic with the grid spacing  $h = \frac{N}{b-a}$ , i.e.  $\mathcal{O}(h^2)$ . It can also be applied to two-dimensional integrations

$$\begin{aligned} \int_a^b dx \int_a^x dy f(x, y) &\sim \int_a^b dx \underbrace{\frac{x-a}{2N} (f(x, y_1) + 2f(x, y_2) + \dots + f(x, y_{N+1}))}_{L(x)} \\ &\sim \frac{b-a}{2N} (L(x_1) + 2L(x_2) + \dots + L(x_{N+1})). \end{aligned} \quad (166)$$

Furthermore, in Ch. 7, we solve Volterra integral equations of the first kind, which are defined as follows

$$\int_0^x K(x, t) y(t) dt = f(x). \quad (167)$$

We identify the kernel  $K(x, t)$  of the integral equation and we aim for solving Eq. 167 for  $y(x)$ . The Volterra equation can be solved numerically by discretizing the variables  $x \rightarrow \{x_i\}$  and  $t \rightarrow \{t_i\}$  on a grid with spacing  $h$  and the integral with a midpoint method:  $\int_0^x \rightarrow \sum_{i=0}^{n-1}$ , where  $n$  is the number of grid points. Hence, Eq. 167 turns into the discretized version

$$h \sum_{i=0}^{n-1} K(x_n, x_{i+1/2}) Y_{i+1/2} = f(x_n), \quad (168)$$

and can be solved by [109]

$$Y_{n-1/2} = \frac{f(x_n)}{hK(x_n, x_{n-1/2})} - \sum_{i=0}^{n-2} \frac{K(x_n, x_{i+1/2})}{K(x_n, x_{n-1/2})} Y_{i+1/2}. \quad (169)$$

Applying the midpoint method to discretize the integral has the advantage that the diagonal of the kernel  $K(x, t)$  is not explicitly used. In cases where the diagonal of the kernel is singular, this turns out to be advantageous. If the kernel is factorizable  $K(x, t) = a(x)b(t)$ , we can simplify Eq. 169 further

$$\begin{aligned} Y_{n-1/2} &= \frac{f(x_n)}{hK(x_n, x_{n-1/2})} - \frac{a(x_n)c(x_{n-3/2})}{K(x_n, x_{n-1/2})}, \\ c(x_{n-3/2}) &= \sum_{i=0}^{n-2} b(x_{i+1/2}) Y_{i+1/2}. \end{aligned} \quad (170)$$

Here, the last term in Eq. 170 can be rewritten such that instead of evaluating the total sum  $\{0 : n-2\}$  at each step  $n$ , we only need to update the term by performing an addition, since  $c(x_{n-3/2}) = c(x_{n-5/2}) + b(x_{n-3/2}) Y_{n-3/2}$ .

### 3.2.8 Fixed-Point Algorithm

To lift the restriction of Taylor-expandability in time on the external potentials, one of the generalizations of the Runge-Gross proof was stated as a fixed-point question [54]. Besides generalizing the Runge-Gross theorem, the fixed-point proof can

be formulated in an iterative algorithm, which yields the external potential. In a Kohn-Sham framework, the fixed-point method can be used to explicitly construct the usually unknown  $\text{xc}$ -potential [110], if the exact many-body densities are known beforehand. The exact  $\text{xc}$ -potential is essential to correctly reproduce the time evolution of a density of an interacting many-body system by the time evolution of a noninteracting Kohn-Sham system. However, only for simple few-electron systems the Schrödinger equation can be solved exactly and the exact potential constructed explicitly. Such systems include low-dimensional systems, three-dimensional Hydrogen or Helium atoms and molecules or various lattice models. In the following, we employ the fixed-point algorithm to the JCH model and real-space models and discuss its specific form in these applications.

### 3.2.8.1 Jaynes-Cummings-Hubbard Model

In the Jaynes-Cummings-Hubbard model discussed in Sec. 3.1.2, the equation of motion for the electron density  $\sigma_z(t)$  (Eq. 148) can be reformulated to yield an iterative equation, which can be used to obtain the external potential via a fixed-point procedure

$$v_{\text{ext}}(t) = \frac{-\ddot{\sigma}_z(t) - 4t_{\text{kin}} (t_{\text{kin}} \hat{\sigma}_z(t) + \lambda \langle \Psi(t) | (\hat{a}^\dagger + \hat{a}) \hat{\sigma}_x | \Psi(t) \rangle)}{4t_{\text{kin}} \sigma_x(t)}. \quad (171)$$

The right-hand side depends implicitly on  $v_{\text{ext}}$  through the wave function  $|\Psi[v_{\text{ext}}, t]\rangle$ . To increase the numerical stability, we change the equation slightly and obtain an iterative equation in a regularized form by adding the parameter  $\alpha$  to avoid a vanishing denominator

$$v_{\text{ext}}^{(k+1)}(t) = \frac{-\ddot{\sigma}_z(t) - 4t_{\text{kin}} (t_{\text{kin}} \hat{\sigma}_z(t) + \lambda \langle \Psi(t) | (\hat{a}^\dagger + \hat{a}) \hat{\sigma}_x | \Psi(t) \rangle - \alpha v_{\text{ext}}^{(k)}(t))}{4t_{\text{kin}} (\sigma_x(t) + \alpha)}. \quad (172)$$

We choose the parameter  $\alpha$  such that  $\sigma_x(t) + \alpha \neq 0$ . Then, we get a stable iteration algorithm in the spirit of Ref. [111]

$$\mathcal{P} : v_0 \rightarrow \text{rhs}[v_0], \quad (173)$$

$$\mathcal{V} : \text{rhs}[v_0] \rightarrow v_1, \quad (174)$$

$$\mathcal{F}[v_0] = (\mathcal{V} \circ \mathcal{P})[v_0] = v_1, \quad (175)$$

and Eqns. 173-175 are solved iteratively until self-consistency is reached. The term  $\text{rhs}$  refers to the right-hand side of Eq. 172, which contains the density  $\sigma_z(t)$  and its second-time derivative  $\ddot{\sigma}_z(t)$ . These two variables have to be given a priori, e.g. by an exact propagation in the total Hilbert or Fock space of the problem.

### 3.2.8.2 Real-space Models and Multi-grid Solver

In real space, the external potential can be also obtained by an iterative algorithm. In this thesis, we follow the procedure outlined in Refs. [110, 111]. We exploit the second time-derivative of the electron density to obtain the direct connection

between the density and the external potential. We can rewrite Eq. 46 to yield an iterative formula

$$\frac{1}{m_e} \vec{\nabla} \cdot \left[ n(\mathbf{r}, t) \vec{\nabla} v^{(k+1)}(\mathbf{r}, t) \right] = -\frac{\partial^2}{\partial t^2} n(\mathbf{r}, t) - \vec{\nabla} \cdot \mathbf{Q}([v^{(k)}], \mathbf{r}, t). \quad (176)$$

Eq. 176 gives us an iterative algorithm such that we can iterate:  $v^{(k)}(\mathbf{r}, t) \rightarrow v^{(k+1)}(\mathbf{r}, t)$ . Since the electron density  $n(\mathbf{r}, t)$  is known a priori, we can use Eq. 176 iteratively to construct the time-dependent external potential  $v(\mathbf{r}, t)$ . However, this equation relies on the explicit evaluation of the expectation value of the electronic stress force  $\mathbf{Q}([v^{(k)}], \mathbf{r}, t)$ , which is numerically expensive. Therefore in practical applications, we replace Eq. 176 by

$$\begin{aligned} -\frac{1}{m_e} \vec{\nabla} \cdot \left[ n(\mathbf{r}, t) \vec{\nabla} v^{(k+1)}(\mathbf{r}, t) \right] &= \frac{\partial^2}{\partial t^2} \left[ n([v^{(k)}], \mathbf{r}, t) - n(\mathbf{r}, t) \right] \\ &\quad - \frac{1}{m_e} \vec{\nabla} \cdot \left[ n([v^{(k)}], \mathbf{r}, t) \vec{\nabla} v^{(k)}(\mathbf{r}, t) \right], \end{aligned} \quad (177)$$

which yields with discretized time [112]

$$\begin{aligned} -\frac{1}{m_e} \vec{\nabla} \cdot \left[ n(\mathbf{r}, t) \vec{\nabla} v^{(k+1)}(\mathbf{r}, t) \right] &= \frac{A}{\Delta t^2} \left[ n([v^{(k)}], \mathbf{r}, t) - n(\mathbf{r}, t) \right] \\ &\quad - \frac{B}{\Delta t} \left[ \vec{\nabla} \cdot \mathbf{J}([v^{(k)}], \mathbf{r}, t) + \frac{\partial}{\partial t} n(\mathbf{r}, t) \right] \\ &\quad - \frac{1}{m_e} \vec{\nabla} \cdot \left[ n([v^{(k)}], \mathbf{r}, t) \vec{\nabla} v^{(k)}(\mathbf{r}, t) \right]. \end{aligned} \quad (178)$$

In the last step, we introduce the continuity equation from Eq. 44 for stability reasons. The constants  $A$  and  $B$  are chosen to  $A = 1.5$  and  $B = 0.5$ . Eq. 178 is solved at each time-step. The left-hand side of this equation contains the Sturm-Liouville operator, which is numerically solvable by applying a multigrid scheme [108] with zero-boundary condition [112]. The conditions on convergence of Eq. 178 can be found in Ref. [113]. To find the fixed-points of Eq. 178 numerically, we first solve the (time-dependent) many-body Schrödinger equation with the Hamiltonian  $\hat{H}([v^{(k)}])$ . For time-dependent problems, we employ the numerical propagation methods discussed in Sec. 3.2.6, whereas for static problems, we use the exact diagonalization method discussed in Sec. 3.2.5 to access the exact many-body wave function. Next we can calculate according to Eq. 40 the corresponding electron density  $n([v^{(k)}], \mathbf{r}, t)$  and the divergence of the current density  $\vec{\nabla} \cdot \mathbf{J}([v^{(k)}], \mathbf{r}, t)$ . Using the input density  $n(\mathbf{r}, t)$  and its time derivative  $\frac{\partial}{\partial t} n(\mathbf{r}, t)$ , we then calculate the right-hand side of Eq. 178. To numerically invert the equation, we employ a full multigrid solver [108] with a red-black Gauss-Seidel algorithm as the smoothing operator and a bilinear interpolation of the coarse-grid. Using this solver, we then invert the equation to obtain  $v^{(k+1)}(\mathbf{r}, t)$ . The whole procedure has to be repeated until self-consistency is reached. As convergence parameter, we typically choose:  $\Delta v = \int d\mathbf{r} |v^{(k+1)} - v^{(k)}| < 10^{-6}$  or  $\Delta n = \int d\mathbf{r} |n[v^{(k+1)}] - n[v^{(k)}]| < 10^{-15}$ . To speed up convergence, we employ a direct inversion in the iterative subspace (DIIS) approach [114]. This method is a standard method in many self-consistent many-body calculations [115] and uses Lagrange multiplier to minimize a set of error vectors obtained from the previous iterations. For our case, we use as error vectors



$\mathcal{E}(\mathbf{r}, t) = \frac{A}{\Delta t^2} \left[ n([v^{(k)}], \mathbf{r}, t) - n(\mathbf{r}, t) \right] - \frac{B}{\Delta t} \left[ \vec{\nabla} \cdot \mathbf{J}([v^{(k)}], \mathbf{r}, t) + \frac{\partial}{\partial t} n(\mathbf{r}, t) \right]$ , which has to vanish for the fixed-point solution.



Part IV

APPLICATIONS



## NONADIABATIC AND TIME-RESOLVED PHOTOEMISSION SPECTROSCOPY FOR MOLECULAR SYSTEMS

---

In recent years, the field of photoelectron spectroscopy has seen rapid progress by novel experimental possibilities. In particular, the advent of femtosecond laser pulses [116] enabled experimentalists to trigger and record dynamical intramolecular processes in real-time using time-dependent pump-probe photoelectron spectroscopy [117]. In pump-probe experiments, two sequential pulses with a delay time  $\Delta t$  are applied to the sample. The first pulse pumps (excites) the sample out of the equilibrium configuration, while the second pulse probes the sample by photoionization. Tuning the delay time  $\Delta t$  between these two successive pulses allows to monitor the dynamical microscopic processes in the sample. Successful applications of time-resolved photoelectron spectroscopy include the characterization of ultrafast photochemical dynamic processes in liquid jets [118], the ultrafast electronic relaxation, the hydrogen-bond-formation and the dissociation dynamics [119], the probing of unimolecular and bimolecular reactions in real-time [120], or the investigation of multidimensional time-resolved dynamics near conical intersections [121], among other processes, but all on a femtosecond timescale.

Using TDDFT, time-dependent pump-probe photoelectron spectroscopy has been first described by Pohl et al. [122]. This theory is based on the calculation of the momentum distribution of Kohn-Sham orbitals far away from a reference point. Only recently, De Giovannini et al. [14] simulated explicitly the pump pulse and the photoelectron, both in real-time, using a mask-function in real space. However, both works share the assumption of the validity of the BOA employing classical nuclei. Beyond the classical nuclei approximation, reduced density-matrices [123], quantum chemistry methods by using the double-harmonic approximation for photoelectron transitions [124], or by Franck-Condon-factors [125] have been used.

In this chapter, we simulate photoelectron spectra of time-independent and time-dependent systems and calculate exact correlated electron-phonon results without invoking the BOA. We use these exact results to assess the quality of the BOA in photoelectron spectroscopy. To this end, we study a model system for Trans-Polyacetylene and treat the electrons and nuclei both quantum-mechanically, on equal footing. This chapter is organized as follows. First, we study to which extent the BOA is justified for the model system in photoelectron experiments. We show that spurious peaks appear in the static photoelectron spectrum, if the BOA is assumed in SHA and DHA. These spurious amplitudes only vanish, if the full correlated electron-nuclear problem is correctly considered. In the second part of this section, we focus on time-dependent photoelectron spectroscopy. We show how the underlying dynamics of the nuclear wave packet can be traced in time-dependent photoelectron spectra. The chapter is based on the theory of photoelectron spectroscopy illustrated in Sec. 2.4 and the SSH Hamiltonian introduced in Sec. 3.1.1.

---

This chapter is based on the work reported in Flick et al. [84], which was performed in close collaboration with all coauthors. I contributed to all aspects of the work.

#### 4.1 SU-SCHRIEFFER-HEEGER HAMILTONIAN

Throughout this chapter, we work with the SSH Hamiltonian of Sec. 3.1.1 with four oligomers. We explicitly construct the matrix representation of all quantum operators present in Eq. 141 in full Fock space, where different numbers of electrons  $N$  are directly accessible. Since, we consider four oligomers, we build the electronic creation and annihilation operators ( $\hat{c}_i^\dagger$  and  $\hat{c}_i$ ) by using the Jordan-Wigner transformation as discussed in Sec. 3.2.2 on a four site basis. The electronic subsystem coupled to two phonon modes (optical and acoustical) is defined on a uniform two-dimensional real-space grid. Derivatives in the phonon operators are constructed using an 8th-order finite-difference scheme. The total electron-phonon Fock space contains up to eight electrons and has a size of  $M_{\text{tot}} = 4^4 \times 35 \times 35 = 313600$  basis functions. The reduced Hilbert spaces with four (three) electrons has  $M_{\text{max}}^{[4]([3])} = 70(56) \times 35 \times 35 = 85750(68600)$  basis functions. We get access to  $M_{\text{tot}}$  eigenvalues  $E_j^{(N)}$  and eigenstates  $|\Psi_j^{(N)}\rangle$  of the system by solving the following correlated eigenvalue problem employing the exact diagonalization technique as discussed in Sec. 3.2.5 with a dense eigensolver

$$\hat{H}_{ssh} |\Psi_j^{(N)}\rangle = E_j^{(N)} |\Psi_j^{(N)}\rangle. \quad (179)$$

The eigenstates  $|\Psi_j^{(N)}\rangle$  and eigenvalues  $E_j^{(N)}$  are the exact correlated stationary states of the combined system of electrons and nuclei in Fock space and their corresponding eigenenergy. To reduce the dimensionality of the problem, we exploit different symmetries (see Sec. 3.2.4), which can be used to block diagonalize the Hamiltonian  $\hat{H}_{ssh}$ , i.e. the spin operators  $\hat{S}_z$ ,  $\hat{S}^2$ , particle number  $\hat{N}$ , and parity  $\hat{P}$ . Throughout this chapter, the superscript  $(N)$  denotes the number of electrons in the state. In the presence of pump and probe pulses, we explicitly propagate the time-dependent Schrödinger equation

$$i\hbar \frac{\partial}{\partial t} |\Phi^{(N)}(t)\rangle = \hat{H}_{ssh} |\Phi^{(N)}(t)\rangle, \quad (180)$$

with an arbitrary initial state  $|\Phi^{(N)}(t)\rangle$  by a Lanczos propagation scheme (see Sec. 3.2.6).

With increasing numbers of oligomers in the SSH chain, the size of the Fock space increases exponentially. This scaling limits the calculation of exact eigenstates and the time evolution of wave functions to only a small SSH chain. In the present case, we study a SSH chain consisting of four oligomers. However, these exact numerical solutions still serve as a valuable reference to assess the quality of approximate schemes, which are also applicable to simulate larger systems.

#### 4.2 BORN-OPPENHEIMER APPROXIMATION FOR THE SSH HAMILTONIAN

This section is dedicated to a comparison of the accuracy of the BOA for the SSH model. In Fig. 11, we illustrate the BO PES in the system. In dashed lines, we compare the exact surfaces to the harmonic approximation, which is shown in solid lines. All PES are plotted along the optical normal mode. For all surfaces, we find a very good agreement between the exact and the harmonic approximation.

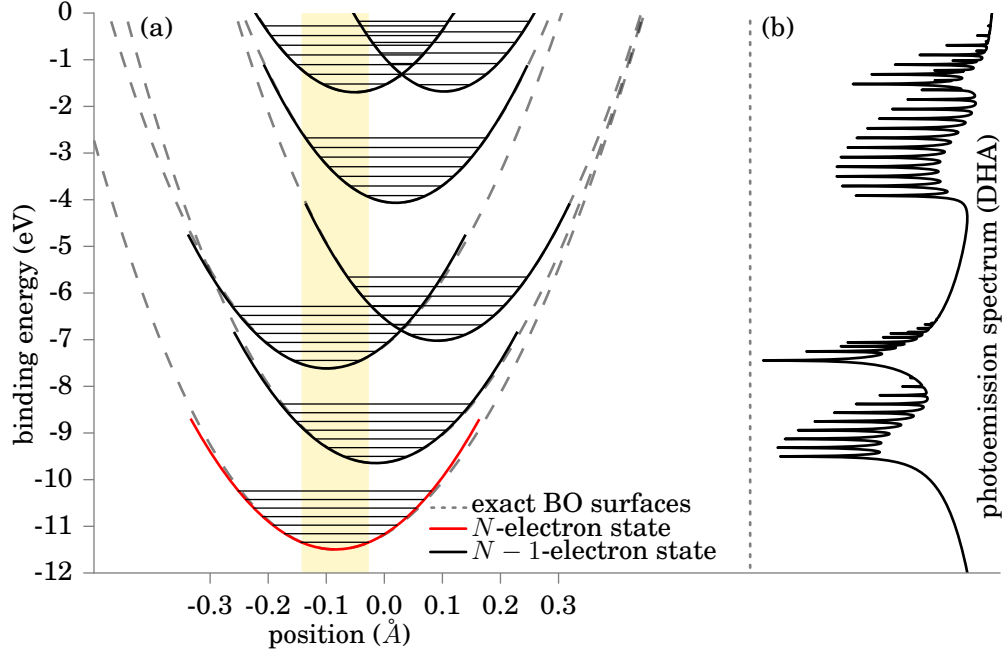


Figure 11: (a) For a Trans-Polyacetylene oligomer, exact BO surfaces (dashed) vs. harmonic approximation (solid) along the optical axis are shown with black lines for  $N - 1$  electron states and the red line for the  $N$ -electron ground state. (b) Photoelectron spectrum in double-harmonic approximation (DHA).

The exact surfaces have already a harmonic character, since the phonon subsystem in the correlated Hamiltonian (Eq. 141) is dominated by the quadratic potential in the phonon Hamiltonian  $\hat{H}_{ph}$ . All anharmonicities are due to the electron-phonon coupling term  $\hat{H}_{\pi-ph}$ , which are rather weak for the chosen set of parameters. More quantitatively, the BOA can also be assessed in terms of eigenenergies or overlaps between exact states and BO states. For the lowest five states and two higher-lying states, Tab. 2 shows the exact BO energies  $E_{BO}^{\text{exact}}$  and the BO energies in harmonic approximation  $E_{BO}^{\text{harmonic}}$  in comparison to the exact many-body energies of the correlated system  $E^{\text{exact}}$ . Additionally, we calculate the corresponding overlaps of BO and exact states. In agreement with the PES, we find low lying BO states in harmonic approximation and exact BO states close to the exact correlated states. The exact BO and the harmonic BO ground state have an overlap of each 99.86% with the exact correlated ground state. Nevertheless, for higher-lying states, the harmonic BO approximation, as well as the exact BOA yield states with less accurate energies and overlaps compared to the exact states (e.g. in state #86: 0.89, and 0.96, respectively). The table also shows that the exact BO energies  $E_{BO}^{\text{exact}}$  provide a lower bound to the exact correlated energies  $E^{\text{exact}}$ .

#### 4.3 NUMERICAL ASPECTS OF THE CALCULATION OF THE SPECTRAL FUNCTION

Experimental photoelectron spectra are typically shown as function of the positive binding energy, see e.g. Fig. 4 in Ref. [80]. The spectra shown in this chapter can

BOA employing the exact BO surfaces

state #	$E^{\text{exact}}$ (eV)	$E_{\text{BO}}^{\text{exact}}$ (eV)	(e,o,a)	overlap
1	-11.3414	-11.3419	1,0,0	0.9986
2	-11.2166	-11.2171	1,0,1	0.9986
3	-11.1583	-11.1588	1,1,0	0.9955
4	-11.0918	-11.0924	1,0,2	0.9986
5	-11.0336	-11.0341	1,1,1	0.9955
86	-9.5155	-9.5157	1,10,0	0.9676
87	-9.5076	-9.5078	1,8,3	0.9740

BOA employing the harmonic BO surfaces

state #	$E^{\text{exact}}$ (eV)	$E_{\text{BO}}^{\text{harmonic}}$ (eV)	(e,o,a)	overlap
1	-11.3414	-11.3419	1,0,0	0.9986
2	-11.2166	-11.2171	1,0,1	0.9986
3	-11.1583	-11.1587	1,1,0	0.9953
4	-11.0918	-11.0923	1,0,2	0.9986
5	-11.0336	-11.0339	1,1,1	0.9953
86	-9.5155	-9.5102	1,10,0	0.8964
87	-9.5076	-9.5023	1,8,3	0.9361

Table 2: Comparison of exact/harmonic BO states to exact correlated states: Exact correlated energies  $E^{\text{exact}}$ , exact BO energies  $E_{\text{BO}}^{\text{exact}}$ , harmonic BO energies  $E_{\text{BO}}^{\text{harmonic}}$  and overlap between exact and BO states. (e,o,a) correspond to BO quantum number of the state (electronic state, optical phonon mode, acoustical phonon mode).

be connected to this convention if the absolute value of the x-axis is considered, which then leads to positive values for the binding energy. Additionally the sum-over-states expressions for the spectral function as e.g. in Eq. 132 only provide the position of the peak and its amplitude. Throughout this chapter, we broaden the peaks of all spectra with a Lorentzian broadening of the form

$$f(E; E_0, \gamma) = \frac{1}{\pi} \frac{\gamma}{(E - E_0)^2 + \gamma^2}. \quad (181)$$

Electronic Green's function calculations typically use a broadening of  $\gamma = 0.1$  eV. However, such a broadening would completely wash out the phonon side bands. To resolve the rich structure of the vibrational side bands a much smaller broadening of  $\gamma = 0.002$  eV has to be used. This broadening is about an order of magnitude smaller than  $1/40$  eV, the typical energy scale for vibronic motions at room temperature. As a consequence, all vibrational sidebands shown in the following sections are experimentally only clearly visible in a low temperature limit.



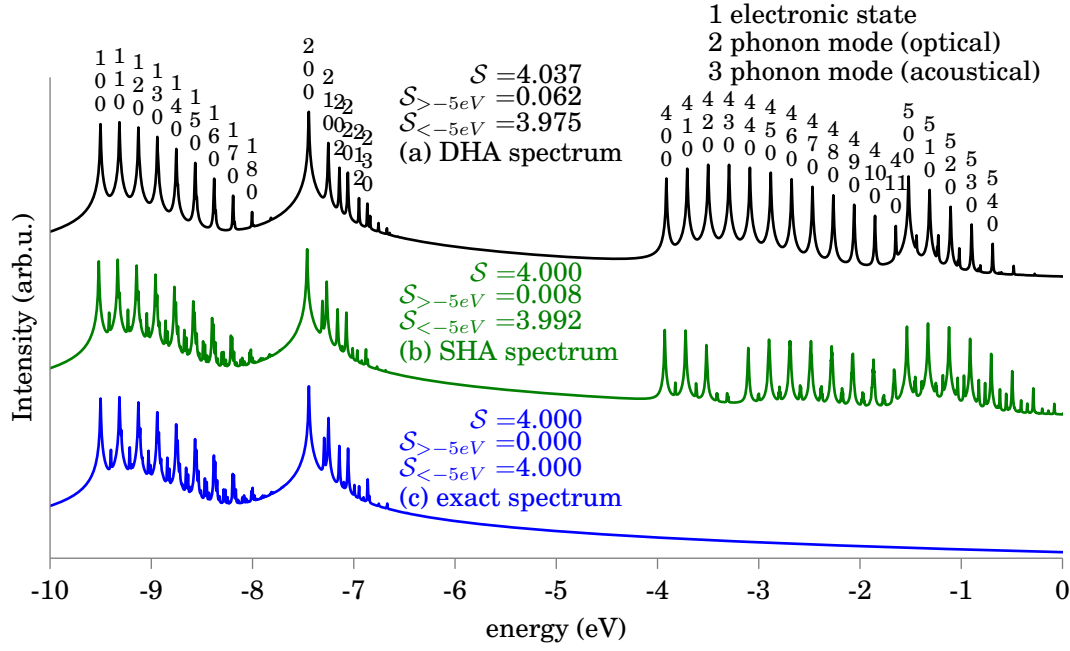


Figure 12: Photoelectron spectra for Trans-Polyacetylene. (a) The ground-state spectrum in double-harmonic approximation (DHA), (b) the ground-state spectrum in single-harmonic approximation (SHA), (c) the exact ground-state spectrum from the full-quantum calculation.  $S$  refers to the value of the sum rule (Eq. 135).  $S_{>-5\text{eV}}$  and  $S_{<-5\text{eV}}$  indicate partial summations in the energy range above  $-5$  eV and below  $-5$  eV, respectively.

#### 4.4 COMPARISON OF BO AND EXACT GROUND-STATE PHOTOELECTRON SPECTRA

In Sec. 2.4.3, we introduced different levels of theory for the calculation of electron-phonon photoelectron spectra in terms of the one-body spectral function. The different levels include the exact spectral function given by Eq. 132, the SHA defined in Eq. 139, and the DHA in Eq. 140. For the SSH model, we can explicitly evaluate the sum-over-states expressions, since we have access to all contributing eigenstates using dense exact diagonalization. Using these eigenstates, we are further able to calculate the sum rule from Eq. 135, which gives us an additional measure for the orthogonality and completeness of the underlying eigenstates. In the present section, we illustrate, how these different levels of approximations perform in the static case for Trans-Polyacetylene.

Fig. 12 shows the spectral functions of the SSH chain in a logarithmic scale for three different cases. The spectral function (a) colored in black is calculated using the DHA (Eq. 140). The green-colored spectrum in (b) depicts the spectrum calculated in SHA, where Eq. 139 has been employed, while spectrum (c) shows the exact correlated ground-state spectrum computed from Eq. 132 in blue. In addition, we plot the value of the total sum-rule  $S$ , the sum-rule only including contributions from energies smaller than  $-5$  eV ( $S_{<-5\text{eV}}$ ), and the sum-rule only including contributions from energies higher than  $-5$  eV ( $S_{>-5\text{eV}}$ ). In spectrum (a) for the DHA, we also associate the peaks with their corresponding quantum number, which consists

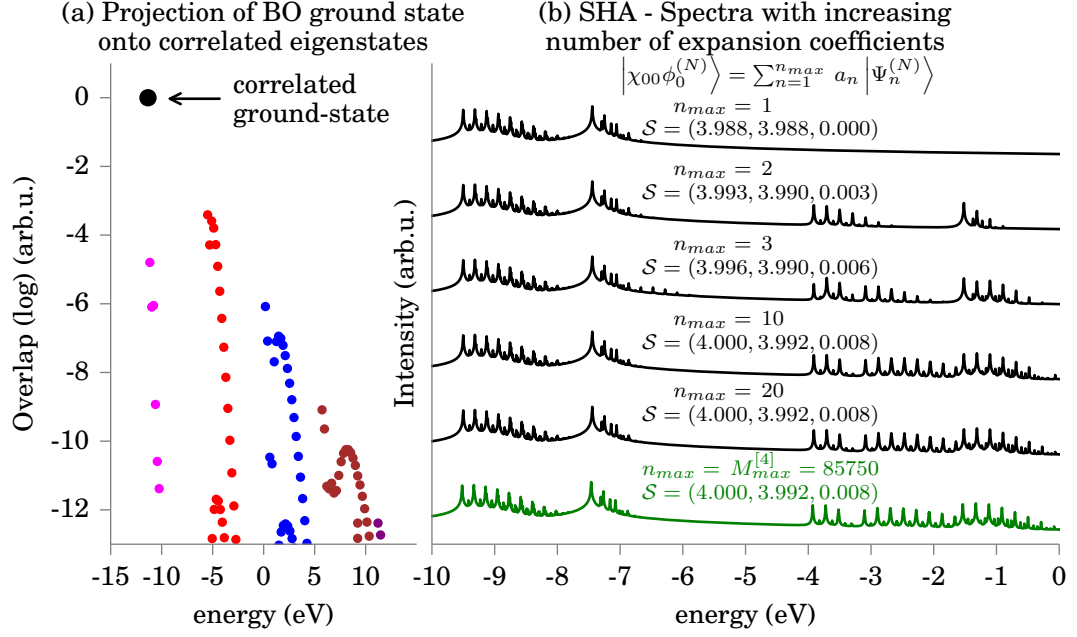


Figure 13: Nonadiabaticity in the BO ground state of the Trans-Polyacetylene chain: (a) projection of the BO ground state onto correlated eigenstates. (b) SHA spectra with increasing number of expansion coefficients.  $S = (S, S_{<-5\text{eV}}, S_{>-5\text{eV}})$ , as in Fig. 12.

of the quantum number of the electronic state, the optical mode and the acoustical mode.

In Fig. 12, we find by comparing to the exact spectral function shown in blue that the DHA and the SHA are both able to accurately predict the peak positions corresponding to the optical phonon modes in the energy range from  $-10$  eV to  $-5$  eV. This feature of the approximations is in agreement with the quality of the overlaps and the eigenenergies shown in Tab. 2. However, the DHA fails in predicting the correct peak height. Peaks, which correspond to optical phonon excitations are most dominant and their peak broadening hides peaks, which correspond to mixed or acoustical phonon excitations. Additionally, the DHA spectrum violates the sum rule due to the incompleteness of the approximation. All three spectra share that most of the spectral amplitude is located in energy areas below  $-5$  eV, while only less than two percent of the spectral weight is located in the energy range above  $-5$  eV in the DHA and SHA spectra. As most prominent difference between the individual spectra, we find that the DHA and SHA acquire spurious peaks above  $-5$  eV compared to the exact correlated ground-state spectrum. These spurious peaks will be discussed in the next section.

#### 4.5 NONADIABATICITY IN GROUND-STATE PHOTOELECTRON SPECTROSCOPY

The differences in the energy range from  $-5$  eV to  $0$  eV between the DHA spectrum and the exact correlated spectrum shown in Fig. 12 can be traced back to two in-

dividual origins. Since in the double-harmonic approximations, we perform two harmonic approximations, meaning the  $N$ -particle ground state is approximated by a harmonic BO state as well as the  $N - 1$  particle eigenstates, which both are necessary to compute the matrix elements in Eq. 140. Both approximations contribute independently to the spurious peaks in the spectrum. This can be seen if we compare to the SHA. Here, only the  $N$ -particle ground state is approximated, while the exact  $N - 1$  particle eigenstates are used. If we compare the sum rule in Fig. 12, we find that the spectral weight of the spurious peaks in the energy range from  $-5$  eV to  $0$  eV is reduced from 1.6% in DHA to 0.2% in SHA. The remaining spectral weight in comparison to the exact spectra can be associated with the factorized nature of the BO  $N$ -particle ground state used in the SHA.

The expansion of the BO ground state in terms of exact correlated eigenstates allows to study the origin of the spurious peaks more closely. This expansion reads as follows

$$|\chi_{00} \phi_0^{(N)}\rangle = \sum_{n=1}^{n_{\max}} \langle \Psi_n^{(N)} | \chi_{00} \phi_0^{(N)} \rangle |\Psi_n^{(N)}\rangle = \sum_{n=1}^{n_{\max}} a_n |\Psi_n^{(N)}\rangle. \quad (182)$$

In Fig. 13 (a), we show the amplitude of the different expansion coefficients  $a_n$  in logarithmic scale. The black dot in the graph indicates the highest overlap, which by construction is found between the BO ground state and the exact correlated ground state. It has a value of 0.9986, as can be also obtained from Tab. 2. All other overlaps are orders of magnitudes smaller. These overlaps can be classified according to which PES in terms of Fig. 11 they originate from. Overlaps stemming from the same PES are shown in the same color in the Figure. In Fig. 13 (b), we show the SHA spectral function for increasing number  $n_{\max}$  in the summation in Eq. 182. The first spectrum shows the case of  $n_{\max} = 1$ . In this case, we only take the wave function with the highest overlap into account, which is the exact correlated ground state. Thus in the spectrum, we recover the shape of the exact spectrum, but with smaller amplitude, since  $a_1 = 0.9986 < 1$ . Because the states in Eq. 182 are not renormalized after truncation  $S \neq 4$ . In the case of  $n_{\max} = 1$ , we find  $S = 4 \cdot a_1^2 = 3.9888$ . If we then include more and more expansion coefficients  $a_n$  with  $n > 1$ , we find a gradual emerging of the artificial peaks in the energy range from  $-5$  eV to  $0$  eV. This spurious amplitude is caused by additional cross and diagonal terms of the spectral function, which involve correlated excited  $N$ -particle eigenstates. We conclude that these additional peaks are a side-effect of the factorized nature of the BO states, since we find them arising in the case of the harmonic approximation as well for exact BO surfaces beyond the harmonic approximation. In both cases, we find more than one term ( $n_{\max} > 1$ ) contributing to Eq. 182, which then leads to the additional cross and diagonal terms in the spectral function.

For the Su-Schrieffer-Heeger model we find that the quality of the BOA is very accurate, since the overlaps between the BO states and the exact correlated states is very high, due to the harmonic nature of the original problem, as shown in Tab. 2. However already in this case, which may be a best-case scenario, we find these artificial peaks with a spectral weight of about 1.6% in DHA. This indicates that for general systems, where the BOA may be less well justified due to anharmonicities in the system, a larger contribution to the spurious spectral peaks can be expected.

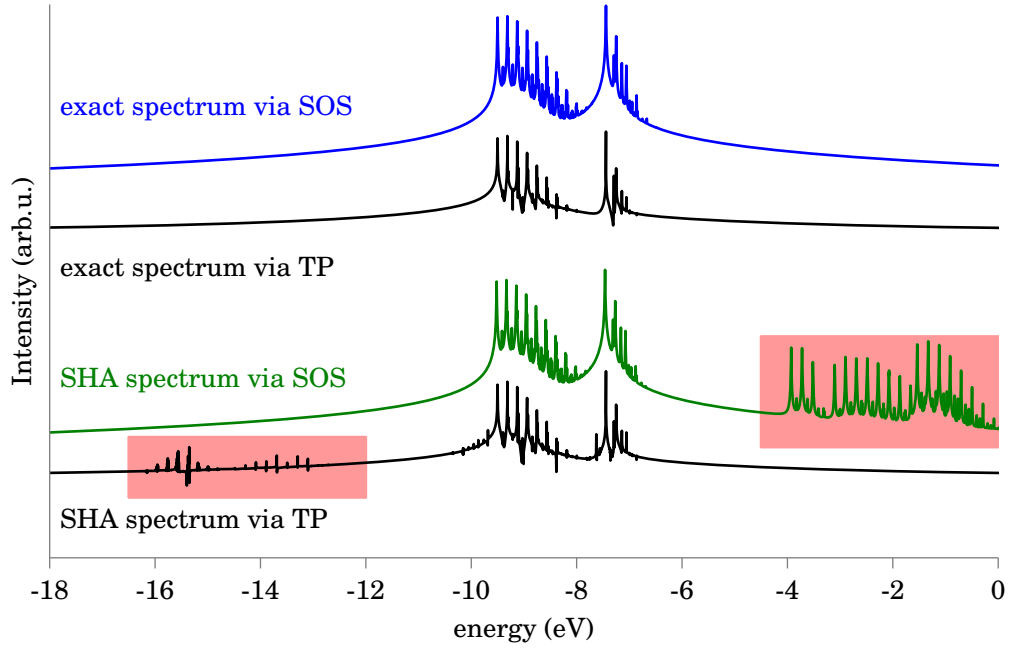


Figure 14: SHA and exact spectra obtained from time-propagations (TP) and sum-over-states (SOS) expression. The red boxes indicate the nonadiabaticity present in the BOA also discussed in Sec. 4.5.

Nevertheless, for larger nuclear masses, the BOA becomes again more accurate until in the limit of infinite nuclear mass, the BO ground state of the system is identical to the correlated ground state, thus both leading to identical spectra.

Routes to correct for these nonadiabatic effects beyond the BOA are not straightforward. Here, possible ways may be the inclusion of nonadiabatic couplings in the Born-Huang expansion (Eq. 14), an explicitly correlated ansatz for the combined electron-nuclear wave function, as e.g. in an electron-nuclear coupled cluster approach [126], a combined multi-component density-functional theory approach for electrons and nuclei [127], or in an electron-phonon Greens function theory [128, 129].

#### 4.6 COMPARISON BETWEEN PROPAGATED SPECTRA AND SUM-OVER-STATES

In Sec. 2.4, we discuss the possibility of calculating photoelectron spectra by a sum-over-states (SOS) expression, which is given by Eq. 132 for the equilibrium case and Eq. 136 for the nonequilibrium case. Additionally, it is also possible to calculate these spectra by an explicit time propagation (TP). Here, the expressions are given in Eq. 134 for the equilibrium case and Eq. 137 for more general nonequilibrium situations. In Fig. 14, we compare these two different ways of obtaining the spectra. We start by discussing the equilibrium scenario, where we use the exact correlated ground state as initial state in the photoemission process. The two upper plots in blue and black in Fig. 14 show the equilibrium case. The first spectrum, shown in blue, corresponds to the exact spectrum evaluated with the sum-over-states expression in Eq. 132. This spectrum is the same spectrum, as shown in Fig. 12 in blue. It

is an equilibrium spectrum, since the correlated many-body ground state is used as initial state for the photoemission process. The second spectrum, shown in black is calculated using an explicit time evolution of two different initial states in the time propagation for Eq. 134. As discussed in Sec. 2.4.1 one of the two involved states is the correlated ground state and the other one is the kicked correlated ground state missing one electron. We find that both equations lead to an almost identical spectrum that only differ due to the additional broadening, which is employed in the calculation of the sum-over-states expression.

The second case we discuss is the nonequilibrium case. Applying the SHA, we find a nonequilibrium scenario, since the Born-Oppenheimer ground state is not an eigenstate of the correlated electron-phonon Hamiltonian as defined in Eq. 141. The two spectra at the bottom of Fig. 14 are nonequilibrium spectra in the SHA. Here, the green spectrum is the same spectrum as shown in Fig. 12. To determine the nonequilibrium spectrum, we use the sum-over-states expression of Eq. 136, in which we neglect the energy dependence of the  $\delta$  function and replace the term  $E_n$  by the energy  $E_0$ . This approximation can be circumvented, if we directly use the explicit time propagation applying Eq. 137. As illustrated in Fig. 14, this approximation does not change the amplitude of the peaks, but shifts low energy peaks to higher energies. In Fig. 14, the red-highlighted area shows the nonadiabaticity as discussed in Sec. 4.5. This approximation in the sum-over-states expressions has no implications on the nonadiabaticity present in the BOA photoelectron spectra, since it only shifts the position of the peaks, but does not change amplitudes. However, it has implications on the time-resolved pump-probe photoelectron spectra discussed in the following section, since the approximation artificially shifts low energy peaks to higher energies. For the SSH model the evaluation of the photoelectron spectrum employing Eq. 137 for pump-probe spectroscopy is infeasible, since we would need to perform calculations on two time axis. Therefore, we use the approximate sum-over-state expression, which only involves a single time axis. For more details, we refer the reader to the appendix D for a detailed derivation for the equilibrium and nonequilibrium spectral function.

## 4.7 TIME-RESOLVED PUMP-PROBE PHOTOELECTRON SPECTRA

So far, we only considered static processes, in which the photoelectron emission is initiated from the ground state. In this section, we study time-dependent processes, where we analyze explicitly time-resolved photoelectron spectra. Therefore, we perform time propagations of given initial states and calculate the photoemission spectra at each time step. To illustrate pump-probe experiments, we analyze two different examples with different initial states. In the first example, we choose a Franck-Condon excitation as initial state, while in the second example, we start in the correlated ground state, which is then excited by a resonant femtosecond laser pulse prior to the photoemission process.

### 4.7.1 Initial Franck-Condon Excitation

In our first example, we study the time-dependent photoelectron spectrum of an electronic excitation out of the ground state. This initial excitation is a Franck-

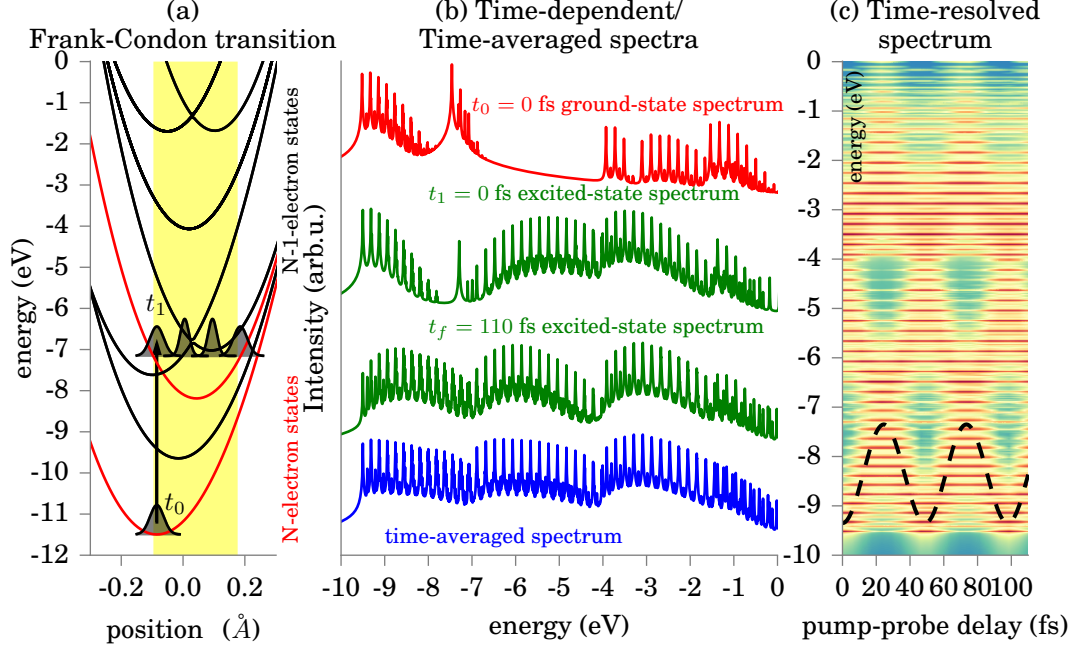


Figure 15: (a) Excitation with Frank-Condon transition: The excited  $N$ -electron initial state propagates on the  $N$ -electron PES of the first excited electronic state.  $N(N-1)$ -electron PES are shown in red (black). The yellow background indicates the oscillation spread of the wave-packet center, while the different shapes refer to the squeezing of the vibronic state. (b) spectra at different time-steps (the first (ground-state) spectrum  $t_0$  correspond to Fig. 12 (b)), (c) all spectra are plotted time-resolved, with high intensity areas shown in red and low intensity areas shown in blue color. The motion of the nuclear wave-packet center as function of pump-probe delay is shown in dashed-black lines.

Condon transition as illustrated in Fig. 15 (a) schematically. Thus, we assume for the excited state a factorized state consisting of the first excited  $N$ -particle electronic state  $|\phi_1^{(N)}\rangle$  and the ground-state configuration  $|\chi_{00}\rangle$ . This excitation can then be written as follows

$$|\Psi^{(N)}(t = t_0)\rangle = |\chi_{00}\phi_1^{(N)}\rangle. \quad (183)$$

After the Franck-Condon transition, the initial state from Eq. 183 is propagated in real-time with the full correlated many-body Hamiltonian in the total Fock space of the system. Since the Franck-Condon initial state is not an eigenstate of the correlated Hamiltonian, its time propagation leads to a wave-packet motion, as typical for harmonic potentials. In Fig. 15 (a), we show the motion of the wave packet schematically. Close to the surface, the wave packet is broader, whereas in the middle of the surface, the wave packet is sharper. We propagate the initial state from  $t_0 = 0$  fs to the final state  $t_f = 110$  fs. The total propagation time corresponds to  $9/4$  of the oscillation period of the nuclear wave packet in the excited state. In Fig. 15 (a), the yellow background indicates the spread of oscillation of the nuclear wave-packet center.

We simulate a probe pulse by calculating the photoelectron spectrum in terms of the one-body spectral function after the delay time  $\tau$  during the time propaga-



tion. Here, we use the time-dependent expression from Eq. 136. In Fig. 15 (b), we show the photoelectron spectra for two different delay times of  $\tau = t_1 = 0$  fs and  $\tau = t_f = 110$  fs in green color. The spectrum shown in red color is the ground-state spectrum (the SHA spectrum as in Fig. 12 (b)) and shows the effects of the initial Franck-Condon excitation. We find that the spectrum reveals different peaks, which gain and lose spectral amplitude after the initial Franck-Condon excitation and during the following time propagation. The blue-colored time-averaged spectrum at the bottom of Fig. 15 (b) shows a broad distribution of the peaks. Instead, the peaks in the ground-state SHA spectrum are localized close to the minimal energy in the PES. During the time propagation, each spectrum is recorded. All recorded spectra are shown in the two-dimensional surface plot in Fig. 15 (c). We plot the one-body spectral function  $A_{lm,\sigma}^{\text{SA}}(\tau, \omega)$  as a continuous function of the delay time  $\tau$ . Thus, every slice of the plot corresponds to a single spectrum obtained at  $\tau$ . The color code corresponds to the amplitude of the peaks. High photoelectron amplitudes are shown in red whereas lower amplitudes are shown in blue. The vertical spacing between neighboring peaks corresponds to different electron-phonon states in the same PES. In addition, in Fig. 15 (c), the dashed black line indicates the center of the nuclear wave packet (first moment) during the time propagation as function of the delay time  $\tau$ . One oscillation period corresponds to  $T_0 = 48.94$  fs. The average along the x-axis of the delay time  $\tau$ , hence over all slices, again yields the average spectrum in Fig. 15 (b) plotted in blue.

In conclusion, the two-dimensional plot of the spectral function illustrates that we can connect the gain and loss of spectral amplitude as function of pump-probe delay time  $\tau$  directly to the underlying motion of the nuclear wave packet. We find similarities to optical pump-probe spectroscopy, which also reveals insight about the nuclear dynamics of the system. In contrast to optical pump-probe experiments, time-resolved photoelectron spectroscopy accesses excitations, which are not charge-neutral. Thus, it allows to observe transitions, which can be dipole forbidden.

#### 4.7.2 Explicit Pump Pulse

In the second example, we explicitly simulate the initial excitation process. While the Franck-Condon excitation is an instantaneous excitation, real excitations in atoms and molecules have a finite transition time. We improve the description of the excitation process by explicitly including the pump pulse into the time propagation. Therefore, we employ the Hamiltonian from Eq. 144 with an electric field  $E(t)$  consisting of a Gaussian envelope with midpoint  $t_0 = -6$  fs, maximum envelope  $E_0 = 0.85$  V/Å and variance  $\sigma = 1.5$  fs. The carrier wave is a sine function with frequency  $\omega_l = \Delta E/\hbar = 6.20$  fs<sup>-1</sup>. We tune the laser frequency in resonance to the Franck-Condon transition, thus  $\Delta E$  is chosen such that it corresponds to the example of a Franck-Condon excited initial state as in Sec. 4.7.1. The correlated Hamiltonian  $\hat{H}_{ssh}(t)$  becomes explicitly time-dependent due to the time-dependent external potential  $E(t)$ . To correctly capture the time-dependence of the Hamiltonian, we use a Lanczos propagator with an exponential midpoint scheme [107]. The initial state at  $t_0 = -10$  fs is the exact correlated ground state, which is then propagated with the correlated many-body Hamiltonian including

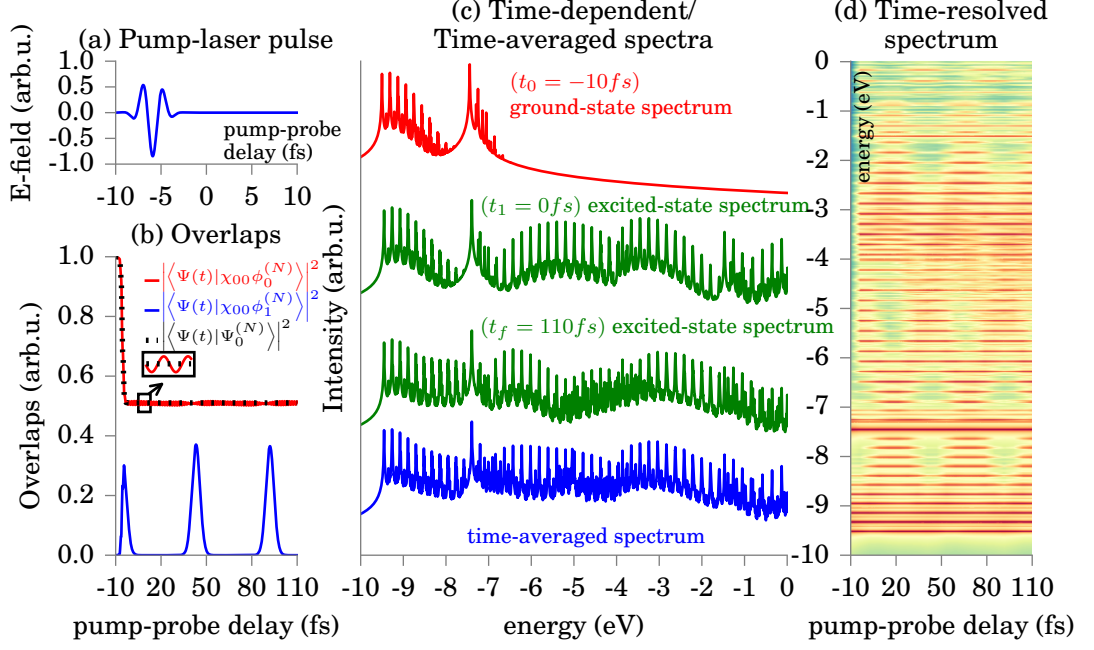


Figure 16: Time-dependent pump-probe photoelectron spectroscopy: (a) Amplitude of the laser-pulse (Eq. 144), (b) overlaps of the time-evolved state with electronic ground and first excited BO states and the exact correlated ground state, (c) spectra at different pump-probe delay times (the first spectrum at  $t_0$  corresponds to Fig. 12 (c)), (d) spectra plotted time-resolved, high intensity shown in red and low intensity shown in blue.

the dipole coupling to the external pump laser as given in Eq. 144.

Fig. 16 (a) shows the electric field  $E(t)$  of the external laser pulse as function of the pump-probe delay time  $\tau$ . The laser pulse starts at  $t = -10$  fs and acts on the system until it is switched off at  $t = 0$  fs. In Fig. 16 (b), we compute the overlaps of the time-propagated state with two BO states in blue and red and with the exact correlated ground state in black as function of time. For the BO overlaps, we plot in red the overlap with the BO ground state and in blue with the Franck-Condon excited state, which was chosen as initial state in Sec. 4.7.1. Using these overlaps, we evaluate which states are populated during the time propagation. Since we pick the exact correlated state as initial state at initial time  $t = -10$  fs the overlap with the BO ground state  $|\chi_{00}\phi_0^{(N)}\rangle$  is 0.9986 (as shown in Tab. 2). While the laser pulse acts on the system, it drives population from the BO ground state to the Frank-Condon state  $|\chi_{00}\phi_0^{(N)}\rangle$ . Here, we identify two competing processes: First, the external laser pulse drives population from  $|\chi_{00}\phi_0^{(N)}\rangle$  to  $|\chi_{00}\phi_1^{(N)}\rangle$ . Afterwards, once this state is populated, a wave packet motion is induced on the first excited PES, as seen in Sec. 4.7.1. Therefore, the system never reaches a situation, where only two states  $|\chi_{00}\phi_0^{(N)}\rangle$  and  $|\chi_{00}\phi_1^{(N)}\rangle$  occur in the system. However, this picture is assumed in the Franck-Condon excitation process. After the laser pulse vanishes at  $t = 0$  fs, the time-propagated state has an overlap of around 50% with the exact correlated ground state. We find small oscillations of the overlap with the BO ground state, as can be seen in the inset of Fig. 16 (b). These oscillations are caused



by the small deviations between the BO ground state and the exact correlated ground state.

In Fig. 16 (c) we show photoelectron spectra for different delay times  $\tau$ . For comparison, we also show the correlated ground-state spectrum of Fig. 12 (c) in red, which is recorded at initial time  $\tau = -10$  fs. In green, we plot two spectra, which were recorded after the laser pulse acted on the system at time  $\tau = 0$  fs and  $\tau = 110$  fs, respectively. The time-averaged spectrum is shown in blue at the bottom of Fig. 16 (c). All spectra have a very high intensity peak at  $-7.5$  eV. This peak can be attributed to the remaining population of the correlated ground state, which stays constant at around 50%. In Fig. 16 (d), we show all recorded spectra as a function of the pump-probe delay time  $\tau$  in a two-dimensional surface plot. In this two-dimensional plot, we can observe the underlying oscillation of the nuclear wave packet as in the example in Sec. 4.7.1. In summary, we find many similarities between Fig. 15 (c) and Fig. 16 (d). This leads us to the conclusion that the initial Franck-Condon excitation captures large parts of the more accurate spectrum obtained by an explicit inclusion of the pump-probe pulse. However, we also find some differences, since the explicit inclusion leaves population in the correlated ground state and the finite time of the excitation process leads to an initial state, which consists of more than a few factorized states. These broader distribution of involved states introduces small nonadiabatic contributions to the spectrum in the energy range from  $-4$  eV to  $-2$  eV.

#### 4.8 SUMMARY

In the first part of this chapter, we have evaluated the quality of the BOA in the Su-Schrieffer-Heeger Hamiltonian. We find high overlaps of the BO states and only small anharmonicities due to the electron-phonon coupling in the Hamiltonian. While the overlaps and eigenenergies of the exact correlated states and the BO states are in good agreement, we find nonadiabatic contributions to the equilibrium and nonequilibrium photoelectron spectra in the model system for Trans-Polyacetylene. These contributions lead to spurious peaks in the double-harmonic approximation and the single-harmonic approximation for the spectral function and only vanish if the full correlated spectral function is considered. However, if either the initial state in the photoemission process or the  $N - 1$  particle eigenstates are replaced by the factorized BO states these spurious amplitudes are nonvanishing. This is why we attribute these spurious spectral weight to the factorized nature of the BO states. An expansion of the BO ground state in the complete set of correlated eigenstates shows that additional cross and diagonal terms, which involve excited correlated eigenstates are the origin for these spurious spectral weight amplitudes.

Additionally, we have shown for an initial Franck-Condon excitation and an explicit simulation of the resonant laser pulse how we can trace the nuclear motion as a function pump-probe delay in the spectral functions with real-time propagations of the Trans-Polyacetylene chain. Future work in this direction could include the study of temperature and pressure dependence of the photoelectron spectra or an extension of the present femtosecond laser excitation to ultrafast photoelectron spectroscopy with attosecond laser pulses. An alternative line of research may

focus on the development of [xc](#)-functionals in a generalization of [TDDFT](#), which includes correlated electron-phonon effects, e.g. based on electron-nuclear multi-component density-functional theory [[127](#)].

In this section the applied external laser pulse in [Sec. 4.7.2](#) was assumed to be classical as described in [Sec 2.3.1](#). This regime is typically well justified in the case of femtosecond laser pulses, due to the high-amount of photons present in the laser pulse. In the following chapters, we study how the quantum nature of electromagnetic fields (e.g. in the few-photon limit) influences the correlated light-matter interaction in interactions of light with molecules and atoms.

## QUANTUM-ELECTRODYNAMICAL DENSITY FUNCTIONAL THEORY IN THE NONRELATIVISTIC LIMIT

---

The original formulation of [TDDFT](#) as discussed in Sec. 2.2.6 treats the many-body problem of interacting electrons. Time-dependent electromagnetic fields can be included by an additional time-dependent external potential  $v_{\text{ext}}(\mathbf{r}, t)$ . Such a treatment of the electromagnetic field implies that the electromagnetic field is treated classically. Typically, the external field only considers the dipole coupling of the electric field, i.e.  $v_{\text{ext}}(\mathbf{r}, t) = \mathbf{E}(\mathbf{r}, t) \cdot e\mathbf{r}$  with the dipole operator  $\mathbf{r}$ . In contrast, the treatment of external magnetic fields goes beyond the original formulation of [TDDFT](#). Magnetic fields can be treated in the framework of [TDCDFT](#) [28], which uses the electron current  $\mathbf{J}$  and an external vector field  $\mathbf{A}_{\text{ext}}$  as conjugated variables. However, [TDCDFT](#) still relies on the classical approximation for the electromagnetic field. In this chapter, we investigate [QEDFT](#), which overcomes the classical approximation to the electromagnetic field. In [QEDFT](#), matter and light are treated quantum mechanically, both on an equal footing. While the classical approximation of the light-matter interaction is justified in the limit of strong laser pulses, in which a high numbers of photons occur, this approximation breaks down in the single-photon limit. While [TDDFT](#) is restricted to purely electronic systems, [QEDFT](#) is applicable to correlated electron-photon systems. This chapter is based on the work published in Refs. [17, 18]. Ref. [17] formulates the foundations of [QEDFT](#) in the nonrelativistic limit, while the work reported in Ref. [18] treats the general theory on various approximations starting from the relativistic Dirac equation with a fully quantized fermionic field and all the way down to the nonrelativistic limit. Earlier work on this topic has been published in Refs. [16, 130].

In this thesis, we focus on the nonrelativistic limit, in which the minimal-coupling Hamiltonian, and the Power-Zienau-Woolley Hamiltonian are an appropriate description of the system. In this chapter, we follow Ref. [17] by outlining the specific aspects of the theory of [QEDFT](#), which is used in the following chapters of this thesis.

In [QEDFT](#), the basic internal variables are an electronic variable and a field variable of the electromagnetic field. These variables form a set of basic (internal) variables, which has an one-to-one correspondence to a set of conjugated (external) variables. Formulated differently: There exists a unique and bijective mapping between the set of internal variables and the set of external variables for each initial state. This unique mapping is the analogue of the one-to-one correspondence between the electron density  $n(\mathbf{r})$  and the external potential  $v_{\text{ext}}(\mathbf{r})$  in ground-state [DFT](#). We refer the reader to Tab. 3 for an overview of different flavors of density-functional theories.

The chapter is organized as follows: We first discuss the setup of the correlated

---

This chapter is partly based on the work reported in Ref. [18], where I contributed to the derivation of the model system, performed all numerical simulations, and prepared the figures shown in the manuscript.

theory	basic variable	$\longleftrightarrow^{1:1}$	conjugated variable	Reference
DFT	$n_0(\mathbf{r})$	$\longleftrightarrow^{1:1}$	$v_{\text{ext}}(\mathbf{r})$	[6]
TDDFT	$n(\mathbf{r}, t)$	$\longleftrightarrow^{1:1}$	$v_{\text{ext}}(\mathbf{r}, t)$	[10]
TDCDFT	$\mathbf{J}(\mathbf{r}, t)$	$\longleftrightarrow^{1:1}$	$\mathbf{A}_{\text{ext}}(\mathbf{r}, t)$	[28]
QEDFT-M	$(\mathbf{J}(\mathbf{r}, t), \mathbf{A}(\mathbf{r}, t))$	$\longleftrightarrow^{1:1}$	$(\mathbf{A}_{\text{ext}}(\mathbf{r}, t), \mathbf{j}_{\text{ext}}(\mathbf{r}, t))$	[17, 18]
QEDFT-L	$(n(\mathbf{r}, t), q_\alpha(t))$	$\longleftrightarrow^{1:1}$	$(v_{\text{ext}}(\mathbf{r}, t), j_{\text{ext}}^{(\alpha)}(t))$	[17]

Table 3: Different levels of density-functional theories including reference papers. QEDFT-M corresponds to the QEDFT framework in the momentum gauge, whereas QEDFT-L refers to QEDFT in the length gauge.

electron-photon problem, then we focus on the equations of motion for the electromagnetic field variables and the electron variable. We use the equations of motion to prove the one-to-one correspondence in the spirit of the original TDDFT proof by Runge-Gross [10] (see Sec. 2.2.6). Afterwards, we setup the Kohn-Sham system and discuss the mean-field approximation that corresponds to the Maxwell-Schrödinger propagation of Sec. 2.3.7. In the last part of this chapter, we present a first explicit example of a QEDFT calculation. For the Jaynes-Cummings-Hubbard model, we compare the quality of the mean-field approximation to exact solutions.

### 5.1 MULTICOMPONENT THEORY

In this chapter, we consider a multicomponent system of  $n_e$  interacting electrons coupled to  $n_m$  quantized electromagnetic field modes. The time evolution of an arbitrary initial state  $|\Psi_0\rangle = |\Psi(t_0)\rangle$  of such quantum systems is given by the time-dependent Schrödinger equation of Eq. 1. Here, the time evolution of the quantum system is governed by the many-body Hamiltonian  $\hat{H}(t)$ . Throughout this thesis we apply for correlated electron-photon problems the Power-Zienau-Woolley Hamiltonian in the length gauge as given in Sec. 2.3.9. For completeness, let us reformulate the Hamiltonian of Eq. 119 in the following way

$$\begin{aligned}
\hat{H}(t) = & \sum_{i=1}^{n_e} \left( -\frac{\hbar^2}{2m_e} \nabla_i^2 + v_{\text{ext}}(\mathbf{r}_i, t) \right) + \frac{e^2}{4\pi\epsilon_0} \sum_{i>j}^{n_e} \frac{1}{|\mathbf{r}_i - \mathbf{r}_j|} \\
& + \sum_{\alpha=1}^{n_m} \frac{1}{2} \left[ \hat{p}_\alpha^2 + \omega_\alpha^2 \left( \hat{q}_\alpha - \frac{\boldsymbol{\lambda}_\alpha}{\omega_\alpha} \cdot \mathbf{R} \right)^2 \right] + \frac{j_{\text{ext}}^{(\alpha)}(t)}{\omega_\alpha} \hat{q}_\alpha.
\end{aligned} \tag{184}$$

In comparison to Eq. 119, we explicitly insert the electron kinetic energy operator  $\hat{T}_e$ , and the electron-electron interaction operator  $\hat{W}_{ee}$  as given by Eq. 5 and Eq. 7, respectively. Additionally, we introduce the collective index  $\alpha = \mathbf{k}\lambda$  that consists of the wave number  $\mathbf{k}$  and the two possible polarization directions of the electromagnetic field  $\lambda$ . Furthermore, we define the electron-photon coupling strength  $\lambda_\alpha = e\mathcal{A}_\alpha(\mathbf{R}_c)/\sqrt{\epsilon_0}$ . In Eq. 184, the electromagnetic field couples to the electrons present in the system by the total electronic dipole moment  $\mathbf{R} = \sum_{i=1}^{n_e} \mathbf{r}_i$ . This allows us to define the  $\alpha$ -th components of the Maxwell field operator  $\hat{\mathbf{A}}_\alpha$  and the

electrical displacement operator  $\hat{\mathbf{D}}_\alpha$  at the position of the charge center  $\mathbf{R}_c$  by the operators  $\hat{p}_\alpha$  and  $\hat{q}_\alpha$  that are defined by Eqns. 106-107. In the following, we fix  $\mathbf{R}_c$  to the origin, hence  $\mathbf{R}_c = 0$ . The  $\alpha$ -th component of the displacement field operator  $\hat{\mathbf{D}}_\alpha$  and the vector field operator  $\hat{\mathbf{A}}_\alpha$  can be calculated as follows

$$\hat{\mathbf{D}}_\alpha = \frac{\epsilon_0 \omega_\alpha \lambda_\alpha}{e} \hat{q}_\alpha, \quad (185)$$

$$\hat{\mathbf{A}}_\alpha = \frac{\lambda_\alpha}{e \omega_\alpha} \hat{p}_\alpha. \quad (186)$$

In addition in Eq. 184, we further introduce an external current  $j_{\text{ext}}^{(\alpha)}(t)$ , which allows to exclusively control the photon field.

In Eq. 184, the electron-photon interaction is incorporated into two terms: (i) the explicit electron-photon interaction Hamiltonian, which can be formulated equivalently by

$$\hat{H}_{\text{int}} = - \sum_{\alpha=1}^{n_m} \omega_\alpha \hat{q}_\alpha \int d\mathbf{r} (\lambda_\alpha \cdot \mathbf{r}) \hat{n}(\mathbf{r}), \quad (187)$$

and (ii) in the electron self-energy term [131]

$$\hat{H}_{\text{es}} = \sum_{\alpha} (\lambda_\alpha \cdot \mathbf{R})^2 / 2, \quad (188)$$

which is a dipole self-interaction term. In Eq. 187, the electron density operator  $\hat{n}(\mathbf{r})$  couples linearly to the photon displacement operator  $\hat{q}_\alpha$ . This direct coupling makes both quantities ideal candidates for the set of basic internal variables in a density-functional scheme for QEDFT<sup>1</sup>. In Eq. 184,  $\hat{n}(\mathbf{r})$  and  $\hat{q}_\alpha$  also couple individually to external variables, the external potential  $v_{\text{ext}}(\mathbf{r}, t)$  and the external current field  $j_{\text{ext}}^{(\alpha)}(t)$ , respectively.

In general, it is possible to classify all solutions of Eq. 184 by the initial state  $|\Psi_0\rangle$  and the external potentials  $(v_{\text{ext}}, j_{\text{ext}})$ . Or stated differently, the Power-Zienau-Woolley Hamiltonian contains an implicit functional dependence on these variables:  $\hat{H}(t) \rightarrow \hat{H}([\Psi_0, v_{\text{ext}}, j_{\text{ext}}], t)$ . Furthermore, the functional dependence of the Hamiltonian is inherited by all possible solutions, namely the time-dependent many-body wave function  $|\Psi(t)\rangle$ . Since all observables are calculated as expectation values of an arbitrary operator  $\hat{O}(\mathbf{r})$  using the many-body wave function, they can be also interpreted as functionals of the initial state and the external potentials  $(v_{\text{ext}}, j_{\text{ext}})$  as

$$O(\mathbf{r}, t) = \langle \Psi(t) | \hat{O}(\mathbf{r}) | \Psi(t) \rangle = O([\Psi_0, v_{\text{ext}}, j_{\text{ext}}], \mathbf{r}, t). \quad (189)$$

In particular, we find that also the basic internal variables can be seen as functionals of the initial state and the external potentials

$$n(\mathbf{r}, t) = n([\Psi_0, v_{\text{ext}}, j_{\text{ext}}], \mathbf{r}, t) \quad (190)$$

$$q_\alpha(t) = q_\alpha([\Psi_0, v_{\text{ext}}, j_{\text{ext}}], t). \quad (191)$$

<sup>1</sup> We note here that the electron density  $\hat{n}(\mathbf{r})$  is a natural quantity of the electronic part of the system, while the photon displacement operator  $\hat{q}_\alpha$  is a mixed field-matter quantity, due to its connection to the displacement field operator  $\hat{\mathbf{D}}_\alpha$  defined in Eq. 185. Please also see the appendix A.

Every density-functional theory is based on the uniqueness and existence of a mapping between a set of basic variables (e.g. the electron density or the electronic current) and a set of external potentials. If this mapping exists and is unique, we can replace the functional dependence on the external potentials in Eqns. 189-191 by a functional dependence on the basic internal variables. This replacement procedure has different advantages, such as the possibility to simulate the dynamics of an interacting system by a noninteracting Kohn-Sham system, which may lead to a reduction in computational effort and makes the density-functional theory a practical method for many-body calculations.

To complete the fundamental theory of QEDFT, we outline the one-to-one proof for fixed initial state  $|\Psi_0\rangle$  as derived in Ref. [17, 18]

$$\left(v_{\text{ext}}(\mathbf{r}, t), j_{\text{ext}}^{(\alpha)}(t)\right) \xleftrightarrow[\Psi_0]{1:1} (n(\mathbf{r}, t), q_\alpha(t)). \quad (192)$$

To this end, in the next section, we first discuss the equations of motion for the quantized electromagnetic field and in a second step the equations of motion for the electrons.

## 5.2 EQUATIONS OF MOTION FOR THE QUANTIZED ELECTROMAGNETIC FIELD

In the following section, we focus on the photon part in the basic variables-potential mapping. As basic variable for the photon field, we use the expectation value of the displacement operator  $q_\alpha(t)$ , which couples in the last term of the Hamiltonian in Eq. 184 to the external potential  $j_{\text{ext}}^{(\alpha)}(t)$  as corresponding conjugated variable. To establish the explicit connection between the conjugated variables, we can use Heisenberg's equation of motion as given in Eq. 42 and find

$$\frac{\partial}{\partial t} q_\alpha(t) = p_\alpha(t), \quad (193)$$

$$\frac{\partial^2}{\partial t^2} q_\alpha(t) = \omega_\alpha \lambda_\alpha \cdot \mathbf{R}(t) - \omega_\alpha^2 q_\alpha(t) - \frac{j_{\text{ext}}^{(\alpha)}(t)}{\omega_\alpha}, \quad (194)$$

with the time-dependent total dipole moment  $\mathbf{R}(t) = \int n(\mathbf{r}, t) \mathbf{r} d\mathbf{r}$ . By calculating the first time-derivative of the photon displacement operator, we recover the connection between  $q_\alpha(t)$  and  $p_\alpha(t)$  known from quantum harmonic oscillators. We find explicitly that  $p_\alpha(t)$  is the conjugated momentum of  $q_\alpha(t)$ . The second time-derivative in Eq. 194, yields a wave equation, as in the case of Maxwell's equations. It contains the effective inhomogeneity

$$j_s^{(\alpha)}(t) = -\omega_\alpha^2 \lambda_\alpha \cdot \mathbf{R}(t) + j_{\text{ext}}^{(\alpha)}(t), \quad (195)$$

such that Eq. 194 can be rewritten as follows

$$\frac{\partial^2}{\partial t^2} q_\alpha(t) = -\omega_\alpha^2 q_\alpha(t) - \frac{j_s^{(\alpha)}(t)}{\omega_\alpha}. \quad (196)$$

Eqns. 194 and 196 already yield a direct connection between the external potential variable  $j_{\text{ext}}^{(\alpha)}(t)$  and the set of internal basic variables  $(n(\mathbf{r}, t), q_\alpha(t))$ . To this end, Eq. 196 can be solved formally as in Eq. 151 by

$$q_\alpha(t) = q_\alpha(t_0) \cos(\omega_\alpha t) + \frac{\dot{q}_\alpha(t_0)}{\omega_\alpha} \sin(\omega_\alpha t) - \frac{1}{\omega_\alpha^2} \int_{t_0}^t dt' \sin(\omega_\alpha(t-t')) j_s^{(\alpha)}(t'), \quad (197)$$

with the initial conditions  $q_\alpha(t_0)$  and  $\dot{q}_\alpha(t_0)$ . Thus, if  $(n(\mathbf{r}, t), q_\alpha(t))$  are given, we can immediately construct the corresponding  $j_{\text{ext}}^{(\alpha)}(t)$  using Eq. 194. Therefore, the existence and uniqueness of the total mapping in Eq. 192 only depends on the mapping  $v_{\text{ext}}(\mathbf{r}, t) \xrightarrow[\Psi_0]{1:1} (n(\mathbf{r}, t), q_\alpha(t))$ . This mapping is investigated in the following section.

### 5.3 EQUATIONS OF MOTION IN THE ELECTRONIC SUBSYSTEM

At this point, we are able to prove the Runge-Gross theorem<sup>2</sup> for the one-to-one correspondence between the sets of conjugated variables as formulated in Eq. 192. This means that we require that two different sets of external potentials  $(v_{\text{ext}}(\mathbf{r}, t), j_{\text{ext}}^{(\alpha)}(t))$  and  $(v'_{\text{ext}}(\mathbf{r}, t), j_{\text{ext}}^{(\alpha)'}(t))$  always lead to two different sets of basic internal variables  $(n(\mathbf{r}, t), q_\alpha(t))$  and  $(n'(\mathbf{r}, t), q'_\alpha(t))$  under the condition that the system evolves from a common initial state  $|\Psi_0\rangle$ .

Using the Hamiltonian in Eq. 184, the second time-derivative of the electron density  $n(\mathbf{r}, t)$  is equal to

$$\begin{aligned} \frac{\partial^2}{\partial t^2} n(\mathbf{r}, t) = & -\vec{\nabla} \cdot \mathbf{Q}(\mathbf{r}, t) + \frac{1}{m_e} \vec{\nabla} \cdot \left( n(\mathbf{r}, t) \vec{\nabla} v_{\text{ext}}(\mathbf{r}, t) \right) \\ & + \sum_{\alpha=1}^{n_m} \frac{1}{m_e} \vec{\nabla} \cdot \lambda_\alpha \langle \Psi(t) | \hat{n}(\mathbf{r}) (\lambda_\alpha \cdot \hat{\mathbf{R}} - \omega_\alpha \hat{q}_\alpha) | \Psi(t) \rangle. \end{aligned} \quad (198)$$

The first line of this equation is in agreement with the equation of motion of purely electronic problems discussed in Eq. 46. Eq. 194 and Eq. 198 allow us to proof the one-to-one correspondence following the reasoning of the original Runge-Gross proof [10] (Sec. 2.2.6) and the references [17, 18]. Let us assume that  $v'_{\text{ext}}(\mathbf{r}, t) \neq v_{\text{ext}}(\mathbf{r}, t) + c(t)$ , and  $j_{\text{ext}}^{(\alpha)'}(t) \neq j_{\text{ext}}^{(\alpha)}(t)$  with the time-dependent function  $c(t)$  that is constant in space. We furthermore assume time analyticity in  $v_{\text{ext}}$  and  $j_{\text{ext}}$ , such that there exists a Taylor series for both quantities around the initial time  $t_0$  (Eq. 48). This implies that there exists a  $k_{\text{min}} = k$  such that

$$\left. \frac{\partial^k}{\partial t^k} (v_{\text{ext}}(\mathbf{r}, t) - v'_{\text{ext}}(\mathbf{r}, t)) \right|_{t=t_0} \neq \text{const} \quad \text{or} \quad \left. \frac{\partial^k}{\partial t^k} (j_{\text{ext}}^{(\alpha)}(t) - j_{\text{ext}}^{(\alpha)'}(t)) \right|_{t=t_0} \neq 0. \quad (199)$$

If  $k_{\text{min}} = 0$ , we find for the electron density

$$\left. \frac{\partial^2}{\partial t^2} (n(\mathbf{r}, t) - n'(\mathbf{r}, t)) \right|_{t=t_0} = \frac{1}{m_e} \vec{\nabla} \cdot \left( n(\mathbf{r}, t_0) \vec{\nabla} [v_{\text{ext}}(\mathbf{r}, t_0) - v'_{\text{ext}}(\mathbf{r}, t_0)] \right), \quad (200)$$

<sup>2</sup> The ground-state proof in analogy to the Hohenberg-Kohn proof discussed in Sec. 2.2.2 has been worked out recently in Ref. [132].



and for the photon displacement coordinate  $q_\alpha(t)$

$$\left. \frac{\partial^2}{\partial t^2} (q_\alpha(t) - q'_\alpha(t)) \right|_{t=t_0} = \frac{j_{\text{ext}}^{(\alpha)'}(t_0)}{\omega_\alpha} - \frac{j_{\text{ext}}^{(\alpha)}(t_0)}{\omega_\alpha}. \quad (201)$$

We find that if one of the right-hand sides of Eqns. 200-201 is nonvanishing, then either  $n(\mathbf{r}, t + \Delta t) - n'(\mathbf{r}, t + \Delta t) \neq 0$  or  $q_\alpha(t + \Delta t) - q'_\alpha(t + \Delta t) \neq 0$  for infinitesimal small  $\Delta t$ . Thus leading to different densities for  $t > t_0$ . In the case of  $k_{\min} = k > 0$ , we have to apply the Heisenberg equation of motion  $k$ -times to find

$$\left. \frac{\partial^{k+2}}{\partial t^{k+2}} (n(\mathbf{r}, t) - n'(\mathbf{r}, t)) \right|_{t=t_0} = \frac{1}{m_e} \vec{\nabla} \cdot \left[ n(\mathbf{r}, t_0) \vec{\nabla} \left( \frac{\partial^k}{\partial t^k} [v_{\text{ext}}(\mathbf{r}, t) - v'_{\text{ext}}(\mathbf{r}, t)] \right) \right] \Big|_{t=t_0}, \quad (202)$$

and for the photon displacement coordinate  $q_\alpha(t)$

$$\left. \frac{\partial^{k+2}}{\partial t^{k+2}} (q_\alpha(t) - q'_\alpha(t)) \right|_{t=t_0} = \frac{\partial^k}{\partial t^k} \left( \frac{j_{\text{ext}}^{(\alpha)'}(t)}{\omega_\alpha} - \frac{j_{\text{ext}}^{(\alpha)}(t)}{\omega_\alpha} \right) \Big|_{t=t_0}. \quad (203)$$

Here, we used explicitly that  $\left. \frac{\partial^k}{\partial t^k} (n(\mathbf{r}, t) - n'(\mathbf{r}, t)) \right|_{t=t_0} = 0$ , since  $k_{\min} = k$ . Since, Eq. 202 is equal to Eq. 52, we can apply the original Runge-Gross proof. Again we find that if one of the right-hand sides is nonvanishing, either  $n(\mathbf{r}, t + \Delta t) - n'(\mathbf{r}, t + \Delta t) \neq 0$  or  $q_\alpha(t + \Delta t) - q'_\alpha(t + \Delta t) \neq 0$  for infinitesimal small  $\Delta t$ . This finding concludes the proof. Since we used the same conditions on  $n(\mathbf{r}, t)$  as in Sec. 2.2.6, we also find that the initial density  $n(\mathbf{r}, t)$  has to be reasonably well behaved [10]. Interestingly, the conditions on  $q_\alpha(t)$  are slightly weaker, only time analyticity on  $q_\alpha(t)$  and  $j_{\text{ext}}^{(\alpha)}(t)$  is required.

#### 5.4 KOHN-SHAM SYSTEM IN QEDFT

The one-to-one correspondence between the set of conjugated variables allows us, in analogy to Sec. 2.2.7, to replace the originally interacting quantum problem by a problem with different interaction operator  $\hat{H}_{\text{int}}$ . A straightforward choice is a noninteracting Kohn-Sham system<sup>3</sup>, which decouples the electronic problem from the photonic problem. The Kohn-Sham system can be setup as follows

$$i\hbar \partial_t \phi_i(\mathbf{r}, t) = -\frac{\hbar^2}{2m_e} \vec{\nabla}^2 \phi_i(\mathbf{r}, t) + v_s(\mathbf{r}, t) \phi_i(\mathbf{r}, t), \quad (204)$$

$$i\hbar \partial_t |\alpha, t\rangle = \frac{1}{2} [\hat{p}_\alpha^2 + \omega_\alpha^2 \hat{q}_\alpha^2] |\alpha, t\rangle + \frac{j_s^{(\alpha)}(t)}{\omega_\alpha} \hat{q}_\alpha |\alpha, t\rangle, \quad (205)$$

where the Kohn-Sham photon wave function is given by  $|\alpha, t\rangle = \sum_n c_n |n, t\rangle$  and  $|n, t\rangle$  are the Fock number states of the  $\alpha$ -th cavity mode. The Kohn-Sham electron wave function  $\Phi_s$  can be calculated using the single-particle orbitals  $\phi_i(\mathbf{r}, t)$  with the help of Eq. 33. The initial electron density  $n(\mathbf{r}, t_0)$  and its time-derivative  $\dot{n}(\mathbf{r}, t_0)$  have to be equal to the coupled many-body system. Formulated differently, we

<sup>3</sup> In principle, different KS systems are possible. An alternative KS system could be chosen such that it still contains specific parts of the electron-photon interaction explicitly.



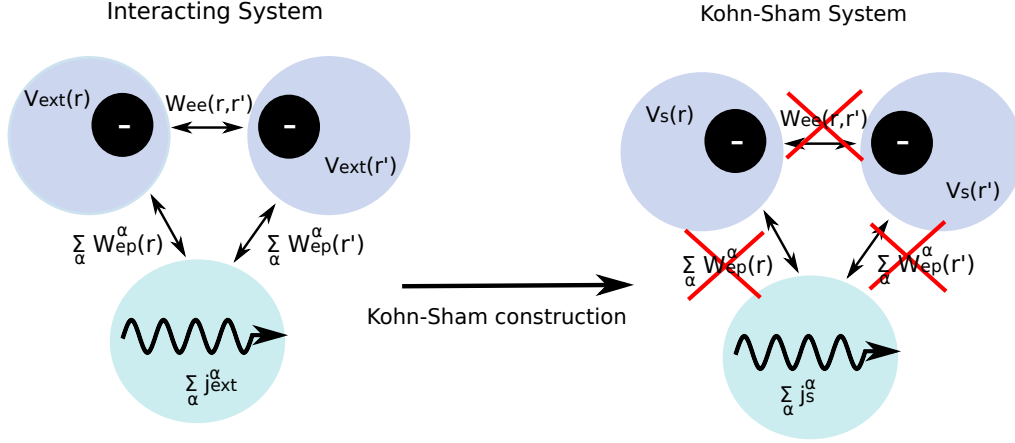


Figure 17: Kohn-Sham construction in QEDFT. The left-hand side shows the interacting electron-photon system, while the right-hand side shows the noninteracting Kohn-Sham system.

have to choose a Kohn-Sham initial state  $\Phi_s(t_0)$  such that it leads to the same electron density and time-derivative on the electron density as the correlated many-body initial state  $\Psi(t_0)$ . The same is also required for the photon displacement operator, which means  $q_\alpha(t_0)$  and  $\dot{q}_\alpha(t_0)$ . However the Kohn-Sham initial state  $\Phi_s(t_0)$  and the exact many-body initial state  $\Psi(t_0)$  can be different in principle, if the initial conditions on the densities are fulfilled. The equations of motion for the Kohn-Sham system then read

$$\frac{\partial^2}{\partial t^2} n(\mathbf{r}, t) = -\vec{\nabla} \cdot \mathbf{Q}^{(s)}(\mathbf{r}, t) + \frac{1}{m_e} \vec{\nabla} \cdot \left( n(\mathbf{r}, t) \vec{\nabla} v_s(\mathbf{r}, t) \right), \quad (206)$$

$$\frac{\partial^2}{\partial t^2} q_\alpha(t) = -\omega_\alpha^2 q_\alpha(t) - \frac{j_s^{(\alpha)}(t)}{\omega_\alpha}, \quad (207)$$

where the Kohn-Sham electronic stress force operator is defined as

$$\mathbf{Q}^{(s)}(\mathbf{r}, t) = -\frac{i}{\hbar} \langle \Phi_s(t) | [\hat{\mathbf{J}}, \hat{T}_e] | \Phi_s(t) \rangle. \quad (208)$$

The Kohn-Sham potential  $v_s(\mathbf{r}, t)$  is defined as [17]

$$v_s(\mathbf{r}, t) = v_{\text{ext}}(\mathbf{r}, t) + v_{\text{Hxc}}(\mathbf{r}, t) + v_{\text{Mxc}}(\mathbf{r}, t), \quad (209)$$

where  $v_{\text{Hxc}}(\mathbf{r}, t)$  is the Hartree-exchange-correlation potential and  $v_{\text{Mxc}}$  is the mean-field-exchange-correlation potential. The photon external field  $j_s^{(\alpha)}(t)$  is defined by Eq. 195. By construction the Kohn-Sham system produces the same time-dependent density  $n(\mathbf{r}, t)$  as the interacting many-body problem. This allows us to define  $v_{\text{Hxc}}(\mathbf{r}, t)$  and  $v_{\text{Mxc}}(\mathbf{r}, t)$  using Eqns. 194, 198, 206, 207 by Sturm-Liouville equations as

$$\frac{1}{m_e} \vec{\nabla} \cdot \left( n(\mathbf{r}, t) \vec{\nabla} v_{\text{Hxc}}(\mathbf{r}, t) \right) = \vec{\nabla} \cdot \left( \mathbf{Q}^{(s)}(\mathbf{r}, t) - \mathbf{Q}(\mathbf{r}, t) \right) \quad (210)$$

$$\frac{1}{m_e} \vec{\nabla} \cdot \left( n(\mathbf{r}, t) \vec{\nabla} v_{\text{Mxc}}(\mathbf{r}, t) \right) = \frac{1}{m_e} \sum_{\alpha=1}^{n_m} \vec{\nabla} \cdot \lambda_\alpha \langle \Psi(t) | \hat{n}(\mathbf{r}) (\lambda_\alpha \cdot \hat{\mathbf{R}} - \omega_\alpha \hat{q}_\alpha) | \Psi(t) \rangle, \quad (211)$$

where the electron stress force  $\mathbf{Q}(\mathbf{r}, t)$  is defined by Eq. 47. If there is no electron-photon interaction present in the system,  $\lambda_\alpha = 0$ , the mean-field-exchange-correlation potential vanishes with  $v_{\text{Mxc}} = 0$  and  $v_{\text{Hxc}}$  reduces to the Hartree-exchange-correlation potential as defined by Eq. 56 in Sec. 2.2.7. For a single electron, where naturally no electron-electron interaction is present in the system, the Hxc potential as defined in Eq. 210 does not vanish,  $v_{\text{Hxc}} \neq 0$ , since in general

$$\langle \Phi_s(t) | [\hat{\mathbf{J}}, \hat{T}_e] | \Phi_s(t) \rangle - \langle \Psi(t) | [\hat{\mathbf{J}}, \hat{T}_e] | \Psi(t) \rangle \neq 0,$$

due to different kinetic energy contributions between the interacting system and the Kohn-Sham system. Nevertheless, we define the Hartree contribution in  $v_{\text{Hxc}}$  as in Eq. 55 for purely electronic problems. To derive the mean-field approximation to Eq. 211, we replace the correlated many-body state  $|\Psi(t)\rangle$  by the Kohn-Sham state  $|\Phi_s(t)\rangle$  and insert the projector  $|\Phi_s(t)\rangle \langle \Phi_s(t)|$ . We end up with the time-dependent expectation values  $n(\mathbf{r}, t)$ ,  $\mathbf{R}(t)$ , and  $q_\alpha(t)$  instead of the operators  $\hat{n}(\mathbf{r})$ ,  $\mathbf{R}$ , and  $\hat{q}_\alpha$ . Using this procedure, we obtain for the mean-field potential

$$v_M(\mathbf{r}, t) = \sum_{\alpha=1}^{n_m} (\lambda_\alpha \cdot \mathbf{R}(t) - \omega_\alpha q_\alpha(t)) \lambda_\alpha \cdot \mathbf{r}. \quad (212)$$

Furthermore, we can insert  $q_\alpha(t)$  directly using Eq. 197

$$v_M(\mathbf{r}, t) = \sum_{\alpha=1}^{n_m} \left\{ \lambda_\alpha \cdot \mathbf{R}(t) + \frac{1}{\omega_\alpha} \int_{t_0}^t dt' \sin(\omega_\alpha(t-t')) \dot{j}_s^{(\alpha)}(t') - \omega_\alpha q_\alpha(t_0) \cos(\omega_\alpha t) - \dot{q}_\alpha(t_0) \sin(\omega_\alpha t) \right\} \lambda_\alpha \cdot \mathbf{r}. \quad (213)$$

Because in Eq. 213 only electronic operators are present, this reformulation allows us to perform QEDFT calculations by only employing an electronic Kohn-Sham system. This is sufficient, since we can then construct the photon displacement coordinates  $q_\alpha(t)$  using Eq. 197 and all photon observables (as well as the electronic observables) have a functional dependence on  $(n(\mathbf{r}, t), q_\alpha(t))$ .

## 5.5 NUMERICAL EXAMPLE FOR THE MODEL QEDFT

In this chapter, we explicitly perform the first numerical simulations in the framework of QEDFT. We apply the Jaynes-Cummings-Hubbard (JCH) model, introduced in Sec. 3.1.2, to demonstrate how a time-dependent QEDFT calculation can be setup. We further study the most obvious question in the QEDFT framework: Is it necessary to develop approximate exchange-correlation potentials for QEDFT, or is it already sufficient to neglect these contributions and treat the correlated electron-field interaction by a mean-field ansatz, which is effectively a classical approximation as the Maxwell-Schrödinger framework that is discussed Sec. 2.3.7. To assess this question, we analyze the quality of the mean-field approximation in the model system. We consider two different examples: In the first example, we choose a factorizable initial state, where the electron is localized on one of the two sites and the photon field is initially in vacuum. This setup corresponds to a true quantum limit, where the single electron interacts with a small number of photons. In this setup, we find regular Rabi oscillations. We further compare this setup in the weak- and the

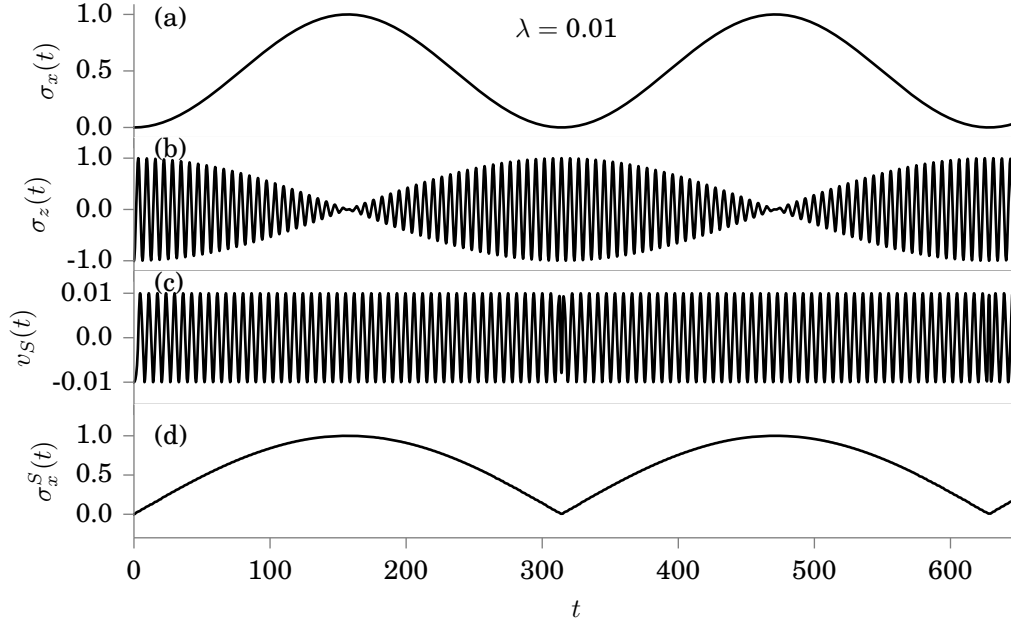


Figure 18: Exact results for the JCH Hamiltonian of Eq. 145 in the weak-coupling limit: (a) Population inversion  $\sigma_x(t)$ , (b) density  $\sigma_z(t)$ , (c) exact Kohn-Sham potential  $v_s(t)$ , and (d) Kohn-Sham population inversion  $\sigma_x^s(t)$ .

strong-coupling limit. In the second example, we choose again a factorizable initial state, where the electron populates the electronic excited state, while the field is in a coherent state with an average number of four photons in the field. Since coherent states are often seen as the *most classical* quantum states [75], we may naively expect only small effects of the exchange-correlation potential for this setup. This setup is in spirit of panel 3 in Fig. 4 of Ref. [93]. In this setup, we find the occurrence of collapses and revivals in the Rabi oscillations.

The theory developed in the previous sections can be directly applied to the Jaynes-Cummings-Hubbard Hamiltonian of Eq. 145. The numerical parameters in the calculation are chosen according to typical values in the literature:  $t_{\text{kin}} = 0.5$ ,  $\omega = 1$ ,  $\lambda = (0.01, 0.1)$ , while we set the external fields to zero  $j_{\text{ext}}(t) = v_{\text{ext}}(t) = 0$ . Here all values are given in atomic units. Since  $t_{\text{kin}} = \omega/2$ , the electronic excitation from the ground state  $|g\rangle$  to the excited state  $|e\rangle$  is in resonance to the field mode  $\omega$ . We can identify the two basic variables, which are the photon coordinate  $q(t) = \sqrt{1/2\omega} \langle \hat{a}^\dagger + \hat{a} \rangle$  and the difference in the electronic on-site density  $\sigma_z(t)$ . The latter is the basic variable in the JCH-model, since the electron density  $n(\mathbf{r}, t)$  has only two degrees of freedom on a two-site model, while one of these two degrees can be fixed by the normalization condition  $\int d\mathbf{r} n(\mathbf{r}, t) = 1$  in the case of single-electron problems. The Kohn-Sham system is given in analogy to Eq. 204-205 by

$$i\hbar\partial_t |x_s, t\rangle = (-t_{\text{kin}}\hat{\sigma}_x + v_s(t)\hat{\sigma}_z) |x_s, t\rangle, \quad (214)$$

$$i\hbar\partial_t |n_s, t\rangle = \frac{1}{2} [\hat{p}^2 + \omega^2 \hat{q}^2] |n_s, t\rangle + \frac{j_s(t)}{\omega} \hat{q} |n_s, t\rangle, \quad (215)$$

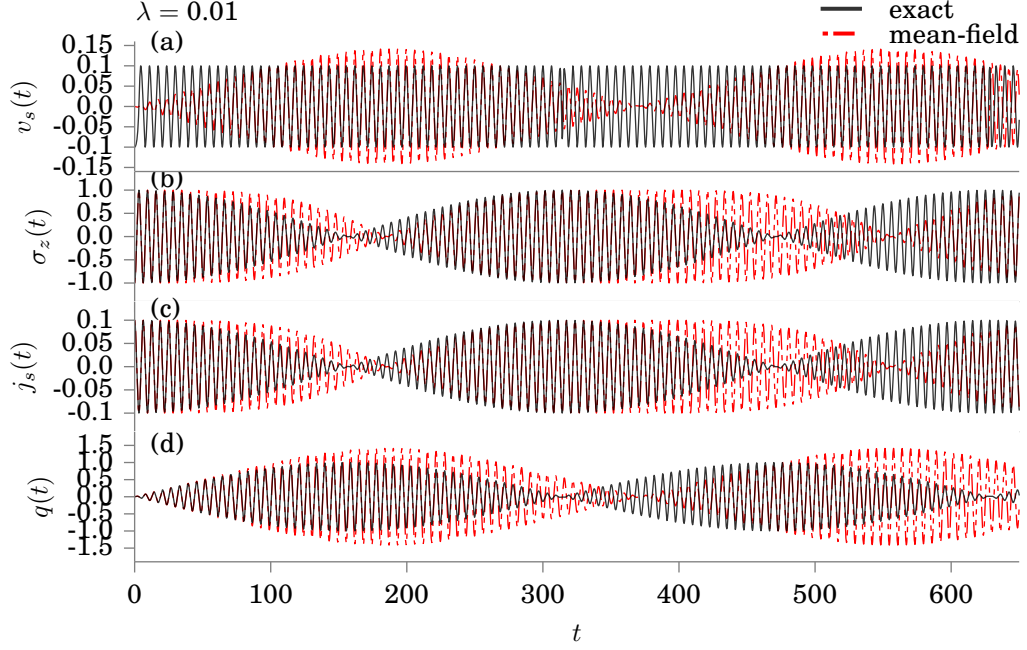


Figure 19: Exact potentials and densities (solid black line) compared to mean-field potentials and densities (dashed red line) in the case of regular Rabi oscillations in the weak-coupling limit  $\lambda = 0.01$ : (a) Kohn-Sham potential  $v_s(t)$  and (b) density  $\sigma_z(t)$ . (c) Kohn-Sham potential  $j_s(t)$  and (d) photon displacement coordinate  $q(t)$ .

with the Kohn-Sham potential  $v_s(t) = v_{\text{Mxc}}(t) + v_{\text{ext}}(t)$ , where the first part is the mean-field-exchange-correlation potential and the second part is the external potential. The wave function  $|x_s, t\rangle$  is defined on an electronic two-site basis with the basis functions  $|1\rangle$  and  $|2\rangle$ , where the electron is located on site 1, or 2, respectively. The photon wave function  $|n_s, t\rangle$  is defined on the photon number states.

In the first numerical example, we study the time evolution of a coupled many-body system and the corresponding uncoupled Kohn-Sham system. Both systems share the same initial state:  $|\Psi(t_0)\rangle = |\Phi(t_0)\rangle = |1\rangle \otimes |0\rangle$ .  $|1\rangle$  is an electronic state, where the electron populates one of the two sites, while  $|0\rangle$  refers to the vacuum photon state. The exact results of the propagation in the correlated many-body system are shown in Fig. 18. In panel (a) of Fig. 18, we plot the expectation value of  $\hat{\sigma}_x$  in time. This observable corresponds to the kinetic energy contribution in the JCH-model. However,  $\sigma_x$  is also known as the population inversion, since  $\sigma_x = [-1, 1]$  and the value  $\sigma_x = -1$  corresponds to the electron populating the excited state  $|e\rangle = \frac{1}{\sqrt{2}}(|1\rangle - |2\rangle)$ , while  $\sigma_x = 1$  corresponds to the electron populating the electronic ground state  $|g\rangle = \frac{1}{\sqrt{2}}(|1\rangle + |2\rangle)$ . For the initial state  $|1\rangle = (|g\rangle + |e\rangle)/\sqrt{2}$ , we find  $\sigma_x(t_0) = 0$ . From the population inversion, we observe regular Rabi oscillations between the values 0 and 1. In the weak-coupling limit, the frequency of these Rabi oscillations is connected to the electron-photon coupling strength  $\lambda$ . In panel (b), we also find regular Rabi oscillations for the density  $\sigma_z(t)$  as a slower oscillation in the envelope of the function. In addition, we observe a fast oscillation. The frequency of this oscillation corresponds to the electron kinetic energy. When

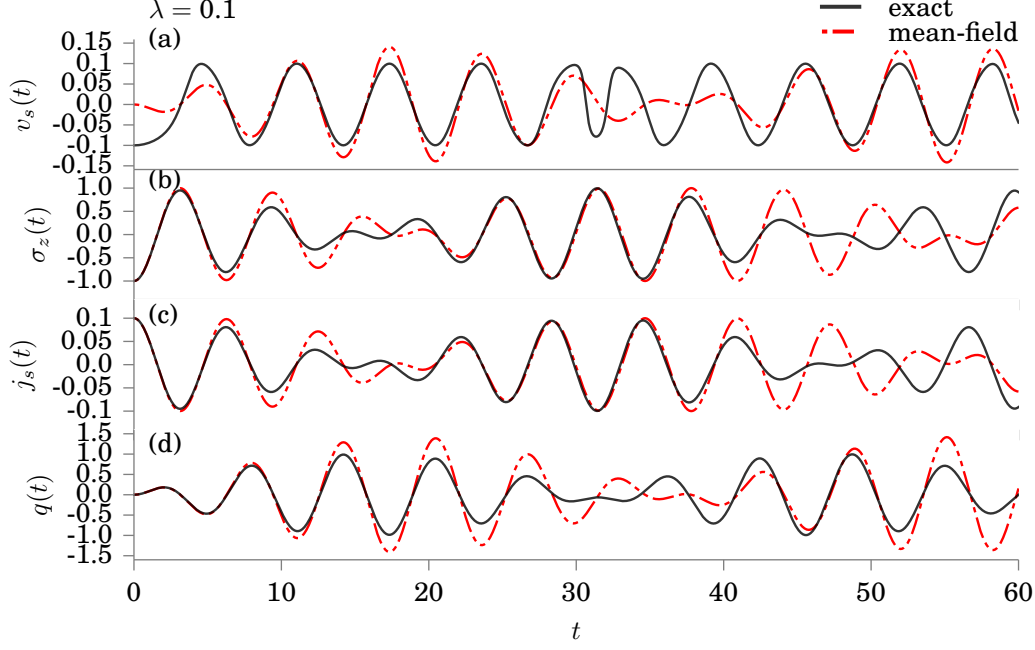


Figure 20: Exact potentials and densities (solid black line) compared to mean-field potentials and densities (dashed red line) in the case of regular Rabi oscillations in the strong-coupling limit  $\lambda = 0.1$ : (a) Kohn-Sham potential  $v_s(t)$  and (b) density  $\sigma_z(t)$ . (c) Kohn-Sham potential  $j_s(t)$  and (d) photon displacement coordinate  $q(t)$ .

the envelope function tends to zero, we observe the neck-like features typical for Rabi oscillations [133]. Having the exact density  $\sigma_z(t)$  at hand, we can perform an explicit fixed-point construction of the exact Kohn-Sham potential  $v_s$  as explained in Sec. 3.2.8.1. For the two-site JCH model, an analytic inversion formula [134, 135] exists, which we use to test the accuracy of the fixed-point method. The exact inversion formula is given by

$$v_s(t) = \pm \frac{\ddot{\sigma}_z(t) + 4t_0^2 \sigma_z(t)}{2\sqrt{4t_0^2 (1 - \sigma_z(t))^2 - \ddot{\sigma}_z(t)}}, \quad (216)$$

where the choice of the sign  $\pm$  depends on the initial state [135]. However in general, the analytic form of the inversion formula is unknown, while the fixed-point construction is a more general method. We plot the corresponding  $v_s$  in panel (c) of Fig. 18. Here again, we find fast oscillations in  $v_s$ . Having the exact  $v_s$  at hand, we perform an explicit Kohn-Sham propagation of the systems in Eq. 214–215. By construction this KS system leads to the same density as the many-body system shown in (b), but leads to a different Kohn-Sham population inversion  $\sigma_x^s(t) = \langle \Phi(t) | \sigma_x | \Phi(t) \rangle$  shown in (d). The exact interacting population inversion  $\sigma_x(t) = \langle \Psi(t) | \sigma_x | \Psi(t) \rangle$  is a functional of the electron density  $\sigma_z(t)$ , the interacting initial state  $\Psi(t_0)$ , and the Kohn-Sham initial state  $\Phi(t_0)$ .

In real KS calculations, the exact KS potential remains unknown. Thus, we have to rely on approximations for the exchange-correlation potential. As a first approxi-

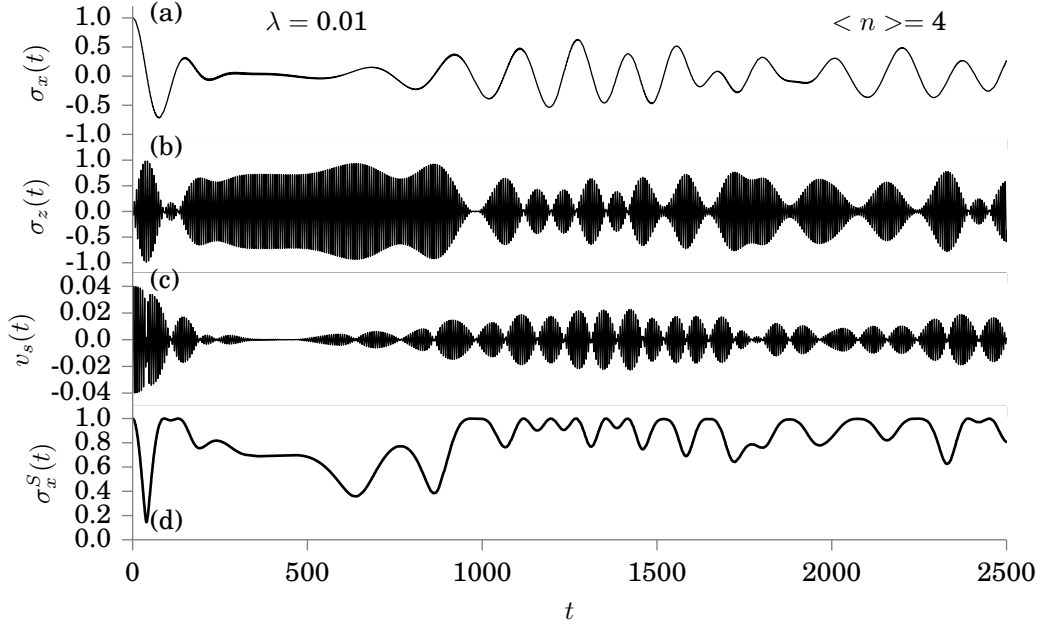


Figure 21: Exact results for the JCH Hamiltonian in the weak-coupling limit: (a) Population inversion  $\sigma_x(t)$ , (b) density  $\sigma_z(t)$  and (c) exact Kohn-Sham potential  $a_{\text{KS}}(t)$ , and (d) the Kohn-Sham population inversion  $\sigma_x^S(t)$  in the case of a coherent initial state (the setup is in spirit of panel 3 in Fig. 4 in Ref. [93])

mation we can regard the mean-field approximation. From Eq. 212, we can derive for the JCH model the simple expression

$$v_M(t) = \lambda \sqrt{2\omega} q(t). \quad (217)$$

In the mean-field approximation, we completely neglect any exchange-correlation contribution to  $v_{\text{Mxc}}$ . For the JCH model, this approximation is related to a coupled Maxwell-Schrödinger propagation (Eq. 75-78) discussed in Sec. 2.3.7. For the JCH model, we expect the mean-field approximation to become exact in the limits  $\lambda \rightarrow 0$  and  $\lambda \rightarrow \infty$ .

In Fig. 19 and Fig. 20, we assess the quality of the mean-field approximation in the weak and strong-coupling limit. Here, the exact densities and exact Kohn-Sham potentials shown in black are compared to mean-field densities and mean-field potentials shown in red, which were calculated in a self-consistent mean-field propagation. Already in the weak-coupling limit shown in Fig. 19, we find large differences. The mean-field potentials in panel (a) and (c) are qualitatively different compared to the exact Kohn-Sham potentials in this resonant setup. Already at the initial time, the exact  $v_s(t_0) \neq v_M(t_0)$ . This difference is then also inherited by the density observables  $\sigma_z(t)$  shown in panel (b) and  $q(t)$  shown in panel (d), causing a difference in the oscillation frequency. Here, the mean-field density oscillates slower than the exact density. The strong-coupling limit is shown in Fig. 20. In this limit, the dynamics show features beyond the rotating-wave approximation. Here, we observe a nonregular feature in the exact Kohn-Sham potential around  $t = 30$ . This feature is not captured by  $v_M(t)$ .



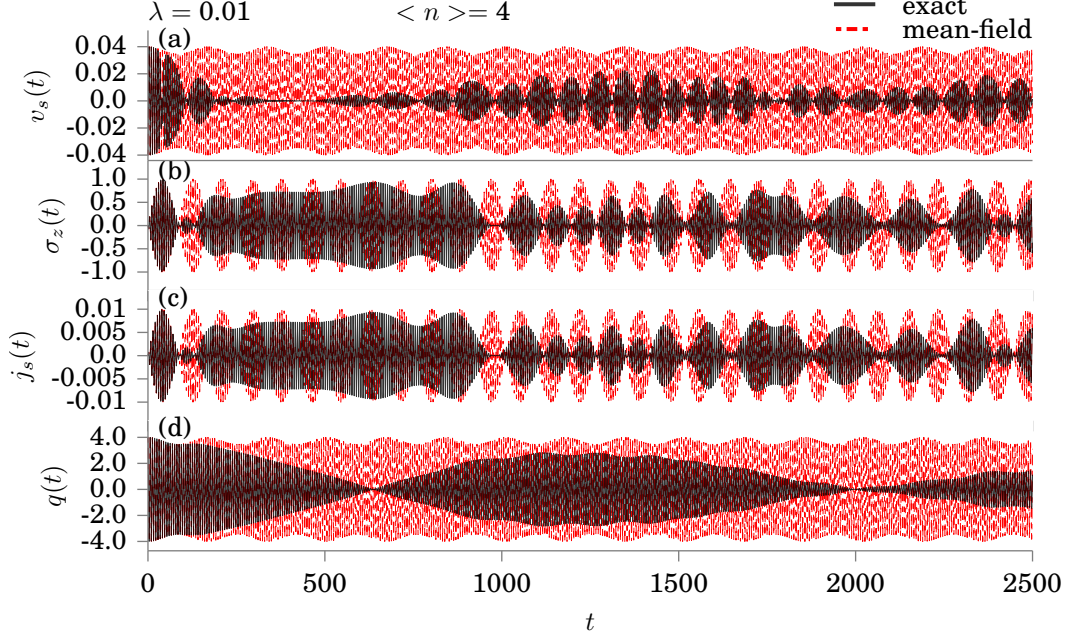


Figure 22: Exact densities and potentials (solid black line) compared to mean-field densities and potentials (dashed red line) in the case of a coherent initial state: (a) Kohn-Sham potential  $v_s(t)$  and (b) density  $\sigma_z(t)$ . (c) Kohn-Sham potential  $j_s(t)$  and (d) density  $q(t)$ .

In the second example, we again choose a factorizable initial state, which consists of the electronic ground state  $|g\rangle$  and a coherent photon state with mean-photon occupation of 4. This example is in the spirit of the calculation in panel 3 shown in Ref. [93]. In our case, we use the following initial states

$$|\Psi_0\rangle = |\Phi_0\rangle = |g\rangle \otimes |\alpha\rangle. \quad (218)$$

For the Kohn-Sham initial state, we choose the exact many-body initial state. Coherent states [136, 137] in single field modes can be written as

$$|a\rangle = \sum_{n=0}^{\infty} f_n(\alpha) |n\rangle, \quad \text{with} \quad f_n(\alpha) = \frac{\alpha^n}{\sqrt{n!}} \exp\left(-\frac{1}{2}|\alpha|^2\right), \quad (219)$$

where  $f_n(\alpha)$  is a Poisson distribution, and in our example  $\alpha^2 = 4$ . Thus, for the initial states, we have  $\langle\Psi(t_0)|\hat{a}^\dagger\hat{a}|\Psi(t_0)\rangle = \langle\Phi(t_0)|\hat{a}^\dagger\hat{a}|\Phi(t_0)\rangle = 4$ . In Fig. 21, we show the exact many-body results in the weak-coupling limit with  $\lambda = 0.01$ . In this example, we find that the population inversion  $\sigma_x(t)$  in panel (a) oscillates with a slower frequency compared to the density  $\sigma_z(t)$  in panel (b). In panel (a), we find the Jaynes-Cummings collapse of Rabi oscillations at  $t = 250$ , which is followed by a quiescence of the oscillation up to  $t = 500$ . After  $t = 800$ , we find the revivals of the Rabi oscillations. In contrast, the density  $\sigma_z(t)$  oscillates rather rapidly during the quiescence time. Therefore, we can conclude that during the quiescence in the population inversion, the system is not at rest, as it may seem from panel (a), but there are dramatic changes in the density  $\sigma_z(t)$ . The exact KS potential is shown in panel (c). It can be used to construct the exact density using a Kohn-Sham scheme.

In panel (d), we find that the Kohn-Sham population inversion  $\sigma_x^s(t)$  is again different to the exact population inversion  $\sigma_x(t)$ . The exact results are contrasted to the mean-field results in Fig. 22. We find that for long propagations of times up to  $t = 2500$ , the mean-field approximation is not a very accurate approximation to the exact dynamics. This means that even in the limit, where the photon field is initially in a coherent state, which resembles a classical state in quantum mechanics, the mean-field approximation is not a sufficient approximation and more advanced approximations are needed to make more accurate predictions [138, 139].

## 5.6 SUMMARY

In this section, we showed the basic theory of QEDFT in the dipole coupling. We outlined the general theory and focused on the one-to-one correspondence between the set of internal variables and external variables. This correspondence can then be used to setup a Kohn-Sham scheme, which allows for numerically feasible calculations, if approximations for the meanfield-exchange-correlation (Mxc) potential are applied. As a first approximation, we considered explicitly the quality of the mean-field potential that resembles a Maxwell-Schrödinger propagation scheme. In all considered numerical examples in this section, we find that the classical description fails to treat the limit of low-photon numbers correctly. This indicates the need to develop more sophisticated approximations for the xc potential. One possibility here is the OEP method, which will be the focus of chapter 7.



In this chapter, we apply the framework of QEDFT discussed in Ch. 5 to a cavity-GaAs model system in real space, which consists of a trapped single electron coupled to a quantized electromagnetic field mode as discussed in Sec. 3.1.3. The setup is a resonant setup, since the cavity mode is tuned in resonance to the first electronic transition. This model enables us to study the real-space features of the exact Mxc potential in correlated electron-photon systems. To construct the full KS potential  $v_s(\mathbf{r}, t)$ , we use the fixed-point inversion scheme, which is discussed in Sec. 3.2.8.2. Comparing the exact KS potential to the corresponding mean-field potential  $v_M(\mathbf{r}, t)$  allows us to identify significant beyond mean-field features in  $v_s(\mathbf{r}, t)$  and assess in which situations we may expect them to occur. As in the case of charge-transfer processes in traditional TDDFT [141, 142], we find also for the case of correlated electron-photon interactions peak and step structures in  $v_s(\mathbf{r}, t)$ , which depend nonlocally in time and space on the electron density. We observe rich peak and step structures, which can be accounted fully to the correlated light-matter interaction in its complete quantum-mechanical nature. These features are independent of the model and can be expected also for general electron-photon coupled situations.

This chapter is organized as follows: In the first part, we study the ground state of the cavity-GaAs model in the weak-coupling regime and the strong coupling regime and calculate the corresponding ground-state KS potential. Then, in the second part, we study three time-dependent examples with different initial states and the time-dependent KS potential. In the last part, we apply the Born-Oppenheimer framework originally developed for electron-nuclear problems as discussed in Sec. 2.1.2 to the cavity-GaAs model and calculate the emerging BO surfaces. We then use these surfaces to analyze the dynamics of the electron-photon system.

## 6.1 KOHN-SHAM SYSTEM OF THE CAVITY-GAAS MODEL

To construct the Kohn-Sham system of the cavity-GaAs model, we can directly apply Eqns. 204-205. Using the fixed-point iteration formula [110] of Eq. 177, we are able to construct the full KS potential. Since in this chapter, we treat a single-electron problem, we can consider the effect of the dipole self-energy  $v_{es} = \sum_{\alpha} (\lambda_{\alpha} \cdot \mathbf{r})^2 / 2$  emerging from Eq. 188 exactly. This means that in the Mxc potential only contributions from the explicit electron-photon interaction Hamiltonian  $\hat{H}_{\text{int}}$  of Eq. 187 remain. This allows us to define the full effective KS potential as:  $v_s(\mathbf{r}, t) = v_{\text{ext}}(\mathbf{r}) + v_{es}(\mathbf{r}) + v_{\text{Mxc}}(\mathbf{r}, t)$ . Since we treat the interaction in dipole coupling, we can work out the mean-field potential analytically as  $v_M(\mathbf{r}, t) = -\omega_{\alpha} q_{\alpha}(t) \lambda_{\alpha} \cdot \mathbf{r}$ , which corresponds to the well-known dipole-coupling term, if the field is treated classically. We furthermore attribute the effects of the

---

This chapter is based on the work reported in Flick et al. [140], which has been performed in close collaboration with all coauthors. I contributed to all aspects of the work.

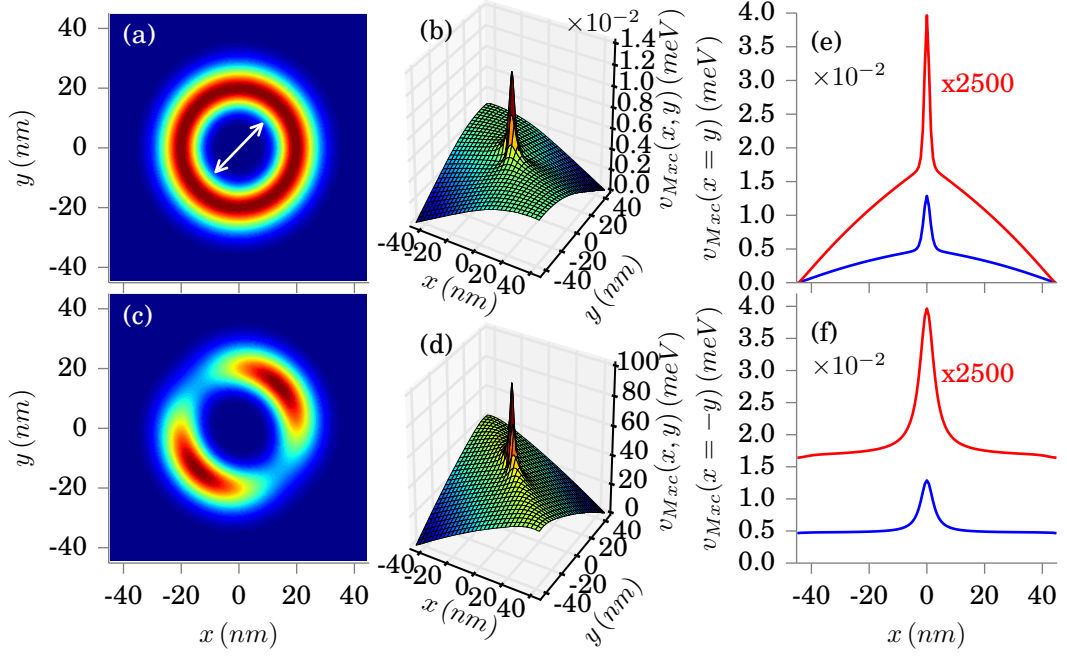


Figure 23: Panel (a) shows the ground-state density, and panel (b) the  $v_{\text{Mxc}}(\mathbf{r})$ , both in weak-coupling ( $\lambda_\alpha = 1.68 \cdot 10^{-3} \text{ meV}^{1/2}/\text{nm}$ ). Panel (c) shows the ground-state density, and panel (d)  $v_{\text{Mxc}}(\mathbf{r})$ , both in strong-coupling ( $\lambda_\alpha = 0.134 \text{ meV}^{1/2}/\text{nm}$ ), (e) diagonal and (f) antidiagonal cuts of  $v_{\text{Mxc}}(\mathbf{r})$  for weak coupling (blue) and strong coupling (red). The white arrow in (a) indicates the polarization direction of the photon mode.

difference of the Kohn-Sham electronic stress force operator and the correlated electronic stress force operator  $\mathbf{Q}^{(s)} - \mathbf{Q}$  in Eq. 210 to  $v_{\text{Mxc}}$ .

## 6.2 NUMERICAL RESULTS IN THE GROUND STATE

We start our discussion with the ground-state calculations for the cavity-GaAs model. The exact ground state is accessible using exact diagonalization as discussed in Sec. 3.2.5. The implemented fixed-point inversion scheme to obtain the exchange-correlation potential  $v_{\text{Mxc}}$  can be benchmarked in the static case by comparing against the exact inversion formula from Eq. 39. The ground-state results are shown in Fig. 23. In panel (a), we show the ground-state density in the case of weak coupling ( $\lambda_\alpha = 1.68 \cdot 10^{-3} \text{ meV}^{1/2}/\text{nm}$ ). We find a slight prolongation perpendicular to the polarization direction  $\epsilon_\alpha = (\mathbf{e}_x + \mathbf{e}_y)$  of the photon field. The polarization direction is indicated by the white arrow. In Fig. 23, we compare the density in the weak-coupling limit to the density in strong-coupling regime for  $\lambda_\alpha = 0.134 \text{ meV}^{1/2}/\text{nm}$ , which is shown in (c). When we approach the strong-coupling regime, we find a splitting of the ground-state electron density along the polarization direction of the photon mode. In the Kohn-Sham system, the prolongation and the splitting of the density has to be modeled by the Mxc potential. Therefore for  $v_{\text{Mxc}}(\mathbf{r})$ , we find in (b) for weak-coupling and (d) for strong-coupling a strong peak in the middle of the cavity, which becomes stronger for stronger  $\lambda_\alpha$ .

	weak coupling	strong coupling
$\lambda_\alpha$	$1.68 \cdot 10^{-3} \text{ meV}^{1/2}/\text{nm}$	$0.1342 \text{ meV}^{1/2}/\text{nm}$
$\langle \hat{a}_\alpha^\dagger \hat{a}_\alpha \rangle$	$1.18 \cdot 10^{-3}$	3.19
$\gamma$	0.999764	0.4919
$Q$	$3.88 \cdot 10^{-4}$	0.4567

Table 4: Ground-state properties of the cavity-GaAs model, photon occupancy  $\langle \hat{a}_\alpha^\dagger \hat{a}_\alpha \rangle$ , purity  $\gamma$  and Mandel  $Q$ -parameter.

In (e) and (f), we show diagonal and antidiagonal cuts through the  $M_{xc}$  potential. We find  $v_{M_{xc}}(\mathbf{r})$  three orders of magnitudes higher in the strong-coupling regime, than in the weak coupling regime, for the considered parameters. The strong peak in the middle of the cavity pushes the density apart and induces the splitting. It is not possible to generate such a charge splitting by a classical static field in the dipole coupling. Thus, already here we find important beyond mean-field contributions.

Next, we investigate the origin of the charge splitting in the strong-coupling regime. In Fig. 24, we plot the lowest six exact eigenenergies of the full correlated electron-photon system. For small coupling, we find that the ground-state energy is well separated from the energy of the first excited state. The ground-state density starts to split, when the ground-state energy comes close to the first excited-state energy. This is also illustrated in Fig. 25, where we plot different densities from the intermediate coupling regime ( $\lambda_\alpha = 0.0671 \text{ meV}^{1/2}/\text{nm}$ ) to the strong-coupling regime ( $\lambda_\alpha = 0.1342 \text{ meV}^{1/2}/\text{nm}$ ). In the strong-coupling regime the electron density changes dramatically. While in the weak-coupling regime the electron density is dominated by contributions, which can be associated with the ground-state density for the cavity-free case, we find in the strong-coupling regime that contributions, which are excited state densities in the cavity-free case become dominant contributions to the electronic ground-state density. These contributions cause the splitting. The excited-state energies in Fig. 24 are also worth analyzing. We find for  $\lambda_\alpha = 0$  a three-fold degeneracy in the first-excited state. This degeneracy is due to the two-dimensionality of the electronic problem and the additional dimensionality introduced by the photon mode. The lower polariton branch (blue) reduces its energy until it merges with the ground-state energy in the strong-coupling regime. Besides the eigenenergies and the densities, we also calculated the photon-number expectation value  $\langle \hat{a}_\alpha^\dagger \hat{a}_\alpha \rangle$ , the purity  $\gamma$  and the Mandel  $Q$ -parameter of the interacting problem. The results are shown in Tab. 4. While we find a very low photon occupation in the ground state for the weak-coupling, which is  $1.18 \cdot 10^{-3}$ , we observe in the strong coupling a significant number of photons, i.e. 3.19. The purity  $\gamma = \text{Tr}(\rho_{\text{ph}}^2)$  is a typical measure for the correlation in the system. Using the purity, we can quantify the electron-photon correlation. A value  $\gamma \sim 1$  indicates a system, which is close to a factorizable system, while a stronger deviation from 1 indicates a system, which is nonseparable [143]. In the weak-coupling, we find  $\gamma = 0.999764$ , while in the strong-coupling, we find  $\gamma = 0.4567$ . This strong deviation from the value 1 indicates a high electron-photon correlation in the ground state for strong-

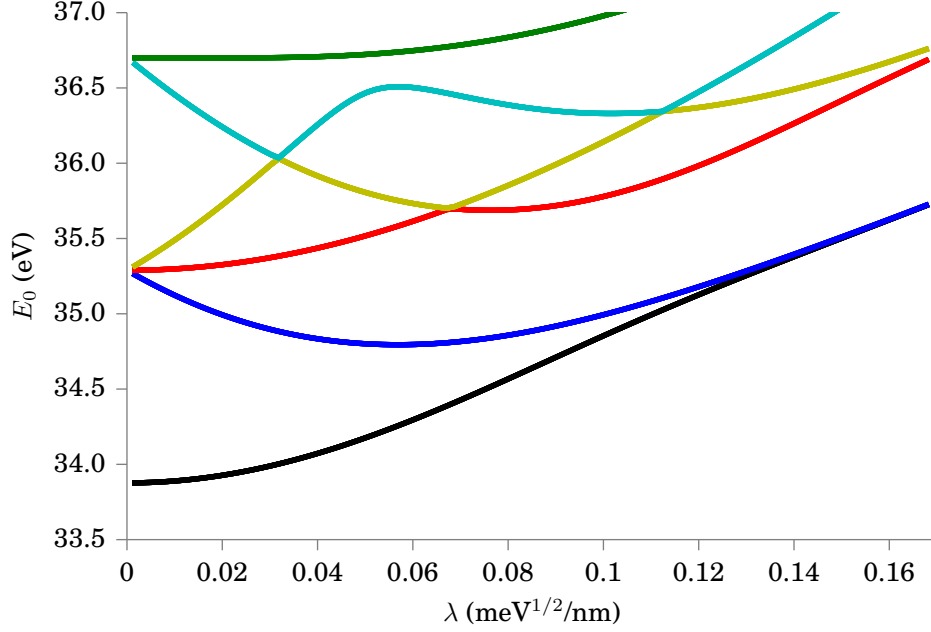


Figure 24: Exact ground-state (black) and excited-state energies (blue, red, yellow, cyan, and green) for the six lowest states in the correlated electron-photon problem for the cavity-GaAs model.

coupling. A second parameter, which we evaluate is the Mandel  $Q$  parameter [144]. It is defined by

$$Q = \frac{\langle \hat{a}_\alpha^\dagger \hat{a}_\alpha^\dagger \hat{a}_\alpha \hat{a}_\alpha \rangle - \langle \hat{a}_\alpha^\dagger \hat{a}_\alpha \rangle^2}{\langle \hat{a}_\alpha^\dagger \hat{a}_\alpha \rangle} \quad (220)$$

and measures the deviation of the field distribution from the Poisson distribution. A value  $Q = 0$  corresponds to the Poisson distribution, hence a classical light field. In coherent pulses, photons reach the detector in random intervals.  $Q > 0$  corresponds to photon bunching, which means that photons reach the detector in bundles. Formulated differently, if the detector detects a photon, then it is highly probable that a second photon will be detected shortly afterwards. Thermal sources, such as black body radiation emit bunched light. In contrast,  $Q < 0$  corresponds to the nonclassical behavior of photons and is referred to as antibunching. Here, photons reach the detector in intervals, which are larger than the random intervals of coherent light. We find for the weak-coupling  $Q = 3.88 \cdot 10^{-4}$  and for the strong-coupling  $Q = 0.4567$ . In particular in the strong-coupling regime, we observe strong electron-photon correlation and a strong deviation of the photon field from a coherent distribution. Additionally, in the weak- as well as in the strong-coupling regime, we find peaks in the  $M_{xc}$  potential, which become more dominant for stronger coupling. This peak leads to a split in the electron density for the ground state in the strong coupling regime.

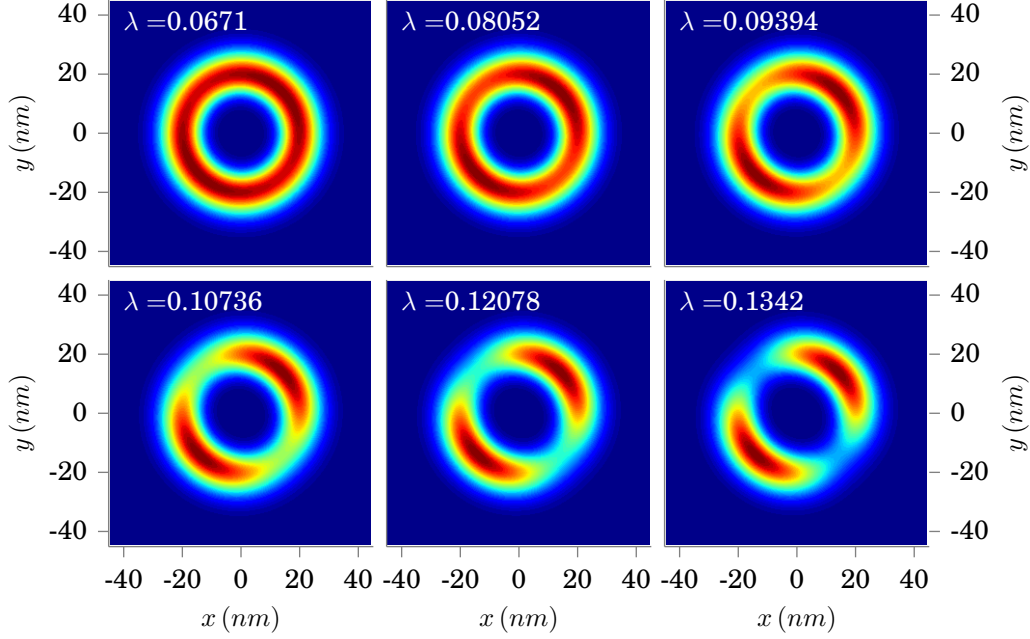


Figure 25: Transition of the ground-state density from the intermediate coupling regime ( $\lambda_\alpha = 0.0671 \text{ meV}^{1/2}/\text{nm}$ ) to the strong-coupling regime ( $\lambda_\alpha = 0.1342 \text{ meV}^{1/2}/\text{nm}$ ).

### 6.3 TIME-DEPENDENT RESULTS USING DIFFERENT INITIAL STATES

In this section, we consider the time-dependent situation to assess the dynamical features present in the time-dependent  $v_{\text{Mxc}}(\mathbf{r}, t)$ . As initial states, we choose three different examples: In the first example (i), we use a factorizable initial state, which consists of the electronic ground state  $|g\rangle$  and a coherent field state. The coherent state of the photon field has initially  $\langle \hat{a}_\alpha^\dagger \hat{a}_\alpha \rangle = 4$ . The second example (ii) considers also a factorizable state, which consists of the electronic ground state  $|g\rangle$  and for the field state, we pick a linear superposition between the vacuum and the one-photon state:  $1/\sqrt{2}(|0\rangle + |1\rangle)$ , thus  $\langle \hat{a}_\alpha^\dagger \hat{a}_\alpha \rangle = 0.5$ . In the third example (iii), we choose a nonfactorizable initial state, namely the correlated electron-photon ground state obtained as discussed in Sec. 6.2. This state is then additionally driven by an external classical laser field. For all three initial state, we choose the electron-photon coupling strength in the weak-coupling regime,  $\lambda_\alpha = 3.36 \cdot 10^{-3} \text{ meV}^{1/2}/\text{nm}$ . All examples are propagated using the Lanczos propagator with (i) 160000, (ii) 360000, and (iii) 20000 time steps with a time step of  $\Delta t = 0.146 \text{ fs}$ . We start our discussion with the first example. Since the initial state is a factorizable state, we choose the Kohn-Sham initial state to be the electronic part of the exact many-body initial state. The results are shown in Fig. 26 and Fig. 27. In Fig. 26 (a), we show the time evolution of the dipole moment  $\epsilon_\alpha \cdot \mathbf{r} = \langle x + y \rangle$ . The mean-field results are shown in red, while the exact results are shown in black. Since the photon field is initially in a coherent state, the dipole moment in the mean-field propagation is for small times, between 0 ps and 6 ps, very close the exact propagation. The dipole moment starts to deviate after  $t = 6 \text{ ps}$ .

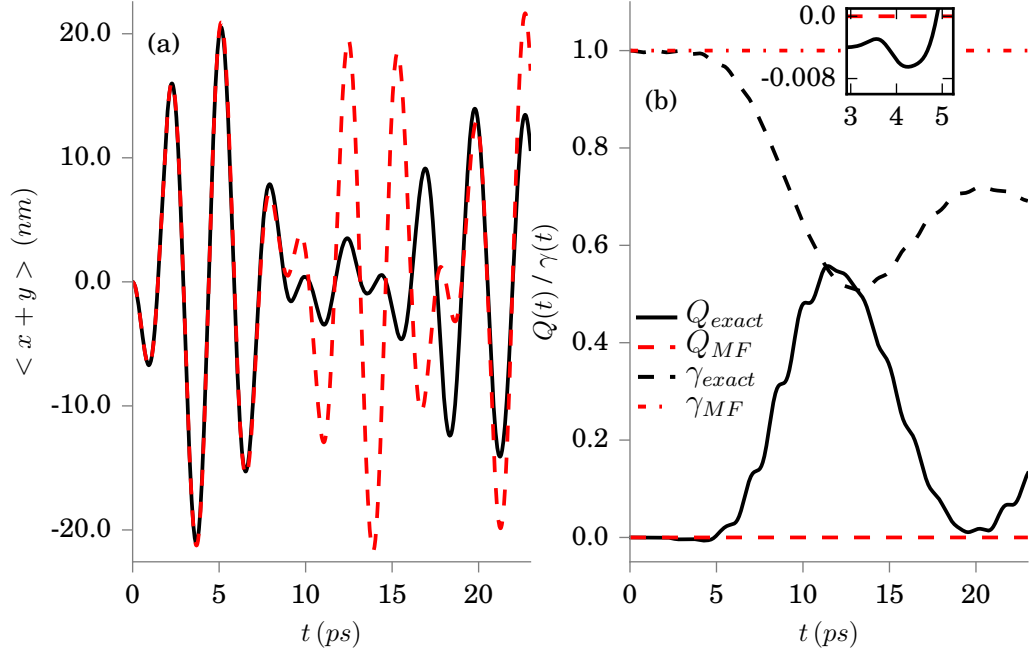


Figure 26: Dynamics of the correlated electron-photon system. Coherent state as initial state for the photon mode: (a) Exact (black) vs. mean field (red) dipole moment  $\langle x(t) + y(t) \rangle$ , (b) Mandel  $Q(t)$  exact (solid black) vs. mean field (dashed red) and purity  $\gamma$  exact (dashed black) vs. mean field (dashed-dotted red). The inset in panel (b) shows  $Q_{exact}(t)$  and  $Q_{MF}(t)$  between 3 ps and 5 ps.

In Fig. 26 (b), we compare the Mandel  $Q$  parameter and the purity  $\gamma$ . As in panel (a), until  $t = 6$  ps, we find that both the purity  $\gamma$  and the Mandel  $Q$  parameter show good agreement between the mean field and the exact propagation. After  $t > 6$  ps, the mean-field results start to deviate drastically from the exact solution. In the case of the Mandel  $Q$  parameter, we find the Kohn-Sham photon field by construction staying in a coherent field  $Q_{MF}(t) = 0$ , while the exact  $Q(t) < 0$  for  $t$  up to  $t = 6$  ps, which indicates nonclassical behavior in the photon field. This is shown in the inset of Fig. 28 (b). After  $t = 6$  ps, the Mandel parameter turns positive, indicating photon bunching and the purity  $\gamma$  deviates strongly from 1, which means that the exact propagation is after that time in a nonfactorizable state. After this time, we can expect beyond mean-field contributions in the  $M_{xc}$  potential, since larger features may be necessary in the  $KS$  potential to correctly reproduce the correlated many-body density  $n(\mathbf{r}, t)$  by the auxiliary noninteracting  $KS$  system. At these times, memory effects become dominant and peaks and steps appear in the Kohn-Sham potential  $v_{Mxc}$ . For the first example, we plot the  $M_{xc}$  potential, the diagonal cuts through  $v_{Mxc}$  and the corresponding density for four different time ( $t = 0, 3.67, 4.53, 7.29$  ps) in Fig. 27. We find that for time  $t < 6$  ps the mean-field contribution is the dominant contribution to  $v_{Mxc}$ , as can be seen in Fig. 27 (a). Nevertheless already in this time-interval, we find large beyond mean-field contributions at the turning points of the time evolution of the dipole moment. At these times, we find several steps and peaks, as shown in Fig. 27 (d) and (g) which can be attributed to the nonclassical electron-photon interaction. After the time



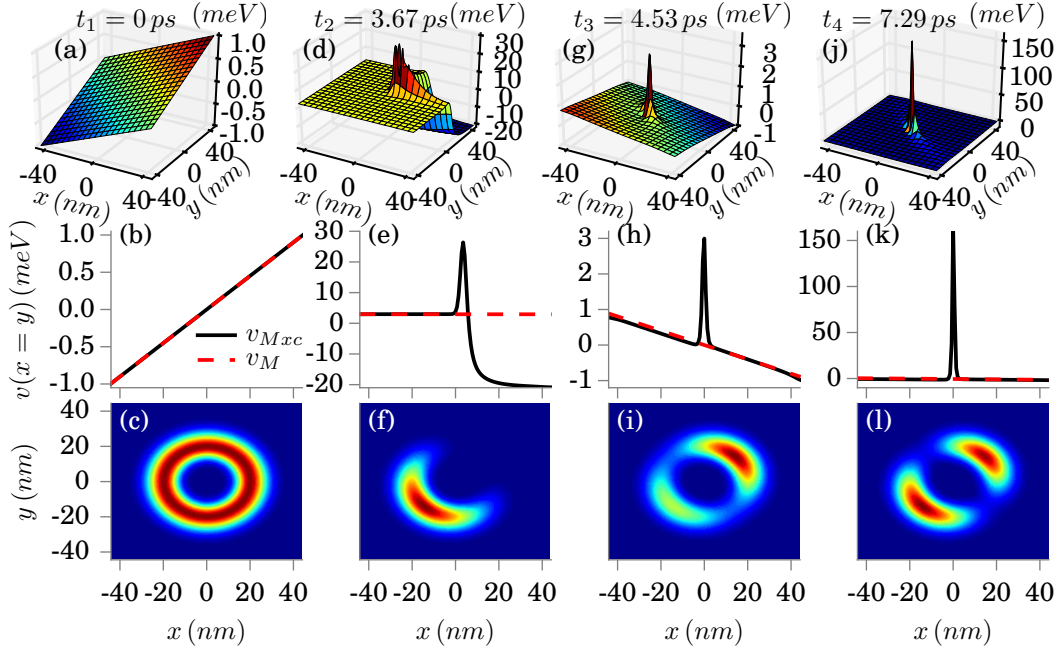


Figure 27: Dynamics of the correlated electron-photon system. Coherent state as initial state for the photon mode: In (a), (d), (g) and (j),  $M_{xc}$  potential at  $t = 0, 3.67, 4.53, 7.29$  ps with the corresponding diagonal cuts in (b),(e),(h),(k) and the corresponding time evolution of the electron density in (c),(f),(i),(l).

$t = 6$  ps, the beyond mean-field contributions become the dominant contributions and a nonvanishing peak in the center of the cavity appears as shown in Fig. 27 (j). The diagonal of the  $KS$  potential is shown in Fig. 27 (b), (e), (h), and (k). These beyond mean-field contributions are then also responsible for the deviation in the observables of the mean-field propagation compared to the exact propagation. In Fig. 27 (c), (f), (i), and (l), we show the time evolution of the exact density and identify oscillating charge transfer processes between the lower left and the upper right section (Fig. 27 (f) and (i)). Next, we analyze the second example. Here, we choose again a factorizable initial state. It consists of the electronic ground state and for the photon field of a superposition of the lowest two Fock number states (vacuum and one-photon state). The time-dependent results are shown in Fig. 28 and Fig. 29. In Fig. 28 (a), we compare the dipole moment of the exact propagation to the mean-field propagation. While in the first example, we choose a coherent state, which resembles a classical state in the quantum limit, we find that in this example for small time, i.e.  $t = 0$  ps to  $t = 2$  ps, also the mean-field approximation is reliable. In this time interval in the exact  $v_{Mxc}$ , the mean-field contribution is the dominant contribution (Fig. 29 (a)). In this example, we find after the first turning point in the dipole moment a peak appearing in the  $M_{xc}$  potential shown in Fig. 29 (d). This peak persists in the following time evolution and causes deviations in the dipole moment. We find that the mean-field dipole moment significantly differs from the exact dipole moment, i.e. the mean-field dipole moment has a lower amplitude compared to the exact dipole moment at  $t \sim 20$  ps. Later in time, we find peaks and steps appearing in  $v_{Mxc}$  shown in Fig. 29 (g) and (j), which have a high

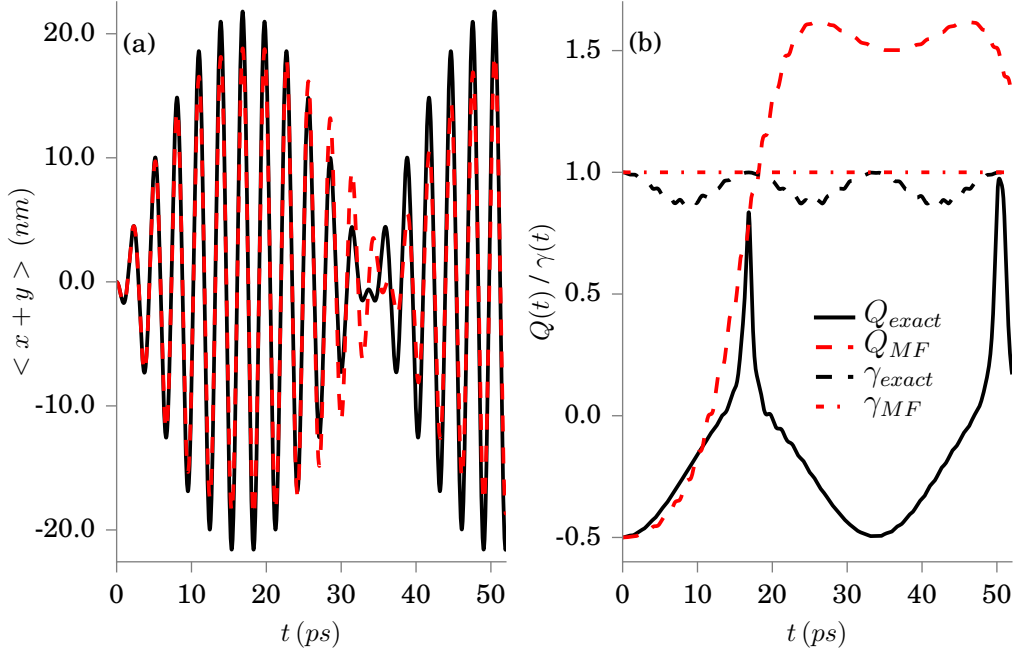


Figure 28: Dynamics of the correlated electron-photon system. Superposition of two Fock number states as initial state for the photon mode: (a) Exact (black) vs. mean field (red) dipole moment  $\langle x(t) + y(t) \rangle$ , (b) Mandel  $Q(t)$  exact (solid black) vs. mean field (dashed red) and purity  $\gamma$  exact (dashed black) vs. mean field (dashed-dotted red).

amplitude. The peak and step structure of the KS potential becomes clearly visible in the diagonal cuts in Fig. 29 (b), (e), (h), (k). In Fig. 28 (b), we compare the Mandel  $Q(t)$  parameter and the purity  $\gamma$  in the exact with the mean-field propagation. After  $t = 2$  ps, both parameters show the breakdown of the mean-field description. The purity indicates an oscillation between a factorizable and a nonfactorizable system, since it oscillates between 1 and 0.8 and the Mandel  $Q$  parameter shows strong nonclassical behavior in the field mode. The density shown in Fig. 29 (c), (f), (i), (l)) shows oscillations.

In the last example, we choose the initial state to be a nonfactorizable state and pick the correlated ground state of the electron photon system as initial state in the exact propagation. For the Kohn-Sham system, we choose an initial state, which is consistent with the initial conditions as discussed in Sec. 6.1. Since we only treat a single electron problem, we can use the exact correlated ground-state density  $n_0(\mathbf{r})$  to calculate the necessary initial state for the Kohn-Sham system as follows

$$\Psi_s(\mathbf{r}, t_0) = \sqrt{n_0(\mathbf{r})}. \quad (221)$$

The system is then driven by an external laser field of the form  $v_L(\mathbf{r}t) = \mathbf{E}(t) \cdot \mathbf{r}$ , which is added to the Hamiltonian. For the electric field amplitude, we choose  $E(t) = E_0 \exp(-(t - t_0)^2/\sigma^2) \sin(\omega t)$  and further choose the following parameters  $t_0 = 0.29$  ps,  $\sigma = 0.058$  ps,  $\hbar\omega = 1.41$  meV and  $E_0 = 0.23$  meV/nm. The results of the time propagation are shown in Fig. 30 and Fig. 31. Overall, we find for this example, that the mean-field propagation performs quite well. In Fig. 30 (a), we



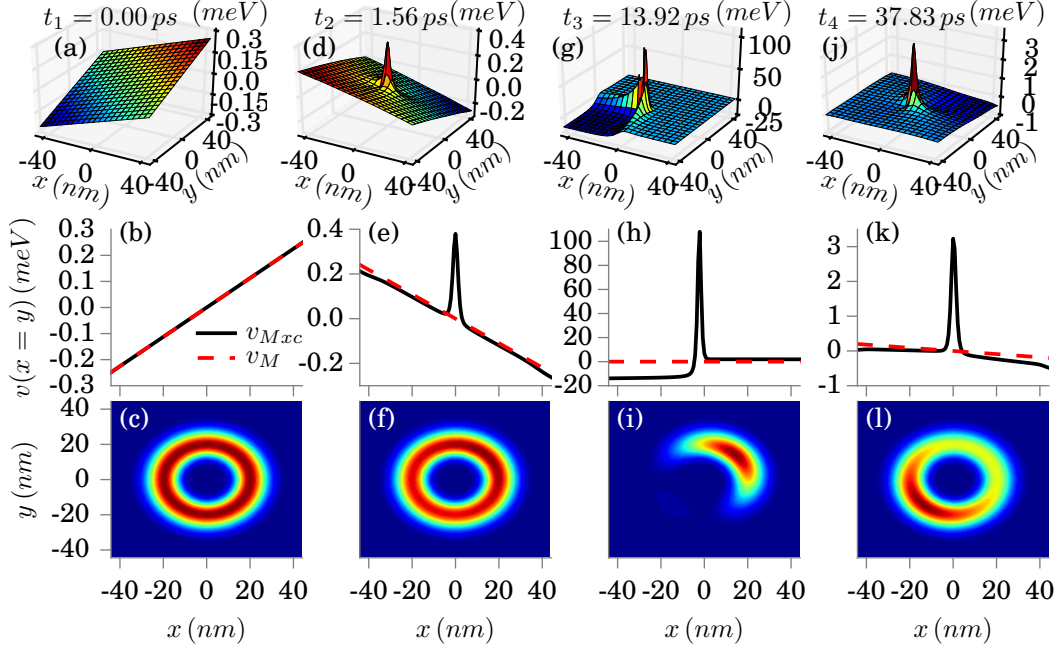


Figure 29: Dynamics of the correlated electron-photon system. Superposition of two Fock number states as initial state for the photon mode: In (a), (d), (g) and (j), Mxc potential at  $t = 0, 1.56, 13.92, 37.83$  ps with the corresponding diagonal cuts in (b),(e),(h),(k) and the corresponding time evolution of the electron density in (c), (f), (i), (l).

show the laser pulse applied to the system. It has its highest amplitude at  $t = 0.3$  ps. In Fig. 30 (b), we compare the mean field to the exact dipole moment. Both agree well. The projections on the electronic eigenstates are shown in Fig. 30 (c). We see dominantly an excitation through the external laser pulse from the ground state to the first-excited state. In Fig. 30 (d) the Mandel  $Q(t)$  and the purity  $\gamma$  are shown. We find for this example that the system remains close to a factorizable system and no large contributions to nonclassical behavior is found in the field mode. The dynamics of the system is mainly driven by the external laser pulse. Although we find beyond mean-field contributions in the KS potential (Fig. 31 (a), (c), (e)), these contributions are rather small compared to the applied external field. The external field drives the density (Fig. 31 (b), (d), (f)) back and forth.

#### 6.4 INTERPRETATION OF THE PEAK AND STEP STRUCTURES IN QEDFT

The nature of the peaks and steps found in this chapter for correlated electron-photon problems in the ground state and time-dependent cases is reminiscent of peaks and steps, which were also found in electron DFT [42]. For the ground-state KS potential it was shown that in the dissociation limit of molecules a peak appears between two atoms, originating from the kinetic correlation term to counterbalance the electronic Coulomb interaction [145]. A step in the KS potential is found, if different ionization potentials between the individual fragments occur. The value of this step is such that it adjusts these two potentials [42]. In TDDFT, dynamical

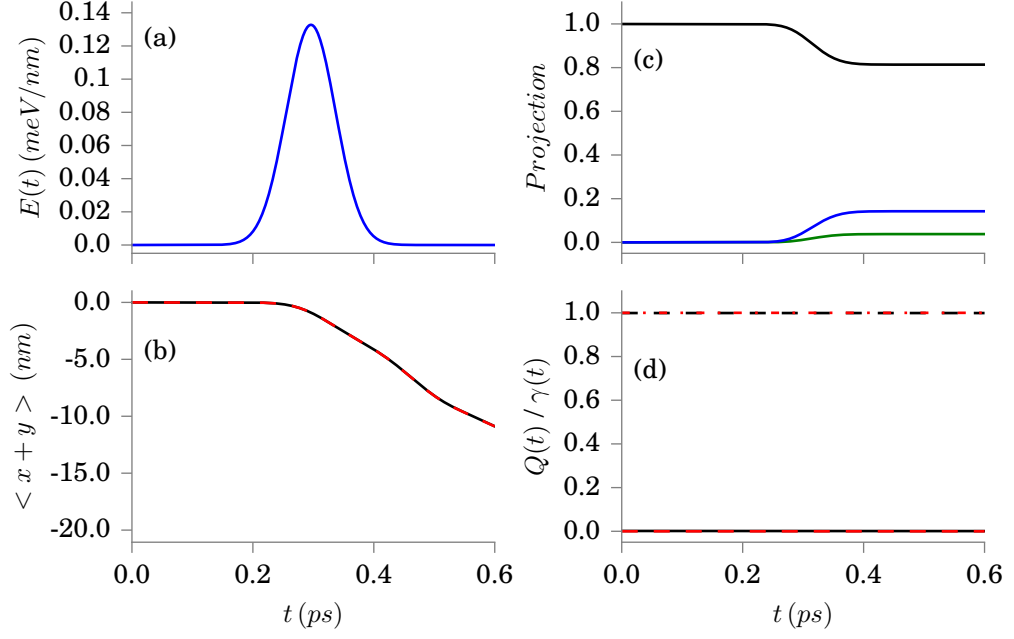


Figure 30: Dynamics of a correlated electron-photon system with nonfactorizable initial state and driven by an external laser pulse: Initially the system populates the combined electron-photon ground state. (a) shows the electric field of the applied external laser pulse, (b) shows the exact (black) and classical (red) dipole moment. (c) shows the projections of the time-dependent wave function on the first three electronic eigenstates. (d) shows the evolution of the Mandel  $Q(t)$  parameter and purity  $\gamma$  for exact (black) and classical approximation (red).

cal steps and peaks occur in nonequilibrium dynamical situations [141], such as charge transfer [142], and are missed by even the exact adiabatic approximation. In Ref. [146] it was shown that in TDDFT the kinetic contribution is often but not always responsible for these peak and step structures and for the ground state, it is shown that step and peak structures appear, whenever more than one determinant is necessary to describe the interacting many-body state.

We can in particular connect to standard electron DFT using the latter reasoning. Also in the time-dependent cases for electron-photon interactions presented in this chapter, we find that peaks and steps are arising, if the purity  $\gamma$  deviates from 1. A value of 1 indicates a factorizable system, which can be factorized into an electronic and a photonic wave function. If  $\gamma$  deviates from 1, then we need more than only a single factorizable state to correctly describe the interacting system. In these cases also the KS potential acquires a peak (and step) structure. Whether this structure originates from kinetic contributions or from contributions, which are explicitly from the electron-photon interaction could be explored in a future work. Since we use the fixed-point algorithm as presented in Eq. 177, the current implementation can not distinguish which individual part of Eq. 198 is responsible for the peak and step structure in the KS potential. However, this identification can be done in principle by using the exact many-body wave function.

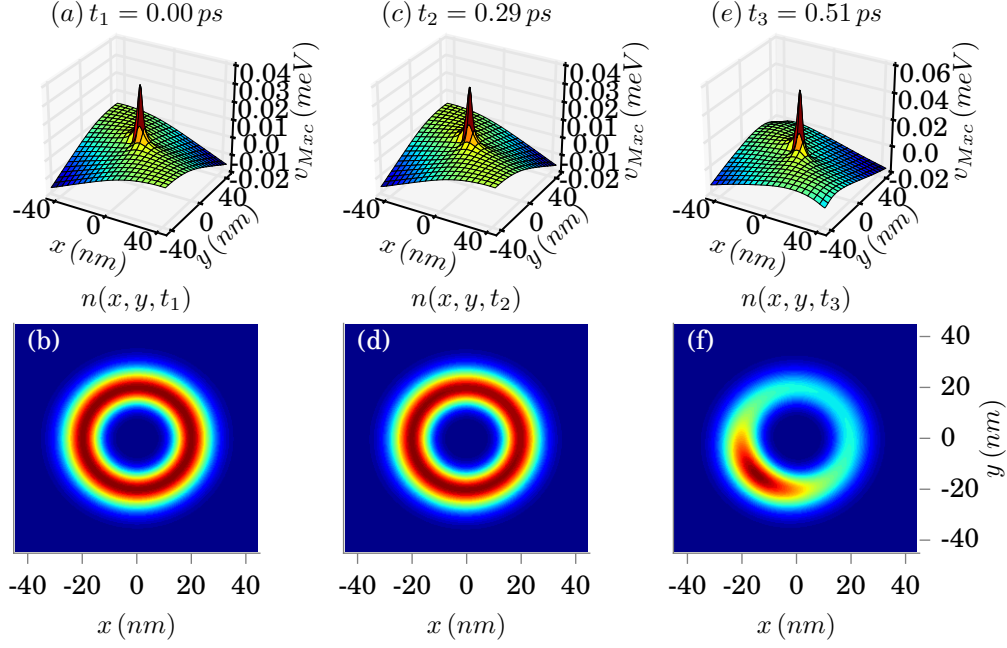


Figure 31: Dynamics of a correlated electron-photon system with nonfactorizable initial state and driven by an external laser pulse: Initially the system populates the combined electron-photon ground state. (a),(c),(e) shows the  $v_{Mxc}$  potential for different times, (b),(d),(f) shows the electron density at the corresponding times.

## 6.5 VALIDATING THE NUMERICAL FIXED-POINT ALGORITHM

To validate the numerical implementation of the fixed-point algorithm, we can compare our numerical results for the ground state to the results obtained from exact diagonalization. Using exact diagonalization, we can also construct with Eq. 39 the exact Kohn-Sham potential and compare to the results obtained using the fixed-point inversion. Defining

$$\delta n^{(k)}(\mathbf{r}) = n([v^{(k)}], \mathbf{r}) - n(\mathbf{r}), \quad (222)$$

where  $n([v^{(k)}], \mathbf{r})$  is the ground-state electron density obtained by the fixed-point iteration after  $k$  iterations and  $n(\mathbf{r})$  is the ground-state density obtained by exact diagonalization. In Fig. 32 (a) and (b), we plot the spatial resolution of  $\delta n(\mathbf{r})$  for the results discussed in Sec. 6.2. In Fig. 32 (a), we plot  $\delta n(\mathbf{r})$  after convergence with  $\lambda_\alpha = 1.68 \cdot 10^{-3} \text{ meV}^{1/2}/\text{nm}$  shown in Fig. 23 (a) and (b) shows  $\delta n$  for the calculation from Fig. 23 (b) with  $\lambda_\alpha = 0.134 \text{ meV}^{1/2}/\text{nm}$  after convergence. We find that the error at each grid-point is very small and has the order of  $\mathcal{O}(10^{-19})$ , which is below numerical double precision. The 1-Norm of  $\delta n(\mathbf{r})$  is plotted in Fig. 32 (c). Here we find a quasi-exponential reduction of the error for each iteration step (Note the logarithm scale of the y-axis in the plot). In both runs, we need 13 iterations to meet the convergence criteria (see Sec. 3.2.8.2). In the plot, we see after 5 iterations a drastic drop in the error. This reduction is due to the employed DIIS step, which we use for each individual fixed-point iteration at each time-step only once, exactly after 5 iterations.

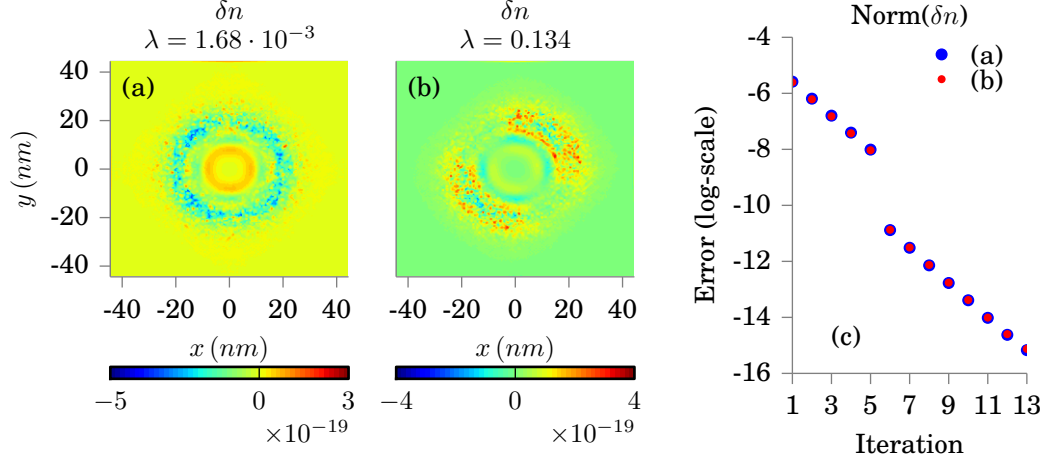


Figure 32: (a) shows  $\delta n$  for the calculation from Fig. 23 (a) with  $\lambda_\alpha = 1.68 \cdot 10^{-3}$  meV<sup>1/2</sup>/nm), (b) shows  $\delta n$  for the calculation from Fig. 23 (b) with  $\lambda_\alpha = 0.134$  meV<sup>1/2</sup>/nm) and (c) shows the 1-norm of  $\delta n$  at each iteration step of the fixed-point iteration.

## 6.6 INTERPRETATION OF THE ELECTRON-PHOTON DYNAMICS IN TERMS OF BO SURFACES

In this section, we analyze the many-body dynamics of the first example discussed in Sec. 6.3, in terms of BO surfaces. In electron-phonon problems, which are treated in Ch. 4, typically adiabatic BO surfaces are calculated. Fig. 11 in Ch. 4 shows an example of such adiabatic surfaces. In this case, the acoustical and optical phonon frequencies are much smaller than the electronic excitation frequency which is the adiabatic limit.

Nevertheless in this chapter, we treat an electron-photon problem, where the photon frequency is in resonance to the first electronic transition. We first define as intermediate regime the weak-coupling regime, where the difference in the electronic energies is in the order of the photon frequency as can be seen in Fig. 24. Next, we define as antiadiabatic limit the strong-coupling regime, where the difference in the electronic eigenenergies are smaller than the photon frequency. This behavior of the electronic system is due to the dipole self-interaction, which renormalizes the electronic eigenenergies and can be also seen from Fig. 24. In this section, we use the Born-Oppenheimer factorization originally developed for electron-nuclear problems to analyze the dynamics in electron-photon systems. Therefore, we consider the electronic BOA Hamiltonian to Eq. 184, where we neglect the photon kinetic energy contribution  $\frac{1}{2}\hat{p}_\alpha^2$  and replace the operator  $\hat{q}_\alpha$  by the coordinate  $q_\alpha$ . The electronic BOA Hamiltonian then reads

$$\begin{aligned} \hat{H}_{\text{BO}}(\{q_\alpha\}, t) = & \sum_{i=1}^{n_e} \left( -\frac{\hbar^2}{2m_e} \vec{\nabla}_i^2 + v_{\text{ext}}(\mathbf{r}_i, t) \right) + \frac{e^2}{4\pi\epsilon_0} \sum_{i>j}^{n_e} \frac{1}{|\mathbf{r}_i - \mathbf{r}_j|} \\ & + \sum_{\alpha=1}^{n_m} \frac{\omega_\alpha^2}{2} \left( q_\alpha - \frac{\lambda_\alpha}{\omega_\alpha} \cdot \mathbf{R} \right)^2 + \frac{j_{\text{ext}}^{(\alpha)}(t)}{\omega_\alpha} q_\alpha, \end{aligned} \quad (223)$$

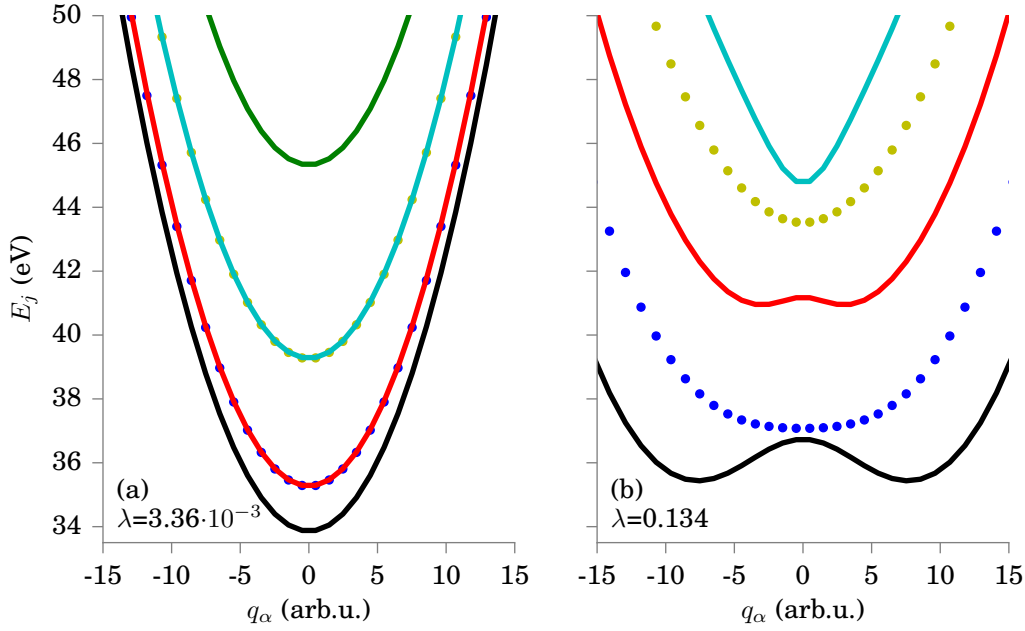


Figure 33: The Born-Oppenheimer surfaces of the correlated electron-photon problem. (a) show the surfaces for  $\lambda_\alpha = 3.36 \cdot 10^{-3} \text{eV}^{-1/2}/\text{nm}$ , which is equal to the interacting strength of the first example in Sec. 6.3. Panel (b) shows the surfaces for  $\lambda_\alpha = 0.134 \text{eV}^{-1/2}/\text{nm}$ , which is equal to the strong-coupling example in Sec. 6.2. The axis denotes the displacement of the photon mode  $q_\alpha$  in arbitrary units.

where the displacement field variables  $q_\alpha$  are reduced to classical parameters and  $\hat{H}_{\text{BO}}$  now parametrically depends on these  $\{q_\alpha\}$ .  $E_j(\{q_\alpha\})$  can be calculated by employing the static Schrödinger equation

$$\hat{H}_{\text{BO}}(\{q_\alpha\}) |\phi_j(\{q_\alpha\})\rangle = E_j(\{q_\alpha\}) |\phi_j(\{q_\alpha\})\rangle,$$

where  $\phi_j(\{q_\alpha\})$  is an electronic wave function. The photonic BOA Hamiltonian is then given in analogy to Eq. 15 as

$$\hat{H}_j(\{q_\alpha\}) = \sum_\alpha \frac{1}{2} \hat{p}_\alpha^2 + E_j(\{q_\alpha\}) + \sum_{i=0}^{\infty} \langle \phi_j \{q_\alpha\} | \hat{T}_{pt} | \phi_i \{q_\alpha\} \rangle, \quad (224)$$

and the BO states then follow as given by Eq. 16. The last term in Eq. 224 describes the nonadiabatic coupling between the individual PES. We neglect these nonadiabatic terms for the following discussion. In Fig. 33 (a), we show the surfaces corresponding BO surfaces  $E_j(\{q_\alpha\})$  for the weak-coupling regime of  $\lambda_\alpha = 3.36 \cdot 10^{-3} \text{eV}^{-1/2}/\text{nm}$ , which is also employed in the first time-dependent example discussed in Sec. 6.3. We find that all PES have a strong harmonic nature, due to the  $\hat{q}_\alpha^2$  term in Eq. 223. All anharmonicity is caused by the electron-photon interaction term  $\hat{H}_{\text{int}}$ . These contributions are small due to the weak-coupling limit. We find the lowest PES shown in black, well separated from the first and second excited PES shown in solid red and dotted blue. The first and second excited PES are close to degeneracy. In contrast to Fig. 24, where we find a three-fold degeneracy for the first-excited state in the weak-coupling limit, we here find only two PES, since

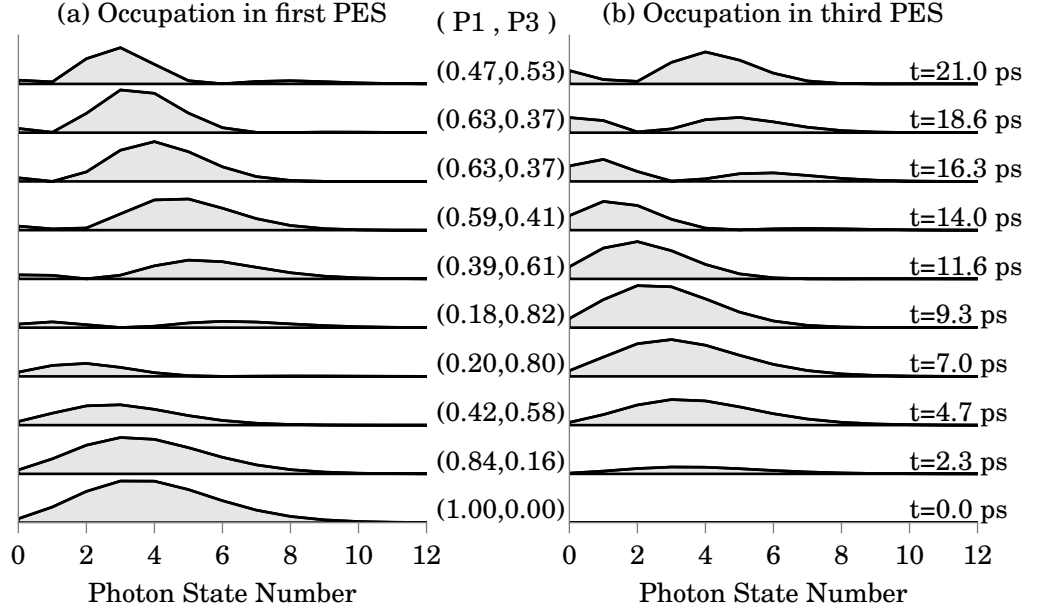


Figure 34: The occupation of the photon number states in (a) the first PES and (b) the third PES for the first time-dependent example discussed in Sec. 6.3. At initial time  $t = 0$  ps, we find a dominant coherent distribution with  $\langle \hat{a}_\alpha^\dagger \hat{a}_\alpha \rangle = 4$  in the first PES. (P1,P3) denotes the total population in the first PES, and third PES, respectively.

the problem is restricted to the two dimensions of the electron. In Fig. 33 (b), we show the PES surfaces in the strong-coupling regime with  $\lambda_\alpha = 0.134 \text{ eV}^{-1/2}/\text{nm}$ , which corresponds to the strong-coupling example of Sec. 6.2. Here, we also find an overall harmonic nature of the problem, but also stronger deviations. In the lowest PES shown in black and the third PES shown in solid red, two minima with a double-well structure appear. In particular the minima in the lowest PES is shifted strongly away from the equilibrium position at 0 arb.units.

In this way, we now use the BO surfaces shown in Fig. 33 (a) to analyze the many-body dynamics of the time-dependent example studied as the first example in Sec. 6.3. In this example, which is shown in Fig. 26-27, we calculated the purity  $\gamma$ , which is a measure separability of the many-body wave function. We found that  $\gamma$  is close to 1 up to  $t = 5$  ps, which means that the many-body wave function is close to a factorizable state. After  $t = 5$  ps,  $\gamma$  deviates strongly from 1 and the system is not factorizable anymore. In Fig. 34, we show the occupation of the photon number states in the first PES in (a) and the third PES in (b). The values (P1,P3) give the population of the first PES and the third PES, respectively. All other PES are populated by order of magnitudes smaller, since  $P1+P3$  is close to 1 for all times. In Fig. 34 (a), we find that at initial time  $t = 0$  ps, the first PES is populated with a photon state, which has a coherent distribution with  $\langle \hat{a}_\alpha^\dagger \hat{a}_\alpha \rangle = 4$ , which is in agreement with our initial condition. During the time propagation, we observe a transfer of population from the first PES to the third PES. In the first PES, we see until  $t = 9.3$  ps a depletion of population, while in the third PES (Fig. 34 (b)),

a growing of the population. After this time, the population is again transferred back from the third PES to the first PES. However, not only the amplitude of the population is changing, but also the center of the wave packets. In principle, if the same photon state would be populated in the two different PES, the system could still be factorizable. For small times, up to  $t = 5$  ps the center of the wave packet in the first PES remains close to its initial value. Later it changes to smaller photon numbers, which indicates photon absorption. We can conclude that the dynamics of the many-body system is dominated by the population transfer from the first PES to the third PES and vice versa. While for this example, a good approximate description may be a two surface approximation for the electronic system, which is similar to a JCH model, we expect a different behavior for more complex BO surfaces. e.g. in many-electron problems, multi-photon modes, or strong-coupling situations.

## 6.7 SUMMARY

In summary, we have shown how a Kohn-Sham scheme can be set up to describe correlated electron-photon problems. Using the fixed-point algorithm allows us to construct the exact KS potential for such problems. In the ground state of the cavity-GaAs, we identify large nonclassical features, which then also manifest in the KS potential. Here we find for the ground state a dominating peak, which even leads to charge splitting in the strong-coupling limit. For the time-dependent scenario we showed three examples. In two of these examples the classical description breaks down after a short time. In the exact Mxc potential, we find peaks and steps appearing. In the last example, where the dynamics of the system is mainly driven by the external potential, the classical description is in good agreement with the exact description, which marks the classical limit.

Further research can focus on the development of approximate Mxc potentials, which then allow for large-scale quantum calculations for correlated electron-photon situations. Additionally as observed in the two examples discussed here, we found for small times a good agreement between the mean-field and the exact propagation, a promising route in improving the xc approximations may be in further studies of memory effects and initial-state dependence. In electron-phonon calculations, many methods such as surface hopping [147] have been developed, future work could therefore also focus on the extension of these method originally developed for electron-phonon applications to electron-photon problems.





## DEVELOPING APPROXIMATIONS TO THE EXCHANGE-CORRELATION POTENTIAL IN QEDFT

In this chapter, we focus on the development of an efficient and practical **xc** potential, which introduces quantum effects of the correlated electron-photon interaction into the electronic **KS** potential. To this end, we study the Hamiltonian presented in Sec. 2.3.9 in the length gauge and follow the route of the **OEP** approach (Sec. 2.2.8.3) to obtain the first approximate  $v_{xc}$  potential for **QEDFT**. We use the Sham-Schlüter equation from Sec. 2.2.8 to get the direct connection between the many-body self-energy  $\Sigma_{xc}$  and the **KS** potential  $v_s$ . The self-energy  $\Sigma_{xc}$  is approximated by a GW approximation, taking the two lowest diagrams, the Hartree and the Fock diagram, into account.

We then apply this theory to a small, yet nontrivial model-system, the **JCH** model. We analyze its correlated ground state and the time evolution of the electron density in this two-site model in different coupling regimes and evaluate the quality of the **OEP** approximation in the offresonant case. This chapter is organized as follows: We first discuss the general **OEP** framework for correlated electron-photon problems. Then we apply this framework to static and time-dependent numerical examples and discuss the accuracy of the numerical implementation.

### 7.1 GENERAL THEORY OF THE OEP APPROXIMATION FOR QEDFT

We consider a system of  $n_e$  electrons with coordinates  $\{\mathbf{r}_i\}$  interacting with  $n_m$  quantized photon modes of corresponding photon displacement coordinates  $\{q_\alpha\}$  and frequencies  $\omega_\alpha$ . The Hamiltonian for this problem is formulated in the length gauge in the usual dipole approximation [68] and given by Eq. 184.

The electron-photon interaction is given by two terms, the explicit electron-photon interaction term  $\hat{H}_{\text{int}}$  from Eq. 187 and the dipole self-energy term  $\hat{H}_{\text{es}}$  from Eq. 188. We recast here both terms in the Heisenberg picture

$$\begin{aligned}\hat{H}_{\text{pt-e}}(t) &= \hat{H}_{\text{int}}(t) + \hat{H}_{\text{es}}(t), \\ \hat{H}_{\text{int}}(t) &= - \sum_{\alpha=1}^{n_m} \omega_\alpha \hat{q}_\alpha(t) \int d\mathbf{r} (\boldsymbol{\lambda}_\alpha \cdot \mathbf{r}) \hat{n}(\mathbf{r}, t), \\ \hat{H}_{\text{es}}(t) &= \sum_{\alpha} (\boldsymbol{\lambda}_\alpha \cdot \mathbf{R}(t))^2 / 2.\end{aligned}$$

These two terms give rise to an additional effective electron-electron interaction of second order in  $\boldsymbol{\lambda}_\alpha$ , which can be motivated by the  $S$ -matrix [57]

$$\begin{aligned}S(-\infty, \infty) &= \mathbb{1} - \frac{i}{\hbar} \int_{-\infty}^{\infty} dt_1 \hat{H}_{\text{pt-e}}(t_1) \\ &\quad - \frac{1}{2\hbar^2} \int_{-\infty}^{\infty} dt_1 \int_{-\infty}^{\infty} dt_2 T [\hat{H}_{\text{pt-e}}(t_1), \hat{H}_{\text{pt-e}}(t_2)] + \dots\end{aligned}\quad (225)$$

This chapter is based on the work reported in Ref. [148], which has been performed in close collaboration with all coauthors. In this work, I implemented and performed all numerical simulations.

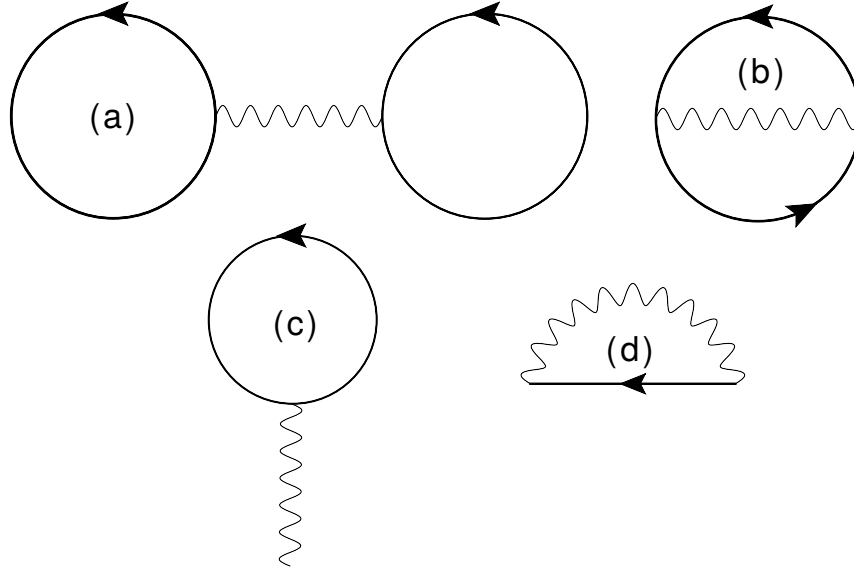


Figure 35: Feynman diagrams: (a) Hartree and (b) Fock diagram in the action functional  $A$ , and the (c) Hartree and (d) Fock diagram in the self-energy  $\Sigma_{xc}$ .

Here, we directly see that the first-order term vanishes due to the even/odd symmetry, while the lowest order contributing is the second-order term in  $\lambda_\alpha$  for  $\hat{H}_{\text{int}}(t)$  and  $\hat{H}_{\text{es}}(t)$ , respectively. To this end, the coupling to the quantized field modes causes an additional effective electron-electron interaction in second order in  $\lambda_\alpha$  of the following form

$$W_{ee}(1,2) = \sum_{\alpha} (\lambda_{\alpha} \mathbf{r}_2) (\lambda_{\alpha} \mathbf{r}_1) \mathcal{W}_{\alpha}(t_1, t_2) \quad (226)$$

$$\mathcal{W}_{\alpha} = \omega_{\alpha}^2 \mathcal{D}_{\alpha}(t_1, t_2) + \delta(t_1 - t_2), \quad (227)$$

where we define the photon displacement propagator  $i\hbar \mathcal{D}_{\alpha}(t_1, t_2) = \langle \hat{T} [\hat{q}_{\alpha}(t_1), \hat{q}_{\alpha}(t_2)] \rangle$  using Wick's time-ordering operator  $\hat{T}$ . The mean-field contribution is defined as [58] and equal to Eq. 212

$$v_M(\mathbf{r}, t) = \int d^3 \mathbf{r}' \int dt' W_{ee}(\mathbf{r}, t, \mathbf{r}', t') n(\mathbf{r}', t'), \quad (228)$$

Using the linearized Sham-Schlüter equation [63] from Eq. 73

$$\int d2 G_S(1,2) v_{xc}(2) G_S(2,1^+) = \int d2 \int d3 G_S(1,2) \Sigma_{xc}(2,3) G_S(3,1^+), \quad (229)$$

we approximate the self-energy  $\Sigma_{xc}$  by the exchange-like (Fock) diagram

$$\Sigma_{xc}(1,2) = i\hbar G_S(1,2) W_{ee}(2,1), \quad (230)$$

where  $W_{ee}$  is given by Eq. 226 and the Kohn-Sham Green's function  $G_S(1,2)$  by Eq. 71. Using the Langreth rules [58] and expressing the Kohn-Sham Green's function in terms of the Kohn-Sham orbitals  $\phi_i$ , we arrive at the following time-dependent OEP equation [148]

$$\frac{i}{\hbar} \sum_{i,j} \int_{-\infty}^t dt_1 [\langle \phi_i(t_1) | v_x(t_1) | \phi_j(t_1) \rangle f_i - S_{ij}(t_1)] \phi_j^*(\mathbf{r}, t) \phi_i(\mathbf{r}, t) + c.c. = 0, \quad (231)$$

where we have introduced the quantity

$$S_{ij}(t_1) = \sum_{k,\alpha} \int_{-\infty}^{t_1} dt_2 d_{ik}^\alpha(t_2) d_{kj}^\alpha(t_1) [(1-f_i)f_k \mathcal{W}^>(t_1, t_2) - f_i(1-f_k) \mathcal{W}^<(t_1, t_2)], \quad (232)$$

with  $\mathcal{W}^\geq(t_1, t_2) = -i\omega_\alpha/2e^{\pm i\omega_\alpha(t_2-t_1)} \pm \delta(t_1 - t_2)$  and  $f_i$  is the fermion occupation number and  $d_{ik}^\alpha(t) = \lambda_\alpha \langle \phi_i(t) | \mathbf{r} | \phi_k(t) \rangle$  is the dipole matrix element projected on the coupling constant  $\lambda_\alpha$ . In Eq. 232, *c.c.* denotes the complex conjugate of the former term. The OEP equation yields a connection between  $v_x(\mathbf{r}, t)$  and the matrix elements  $S_{ij}$  that depend on the self-energy  $\Sigma_{xc}$ . Therefore,  $S_{ij}$  describes correlated electron-photon processes in the system such as the creation and annihilation of electron-hole pairs caused by photon absorption and emission. Furthermore the OEP equation in the presented form involves the evaluation of all occupied and all unoccupied orbitals, since the sums over  $i, j, k$  in Eq. 231 are in principle unrestricted with limits  $[1, \infty]$ . This is in contrast to the electron *x*-only OEP equation [65] that can be constructed using Sternheimer equations such that only occupied orbitals are involved.

If we assume initial states with  $\dot{q}_\alpha(t_0) = 0$ , we can directly evaluate the mean-field contribution. It is given by Eq. 212 and reads here

$$v_M(\mathbf{r}, t) = - \sum_{\alpha} \omega_{\alpha} (\lambda_{\alpha} \mathbf{r}) \int_0^t dt_1 \sin[\omega_{\alpha}(t - t_1)] (\lambda_{\alpha} \mathbf{R}(t_1)) - \sum_{\alpha} (\lambda_{\alpha} \mathbf{r}) [(\lambda_{\alpha} \mathbf{R}(0)) \cos(\omega_{\alpha} t) - \lambda_{\alpha} \mathbf{R}(t)], \quad (233)$$

where  $\mathbf{R}(t) = \int d^3\mathbf{r} \mathbf{r} n(\mathbf{r}, t)$ . Further, in the case of a time-independent external potential, the time-dependent OEP equation reduces to the static OEP equation. To derive this limit, we can integrate out the explicit time-dependence and perform a Fourier transformation. The static OEP equation then follows as

$$\sum_{i,j} \left[ \frac{\langle \phi_i | v_x | \phi_j \rangle}{\epsilon_i - \epsilon_j - i\eta} f_i - S_{ij} \right] \phi_j^*(\mathbf{r}) \phi_i(\mathbf{r}) + c.c. = 0, \quad (234)$$

where the matrix elements  $S_{ij}$  are defined as

$$S_{ij} = \sum_{k,\alpha} \frac{d_{ik}^\alpha d_{kj}^\alpha (\epsilon_i - \epsilon_k - i\eta)}{2 (\epsilon_i - \epsilon_j - i\eta)} \left[ \frac{(1-f_k)f_i}{\epsilon_i - \epsilon_k - \hbar\omega_{\alpha} - i\eta} + \frac{(1-f_i)f_k}{\epsilon_i - \epsilon_k - \hbar\omega_{\alpha} - i\eta} \right]. \quad (235)$$

Further, we assume the limit  $\eta \rightarrow 0$ . This static equation then leads to a second-order correction to the ground-state energy of the following form

$$E_x = -\frac{1}{2} \sum_{i,k,\alpha} |d_{ik}^\alpha|^2 \left[ \hbar\omega_{\alpha} \frac{(1-f_i)f_k}{\epsilon_i - \epsilon_k + \hbar\omega_{\alpha}} - (1-f_i)f_k \right], \quad (236)$$

and is directly connected to the Lamb shift [149]. As in Sec. 6, if we treat single electron problems, we can consider the effects of the dipole-self interaction Hamiltonian  $\hat{H}_{es}$  exactly. In the following numerical example, we therefore define as classical potential  $v_c(\mathbf{r}, t) = v_M(\mathbf{r}, t) + v_{es}(\mathbf{r})$ .

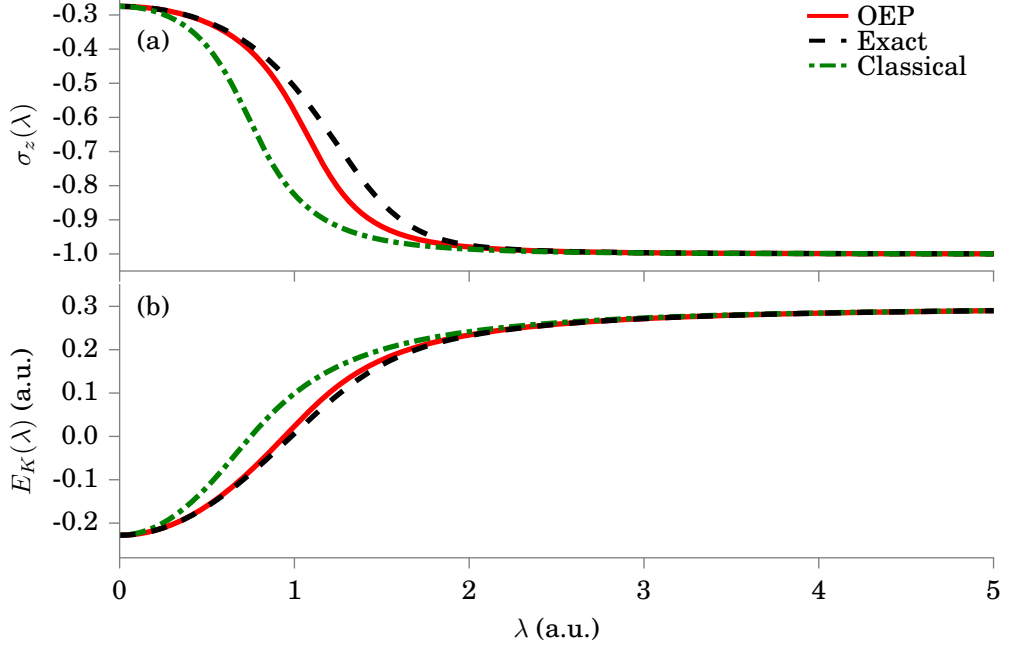


Figure 36: Exact (black), OEP (red) and classical (green) static OEP results: (a) shows the electron density  $\sigma_z$  as a function of the electron-photon coupling strength  $\lambda$ . (b) shows the total energy  $E_K$  as a function of  $\lambda$ .

## 7.2 MODEL SYSTEM: STATIC CALCULATION

We now apply the introduced OEP formalism to a small, yet nontrivial, model system, the Jaynes-Cummings-Hubbard model system. The model Hamiltonian is defined in Sec. 3.1.2. To be consistent with the many-body Hamiltonian Eq. 184, we add two additional constants to the Hamiltonian of Eq. 145: The constant  $\lambda^2/2$  to account for the dipole self-energy and the photon vacuum energy constant  $\omega/2$ . Further we replace the electron-photon coupling strength by  $\lambda \rightarrow \sqrt{\frac{\omega}{2}}\lambda$ . The Hamiltonian then reads

$$\hat{H} = -T\hat{\sigma}_x + \left[ \sqrt{\frac{\omega}{2}}\lambda (\hat{a} + \hat{a}^\dagger) + v_{\text{ext}}(t) \right] \hat{\sigma}_z + \omega \left( \hat{a}^\dagger \hat{a} + \frac{1}{2} \right) + \frac{\lambda^2}{2}. \quad (237)$$

As numerical parameters, we choose  $\omega = 1$ ,  $v_{\text{ext}} = 0.2$ ,  $T = 0.7$  all given in atomic units. In the static case, we find the static  $v_x$  potential as

$$v_x = -\lambda^2 \frac{v_s}{W} \left[ \frac{\omega(\omega + 3W)}{(\omega + 2W)^2} - 1 \right], \quad (238)$$

and the ground-state energy functional then takes the following form

$$E_K[v_s] = -T \langle \hat{\sigma}_x \rangle + v_{\text{ext}} \langle \hat{\sigma}_z \rangle + E_x[v_s] + \frac{\omega}{2}, \quad (239)$$

with  $E_x = \frac{\lambda^2 T^2}{W(\omega + 2W)}$ , where  $W$  is the Kohn-Sham eigenvalue, i.e. the ground-state (g) KS orbital has energy  $\epsilon_g = -W$ , while the excited-state (e) KS orbital has energy  $\epsilon_e = W$  and the electron density  $\sigma_z$  that is the on-site population difference  $\sigma_z$ . In

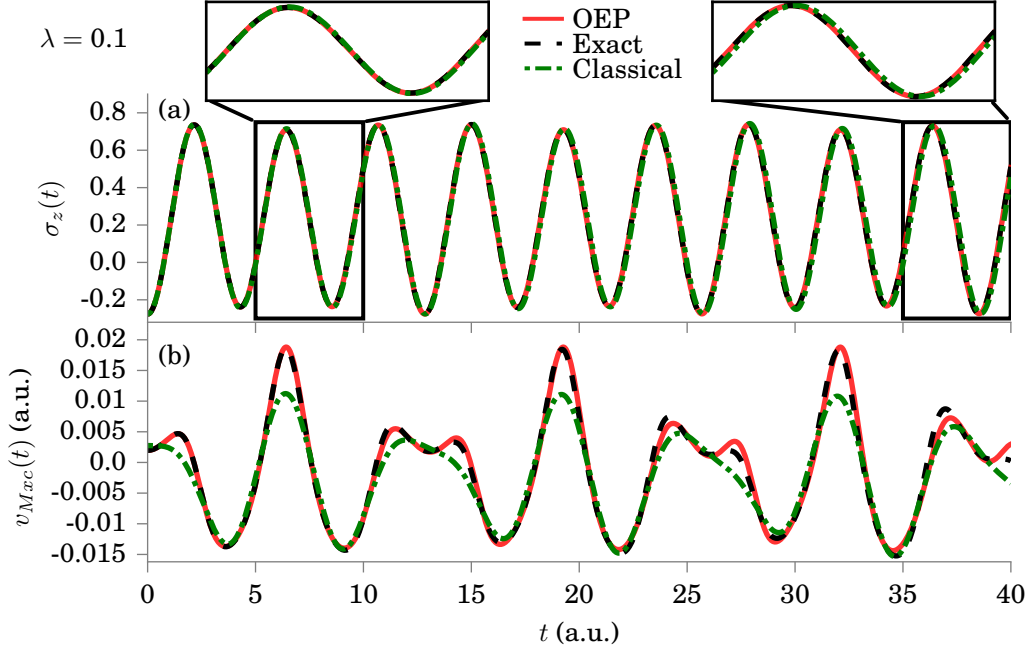


Figure 37: Time-dependent OEP results for  $\lambda = 0.1$  with comparison of OEP (red), exact (black) and classical (green) results: (a) shows the time evolution of the electron density  $\sigma_z(t)$  and (b) shows the time evolution of the Mxc potential in the case of the sudden switch of the external potential  $v_{Mxc}$ .

Fig. 36, we compare the quality of the OEP approximation in the static case with the classical approximation and the exact results for the case of the JCH dimer. Fig. 36 (a) shows the electron density  $\sigma_z$  as a function of the electron-photon coupling strength  $\lambda$ . In the static case, we find an overall very good agreement for the OEP approximation with the exact results, which is in the weak-coupling limit for  $\lambda < 0.5$  and in the strong-coupling limit for  $\lambda > 2$ . In particular, the OEP approximation shows a clear improvement over the classical approximation, which provides only accurate results in the limits  $\lambda \rightarrow 0$  and  $\lambda > 2$ . In the intermediate regime, here  $0.5 < \lambda < 2$ , the OEP shows relatively small deviations from the exact results. Similar behavior can be also found for the case of the total energy  $E_K$  as shown in Fig. 36 (b). Here, the OEP result is in very good agreement to the exact result, with only small deviations in the intermediate regime  $0.5 < \lambda < 2$ . In contrast, the classical approximation shows clear deviations and performs for all coupling strength worse than the OEP approximation.

### 7.3 MODEL SYSTEM: TIME-DEPENDENT CALCULATION

In the time-dependent case, the time-dependent OEP equation for the JCH model reads

$$\begin{aligned}
 & i \int_{-\infty}^t dt_1 \tilde{v}_x(t_1) d_{ge}(t_1) d_{eg}(t) + c.c. \\
 & = \lambda^2 \omega \int_{-\infty}^t dt_1 \int_{-\infty}^{t_1} dt_2 c(t, t_1) d_{eg}(t_2) e^{i\omega(t_2-t_1)} + c.c.,
 \end{aligned} \tag{240}$$

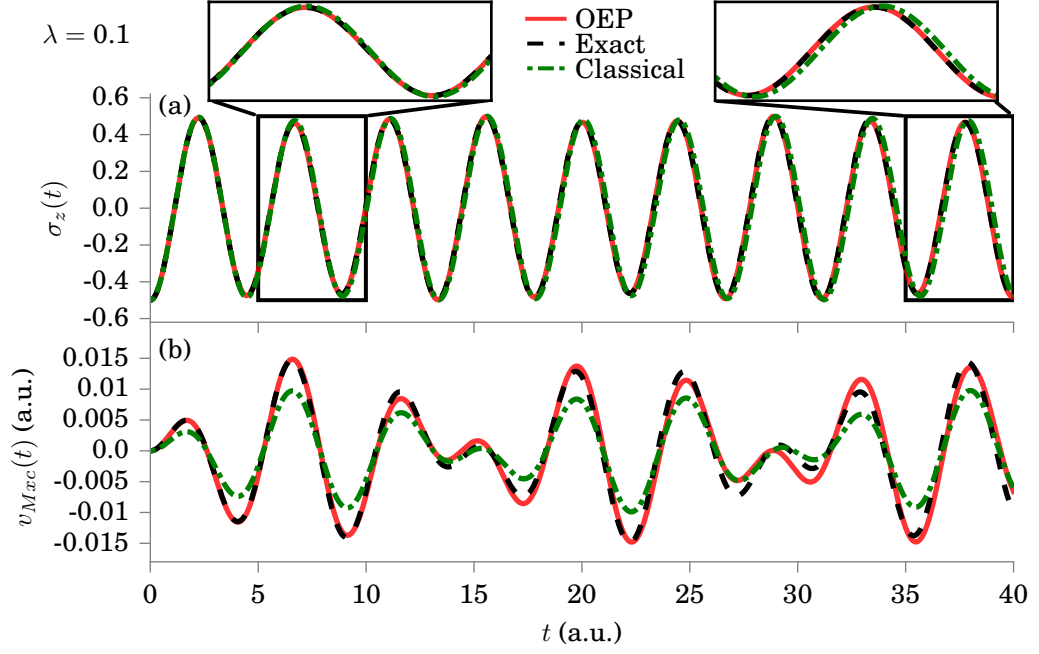


Figure 38: Time-dependent OEP results for  $\lambda = 0.1$  with comparison of OEP (red), exact (black) and classical (green) results: (a) shows the time evolution of the electron density  $\sigma_z(t)$  and (b) shows the time evolution of the Mxc potential in the case of a factorizable initial state.

where  $\tilde{v}_x(t) = v_x(t) + \lambda^2 \sigma_z(t)$ . The dipole matrix elements between the electronic ground state ( $g$ ) and the excited state ( $e$ ) are defined as  $d_{ge}(t) = \langle \phi_g(t) | \hat{\sigma}_z | \phi_e(t) \rangle$  and enter the quantity  $c(t, t_1) = d_{ge}(t) \sigma_z(t_1) - d_{ge}(t_1) \sigma_z(t)$ . The mean-field potential is given by

$$v_M(t) = -\lambda^2 \omega \int_0^t dt_1 \sin[\omega(t - t_1)] \sigma_z(t_1) - \lambda^2 \sigma_z(t_0) \cos(\omega t) + \lambda^2 \sigma_z(t). \quad (241)$$

To solve the cavity time-dependent optimized effective potential (TDOEP) scheme numerically, we employ a similar procedure as presented in Ref. [66] within the standard numerical TDOEP approach. We simultaneously solve the time-dependent Kohn-Sham equation and the TDOEP equation (Eq. 240) in the interval  $[0, T]$ . This can be achieved by an iterative loop, which takes at each time step the Kohn-Sham orbitals obtained by the KS equation as input to Eq. 240, which then yields a new  $v_{Mxc}$  potential. This new  $v_{Mxc}$  potential is then used to repeat the propagation of the KS equation. This loop is repeated until self-consistency in  $v_{Mxc}$  is reached. Previous  $v_{Mxc}$  values are used as initialization of the loop. We propagate the time-dependent KS equation using an exponential midpoint propagator (see Sec. 3.2.6) for high accuracy. The numerical integration of the TDOEP equation, which is a Volterra integral equation of the first kind, is performed using a midpoint integration scheme combined with the trapezoidal rule [109]. In Fig. 37, we show the time evolution for the case of the initial state being the correlated ground state of the system with the parameters  $\lambda = 0.1$  and  $v_{ext} = -0.2$ . At the initial time, we change the sign of the external potential to  $v_{ext} = 0.2$ . This induces a density oscillation in

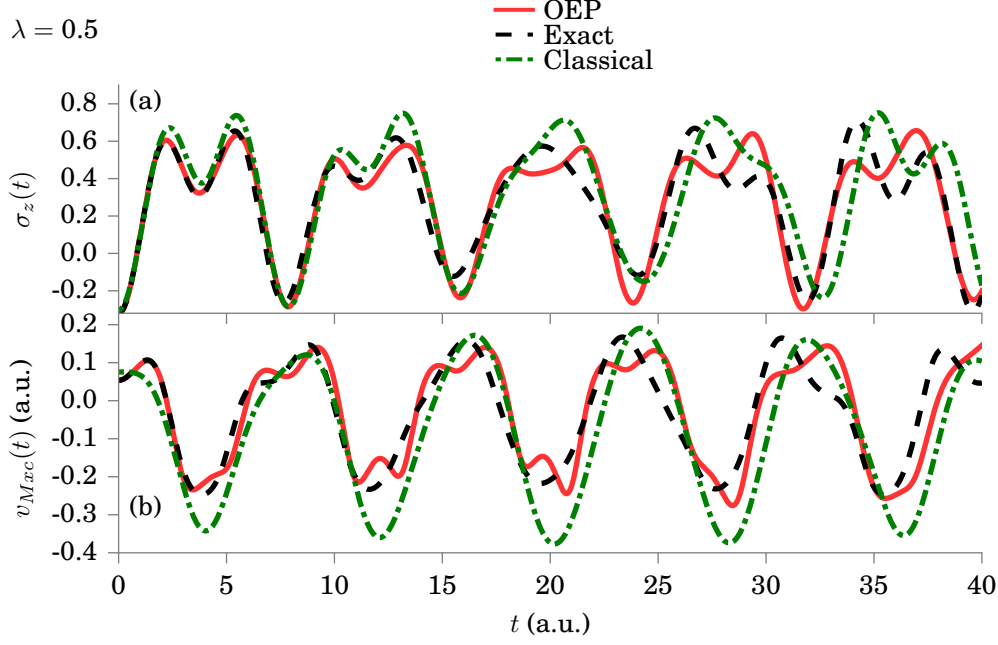


Figure 39: Time-dependent OEP results for  $\lambda = 0.5$  with comparison of OEP (red), exact (black) and classical (green) results: (a) shows the time evolution of the electron density  $\sigma_z(t)$  and (b) shows the time evolution of the Mxc potential.

the system as shown in Fig. 37 (a). We plot the classical results in green, the exact results in black and the OEP results in red. For small times, we find a good agreement of all three propagations, but after  $t = 30$  a.u., the classical density starts to change slightly. This behavior is further highlighted in the inset of Fig. 37 (a). The OEP result is in good agreement with the exact result. In Fig. 37 (b), we show the  $v_{\text{Mxc}}(t)$ , which shows more deviations. Here, we find a clear improvement of the OEP over the classical approximation. The OEP only changes at later time slightly with respect to the exact propagation.

In Fig. 38, we show the time evolution for the case of a factorizable initial state,  $\lambda = 0.1$  and  $v_{\text{ext}}(t) = 0$ . The photon field is initially in the vacuum, while the electron is in a superposition state:  $\Psi = \left(1/2|1\rangle + \sqrt{3}/2|2\rangle\right) \otimes |0\rangle$ , where  $|1\rangle$  and  $|2\rangle$  denote site 1 and 2, respectively and the photon state  $|0\rangle$  refers to the field in the vacuum state. The results of the time propagation are shown in Fig. 38 (a) for the electron density and (b) for the  $v_{\text{Mxc}}$  potential. We find the same qualitative behavior as in the previous example, as the OEP shown in red clearly improves the classical results shown in green compared to the exact results shown in black. The differences between small times ( $5 < t < 10$ ) and later times ( $35 < t < 40$ ) is highlighted in the inset of Fig. 38 (a).

In the last example in this chapter, we choose a stronger coupling example with  $\lambda = 0.5$ . We again choose a similar setup as in Fig. 37. Initially the system is in the ground state of the external potential  $v_{\text{ext}} = -0.2$  and the sign of the potential is flipped at the initial time of the time propagation. The density of this example is shown in Fig. 39 (a). Here, we find larger deviations between the OEP results shown in red and the exact results shown in black. We observe for small times

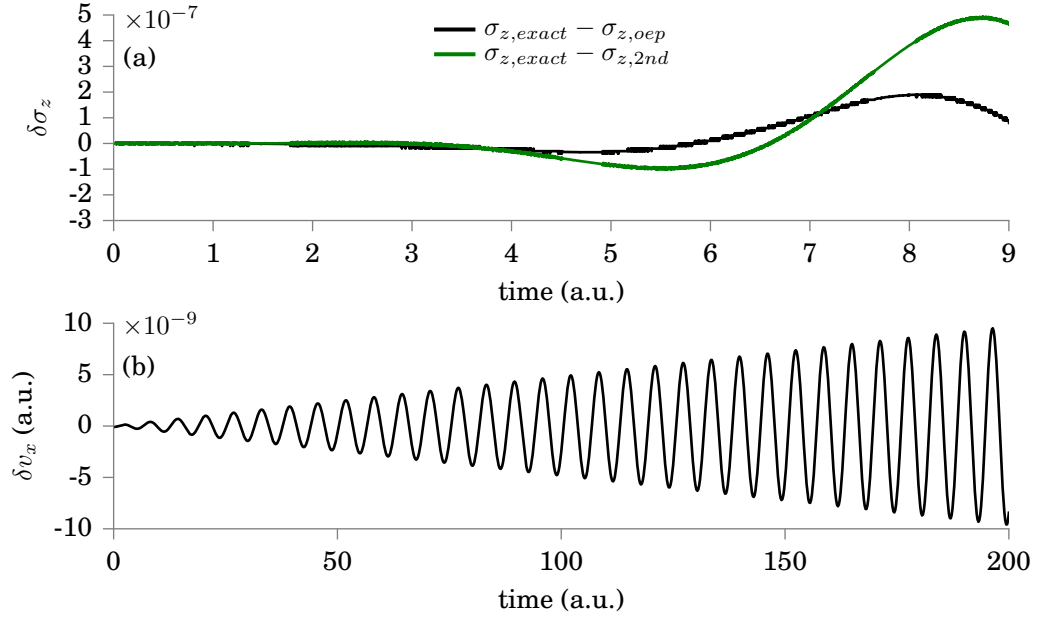


Figure 40: Validation of our numerical implementation: (a) shows the difference of the  $\delta\sigma_z$ :  $\sigma_{z,exact} - \sigma_{z,oev}$  in black and  $\sigma_{z,exact} - \sigma_{z,2nd}$  in green. (b) shows the difference of  $\delta v_x = v_{x,numerical} - v_{x,analytical}$ .

( $t < 10$  a.u.) a good agreement between [OEP](#) and exact results, and in particular an improvement over the classical result shown in green. After  $t = 10$  a.u., however also the [OEP](#) starts to deviate from the exact results. This finding is also inherited in the  $v_{Mxc}$  potential shown in Fig. 39 (b). Here we find for small times  $t < 5$  a.u. the [OEP](#) potential on top of the exact potential and the classical potential deviates already at  $t = 0$  a.u. However for longer times also the [OEP](#) starts to deviate.

#### 7.4 VALIDATION OF THE NUMERICAL IMPLEMENTATION

We validate our numerical results by comparing to corresponding analytic expressions. If we assume the initial state as  $\Psi = (u|1\rangle + v|2\rangle) \otimes |0\rangle$ , as in the second example in Sec. 7.3 and apply time-dependent perturbation theory [150] for the [JCH](#) model in resonance ( $2T = \omega$ ), we obtain the following formula for the density  $\sigma_z$  up to second order in  $\lambda$

$$\sigma_{z,2nd}(t) = (u^2 - v^2) \left( \cos(\omega t) + \frac{\lambda^2}{4} \left( \frac{t}{\omega} \sin(\omega t) - t^2 \cos(\omega t) \right) \right) + \mathcal{O}(\lambda^4). \quad (242)$$

The coefficients  $u$  and  $v$  are given by the electronic initial state and subject to the normalization condition  $u^2 + v^2 = 1$ . In the second example in Sec. 7.3, we use  $u = 1/2$ , and  $v = \sqrt{3}/2$ .

By construction, the density calculated within the [OEP](#) framework is correct up to the second order in the coupling  $\lambda$ . Due to the self-consistency, we can expect the [OEP](#) density to be slightly more accurate than the perturbation formula of Eq. 242.



In Fig. 40 (a), we show the difference between the density obtained by an OEP run as in the previous sections and the analytic formula up to second order in  $\lambda$ , both with respect to the exact density  $\sigma_{z,exact}$ . We choose a small  $\lambda = 0.01$ . In Fig. 40, we find that the error of  $\sigma_{z,2nd}$  is larger than the error of  $\sigma_{z,OEP}$ , which verifies the correctness of the implemented OEP approach.

A second measure can be given by solving the TDOEP equation from Eq. 240 analytically by inserting the zero-order density  $\sigma_{z,0th} = 2uv \cos(\omega t)$  and transition density  $d_{12,0th} = (u+v)^2 \exp\{-i\omega t\}/2 - (u-v)^2 \exp\{i\omega t\}/2$ . We then find the following formula

$$v_{x,2nd}(t) = -\frac{(u-v)^3 (u+v) \omega t \sin(\omega t) \lambda^2}{4uv} + \theta(\lambda^4). \quad (243)$$

This analytic formula can now be compared to the numerical results, which we obtain, if we use  $\sigma_{z,0th}$  and  $d_{12,0th}$  as input in our numerical OEP equation solver. In Fig. 40 (b), we show the difference between the numerical results and the analytic results. In this case, the accuracy is only limited by the time step, which is used in the solver for the Volterra integral equation (see Sec. 3.2.7). We find a very small error of  $\mathcal{O}(10^{-9})$  for  $\Delta t = 0.01$ . The accuracy of the numerical solution of the integral equation is in this case further limited due to the singularity of the diagonal of the kernel  $K(x_n, x_n) = 0$  in the Volterra integral equation. Even more accurate results can be obtained, if this singularity is lifted e.g. by replacing the OEP equation by its time-derivative version. For all presented results in this chapter, the obtained accuracy using the form of the OEP equation of Eq. 240 is sufficient.

## 7.5 SUMMARY

In this section we have shown the first calculations within the OEP framework of QEDFT. We find clear improvements of OEP over the mean-field approximation for the ground state from the weak to the strong-coupling. Further, we analyzed the performance of the TDOEP scheme in the time-dependent case. Here we find good agreement to the exact results in an offresonant setup and in the weak-coupling regime. Additionally, we validated the numerical implementation by comparing its results to analytic formulas. Further research may focus on the analysis of the OEP behavior in stronger coupling situations as shown in the last example. One different route lies in the study of approximations to the OEP on the lines of the KLI approximation [64, 67]. Additionally an exact or approximate reformulation of the OEP equation without involving the unoccupied orbitals is desirable to bring the calculations to three dimensions and further study the real-space features of the OEP approach.



## THE HYDROGEN-DEUTERIUM DIMER IN AN OPTICAL CAVITY

---

### 8.1 INTRODUCTION

In the last years, tremendous experimental progress has enabled scientists to obtain new insights into the interaction of quantized photons correlated with matter. These experiments show, e.g. that the conductivity in organic semiconductors can be improved by an order of magnitude through hybridization with the vacuum field [152]. Other experiments have shown that the coherent coupling of molecular resonators with a micro-cavity mode shows large shifts in the vibrational frequency [153] or that strong coupling allows to tune the work function in organic materials [154]. All these different experiments indicate new states of matter and different chemistry, if the quantized nature of light becomes important. Nowadays the strong-coupling limit is achieved routinely in the fields of current quantum electrodynamics (current-QED) [155, 156] or cavity-QED [157, 158].

In this chapter, we study a model system, which contains nuclear, electronic and photonic degrees of freedom explicitly. It consists of an artificial molecule, which contains two nuclei and two electrons confined to one-dimension, which is orthogonal to the propagation direction of the photon field in the cavity. This model system is located in an optical cavity, where it couples to a single photon mode. We show how the correlated light-matter interaction changes the electronic BO surfaces. These changes have immediate consequences [159], e.g. in the bond length of the molecule or the absorption spectrum. Additionally, we show how the new ground state acquires a new electron-nuclear-(vibronic) photon quasiparticle character.

### 8.2 CAVITY BORN-OPPENHEIMER APPROXIMATION

In this section, we study a vibro-photon system for a model consisting of two nuclei and two electrons, which are coupled to a single cavity mode of the cavity. The cavity mode is tuned in resonance to the first vibrational excitation of the dimer system. We schematically depict such a system in Fig. 41. The molecule in the cavity is shown on the left. It is exposed to the cavity mode, which is defined by the cavity frequency  $\omega_\alpha$  and the matter-photon coupling strength  $\lambda_\alpha$ . On the right-hand side, we depict a simplified picture of the hybridization of the system, therefore we show the BO surface depending on the nuclear coordinate  $X$  in atomic units (Bohr). We show the eigenstates of the molecular system in BOA. In the ground state, the electrons are subjected to the ground-state BO surface, which is shown in dashed-black lines. The harmonic approximation to the exact

---

This chapter is part of the review article [151] that is currently in preparation.

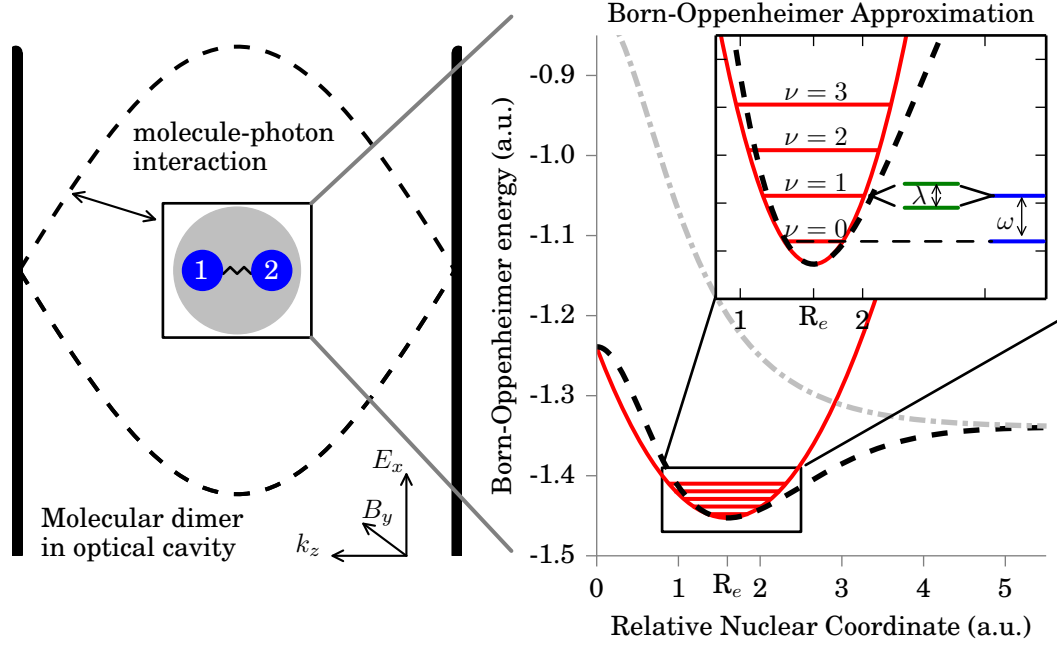


Figure 41: Left: Molecular dimer in a cavity with cavity-frequency  $\omega$ . Right: Exact ground-state BO surface in black dashed lines, harmonic ground-state BO surface in solid red lines, and exact first excited-state BO surface in dashed-gray lines,  $\nu$  indicates the phonon excitation,  $R_e$  denotes the BO equilibrium distance, and  $\lambda$  denotes the Rabi splitting by the phonon-photon hybridization and the matter-photon interaction strength.

BO surface is shown in solid red lines. The individual harmonic excitations of the nuclear (phonon) subsystem are indicated by  $\nu$ . Since the cavity mode is tuned in resonance, we find Rabi splitting [93] of the first vibrational excitation, which is proportional to the matter-photon coupling constant  $\lambda_\alpha$ . The first excited electronic BO surface is shown in gray-dashed lines. This surface has no minima, hence featuring the dissociation of the molecule. In the dissociation limits that is for  $X > 5$  a.u., the ground-state and the first-excited BO surfaces merge. In Fig. 41 (a), we furthermore denote the electric field component  $E_x$ , the magnetic field component  $B_y$  and the wave vector of the photon field mode  $k_z$  that build a triad as discussed in Sec. 2.3.3.

We consider such systems in the dipole approximation and length gauge. In this setup, the correlated electron-nuclear-photon Hamiltonian for the dimer in a cavity

can be written as a sum of the electron-nuclear Hamiltonian  $\hat{H}_{\text{en}}$  and the photon Hamiltonian  $\hat{H}_{\text{pt}}$ . It follows [17, 68, 140, 148]

$$\hat{H} = \hat{H}_{\text{en}} + \hat{H}_{\text{pt}}, \quad (244)$$

$$\begin{aligned} \hat{H}_{\text{en}} = & -\frac{\hbar^2}{2M_1} \vec{\nabla}_{\mathbf{X}_1}^2 - \frac{\hbar^2}{2M_2} \vec{\nabla}_{\mathbf{X}_2}^2 - \frac{\hbar^2}{2m_3} \vec{\nabla}_{\mathbf{x}_3}^2 - \frac{\hbar^2}{2m_4} \vec{\nabla}_{\mathbf{x}_4}^2 \\ & + \frac{Z_1 Z_2 e^2}{4\pi\epsilon_0 \sqrt{(\mathbf{X}_1 - \mathbf{X}_2)^2 + 1}} - \frac{Z_1 e^2}{4\pi\epsilon_0 \sqrt{(\mathbf{X}_1 - \mathbf{x}_3)^2 + 1}} \\ & - \frac{Z_1 e^2}{4\pi\epsilon_0 \sqrt{(\mathbf{X}_1 - \mathbf{x}_4)^2 + 1}} - \frac{Z_2 e^2}{4\pi\epsilon_0 \sqrt{(\mathbf{X}_2 - \mathbf{x}_3)^2 + 1}} \\ & - \frac{Z_2 e^2}{4\pi\epsilon_0 \sqrt{(\mathbf{X}_2 - \mathbf{x}_4)^2 + 1}} + \frac{e^2}{4\pi\epsilon_0 \sqrt{(\mathbf{x}_3 - \mathbf{x}_4)^2 + 1}}, \end{aligned} \quad (245)$$

$$\hat{H}_{\text{pt}} = \frac{1}{2} \sum_{\alpha} \left[ \hat{p}_{\alpha}^2 + \omega_{\alpha}^2 \left( \hat{q}_{\alpha} + \frac{\lambda_{\alpha}}{\omega_{\alpha}} \cdot \mathbf{R} \right)^2 \right], \quad (246)$$

$$\mathbf{R} = Z_1 \mathbf{X}_1 + Z_2 \mathbf{X}_2 - \mathbf{x}_3 - \mathbf{x}_4. \quad (247)$$

Here, the capital variables,  $\mathbf{X}_1$  and  $\mathbf{X}_2$ , denote the nuclear coordinates, while the small variables  $\mathbf{x}_3$  and  $\mathbf{x}_4$  denote the electronic coordinates, and  $\hat{q}_{\alpha} = \sqrt{\frac{\hbar}{2\omega_{\alpha}}} (\hat{a}_{\alpha}^{\dagger} + \hat{a}_{\alpha})$  defines the photon displacement coordinate using the electronic creation and annihilation operators [17, 148]. Furthermore, we only describe the two valence electrons explicitly and we choose for the nuclear masses  $M_1 = m_p$  and  $M_2 = m_p$ , where  $m_p$  is the proton mass. For the nuclear charges, we select  $Z_1 = 1.2$ , and  $Z_2 = 0.8$ . The masses  $m_3$  and  $m_4$  are set to the electron mass  $m_e$ , i.e.  $m_3 = m_4 = m_e$ . In one-dimensional problems the electronic Coulomb interaction is routinely modeled by a soft-coulomb interaction [160]. In the photon Hamiltonian  $\hat{H}_{\text{pt}}$ , we consider the electron-nuclear-photon coupling in dipole approximation using the coupling constant  $\lambda_{\alpha}$  and the electron-nuclear dipole operator  $\mathbf{R}$ . The latter consists of an electronic and a nuclear contribution  $\mathbf{R} = \mathbf{R}_n + \mathbf{R}_e$ , where  $\mathbf{R}_n = Z_1 \mathbf{X}_1 + Z_2 \mathbf{X}_2$  and  $\mathbf{R}_e = -\mathbf{x}_3 - \mathbf{x}_4$ . The complete many-body problem including two electrons, two nuclei and one photon mode is a five-dimensional problem. To reduce the computational complexity, we use the following relative coordinates: the electron distance coordinate  $\mathbf{x} = \mathbf{x}_1 - \mathbf{x}_2$ , the nuclear distance coordinate  $\mathbf{X} = \mathbf{X}_1 - \mathbf{X}_2$ , the distance between the electronic and the nuclear center of masses  $\boldsymbol{\xi}$  and the global center of mass  $\mathbf{X}_{\text{CM2}}$  [161]. For more details, we also refer the reader to the appendix E. These relative coordinates allow to reduce the dimensionality of the problem to four dimensions. We use the following real-space grid:  $N_X = 61$ ,  $dX = 0.08$ ,  $N_x = 41$ ,  $dx = 0.5$ ,  $N_{\xi} = 51$ ,  $d\xi = 0.2$ ,  $N_{pt} = 40$ , where the latter describes the maximum number of photons in the system. For clarity, we will use throughout this section, the original coordinates  $\mathbf{X}_1, \mathbf{X}_2, \mathbf{x}_3, \mathbf{x}_4$  in all formulas. The cavity frequency  $\omega_{\alpha}$  is chosen to be in resonance to the first vibronic transition  $\omega_{12}$ , hence  $\omega_{\alpha} = \omega_{12} = 0.01216$  a.u.. The dipole moment of this transition has a value of  $d_{12} = 0.01869$  a.u..

The Hamiltonian in Eq. 244 contains two matter-photon interaction terms, the explicit matter-photon interaction  $\hat{H}_{\text{int}} = \sum_{\alpha} \omega_{\alpha} \hat{q}_{\alpha} (\lambda_{\alpha} \cdot \mathbf{R})$  and the quadratic electron-nuclear self-energy term  $\hat{H}_{\text{es}} = \sum_{\alpha} (\lambda_{\alpha} \cdot \mathbf{R})^2 / 2$ . By introducing the electron-photon

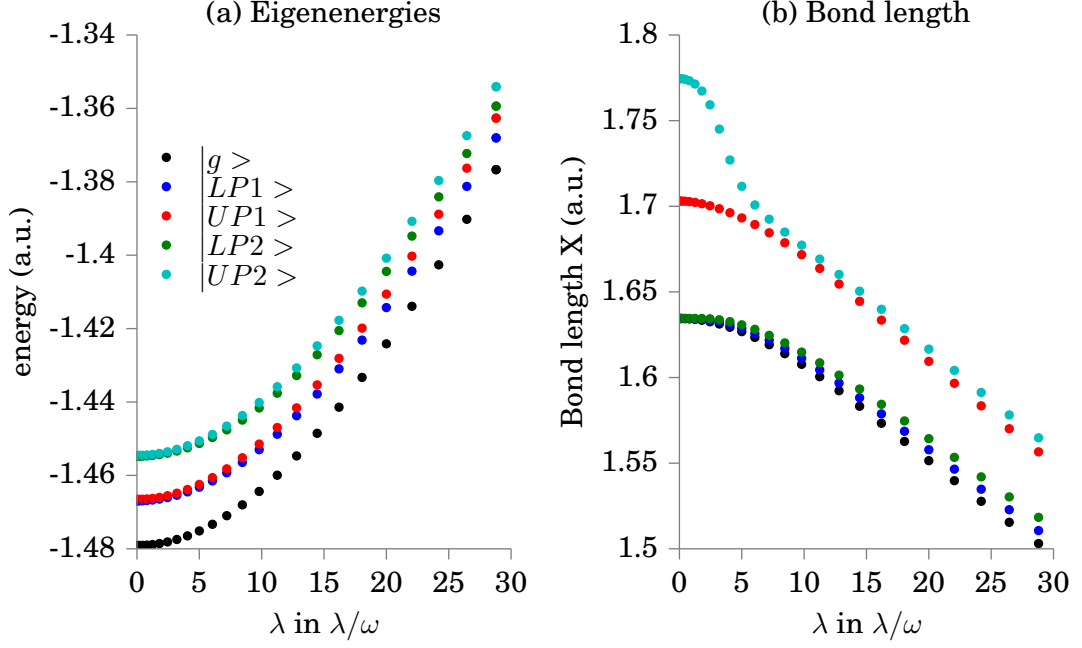


Figure 42: (a) shows the eigenenergies for different values of the matter-photon interaction strength  $\lambda$ , (b) shows the bond length  $\langle \mathbf{X}_1 - \mathbf{X}_2 \rangle$ . Black dots correspond to the ground-state  $|g\rangle$ , blue dots to the lower-polariton state  $|LP\rangle$  and red dots to the upper-polariton state  $|UP\rangle$ , green dots to the second lower-polariton state  $|LP2\rangle$  and cyan plots to the second upper-polariton state  $|UP2\rangle$ .

coupling constant  $\mathbf{g}_\alpha = \sqrt{\hbar\omega_\alpha}\lambda_\alpha/\sqrt{2}$ , we can explicitly connect to typical strong-coupling calculations, as in Ref. [159]. The quadratic electron-nuclear self-energy term is the analogue of the  $\mathbf{A}^2$  dependence in the momentum gauge. To our knowledge this term is often neglected and only rarely considered [162, 163]. The approximation neglecting  $\hat{H}_{\text{es}}$  is surely valid in the inter-molecular region, where it cancels the inter-molecular Coulomb interaction [70]. However in the intra-molecular region, which is the focus of the present study this term has to be taken into account. Additionally, we emphasize that in Eq. 244, the Coulomb interaction is considered in the cavity-free limit. In real-systems, we also expect a different form of the Coulomb interaction for cavity-systems, in particular in the strong-coupling regime.

Since the cavity frequency is close to the vibrational frequency and far from any electronic resonance, we consider the following approximation: The photons couple only to the nuclear coordinates, but not to the electronic coordinates. Therefore, we set  $\mathbf{R}^{(BO)}(\mathbf{X}_1, \mathbf{X}_2) = \mathbf{R}_n + \langle \mathbf{R}_e(\mathbf{X}_1, \mathbf{X}_2) \rangle$ , in the electron-nuclear-photon interaction Hamiltonian, while we keep the full  $\mathbf{R}$  dependence in the electron-nuclear self-energy Hamiltonian  $\hat{H}_{\text{es}}$ . In the following, we denote this approximation as cavity Born-Oppenheimer approximation (CBOA). To solve the BO problem, we first solve the electronic problem

$$\hat{H}_e(\mathbf{X}_1, \mathbf{X}_2) |\phi_j(\mathbf{X}_1, \mathbf{X}_2)\rangle = E_j(\mathbf{X}_1, \mathbf{X}_2) |\phi_j(\mathbf{X}_1, \mathbf{X}_2)\rangle, \quad (248)$$

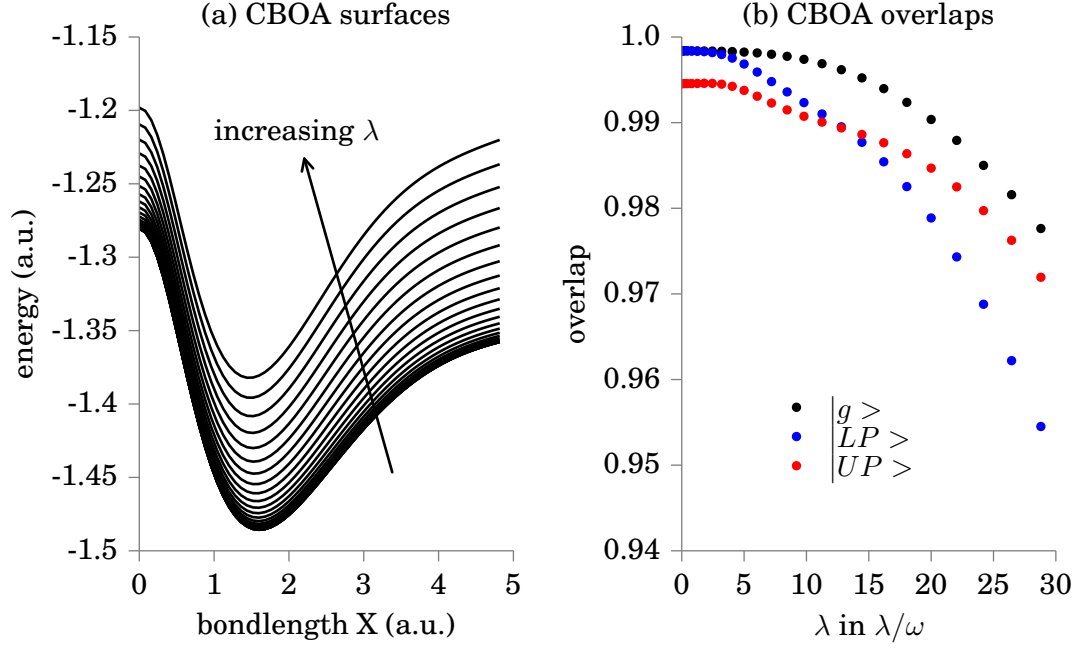


Figure 43: (a) shows the CBOA surfaces for different values of the matter-photon interaction strength  $\lambda$ , (b) shows the overlap of the exact states with the CBOA states. Black dots correspond to the ground state  $|g\rangle$ , blue dots to the lower-polariton state  $|LP\rangle$  and red dots to the upper-polariton state  $|UP\rangle$ .

with

$$\begin{aligned}
 \hat{H}_e(\mathbf{X}_1, \mathbf{X}_2) = & -\frac{\hbar^2}{2m_3} \vec{\nabla}_{\mathbf{x}_3}^2 - \frac{\hbar^2}{2m_4} \vec{\nabla}_{\mathbf{x}_4}^2 \\
 & + \frac{e^2}{4\pi\epsilon_0 \sqrt{(\mathbf{x}_3 - \mathbf{x}_4)^2 + 1}} - \frac{Z_1 e^2}{4\pi\epsilon_0 \sqrt{(\mathbf{X}_1 - \mathbf{x}_3)^2 + 1}} \\
 & - \frac{Z_1 e^2}{4\pi\epsilon_0 \sqrt{(\mathbf{X}_1 - \mathbf{x}_4)^2 + 1}} - \frac{Z_2 e^2}{4\pi\epsilon_0 \sqrt{(\mathbf{X}_2 - \mathbf{x}_3)^2 + 1}} \\
 & - \frac{Z_2 e^2}{4\pi\epsilon_0 \sqrt{(\mathbf{X}_2 - \mathbf{x}_4)^2 + 1}} + \frac{1}{2} \sum_{\alpha} (\lambda_{\alpha} \cdot \mathbf{R})^2.
 \end{aligned} \tag{249}$$

In a second step, we then solve the nuclear-photon problem

$$\begin{aligned}
 \hat{H}_j(\mathbf{X}_1, \mathbf{X}_2) = & -\frac{\hbar^2}{2M_1} \vec{\nabla}_{\mathbf{x}_1}^2 - \frac{\hbar^2}{2M_2} \vec{\nabla}_{\mathbf{x}_2}^2 + U_j(\mathbf{X}_1, \mathbf{X}_2) \\
 & + \sum_{\alpha} \frac{1}{2} [\hat{p}_{\alpha}^2 + \omega_{\alpha}^2 \hat{q}_{\alpha}^2] + \omega_{\alpha} \hat{q}_{\alpha} \lambda_{\alpha} \cdot \mathbf{R}^{(BO)}
 \end{aligned} \tag{250}$$

with the potential-energy surfaces (PES) in analogy to Eq. 13

$$U_j(\mathbf{X}_1, \mathbf{X}_2) = E_j(\mathbf{X}_1, \mathbf{X}_2) + \frac{Z_1 Z_2 e^2}{4\pi\epsilon_0 \sqrt{(\mathbf{X}_1 - \mathbf{X}_2)^2 + 1}}. \tag{251}$$

This procedure allows us to effectively decouple the system into an electronic and a nuclear-photon part. Using  $\hat{H}_j(\mathbf{X}_1, \mathbf{X}_2) |\chi_{ij}(\mathbf{X}_1, \mathbf{X}_2)\rangle = \epsilon_i(\mathbf{X}_1, \mathbf{X}_2) |\chi_{ij}(\mathbf{X}_1, \mathbf{X}_2)\rangle$ , where

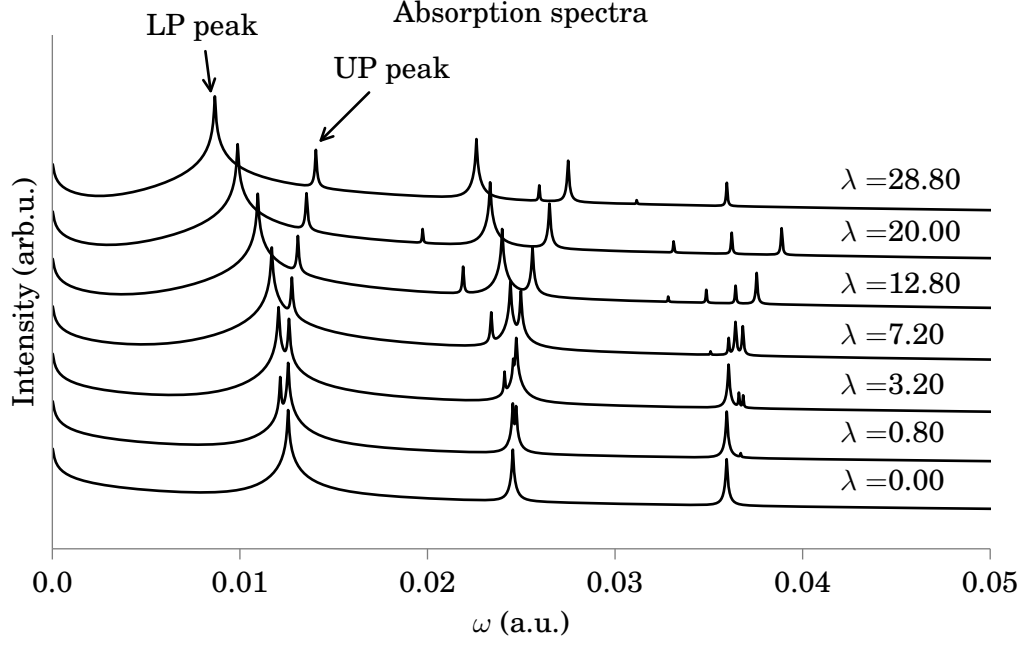


Figure 44: Absorption spectra for different matter-photon coupling strength  $\lambda_\alpha$ . *LP* denotes the lower-polariton peak and *UP* the upper-polariton peak.

$|\chi_{ij}\rangle$  denotes a correlated nuclear-photon wave function, we can construct the BO states, i.e. for the BO ground state  $|\Psi_0\rangle = |\chi_{00}\phi_0\rangle$ . Such a procedure reduces for  $\lambda_\alpha = 0$  to the usual BOA [26], where no matter-field interaction is present.

In the following, we present our results applying the CBOA. For the matter-photon coupling strength, we choose values between  $0 \leq \lambda_\alpha \leq 30\omega_\alpha$ .

In Fig. 42 (a), we show the eigenenergies of the cavity system as function of the matter-photon coupling strength  $\lambda_\alpha$ . The general harmonic trend is given by the self-energy term, which is nonnegligible for the given system. In black, we plot the ground-state energy, in red/blue (cyan/green), we plot the first (second) upper and lower-polariton states. The matter-photon coupling induces the Rabi splitting in the energy, as illustrated in Fig. 41. With increasing  $\lambda_\alpha$ , we find an increasing Rabi splitting. The bond length,  $X$  of the individual states is plotted in Fig. 42 (b). For this plot the same color code as in panel (a) applies. We find that the matter-photon coupling introduces large changes in the bond length, in our case the bond length is reduced from 1.63 a.u. to 1.50 a.u. for the ground state.

In Fig. 43 (a), we explicitly show different CBOA surfaces obtained from the CBOA Hamiltonian Eq. 249. These surfaces depend on the nuclear coordinate  $X$ , which is also a measure for the nuclear bond length. We find that for increasing  $\lambda_\alpha$  the matter self-energy term introduces a harmonic (parabolic) potential, which introduces major changes in the BO surfaces. The lowest surfaces in the figure corresponds to the cavity-free limit. The results illustrate that tuning  $\lambda_\alpha$  allows to shape the BO surfaces harmonically. In general, changes in the BO surfaces change the chemistry of the system, with implications on various quantities e.g. the bond length, tunneling barriers, or band gaps. Additionally in Fig. 42, we find that an increasing value of  $\lambda_\alpha$  shifts the bond length to smaller values. In Fig. 43 (b), we assess the quality of the CBOA approximation. While for small



values of  $\lambda_\alpha$  the CBOA has the same quality as the cavity-free electronic BOA, we observe the break-down of the CBOA for strong matter-photon interaction. The overlap of the CBOA ground state with the exact correlated ground state drops to 97%. Similar to the usual BOA, the quality of higher-lying states, which are here the upper and the lower-polariton states, is smaller compared to the quality of the ground state. In Fig. 44, we show an example for a spectroscopic quantity, which is highly influenced by the strong matter-photon coupling. The ground-state absorption spectrum can be calculated using a sum-over-states expression [159]

$$\sigma(\omega) = \frac{4\pi\omega}{c} \text{Im} \lim_{\delta \rightarrow 0} \frac{|\langle \Psi_k | \mathbf{R} | \Psi_0 \rangle|^2}{\omega_k - \omega_0 - \omega - i\delta}. \quad (252)$$

The correlated ground-state is denoted by  $|\Psi_0\rangle$  and has the eigenenergy  $\hbar\omega_0$ . In the numerical calculations, we apply a broadening of the individual peaks, as presented in Ref. [140] and in Chap. 4 for electron-phonon problems for photoelectron spectroscopy. In Fig. 44, we show spectra for different matter-photon coupling strength  $\lambda_\alpha$ . For increasing coupling, we find a clear signature of the Rabi splitting. In the spectra, we explicitly denote the lower-polaritonic and the upper-polaritonic peak, which are clearly visible in the strong-coupling limit. Additionally higher-lying excitations also show the Rabi splitting, e.g. the second peak shows a three-fold degeneracy.

### 8.3 SUMMARY

In summary, in this chapter we have shown how a correlated electron-phonon-photon calculation can be performed. We find that adding the photonic degrees of freedom introduces major changes in the electronic structure of the system. We find that in the strong-coupling regime, chemical quantities of the system change quite dramatically, e.g the BO surfaces, the bond length, or the absorption spectrum. All these findings suggest a wealth of novel applications by modifying and shaping the chemical landscape or the reaction barriers with the help of the strong-coupling regime in optical cavities.



Part V

CONCLUSION



## SUMMARY, CONCLUSIONS AND OUTLOOK

---

In this thesis, we treated electron-nuclear, electron-photon and electron-nuclear-photon problems. The electron-nuclear problem is typically treated by employing the BOA, where the nuclei enter the electronic equations as classical parameters. A similar approximation is typically used in electron-photon problems. Here, in typical electronic structure calculations, the effect of the photon field enters through a (time-dependent) external potential. To study effects beyond these classical approximations is the prime goal of this thesis.

The electron-nuclear problem in photoelectron spectroscopy was studied in chapter 4. Here, we showed that the BOA introduces artificial peaks in the photoelectron spectra, which can be attributed to the factorized nature of the BOA. These peaks only vanish, if the exact correlated eigenfunctions are known. Naturally the question arises, how we can extend the present theory to incorporate these beyond BOA effects. Here, some theoretical development has already been taken place such as the electron-nuclear coupled cluster approach [126], the multi-component density-functional theory approach for electrons and nuclei [127], or an explicit electron-phonon Greens function theory [128, 129]. However, all these theories are still in their infancy and complete calculations, which treat many electrons and many nuclei on the same footing are still not feasible.

The chapters 5-7 have been devoted to the correlated electron-photon problem. At present, the description of electron-photon interactions using the density-functional approach QEDFT is still at a very early stage. QEDFT opens the possibility to perform a large kind of different calculations, which all treat both subsystems, the photons and the electrons on an equal footing. Although, the first steps towards the developments of a proper xc-functional using an OEP approach as discussed in Ch. 7 are very promising, there remain many open questions. For instances, is it possible to develop for electron-photon applications an analogue of the very successful LDA functional, which is among the most popular functionals in the electronic DFT? The usefulness of the QEDFT approach will highly depend on the quality of available functionals. This means that more research is necessary to develop new functionals. However, the quality of existing functionals (mean field and OEP) needs also be assessed in real space and many-electrons calculations to properly evaluate their validity. One further promising route may lie in directly applying the Green's function framework [164] to these correlated electron-photon problems. In this way, some of the problems of QEDFT may be circumvented.

The framework of QEDFT could also be extended to phonon problems. Since, phonons and photons both have bosonic character an extension may be doable. However, the extension to phonon-phonon interactions and in particular the study of the role of the dipole self-energy term requires further research and makes the extension not straightforward.

In the last chapter 8, we studied a correlated electron-photon-phonon problem. Here, we were able to show that the strong-coupling of the matter and the photon

field changes the chemical landscape quite dramatically. This new field is particularly driven by experiment [152, 153], which is now capable of studying ensembles of molecules strongly coupled to a resonant field mode. All these experiments are theoretically not very well understood, which shows the need of the development and extension of existing theory as well as the design of new algorithms. Additionally, ab-initio three-dimensional calculations are necessary to correctly explain, but also to predict the results of such experiments.

Part VI

APPENDIX





The minimal-coupling (momentum-gauge) Hamiltonian in Coulomb gauge with  $\vec{\nabla} \cdot \hat{\mathbf{A}}(\mathbf{r})$ , from Eq. 104 is written as

$$\hat{H}_{\min} = \sum_{i=1}^{n_e} \frac{1}{2m_e} [\hat{\mathbf{p}}_i - e\hat{\mathbf{A}}(\mathbf{r}_i)]^2 + \hat{W}_{ee} + \hat{W}_{eN}(\{\mathbf{R}\}) + \frac{\epsilon_0}{2} \int d^3\mathbf{r} [\hat{\mathbf{E}}_T^2(\mathbf{r}) + c^2\hat{\mathbf{B}}^2(\mathbf{r})]. \quad (253)$$

This form of the Hamiltonian may be inconvenient for the following reasons:

- The canonical momentum conjugated to the position operator  $\mathbf{r}_i$  is not the kinetic momentum as in field-free situations:

$$m_e \frac{\partial}{\partial t} \hat{\mathbf{r}}_i = \frac{im_e}{\hbar} [\hat{H}_{\min}, \mathbf{r}_i] = \hat{\mathbf{p}}_i - e\hat{\mathbf{A}}(\mathbf{r}_i), \quad (254)$$

but consists of two terms,  $\hat{\mathbf{p}}_i$  that is a matter quantity and  $\hat{\mathbf{A}}(\mathbf{r}_i)$  that is a field quantity. In contrast, the canonical momentum to the vector field (calculated by using the commutation relations for  $\hat{\mathbf{E}}_T(\mathbf{r})$  and  $\hat{\mathbf{A}}(\mathbf{r})$  from Eq. 102

$$\frac{\partial}{\partial t} \hat{\mathbf{A}}(\mathbf{r}) = \frac{i}{\hbar} [\hat{H}_{\min}, \hat{\mathbf{A}}(\mathbf{r})] = -\hat{\mathbf{E}}_T(\mathbf{r}) \quad (255)$$

is the transverse electric field operator, which is a gauge-invariant field quantity.

- The Hamiltonian in Eq. 104 contains a term proportional to  $\hat{\mathbf{A}}^2(\mathbf{r}_i)$ . This term yields operators, which create and destroy two photons. Furthermore, this term mediates a nonlinear interaction between particles.
- The matter-field interaction is given by the term  $\hat{\mathbf{p}}_i \cdot \hat{\mathbf{A}}(\mathbf{r}_i)$ . Since  $\hat{\mathbf{A}}$  is not gauge-invariant (see Chap. 2.3.2), also the interaction is not explicitly written in a gauge-invariant form.

All these reasons make it desirable to cast Eq. 104 in a different form. Some of above problems can be cured by considering the Power-Zienau-Woolley transformation [70, 131]. This unitary transformation is defined by the transformation operator

$$\hat{S} = \frac{1}{\hbar c} \int d\mathbf{r} \hat{\mathbf{P}}(\mathbf{r}) \cdot \hat{\mathbf{A}}(\mathbf{r}). \quad (256)$$

Here,  $\hat{\mathbf{P}}(\mathbf{r})$  denotes the *electric polarization field operator* and is defined formally as [70]

$$\hat{\mathbf{P}}(\mathbf{r}) = e \int d\lambda \mathbf{r}' \delta(\mathbf{r} - \lambda \mathbf{r}'). \quad (257)$$

All operators are transformed into the new frame by

$$\hat{U}^T \hat{F} \hat{U} = e^{i\hat{S}} \hat{F} e^{-i\hat{S}} = \hat{F} + i [\hat{S}, \hat{F}] - \frac{1}{2} [\hat{S}, [\hat{S}, \hat{F}]] \dots \quad (258)$$

Many operators (in particular  $\mathbf{r}_i$  and  $\hat{\mathbf{A}}(\mathbf{r})$ ) appearing in Eq. 104 remain invariant under the Power-Zienau-Woolley Transformation, however two operators change

$$\hat{U}^T \hat{\mathbf{p}}_i \hat{U} = \hat{\mathbf{p}}_i + e \hat{\mathbf{A}}(\mathbf{r}_i) - \int d^3\mathbf{r} \hat{\boldsymbol{\theta}}(\mathbf{r}) \times \hat{\mathbf{B}}(\mathbf{r}), \quad (259)$$

$$\hat{U}^T \hat{\mathbf{E}}_T(\mathbf{r}) \hat{U} = \hat{\mathbf{E}}_T(\mathbf{r}) - \frac{1}{\epsilon_0} \hat{\mathbf{P}}(\mathbf{r}), \quad (260)$$

with  $\hat{\boldsymbol{\theta}}(\mathbf{r}) = e \mathbf{r}' \int_0^1 d\lambda \lambda \delta(\mathbf{r} - \lambda \mathbf{r}')$ . This vector fields definition is similar to the electric polarization operator, but differs by a  $\lambda$  under the integrand. The *new* operators on the right-hand side of the above equations are in general not equal to their *old* equivalent. For clarification, we replace the quantity  $\hat{\mathbf{E}}_T(\mathbf{r})$  appearing on the right-hand side of Eq. 260, by  $\hat{\mathbf{D}}_T(\mathbf{r})/\epsilon_0$ , where  $\hat{\mathbf{D}}_T(\mathbf{r})$  is the displacement field operator. We note, that the same is the case for the momentum operator  $\hat{\mathbf{p}}$ , i.e. the operator  $\hat{\mathbf{p}}$  in the *old* frame is different to the operator  $\hat{\mathbf{p}}$  in the *new* frame. However, we leave the symbol to be consistent with literature. Plugging Eqns. 259-260 into Eq. 104 leads us to the Power-Zienau-Woolley or multipolar/length-gauge Hamiltonian

$$\begin{aligned} \hat{H}_{PZ} = & \sum_{i=1}^{n_e} \frac{1}{2m_e} \left[ \hat{\mathbf{p}}_i - \int d^3\mathbf{r} \hat{\boldsymbol{\theta}}(\mathbf{r}) \times \hat{\mathbf{B}}(\mathbf{r}) \right]^2 + \hat{W}_{ee} + \hat{W}_{eN}(\{\mathbf{R}\}) \\ & + \frac{1}{2} \int d^3\mathbf{r} \left[ \hat{\mathbf{D}}_T^2(\mathbf{r})/\epsilon_0 + \epsilon_0 c^2 \hat{\mathbf{B}}^2(\mathbf{r}) \right] + \frac{1}{2\epsilon_0} \int d^3\mathbf{r} \hat{\mathbf{P}}^2(\mathbf{r}) - \frac{1}{\epsilon_0} \int d^3\mathbf{r} \hat{\mathbf{P}}(\mathbf{r}) \cdot \hat{\mathbf{D}}(\mathbf{r}), \end{aligned} \quad (261)$$

which is equal to Eq. 119 in the dipole approximation. Formally, we now cured most of the previously mentioned shortcomings: The new canonical momenta in the dipole approximation are as follows

$$m_e \frac{\partial}{\partial t} \mathbf{r}_i = \frac{im_e}{\hbar} [\hat{H}_{PZ}, \mathbf{r}_i] = \hat{\mathbf{p}}_i, \quad (262)$$

$$\frac{\partial}{\partial t} \hat{\mathbf{A}}(\mathbf{r}) = \frac{i}{\hbar} [\hat{H}_{PZ}, \hat{\mathbf{A}}(\mathbf{r})] = -\frac{1}{\epsilon_0} (\hat{\mathbf{D}}_T(\mathbf{r}) - \hat{\mathbf{P}}_T(\mathbf{r})). \quad (263)$$

The canonical momentum to the position operator  $\mathbf{r}_i$  is now again the kinetic momentum, as in field-free situations. However, the canonical momentum to the vector potential operator  $\hat{\mathbf{A}}(\mathbf{r})$  now consists of the displacement field operator  $\hat{\mathbf{D}}_T(\mathbf{r})$  and the matter quantity, the polarization operator  $\hat{\mathbf{P}}(\mathbf{r})$ . In addition, in the Power-Zienau-Woolley Hamiltonian, the matter-field interaction is written explicitly in a gauge-invariant form, namely  $\hat{\mathbf{P}}_T(\mathbf{r}) \cdot \hat{\mathbf{D}}_T(\mathbf{r})$  and also the two-photon operators stemming from the quadratic  $\hat{\mathbf{A}}^2(\mathbf{r})$ -term are avoided.

However, we emphasize that the physical behavior of the system, i.e. the observables, is the same either in the length gauge and the momentum gauge. Which form of the Hamiltonian is more convenient for the practical calculation depends on the specific problem.

GAUGE CONDITIONS ON  $a_{\text{ext}}$ B.1 COUPLING OF  $a_{\text{ext}}^0$  TO THE ELECTRON DENSITY

In this section, we show how the Pauli-Fierz Hamiltonian of Eq. 108 can be rewritten such that the external potential  $a_{\text{ext}}^0$  couples to the electron density. Furthermore, we recover the momentum-gauge Hamiltonian from Eq. 104. The Pauli-Fierz Hamiltonian in Ref. [18] is defined as follows

$$\begin{aligned}\hat{H}(t) = & \hat{H}_{\text{M}} + \hat{H}_{\text{EM}} + \hat{H}_{\text{C}} - \int d^3\mathbf{r} \hat{\mathbf{J}}(\mathbf{r}, t) \cdot \hat{\mathbf{A}}(\mathbf{r}) \\ & + \frac{1}{c} \int d^3\mathbf{r} \hat{J}_0(\mathbf{r}) \left( A_{\text{tot}}^0(\mathbf{r}, t) - \frac{e}{2m} \hat{\mathbf{A}}_{\text{tot}}^2(\mathbf{r}) \right) \\ & - \int d^3\mathbf{r} (\hat{\mathbf{J}}(\mathbf{r}, t) \cdot \mathbf{a}_{\text{ext}}(\mathbf{r}, t) + \hat{\mathbf{A}}(\mathbf{r}) \cdot \mathbf{j}_{\text{ext}}(\mathbf{r}, t)).\end{aligned}\quad (264)$$

As next step, we apply the following gauge condition  $\mathbf{a}_{\text{ext}}(\mathbf{r}, t) = 0, j_{\text{ext}}^0(\mathbf{r}, t) = 0$  and neglect any magnetization

$$\begin{aligned}\hat{H}(t) = & \hat{H}_{\text{M}} + \hat{H}_{\text{EM}} + \hat{H}_{\text{C}} - \int d^3\mathbf{r} \hat{\mathbf{J}}_{\text{p}}(\mathbf{r}) \cdot \hat{\mathbf{A}}(\mathbf{r}) + \frac{e}{2mc} \int d^3\mathbf{r} \hat{J}_0(\mathbf{r}) \hat{\mathbf{A}}^2(\mathbf{r}) \\ & - \int d^3\mathbf{r} \left( \hat{\mathbf{A}}(\mathbf{r}) \cdot \mathbf{j}_{\text{ext}}(\mathbf{r}, t) - \frac{1}{c} \hat{J}_0(\mathbf{r}) a_{\text{ext}}^0(\mathbf{r}, t) \right).\end{aligned}\quad (265)$$

Next, we plug in the definitions of  $\mathbf{J}_{\text{p}}(\mathbf{r})$  from Eq. 112 and the zero component of the current  $\hat{J}_0(\mathbf{r}) = ec \hat{\Psi}^\dagger(\mathbf{r}) \hat{\Psi}(\mathbf{r})$ . Further, we use integration by parts such that

$$\begin{aligned}\int d^3\mathbf{r} \left( \vec{\nabla} \hat{\Psi}^\dagger(\mathbf{r}) \right) \hat{\mathbf{A}}(\mathbf{r}) \hat{\Psi}(\mathbf{r}) = & \hat{\Psi}^\dagger(\mathbf{r}) \hat{\mathbf{A}}(\mathbf{r}) \hat{\Psi}(\mathbf{r}) \Big|_{\Omega} \\ & - \int d^3\mathbf{r} \hat{\Psi}^\dagger(\mathbf{r}) \vec{\nabla} \cdot (\hat{\mathbf{A}}(\mathbf{r}) \hat{\Psi}(\mathbf{r})),\end{aligned}\quad (266)$$

where the first term at the right-hand side is evaluated at the boundary of the integration volume  $\Omega$ . We assume that this term vanishes. Making use of these simplifications, we end up with

$$\begin{aligned}\hat{H}(t) = & \frac{1}{2m} \int d^3\mathbf{r} \hat{\Psi}^\dagger(\mathbf{r}) (\hat{\mathbf{p}} - e\hat{\mathbf{A}}(\mathbf{r}))^2 \hat{\Psi}(\mathbf{r}) + \hat{H}_{\text{EM}} + \hat{H}_{\text{C}} \\ & - \int d^3\mathbf{r} (\hat{\mathbf{A}}(\mathbf{r}) \cdot \mathbf{j}_{\text{ext}}(\mathbf{r}, t) - e\hat{n}(\mathbf{r}) a_{\text{ext}}^0(\mathbf{r}, t)),\end{aligned}\quad (267)$$

which is the minimal coupling Hamiltonian from Eq. 104 with additional coupling terms of the basic variables to the external fields and potentials. In the last term, we identify the explicit coupling of the external potential  $a_{\text{ext}}^0(\mathbf{r}, t)$  to the electron density  $\hat{n}(\mathbf{r})$ .

B.2 COUPLING OF  $\mathbf{a}_{\text{ext}}$  TO THE ELECTRON CURRENT

We apply the following gauge condition  $a_{\text{ext}}^0(\mathbf{r}, t) = 0, j_{\text{ext}}^0(\mathbf{r}, t) = 0$  with the goal rewrite the Pauli-Fierz Hamiltonian of Eq. 108 such that the external vector field  $\mathbf{a}_{\text{ext}}$  couples explicitly to the electron current operator. We find

$$\begin{aligned} \hat{H}(t) = & \hat{H}_{\text{M}} + \hat{H}_{\text{EM}} + \hat{H}_{\text{C}} \\ & - \int d^3\mathbf{r} \hat{\mathbf{J}}(\mathbf{r}, t) \cdot \hat{\mathbf{A}}_{\text{tot}}(\mathbf{r}) - \frac{e}{2mc} \int d^3\mathbf{r} \hat{j}_0(\mathbf{r}) \hat{\mathbf{A}}_{\text{tot}}^2(\mathbf{r}) \\ & - \int d^3\mathbf{r} \hat{\mathbf{A}}(\mathbf{r}) \cdot \mathbf{j}_{\text{ext}}(\mathbf{r}, t), \end{aligned} \quad (268)$$

then leads directly to

$$\begin{aligned} \hat{H}(t) = & \frac{1}{2m} \int d^3\mathbf{r} \hat{\Psi}^\dagger(\mathbf{r}) (\hat{\mathbf{p}} - e\hat{\mathbf{A}}_{\text{tot}}(\mathbf{r}))^2 \hat{\Psi}(\mathbf{r}) + \hat{H}_{\text{EM}} + \hat{H}_{\text{C}} \\ & - \int d^3\mathbf{r} \hat{\mathbf{A}}(\mathbf{r}) \cdot \mathbf{j}_{\text{ext}}(\mathbf{r}, t), \end{aligned} \quad (269)$$

which is the minimal coupling Hamiltonian of Eq. 104 with additional coupling terms of the basic variables to external fields and potentials.

## DERIVATION OF JAYNES-CUMMINGS-HUBBARD MODEL FROM THE NONRELATIVISTIC HAMILTONIAN

To derive the Jaynes-Cummings model system studied in Sec. 5.5 from the Hamiltonian in Eq. 267, we consider only one single-electron and one single-photon mode. Therefore  $\hat{H}_{EM} = -\frac{\hbar\omega}{2} \frac{d^2}{dq^2} + \frac{\hbar\omega}{2} q^2$  with  $\hat{\mathbf{A}} = \mathcal{C} \frac{q\boldsymbol{\epsilon}}{\sqrt{\omega}}$ , where we use  $\mathcal{C} = \left(\frac{\hbar}{\epsilon_0 L^3}\right)^{1/2}$ . Under these assumptions, Eq. 267 becomes

$$\begin{aligned} \hat{H}(t) = & \frac{1}{2m} \left( \frac{\hbar}{i} \vec{\nabla} - e\hat{\mathbf{A}} \right)^2 - \frac{\hbar\omega}{2} \frac{d^2}{dq^2} + \frac{\hbar\omega}{2} q^2 \\ & + ea_{\text{ext}}^0(\mathbf{r}, t) - \mathbf{j}_{\text{ext}}(t) \cdot \hat{\mathbf{A}}, \end{aligned} \quad (270)$$

In the next step, we perform the Power-Zienau-Woolley transformation (Sec. A) explicitly. The unitary transformation operator reads

$$\hat{U} = \exp \left[ \frac{i}{\hbar} \left( \mathcal{C} e \frac{\boldsymbol{\epsilon} \cdot \mathbf{r}}{\sqrt{\omega}} q \right) \right] = \exp \left[ \frac{i}{\hbar} (e\mathbf{r} \cdot \hat{\mathbf{A}}) \right]. \quad (271)$$

We need to transform the following two operators

$$\hat{U}^\dagger \frac{\hbar}{i} \vec{\nabla} \hat{U} = \frac{\hbar}{i} \vec{\nabla} + e\hat{\mathbf{A}}, \quad (272)$$

$$\hat{U}^\dagger \frac{d}{dq} \hat{U} = \frac{d}{dq} + \frac{i}{\hbar} \left( \mathcal{C} e \frac{\boldsymbol{\epsilon} \cdot \mathbf{r}}{\sqrt{\omega}} \right), \quad (273)$$

with the substitution  $id/dq \rightarrow p$  and  $q \rightarrow -id/dp$ , we end up with the Power-Zienau-Woolley Hamiltonian

$$\begin{aligned} \hat{H}(t) = & -\frac{\hbar^2}{2m} \vec{\nabla}^2 + \frac{\hbar\omega}{2} \left( p - \frac{\mathcal{C} e \boldsymbol{\epsilon} \cdot \mathbf{r}}{\hbar \sqrt{\omega}} \right)^2 - \frac{\hbar\omega}{2} \frac{d^2}{dp^2} \\ & + ea_{\text{ext}}^0(\mathbf{r}, t) + \frac{i\mathcal{C}}{\sqrt{\omega}} \boldsymbol{\epsilon} \cdot \mathbf{j}_{\text{ext}}(t) \frac{d}{dp}. \end{aligned} \quad (274)$$

We continue with yet another time-dependent gauge transformation (here we use  $\frac{d}{dx} \int_a^x f(t) dt = f(x)$ )

$$\hat{U}(t) = \exp \left[ \frac{i\mathcal{C}}{\hbar\omega^{\frac{3}{2}}} \left( j_{\text{ext}}(t)p + \frac{\mathcal{C}}{2\hbar\sqrt{\omega}} \int_0^t j_{\text{ext}}^2(t') dt' \right) \right]. \quad (275)$$

Then

$$\hat{U}^\dagger \frac{d}{dp} \hat{U} = \frac{d}{dp} + \frac{i\mathcal{C}}{\hbar\omega^{\frac{3}{2}}} j_{\text{ext}}(t), \quad (276)$$

$$\hat{U}^\dagger \partial_t \hat{U} = \frac{i\mathcal{C}}{\hbar\omega^{\frac{3}{2}}} \left( \partial_t j_{\text{ext}}(t)p + \frac{\mathcal{C}}{2\hbar\sqrt{\omega}} j_{\text{ext}}^2(t) \right). \quad (277)$$

Hence, the new Hamiltonian takes the form

$$\begin{aligned}\hat{H}(t) = & -\frac{\hbar^2}{2m}\vec{\nabla}^2 + \frac{\hbar\omega}{2}\left(p - \frac{Ce}{\hbar}\frac{\boldsymbol{\epsilon} \cdot \mathbf{r}}{\sqrt{\omega}}\right)^2 - \frac{\hbar\omega}{2}\frac{d^2}{dp^2} \\ & + ea_{\text{ext}}^0(\mathbf{r}, t) + \frac{C}{\omega^{\frac{3}{2}}}j_{\text{ext}}(t)p,\end{aligned}\quad (278)$$

where  $j_{\text{ext}}(t) = \boldsymbol{\epsilon} \cdot \mathbf{j}_{\text{ext}}(t)$ . In the last step, we discretize the matter part and employ a two-site approximation for the single electron

$$-\frac{\hbar^2}{2m}\vec{\nabla}^2 \rightarrow -t_{\text{kin}}\hat{\sigma}_x, \quad (279)$$

$$e\omega\boldsymbol{\epsilon} \cdot \mathbf{r} \rightarrow e\omega\boldsymbol{\epsilon} \cdot \mathbf{l}\hat{\sigma}_z = e\hat{J}, \quad (280)$$

$$ea_{\text{ext}}^0(\mathbf{r}, t) \rightarrow eea_{\text{ext}}^0(t)\hat{\sigma}_z = -a_{\text{ext}}(t)\hat{J}, \quad (281)$$

$$\partial_t j_{\text{ext}}(t) \rightarrow \omega\tilde{j}_{\text{ext}}(t), \quad (282)$$

$$\frac{C}{\sqrt{\omega}}p \rightarrow \hat{A} = \frac{C}{\sqrt{2\omega}}(\hat{a}^\dagger + \hat{a}). \quad (283)$$

Using these replacements, we end up with the Hamiltonian in Eq. 145.

## DERIVATION OF THE SPECTRAL FUNCTION

The one-body spectral function is defined as follows [58]

$$\begin{aligned}
 A_{ij}(t, t') &= \langle \Psi_0 | \{ \hat{c}_i(t) \hat{c}_j^\dagger(t') \} | \Psi_0 \rangle \\
 A_{ij}(t, t') &= \langle \Psi_0 | \hat{c}_j^\dagger(t') \hat{c}_i(t) + \hat{c}_i(t) \hat{c}_j^\dagger(t') | \Psi_0 \rangle \\
 A_{ij}(t, t') &= A_{ij}^<(t, t') + A_{ij}^>(t, t'),
 \end{aligned} \tag{284}$$

with  $t' > t$ . The operators  $\hat{c}$  and  $\hat{c}^\dagger$  are here written in the Heisenberg picture. The index refers to a combined index  $i = (n, \sigma)$  and  $j = (m, \sigma')$ , where  $n$  and  $m$  refer to the site number and  $\sigma$  and  $\sigma'$  refer to spin up or spin down.

In this work, we only consider the first part of the commutator  $A_{ij}^<(t, t')$ , since we are interested in photoemission spectra. The second term  $A_{ij}^>(t, t')$  leads to inverse photoemission spectra [58]. In the following discussion, we distinguish two cases: (i) if  $\Psi_0$  is an eigenstate of the Hamiltonian  $\hat{H}$  of the system, we work in an equilibrium framework, (ii) if  $\Psi_0$  is not an eigenstate of the Hamiltonian  $\hat{H}$ , we have to work in a nonequilibrium framework.

## D.1 EQUILIBRIUM SPECTRAL FUNCTION

The equilibrium spectral function applies for situations, where  $\Psi_0$  is an eigenstate of the corresponding many-body Hamiltonian  $\hat{H}$  of the system. Hence, we can write Eq. 284 in terms of a time-correlation function

$$\begin{aligned}
 A_{ij}(t, t') &= \langle \Psi_0 | \hat{c}_j^\dagger(t') \hat{c}_i(t) | \Psi_0 \rangle \\
 &= \langle \Psi_0 | e^{i\hat{H}t'/\hbar} \hat{c}_j^\dagger e^{-i\hat{H}t'/\hbar} e^{i\hat{H}t/\hbar} \hat{c}_i e^{-i\hat{H}t/\hbar} | \Psi_0 \rangle \\
 &= \langle \Psi_0 | \hat{c}_j^\dagger e^{-i\hat{H}(t'-t)/\hbar} \hat{c}_i | \Psi_0 \rangle e^{iE_0(t'-t)/\hbar} \\
 &= \langle \Psi_0(\tau) | \hat{c}_j^\dagger | \tilde{\Psi}(\tau) \rangle,
 \end{aligned} \tag{285}$$

with  $\tau = t' - t$  and the initial condition  $|\tilde{\Psi}(\tau = \tau_0)\rangle = \hat{c}_i |\Psi_0\rangle$ .

Eq. 284 can be reformulated to get a sum-over-states expression. This is accom-

plished by the insertion of an complete set of states  $\sum_m |\Psi_m\rangle \langle \Psi_m| = \mathbb{1}$  and a Fourier transform with respect to the time-difference  $\tau = t' - t$

$$\begin{aligned} A_{ij}^<(t, t') &= \langle \Psi_0 | \hat{c}_j^\dagger(t') \hat{c}_i(t) | \Psi_0 \rangle \\ &= \langle \Psi_0 | e^{i\hat{H}t'/\hbar} \hat{c}_j^\dagger e^{-i\hat{H}t'/\hbar} e^{i\hat{H}t/\hbar} \hat{c}_i e^{-i\hat{H}t/\hbar} | \Psi_0 \rangle \\ &= \sum_m \langle \Psi_0 | \hat{c}_j^\dagger | \Psi_m \rangle \langle \Psi_m | \hat{c}_i | \Psi_0 \rangle e^{i(E_0 - E_m)(t' - t)/\hbar}, \end{aligned} \quad (286)$$

$$\begin{aligned} A_{ij}^<(\omega) &= \int_{-\infty}^{\infty} \frac{d\tau}{2\pi} \sum_m \langle \Psi_0 | \hat{c}_j^\dagger | \Psi_m \rangle \langle \Psi_m | \hat{c}_i | \Psi_0 \rangle \\ &\quad \times e^{i(E_0 - E_m - \hbar\omega)\tau/\hbar} \\ &= \sum_m \langle \Psi_0 | \hat{c}_j^\dagger | \Psi_m \rangle \langle \Psi_m | \hat{c}_i | \Psi_0 \rangle \delta(E_0 - E_m - \hbar\omega), \end{aligned} \quad (287)$$

$$A_{ii}^<(\omega) = \sum_m |\langle \Psi_0 | \hat{c}_i^\dagger | \Psi_m \rangle|^2 \delta(E_0 - E_m - \hbar\omega). \quad (288)$$

## D.2 NONEQUILIBRIUM SPECTRAL FUNCTION

In nonequilibrium situations,  $\Psi_0$  is not an eigenstate of the many-body Hamiltonian  $\hat{H}$ . Nevertheless, it is also possible to formulate the spectral function in Eq. 284 as time-correlation function involving propagated states

$$\begin{aligned} A_{ij}^<(t, t') &= \langle \Psi_0 | \hat{c}_j^\dagger(t') \hat{c}_i(t) | \Psi_0 \rangle \\ &= \langle \Psi_0 | e^{i\hat{H}t'/\hbar} \hat{c}_j^\dagger e^{-i\hat{H}t'/\hbar} e^{i\hat{H}t/\hbar} \hat{c}_i e^{-i\hat{H}t/\hbar} | \Psi_0 \rangle \\ &= \langle \Psi_0(t') | \hat{c}_j^\dagger e^{-i\hat{H}(t' - t)/\hbar} \hat{c}_i | \Psi_0(t) \rangle, \end{aligned} \quad (289)$$

$$A_{ij}^<(t, \tau) = \langle \Psi_0(\tau + t) | \hat{c}_j^\dagger | \tilde{\Psi}(\tau + t, t) \rangle. \quad (290)$$

We introduce the relative time  $\tau = t' - t$ , as in Sec. D.1, while  $t$  keeps its initial notation. The state  $|\tilde{\Psi}(\tau + t, t)\rangle$  is defined as  $|\tilde{\Psi}(\tau + t, t)\rangle = e^{-i\hat{H}\tau/\hbar} \hat{c}_i | \Psi_0(t) \rangle$ , meaning the kick  $\hat{c}_i$  on the wave function that removes one electron from the system acts at time  $t$  during the time propagation. A Fourier transform with respect to the relative time  $\tau$  yields the general expression for the sum-over-states expression

$$\begin{aligned} A_{ij}^<(t, t') &= \langle \Psi_0 | \hat{c}_j^\dagger(t') \hat{c}_i(t) | \Psi_0 \rangle, \\ A_{ij}^<(t, \tau) &= \langle \Psi_0 | e^{i\hat{H}(\tau + t)/\hbar} \hat{c}_j^\dagger e^{-i\hat{H}\tau/\hbar} \hat{c}_i e^{-i\hat{H}t/\hbar} | \Psi_0 \rangle \\ &= \sum_{n, n', m} e^{i\tau/\hbar(E_{n'} - E_m) + it/\hbar(E_{n'} - E_n)} \\ &\quad \times \langle \Psi_0 | \Psi_{n'} \rangle \langle \Psi_{n'} | \hat{c}_j^\dagger | \Psi_m \rangle \langle \Psi_m | \hat{c}_i | \Psi_n \rangle \langle \Psi_n | \Psi_0 \rangle, \end{aligned} \quad (291)$$

$$\begin{aligned} A_{ij}^<(t, \omega) &= \int_{-\infty}^{\infty} \frac{d\tau}{2\pi} \sum_{n, n', m} e^{i\tau/\hbar(E_{n'} - E_m - \hbar\omega) + it/\hbar(E_{n'} - E_n)} \\ &\quad \times \langle \Psi_0 | \Psi_{n'} \rangle \langle \Psi_{n'} | \hat{c}_j^\dagger | \Psi_m \rangle \langle \Psi_m | \hat{c}_i | \Psi_n \rangle \langle \Psi_n | \Psi_0 \rangle \\ &= \sum_{n, n', m} e^{it/\hbar(E_{n'} - E_n)} \delta(E_{n'} - E_m - \hbar\omega) \\ &\quad \times \langle \Psi_0 | \Psi_{n'} \rangle \langle \Psi_{n'} | \hat{c}_j^\dagger | \Psi_m \rangle \langle \Psi_m | \hat{c}_i | \Psi_n \rangle \langle \Psi_n | \Psi_0 \rangle. \end{aligned} \quad (292)$$



In our simulations, we neglect the energy dependence of the delta function in the last equation. Hence, we replace the term  $E_{n'}$  by the energy  $E_0$  of the state  $\Psi_0$ . This leads to

$$\begin{aligned}
 A_{ij}^<(t, \omega) &= \sum_{n, n', m} e^{it/\hbar(E_{n'} - E_n)} \delta(E_0 - E_m - \hbar\omega) \\
 &\quad \times \langle \Psi_0 | \Psi_{n'} \rangle \langle \Psi_{n'} | \hat{c}_j^\dagger | \Psi_m \rangle \langle \Psi_m | \hat{c}_i | \Psi_n \rangle \langle \Psi_n | \Psi_0 \rangle \\
 &= \sum_m \langle \Psi_0(t) | \hat{c}_j^\dagger | \Psi_m \rangle \langle \Psi_m | \hat{c}_i | \Psi_0(t) \rangle \delta(E_0 - E_m - \hbar\omega), \tag{293}
 \end{aligned}$$

$$A_{ii}^<(t, \omega) = \sum_m |\langle \Psi_0(t) | \hat{c}_i^\dagger | \Psi_m \rangle|^2 \delta(E_0 - E_m - \hbar\omega). \tag{294}$$



## COORDINATE TRANSFORMATION FOR DIATOMIC MOLECULES

In this chapter, we derive the coordinate transformation, which allows to separate the center-of-mass motion of the Hamiltonian in Eq. 244. This goal is achieved by using relative coordinates, which are similar to the transformation used in Ref. [161] for the case of a neutral homonuclear diatomic molecule. We start with the Hamiltonian  $\hat{H}_{\text{en}}$  of Eq. 244

$$\begin{aligned} \hat{H}_{\text{en}} = & -\frac{\hbar^2}{2M_1m_p}\vec{\nabla}_{\mathbf{x}_1}^2 - \frac{\hbar^2}{2M_2m_p}\vec{\nabla}_{\mathbf{x}_2}^2 - \frac{\hbar^2}{2m_e}\vec{\nabla}_{\mathbf{x}_3}^2 - \frac{\hbar^2}{2m_e}\vec{\nabla}_{\mathbf{x}_4}^2 \\ & + \frac{e^2}{4\pi\epsilon_0}\frac{Z_1Z_2}{\sqrt{(\mathbf{X}_1 - \mathbf{X}_2)^2 + 1}} + \frac{e^2}{4\pi\epsilon_0}\frac{1}{\sqrt{(\mathbf{x}_3 - \mathbf{x}_4)^2 + 1}} - \frac{e^2}{4\pi\epsilon_0}\frac{Z_1}{\sqrt{(\mathbf{X}_1 - \mathbf{x}_3)^2 + 1}} \\ & - \frac{e^2}{4\pi\epsilon_0}\frac{Z_1}{\sqrt{(\mathbf{X}_1 - \mathbf{x}_4)^2 + 1}} - \frac{e^2}{4\pi\epsilon_0}\frac{Z_2}{\sqrt{(\mathbf{X}_2 - \mathbf{x}_3)^2 + 1}} - \frac{e^2}{4\pi\epsilon_0}\frac{Z_2}{\sqrt{(\mathbf{X}_2 - \mathbf{x}_4)^2 + 1}}. \end{aligned} \quad (295)$$

Here,  $\mathbf{X}_1$  is a nuclear coordinate corresponding to a nucleus with mass  $m_1 = M_1m_p$  and charge  $Q_1 = Z_1e$ ,  $\mathbf{X}_2$  is a nuclear coordinate corresponding to a nucleus with mass  $m_2 = M_2m_p$  and charge  $Q_2 = Z_2e$ ,  $\mathbf{x}_3$ , and  $\mathbf{x}_4$ , are electronic coordinates with masses  $m_3 = m_4 = m_e$ , where  $m_e$  is the electron mass,  $m_p$  the mass of a proton and  $Z_1, Z_2, M_1, M_2$  are dimensionless scalars. The total charge is fixed to  $Q_1 + Q_2 = 2$ . We now introduce the following new coordinates:

electronic center of mass coordinate	$\mathbf{x}_{\text{CM1}} = \frac{\mathbf{x}_1 + \mathbf{x}_2}{2},$
distance between electrons	$\mathbf{x} = \mathbf{x}_2 - \mathbf{x}_1,$
nuclear center of mass coordinate	$\mathbf{X}_{\text{CM1}} = \frac{M_1\mathbf{X}_1 + M_2\mathbf{X}_2}{M_1 + M_2},$
distance between nuclei	$\mathbf{X} = \mathbf{X}_2 - \mathbf{X}_1.$

These relative coordinates can now be used to perform a global center of mass transformation, but keeping the nuclear and electronic distance coordinates  $\mathbf{x}$  and  $\mathbf{X}$

global center of mass	$\mathbf{X}_{\text{CM2}} = \frac{(M_1 + M_2)m_p\mathbf{X}_{\text{CM1}} + 2m_e\mathbf{x}_{\text{CM1}}}{M},$
distance between $\mathbf{X}_{\text{CM1}}$ and $\mathbf{x}_{\text{CM1}}$	$\boldsymbol{\xi} = \mathbf{x}_{\text{CM1}} - \mathbf{X}_{\text{CM1}},$

with the total mass  $M = (M_1 + M_2) m_p + 2m_e$ . The coordinate definitions can also be formulated in terms of the following transformation matrices

$$\begin{pmatrix} \mathbf{X} \\ \mathbf{x} \\ \xi \\ \mathbf{x}_{CM2} \end{pmatrix} = \begin{pmatrix} -1 & 1 & 0 & 0 \\ 0 & 0 & -1 & 1 \\ -\frac{M_1}{M_1+M_2} & -\frac{M_2}{M_1+M_2} & \frac{1}{2} & \frac{1}{2} \\ \frac{M_1 m_p}{M} & \frac{M_2 m_p}{M} & \frac{m_e}{M} & \frac{m_e}{M} \end{pmatrix} \begin{pmatrix} \mathbf{X}_1 \\ \mathbf{X}_2 \\ \mathbf{x}_1 \\ \mathbf{x}_2 \end{pmatrix},$$

$$\begin{pmatrix} \mathbf{p}_{\mathbf{X}_1} \\ \mathbf{p}_{\mathbf{X}_2} \\ \mathbf{p}_{\mathbf{x}_1} \\ \mathbf{p}_{\mathbf{x}_2} \end{pmatrix} = \begin{pmatrix} -1 & 0 & -\frac{M_1 m_p}{M} & \frac{M_1 m_p}{M} \\ 1 & 0 & -\frac{M_2 m_p}{M} & \frac{M_2 m_p}{M} \\ 0 & -1 & \frac{1}{2} & \frac{m_e}{M} \\ 0 & 1 & \frac{1}{2} & \frac{m_e}{M} \end{pmatrix} \begin{pmatrix} \mathbf{p}_{\mathbf{X}} \\ \mathbf{p}_{\mathbf{x}} \\ \mathbf{p}_{\xi} \\ \mathbf{p}_{\mathbf{x}_{CM2}} \end{pmatrix}.$$

If we plug both into Eq. 295, we obtain the following Hamiltonian

$$\begin{aligned} \hat{H}_{\text{en}} = & \frac{M_1 + M_2}{2M_1 M_2 m_p} \mathbf{p}_{\mathbf{X}}^2 + \frac{1}{m_e} \mathbf{p}_{\mathbf{x}}^2 + \frac{2m_e + (M_1 + M_2) m_p}{4(M_1 + M_2) m_e m_p} \mathbf{p}_{\xi}^2 + \frac{1}{2M} \mathbf{p}_{\mathbf{x}_{CM2}}^2 \\ & + \frac{e^2}{4\pi\epsilon_0} \frac{Z_1 Z_2}{\sqrt{\mathbf{X}^2 + 1}} + \frac{e^2}{4\pi\epsilon_0} \frac{1}{\sqrt{\mathbf{x}^2 + 1}} - \frac{e^2}{4\pi\epsilon_0} \frac{Z_1}{\sqrt{\left(\xi - \frac{1}{2}\mathbf{x} + \frac{M_2}{M_1+M_2}\mathbf{X}\right)^2 + 1}} \\ & - \frac{e^2}{4\pi\epsilon_0} \frac{Z_1}{\sqrt{\left(\xi + \frac{1}{2}\mathbf{x} + \frac{M_2}{M_1+M_2}\mathbf{X}\right)^2 + 1}} - \frac{e^2}{4\pi\epsilon_0} \frac{Z_2}{\sqrt{\left(-\xi + \frac{1}{2}\mathbf{x} + \frac{M_2}{M_1+M_2}\mathbf{X}\right)^2 + 1}} \\ & - \frac{e^2}{4\pi\epsilon_0} \frac{Z_2}{\sqrt{\left(-\xi - \frac{1}{2}\mathbf{x} + \frac{M_2}{M_1+M_2}\mathbf{X}\right)^2 + 1}}. \end{aligned}$$

The dipole operator is defined in old and new coordinates as

$$\hat{\mathbf{d}} = e(Z_1 \mathbf{X}_1 + Z_2 \mathbf{X}_2 - \mathbf{x}_3 - \mathbf{x}_4) = e\left(-2\xi + \frac{M_1 Z_2 - M_2 Z_1}{M_1 + M_2} \mathbf{X}\right).$$

## ATOMIC UNITS

### F.1 HARTREE ATOMIC UNITS

We shortly review the Hartree atomic units. In these units, we set  $m_e = e = \hbar = 1/4\pi\epsilon_0 = 1$ . These quantities correspond to the following values in SI units

Name	Symbol	Value in SI
electron rest mass	$m_e$	$9.11 \cdot 10^{-31}$ kg
elementary electric charge	$e$	$1.60 \cdot 10^{-19}$ C
reduced Planck's constant	$\hbar$	$1.05 \cdot 10^{-34}$ Js
electric constant <sup>-1</sup>	$\frac{1}{4\pi\epsilon_0}$	$8.99 \cdot 10^9$ kg m <sup>3</sup> s <sup>-2</sup> C <sup>-2</sup>

Using this definition derived units for the length, energy and time take the following form

Name	Symbol	Expression	Value in SI
length	$a_0$	$4\pi\epsilon_0\hbar^2/(m_e e^2)$	$5.2918 \cdot 10^{-11}$ m
energy	$E_h$	$m_e e^4/(4\pi\epsilon_0\hbar)^2$	$4.5397 \cdot 10^{-18}$ J
time	$u_t$	$\hbar/E_h$	$2.4189 \cdot 10^{-17}$ s

### F.2 EFFECTIVE ATOMIC UNITS FOR A GAAS SYSTEM

In Ch. 6, we use an effective atomic unit system for the model system of GaAs. We use the values from a GaAs semiconductor, with:

$m^* = 0.067m_e$  and  $\zeta = 12.7\epsilon_0$  as given in Ref. [96]. This effectively means that in the effective atomic units  $m^* = \frac{1}{4\pi\zeta} = \hbar = e = 1$ . We can use the above table to derive the following effective units

$$\begin{aligned}
 E_h^* &= m^* e^4 / (4\pi\zeta\hbar)^2 = \frac{0.067}{12.7^2} E_h = 11.30 \text{ meV}, \\
 a_0^* &= 4\pi\epsilon_0\hbar^2 / (m_e e^2) = \frac{12.7}{0.067} a_0 = 10.03 \text{ nm}, \\
 u_t^* &= \hbar / E_h^* = \frac{12.7^2}{0.067} u_t = 58.23 \text{ fs}.
 \end{aligned}$$



## BIBLIOGRAPHY

---

- [1] J. C. Maxwell, *A Dynamical Theory of the Electromagnetic Field*, Phil. Trans. R. Soc. London **155**, 459–512 (1865) (cit. on p. 3).
- [2] *Nobel Lectures in Physics, 1901-1921*, Nobel Lectures in Physics, World Scientific Publishing, 1998, ISBN: 9819234915 (cit. on p. 3).
- [3] *Nobel Lectures in Physics, 1922-1941*, Nobel Lectures in Physics, World Scientific Publishing, 1998, ISBN: 9810234023 (cit. on p. 3).
- [4] E. Schrödinger, *An Undulatory Theory of the Mechanics of Atoms and Molecules*, Phys. Rev. **28**, 6, 1049–1070 (1926), DOI: [10.1103/PhysRev.28.1049](#) (cit. on pp. 3, 9).
- [5] W. Kohn, *Nobel Lecture: Electronic structure of matter—wave functions and density functionals*, Rev. Mod. Phys. **71**, 5, 1253–1266 (1999), DOI: [10.1103/RevModPhys.71.1253](#) (cit. on pp. 3, 15, 16).
- [6] P. Hohenberg and W. Kohn, *Inhomogeneous Electron Gas*, Phys. Rev. **136**, 3B, 864–871 (1964), DOI: [10.1103/PhysRev.136.B864](#) (cit. on pp. 3, 16, 17, 78).
- [7] L. H. Thomas, *The calculation of atomic fields*, Math. Proc. Cambridge **23**, 05, 542–548 (1927), DOI: [10.1017/S0305004100011683](#) (cit. on p. 3).
- [8] W. Kohn and L. J. Sham, *Self-Consistent Equations Including Exchange and Correlation Effects*, Phys. Rev. **140**, 4A, 1133–1138 (1965), DOI: [10.1103/PhysRev.140.A1133](#) (cit. on pp. 3, 18, 20).
- [9] A. D. Becke, *Density-functional exchange-energy approximation with correct asymptotic behavior*, Phys. Rev. A **38**, 6, 3098–3100 (1988), DOI: [10.1103/PhysRevA.38.3098](#) (cit. on pp. 3, 21).
- [10] E. Runge and E. K. U. Gross, *Density-Functional Theory for Time-Dependent Systems*, Phys. Rev. Lett. **52**, 12, 997–1000 (1984), DOI: [10.1103/PhysRevLett.52.997](#) (cit. on pp. 4, 22, 24, 78, 81, 82).
- [11] B. F. Milne, Y. Toker, A. Rubio, and S. B. Nielsen, *Unraveling the Intrinsic Color of Chlorophyll*, Angew. Chem. Int. Edit. **127**, 7, 2198–2201 (2015), DOI: [10.1002/ange.201410899](#) (cit. on p. 4).
- [12] J. Jornet-Somoza, J. Alberdi-Rodriguez, B. F. Milne, X. Andrade, M. A. L. Marques, F. Nogueira, M. J. T. Oliveira, J. J. P. Stewart, and A. Rubio, *Insights into colour-tuning of chlorophyll optical response in green plants*, Phys. Chem. Chem. Phys. **17**, 40, 26599–26606 (2015), DOI: [10.1039/c5cp03392f](#) (cit. on pp. 4, 37).
- [13] U. De Giovannini, D. Varsano, M. A. L. Marques, H. Appel, E. K. U. Gross, and A. Rubio, *Ab initio angle- and energy-resolved photoelectron spectroscopy with time-dependent density-functional theory*, Phys. Rev. A **85**, 6, 062515 (2012), DOI: [10.1103/PhysRevA.85.062515](#) (cit. on pp. 4, 9).

- [14] U. De Giovannini, G. Brunetto, A. Castro, J. Walkenhorst, and A. Rubio, *Simulating Pump–Probe Photoelectron and Absorption Spectroscopy on the Attosecond Timescale with Time-Dependent Density Functional Theory*, *ChemPhysChem* **14**, 7, 1363–1376 (2013), DOI: [10.1002/cphc.201201007](#) (cit. on pp. [4](#), [63](#)).
- [15] M. Born and R. Oppenheimer, *Zur Quantentheorie der Molekeln*, *Ann. Phys.* **389**, 20, 457–484 (1927), DOI: [10.1002/andp.19273892002](#) (cit. on pp. [4](#), [11](#)).
- [16] M. Ruggenthaler, F. Mackenroth, and D. Bauer, *Time-dependent Kohn-Sham approach to quantum electrodynamics*, *Phys. Rev. A* **84**, 4, 042107 (2011), DOI: [10.1103/PhysRevA.84.042107](#) (cit. on pp. [4](#), [77](#)).
- [17] I. V. Tokatly, *Time-Dependent Density Functional Theory for Many-Electron Systems Interacting with Cavity Photons*, *Phys. Rev. Lett.* **110**, 23, 233001 (2013), DOI: [10.1103/PhysRevLett.110.233001](#) (cit. on pp. [4](#), [22](#), [77](#), [78](#), [80](#), [81](#), [83](#), [119](#)).
- [18] M. Ruggenthaler, J. Flick, C. Pellegrini, H. Appel, I. V. Tokatly, and A. Rubio, *Quantum-electrodynamical density-functional theory: Bridging quantum optics and electronic-structure theory*, *Phys. Rev. A* **90**, 1, 012508 (2014), DOI: [10.1103/PhysRevA.90.012508](#) (cit. on pp. [4](#), [15](#), [30](#), [34](#), [77](#), [78](#), [80](#), [81](#), [133](#)).
- [19] T. Renner, *Quantities, Units and Symbols in Physical Chemistry*, ed. by E. R. Cohen, T. Cvitas, J. G. Frey, B. Holstrom, K. Kuchitsu, R. Marquardt, I. Mills, F. Pavese, M. Quack, J. Stohner, H. L. Strauss, M. Takami, and A. J. Thor, The Royal Society of Chemistry, 2007, P001–232, ISBN: 978-0-85404-433-7, DOI: [10.1039/9781847557889](#) (cit. on pp. [9](#), [29](#), [37](#)).
- [20] T. M. Gibbons, B. Kang, S. K. Estreicher, and C. Carbogno, *Thermal conductivity of Si nanostructures containing defects: Methodology, isotope effects, and phonon trapping*, *Phys. Rev. B* **84**, 3, 035317 (2011), DOI: [10.1103/PhysRevB.84.035317](#) (cit. on p. [9](#)).
- [21] X. Ge, I. Timrov, S. Binnie, A. Biancardi, A. Calzolari, and S. Baroni, *Accurate and Inexpensive Prediction of the Color Optical Properties of Anthocyanins in Solution*, *J. Phys. Chem. A* **119**, 16, 3816–3822 (2015), DOI: [10.1021/acs.jpca.5b01272](#) (cit. on p. [9](#)).
- [22] S. Bhattacharya, S. V. Levchenko, L. M. Ghiringhelli, and M. Scheffler, *Efficient ab initio schemes for finding thermodynamically stable and metastable atomic structures: benchmark of cascade genetic algorithms*, *New J. Phys.* **16**, 12, 123016 (2014), DOI: [10.1088/1367-2630/16/12/123016](#) (cit. on p. [9](#)).
- [23] A. Szabo and N. Ostlund, *Modern Quantum Chemistry: Introduction to Advanced Electronic Structure Theory*, Dover Books on Chemistry, Dover Publications, 1989, ISBN: 9780486691862 (cit. on p. [10](#)).
- [24] J. Kohanoff, *Electronic Structure Calculations for Solids and Molecules: Theory and Computational Methods*, Cambridge University Press, 2006, ISBN: 9781139453486 (cit. on p. [10](#)).
- [25] W. Heisenberg, *Über den anschaulichen Inhalt der quantentheoretischen Kinetik und Mechanik*, *z. Phys.* **43**, 3-4, 172–198 (1927), DOI: [10.1007/BF01397280](#) (cit. on p. [10](#)).



- [26] E. Gross, E. Runge, and O. Heinonen, *Many-Particle Theory*, Adam Hilger, 1991, ISBN: 9780750300728 (cit. on pp. 11, 21, 122).
- [27] M. Born and K. Huang, *Dynamical Theory of Crystal Lattices*, Oxford University Press: London, 1956 (cit. on p. 11).
- [28] G. Vignale and W. Kohn, *Current-Dependent Exchange-Correlation Potential for Dynamical Linear Response Theory*, Phys. Rev. Lett. **77**, 10, 2037–2040 (1996), DOI: [10.1103/PhysRevLett.77.2037](#) (cit. on pp. 15, 77, 78).
- [29] H. Eschrig, *The fundamentals of density functional theory*, Teubner-Texte zur Physik, Teubner, 1996, ISBN: 9783815430309 (cit. on p. 15).
- [30] C. Fiolhais, F. Nogueira, and M. Marques, *A Primer in Density Functional Theory*, Lecture Notes in Physics, Springer, 2003, ISBN: 9783540030836 (cit. on p. 15).
- [31] K. Capelle, *A bird's-eye view of density-functional theory*, Braz. J. Phys. **36**, 4a, 1318–1343 (2006), DOI: [10.1590/S0103-97332006000700035](#) (cit. on pp. 15, 16, 18, 19).
- [32] E. Engel and R. Dreizler, *Density Functional Theory: An Advanced Course*, Theoretical and Mathematical Physics, Springer, 2011, ISBN: 9783642140907 (cit. on p. 15).
- [33] T. L. Gilbert, *Hohenberg-Kohn theorem for nonlocal external potentials*, Phys. Rev. B **12**, 6, 2111–2120 (1975), DOI: [10.1103/PhysRevB.12.2111](#) (cit. on p. 16).
- [34] J. E. Harriman, *Orthonormal orbitals for the representation of an arbitrary density*, Phys. Rev. A **24**, 2, 680–682 (1981), DOI: [10.1103/PhysRevA.24.680](#) (cit. on p. 16).
- [35] M. Levy, *Universal variational functionals of electron densities, first-order density matrices, and natural spin-orbitals and solution of the  $v$ -representability problem*, Proc. Natl. Acad. Sci. USA **76**, 12, 6062–6065 (1979), DOI: [10.1073/pnas.76.12.6062](#) (cit. on p. 17).
- [36] T. Dimitrov, H. Appel, J. I. Fuks, and A. Rubio, *Exact maps in density functional theory for lattice models*, New J. Phys. **18**, 8, 083004 (2016) (cit. on p. 18).
- [37] W. Kohn,  *$v$ -Representability and Density Functional Theory*, Phys. Rev. Lett. **51**, 17, 1596–1598 (1983), DOI: [10.1103/PhysRevLett.51.1596](#) (cit. on p. 18).
- [38] M. Levy, *Electron densities in search of Hamiltonians*, Phys. Rev. A **26**, 3, 1200–1208 (1982), DOI: [10.1103/PhysRevA.26.1200](#) (cit. on p. 18).
- [39] E. H. Lieb, *Density functionals for coulomb systems*, Int. J. Quantum Chem. **24**, 3, 243–277 (1983), DOI: [10.1002/qua.560240302](#) (cit. on p. 18).
- [40] A. Tkatchenko and M. Scheffler, *Accurate Molecular Van Der Waals Interactions from Ground-State Electron Density and Free-Atom Reference Data*, Phys. Rev. Lett. **102**, 7, 073005 (2009), DOI: [10.1103/PhysRevLett.102.073005](#) (cit. on pp. 20, 21).
- [41] R. van Leeuwen and E. J. Baerends, *Exchange-correlation potential with correct asymptotic behavior*, Phys. Rev. A **49**, 4, 2421–2431 (1994), DOI: [10.1103/PhysRevA.49.2421](#) (cit. on p. 20).

- [42] N. Helbig, I. V. Tokatly, and A. Rubio, *Exact Kohn–Sham potential of strongly correlated finite systems*, J. Chem. Phys. **131**, 22, 224105 (2009), DOI: [10.1063/1.3271392](#) (cit. on pp. [20](#), [99](#)).
- [43] M. A. Marques, M. J. Oliveira, and T. Burnus, *Libxc: A library of exchange and correlation functionals for density functional theory*, Comput. Phys. Comm. **183**, 10, 2272–2281 (2012), DOI: [10.1016/j.cpc.2012.05.007](#) (cit. on p. [20](#)).
- [44] A. D. Becke, *Completely numerical calculations on diatomic molecules in the local-density approximation*, Phys. Rev. A **33**, 4, 2786–2788 (1986), DOI: [10.1103/PhysRevA.33.2786](#) (cit. on p. [20](#)).
- [45] J. P. Perdew and A. Zunger, *Self-interaction correction to density-functional approximations for many-electron systems*, Phys. Rev. B **23**, 10, 5048–5079 (1981), DOI: [10.1103/PhysRevB.23.5048](#) (cit. on p. [21](#)).
- [46] J. P. Perdew, J. A. Chevary, S. H. Vosko, K. A. Jackson, M. R. Pederson, D. J. Singh, and C. Fiolhais, *Atoms, molecules, solids, and surfaces: Applications of the generalized gradient approximation for exchange and correlation*, Phys. Rev. B **46**, 11, 6671–6687 (1992), DOI: [10.1103/PhysRevB.46.6671](#) (cit. on p. [21](#)).
- [47] J. P. Perdew, K. Burke, and M. Ernzerhof, *Generalized Gradient Approximation Made Simple*, Phys. Rev. Lett. **77**, 18, 3865–3868 (1996), DOI: [10.1103/PhysRevLett.77.3865](#) (cit. on p. [21](#)).
- [48] J. P. Perdew, A. Ruzsinszky, G. I. Csonka, O. A. Vydrov, G. E. Scuseria, L. A. Constantin, X. Zhou, and K. Burke, *Restoring the Density-Gradient Expansion for Exchange in Solids and Surfaces*, Phys. Rev. Lett. **100**, 13, 136406 (2008), DOI: [10.1103/PhysRevLett.100.136406](#) (cit. on p. [21](#)).
- [49] T. Tsuneda, *Density Functional Theory in Quantum Chemistry*, SpringerLink: Bücher, Springer Japan, 2014, ISBN: 9784431548256 (cit. on p. [21](#)).
- [50] J. Heyd, G. E. Scuseria, and M. Ernzerhof, *Hybrid functionals based on a screened Coulomb potential*, J. Chem. Phys. **118**, 18, 8207–8215 (2003), DOI: [10.1063/1.1564060](#) (cit. on p. [21](#)).
- [51] M. Marques, N. Maitra, F. Nogueira, E. Gross, and A. Rubio, *Fundamentals of Time-Dependent Density Functional Theory*, Lecture Notes in Physics, Springer Berlin Heidelberg, 2012, ISBN: 9783642235177 (cit. on p. [21](#)).
- [52] C. Ullrich, *Time-Dependent Density-Functional Theory: Concepts and Applications*, Oxford Graduate Texts, OUP Oxford, 2012, ISBN: 9780199563029 (cit. on p. [21](#)).
- [53] R. van Leeuwen, *Mapping from Densities to Potentials in Time-Dependent Density-Functional Theory*, Phys. Rev. Lett. **82**, 19, 3863–3866 (1999), DOI: [10.1103/PhysRevLett.82.3863](#) (cit. on pp. [22](#), [23](#)).
- [54] M. Ruggenthaler and R. van Leeuwen, *Global fixed-point proof of time-dependent density-functional theory*, EPL **95**, 1, 13001 (2011), DOI: [10.1209/0295-5075/95/13001](#) (cit. on pp. [23](#), [56](#)).
- [55] M. Ruggenthaler, K. J. H. Giesbertz, M. Penz, and R. van Leeuwen, *Density-potential mappings in quantum dynamics*, Phys. Rev. A **85**, 5, 052504 (2012), DOI: [10.1103/PhysRevA.85.052504](#) (cit. on p. [23](#)).

- [56] G. Strinati, *Application of the Green's functions method to the study of the optical properties of semiconductors*, Riv. Nuovo Cim. **11**, 12, 1–86 (1988), DOI: [10.1007/BF02725962](#) (cit. on p. [25](#)).
- [57] G. Mahan, *Many-Particle Physics*, Physics of Solids and Liquids, Springer, 2000, ISBN: 9780306463389 (cit. on pp. [25](#), [107](#)).
- [58] G. Stefanucci and R. van Leeuwen, *Nonequilibrium Many-Body Theory of Quantum Systems: A Modern Introduction*, Cambridge University Press: Cambridge, England, 2013, 190–202, ISBN: 9780521766173 (cit. on pp. [25](#), [28](#), [108](#), [137](#)).
- [59] F. Caruso, *Self-consistent GW approach for the unified description of ground and excited states of finite systems*, PhD thesis, Freie Universität Berlin, 2013 (cit. on pp. [25](#), [28](#)).
- [60] M. A. Marques, C. A. Ullrich, F. Nogueira, A. Rubio, K. Burke, and E. K. U. Gross, *Time-dependent density functional theory*, vol. 706, Springer, 2006 (cit. on p. [26](#)).
- [61] R. P. Feynman, *Space-Time Approach to Quantum Electrodynamics*, Phys. Rev. **76**, 6, 769–789 (1949), DOI: [10.1103/PhysRev.76.769](#) (cit. on p. [27](#)).
- [62] L. J. Sham and M. Schlüter, *Density-Functional Theory of the Energy Gap*, Phys. Rev. Lett. **51**, 20, 1888–1891 (1983), DOI: [10.1103/PhysRevLett.51.1888](#) (cit. on p. [28](#)).
- [63] R. van Leeuwen, *The Sham-Schlüter Equation in Time-Dependent Density-Functional Theory*, Phys. Rev. Lett. **76**, 19, 3610–3613 (1996), DOI: [10.1103/PhysRevLett.76.3610](#) (cit. on pp. [28](#), [108](#)).
- [64] S. Kümmel and L. Kronik, *Orbital-dependent density functionals: Theory and applications*, Rev. Mod. Phys. **80**, 1, 3–60 (2008), DOI: [10.1103/RevModPhys.80.3](#) (cit. on pp. [28](#), [29](#), [115](#)).
- [65] S. Kümmel and J. P. Perdew, *Simple Iterative Construction of the Optimized Effective Potential for Orbital Functionals, Including Exact Exchange*, Phys. Rev. Lett. **90**, 4, 043004 (2003), DOI: [10.1103/PhysRevLett.90.043004](#) (cit. on pp. [29](#), [109](#)).
- [66] H. O. Wijewardane and C. A. Ullrich, *Real-Time Electron Dynamics with Exact-Exchange Time-Dependent Density-Functional Theory*, Phys. Rev. Lett. **100**, 5, 056404 (2008), DOI: [10.1103/PhysRevLett.100.056404](#) (cit. on pp. [29](#), [112](#)).
- [67] J. B. Krieger, Y. Li, and G. J. Iafrate, *Construction and application of an accurate local spin-polarized Kohn-Sham potential with integer discontinuity: Exchange-only theory*, Phys. Rev. A **45**, 1, 101–126 (1992), DOI: [10.1103/PhysRevA.45.101](#) (cit. on pp. [29](#), [115](#)).
- [68] F. H. Faisal, *Theory of Multiphoton Processes*, Berlin: Springer, 1987 (cit. on pp. [29](#), [36](#), [107](#), [119](#)).
- [69] C. Cohen-Tannoudji, J. Dupont-Roc, and G. Grynberg, *Photons and Atoms: Introduction to Quantum Electrodynamics*, Wiley, 1997, ISBN: 9780471184331 (cit. on p. [29](#)).

- [70] D. Craig and T. Thirunamachandran, *Molecular Quantum Electrodynamics: An Introduction to Radiation-molecule Interactions*, Dover Books on Chemistry Series, Dover Publications, 1998, ISBN: 9780486402147 (cit. on pp. 29–34, 36, 120, 131).
- [71] R. Loudon, *The Quantum Theory of Light*, Oxford University Press, 2000 (cit. on p. 29).
- [72] J. Jackson, *Classical Electrodynamics*, Wiley, 1999, ISBN: 9780471309321 (cit. on p. 29).
- [73] L. Silberstein, *Elektromagnetische Grundgleichungen in bivectorieller Behandlung*, Ann. Phys. **327**, 3, 579–586 (1907), DOI: [10.1002/andp.19073270313](#) (cit. on p. 32).
- [74] I. Bialynicki-Birula and Z. Bialynicka-Birula, *The role of the Riemann-Silberstein vector in classical and quantum theories of electromagnetism*, J. Phys. A Math. Theor. **46**, 5, 053001 (2013), DOI: [10.1088/1751-8113/46/15/159501](#) (cit. on p. 32).
- [75] C. Gerry and P. Knight, *Introductory Quantum Optics*, Cambridge University Press, 2005, ISBN: 9780521527354 (cit. on pp. 32, 47, 85).
- [76] K. Yabana, T. Sugiyama, Y. Shinohara, T. Otobe, and G. F. Bertsch, *Time-dependent density functional theory for strong electromagnetic fields in crystalline solids*, Phys. Rev. B **85**, 4, 045134 (2012), DOI: [10.1103/PhysRevB.85.045134](#) (cit. on p. 35).
- [77] R. G. Woolley, *Gauge invariant wave mechanics and the Power-Zienau-Woolley transformation*, J. Phys. A: Math. Gen **13**, 8, 2795 (1980) (cit. on p. 36).
- [78] M. Babiker and R. Loudon, *Derivation of the Power-Zienau-Woolley Hamiltonian in Quantum Electrodynamics by Gauge Transformation*, Proc. R. Soc. London, A **385**, 1789, 439–460 (1983), DOI: [10.1098/rspa.1983.0022](#) (cit. on p. 36).
- [79] S. Hüfner, *Photoelectron Spectroscopy*, vol. 3rd edn, Springer: Berlin, Germany, 2003 (cit. on pp. 37–39).
- [80] F. Reinert and S. Hüfner, *Photoemission spectroscopy—from early days to recent applications*, New J. Phys. **7**, 1, 97 (2005), DOI: [10.1088/1367-2630/7/1/097](#) (cit. on pp. 37–39, 65).
- [81] L. Hedin, *On correlation effects in electron spectroscopies and the GW approximation*, J. Phys.: Condens. Matter **11**, 42, R489 (1999), DOI: [10.1088/0953-8984/11/42/201](#) (cit. on p. 38).
- [82] C.-O. Almbladh and L. Hedin, *Beyond the one-electron model: many-body effects in atoms, molecules, and solids*, in: *Handbook on Synchrotron Radiation*, vol. 1B, North-Holland Publishing Company: Amsterdam, Netherlands, 1983, 611–1165 (cit. on p. 38).
- [83] G. Onida, L. Reining, and A. Rubio, *Electronic excitations: density-functional versus many-body Green's-function approaches*, Rev. Mod. Phys. **74**, 2, 601–659 (2002), DOI: [10.1103/RevModPhys.74.601](#) (cit. on pp. 38, 39).

- [84] J. Flick, H. Appel, and A. Rubio, *Nonadiabatic and Time-Resolved Photoelectron Spectroscopy for Molecular Systems*, J. Chem. Theory Comput. **10**, 4, 1665–1676 (2014), DOI: [10.1021/ct4010933](#) (cit. on pp. [38](#), [63](#)).
- [85] L. Hedin and J. Lee, *Sudden approximation in photoemission and beyond*, J. Electron Spectrosc. Relat. Phenom. **124**, 2–3, 289–315 (2002), DOI: [10.1016/S0368-2048\(02\)00060-9](#) (cit. on p. [38](#)).
- [86] R. van Leeuwen, *First-principles approach to the electron-phonon interaction*, Phys. Rev. B **69**, 11, 115110 (2004), DOI: [10.1103/PhysRevB.69.115110](#) (cit. on p. [40](#)).
- [87] W. P. Su, J. R. Schrieffer, and A. J. Heeger, *Solitons in Polyacetylene*, Phys. Rev. Lett. **42**, 25, 1698–1701 (1979), DOI: [10.1103/PhysRevLett.42.1698](#) (cit. on p. [45](#)).
- [88] A. J. Heeger, S. Kivelson, J. R. Schrieffer, and W. P. Su, *Solitons in conducting polymers*, Rev. Mod. Phys. **60**, 3, 781–850 (1988), DOI: [10.1103/RevModPhys.60.781](#) (cit. on p. [45](#)).
- [89] I. Franco, A. Rubio, and P. Brumer, *Long-lived oscillatory incoherent electron dynamics in molecules: trans -polyacetylene oligomers*, New J. Phys. **15**, 4, 043004 (2013), DOI: [10.1088/1367-2630/15/4/043004](#) (cit. on p. [45](#)).
- [90] N. Ashcroft and N. Mermin, *Solid State Physics*, HRW international editions, Holt, Rinehart and Winston, 1976, ISBN: 9780030839931 (cit. on p. [45](#)).
- [91] A. J. Leggett, S. Chakravarty, A. T. Dorsey, M. P. A. Fisher, A. Garg, and W. Zwerger, *Dynamics of the dissipative two-state system*, Rev. Mod. Phys. **59**, 1, 1–85 (1987), DOI: [10.1103/RevModPhys.59.1](#) (cit. on p. [47](#)).
- [92] B. Shore, *The Theory of Coherent Atomic Excitation: Multilevel atoms and incoherence*, The Theory of Coherent Atomic Excitation, Wiley, 1990, ISBN: 9780471524168 (cit. on p. [47](#)).
- [93] B. W. Shore and P. L. Knight, *The Jaynes-Cummings Model*, J. Mod. Opt. **40**, 7, 1195–1238 (1993), DOI: [10.1080/09500349314551321](#) (cit. on pp. [47](#), [48](#), [85](#), [88](#), [89](#), [118](#)).
- [94] D. Braak, *Integrability of the Rabi Model*, Phys. Rev. Lett. **107**, 10, 100401 (2011), DOI: [10.1103/PhysRevLett.107.100401](#) (cit. on pp. [47](#), [48](#)).
- [95] J. Casanova, G. Romero, I. Lizuain, J. J. García-Ripoll, and E. Solano, *Deep Strong Coupling Regime of the Jaynes-Cummings Model*, Phys. Rev. Lett. **105**, 26, 263603 (2010), DOI: [10.1103/PhysRevLett.105.263603](#) (cit. on p. [48](#)).
- [96] E. Räsänen, A. Castro, J. Werschnik, A. Rubio, and E. K. U. Gross, *Optimal Control of Quantum Rings by Terahertz Laser Pulses*, Phys. Rev. Lett. **98**, 15, 157404 (2007), DOI: [10.1103/PhysRevLett.98.157404](#) (cit. on pp. [48](#), [49](#), [143](#)).
- [97] T. Niemczyk, F. Deppe, H. Huebl, E. P. Menzel, F. Hocke, M. J. Schwarz, J. J. Garcia-Ripoll, D. Zueco, T. Hummer, E. Solano, A. Marx, and R. Gross, *Circuit quantum electrodynamics in the ultrastrong-coupling regime*, Nat. Phys. **6**, 10, 772–776 (2010), DOI: [10.1038/nphys1730](#) (cit. on p. [49](#)).



- [98] P. Forn-Díaz, J. Lisenfeld, D. Marcos, J. J. García-Ripoll, E. Solano, C. J. P. M. Harmans, and J. E. Mooij, *Observation of the Bloch-Siegert Shift in a Qubit-Oscillator System in the Ultrastrong Coupling Regime*, *Phys. Rev. Lett.* **105**, 23, 237001 (2010), DOI: [10.1103/PhysRevLett.105.237001](https://doi.org/10.1103/PhysRevLett.105.237001) (cit. on p. 49).
- [99] R. Ditchfield, W. J. Hehre, and J. A. Pople, *Self-Consistent Molecular-Orbital Methods. IX. An Extended Gaussian-Type Basis for Molecular-Orbital Studies of Organic Molecules*, *J. Chem. Phys.* **54**, 2, 724 (1971), DOI: [10.1063/1.1674902](https://doi.org/10.1063/1.1674902) (cit. on p. 50).
- [100] A. Gulans, S. Kontur, C. Meisenbichler, D. Nabok, P. Pavone, S. Rigamonti, S. Sagmeister, U. Werner, and C. Draxl, *exciting: a full-potential all-electron package implementing density-functional theory and many-body perturbation theory*, *J. Phys.: Condens. Matter* **26**, 36, 363202 (2014), DOI: [10.1088/0953-8984/26/36/363202](https://doi.org/10.1088/0953-8984/26/36/363202) (cit. on p. 50).
- [101] V. Blum, R. Gehrke, F. Hanke, P. Havu, V. Havu, X. Ren, K. Reuter, and M. Scheffler, *Ab initio molecular simulations with numeric atom-centered orbitals*, *Comput. Phys. Comm.* **180**, 11, 2175–2196 (2009), DOI: [10.1016/j.cpc.2009.06.022](https://doi.org/10.1016/j.cpc.2009.06.022) (cit. on p. 50).
- [102] X. Andrade, D. Strubbe, U. D. Giovannini, A. H. Larsen, M. J. T. Oliveira, J. Alberdi-Rodriguez, A. Varas, I. Theophilou, N. Helbig, M. J. Verstraete, L. Stella, F. Nogueira, A. Aspuru-Guzik, A. Castro, M. A. L. Marques, and A. Rubio, *Real-space grids and the Octopus code as tools for the development of new simulation approaches for electronic systems*, *Phys. Chem. Chem. Phys.* **17**, 47, 31371–31396 (2015), DOI: [10.1039/c5cp00351b](https://doi.org/10.1039/c5cp00351b) (cit. on p. 50).
- [103] P. Jordan and E. Wigner, *Über das Paulische Äquivalenzverbot*, *Z. Phys.* **47**, 9-10, 631–651 (1928), DOI: [10.1007/BF01331938](https://doi.org/10.1007/BF01331938) (cit. on p. 50).
- [104] A. I. Streltsov, O. E. Alon, and L. S. Cederbaum, *General mapping for bosonic and fermionic operators in Fock space*, *Phys. Rev. A* **81**, 2, 022124 (2010), DOI: [10.1103/PhysRevA.81.022124](https://doi.org/10.1103/PhysRevA.81.022124) (cit. on p. 54).
- [105] T. J. Park and J. C. Light, *Unitary quantum time evolution by iterative Lanczos reduction*, *J. Chem. Phys.* **85**, 10, 5870–5876 (1986), DOI: [10.1063/1.451548](https://doi.org/10.1063/1.451548) (cit. on p. 55).
- [106] M. Hochbruck and C. Lubich, *On Krylov subspace approximations to the matrix exponential operator*, *SIAM J. Numer. Anal.* **34**, 5, 1911–1925 (1997), DOI: [10.1137/S0036142995280572](https://doi.org/10.1137/S0036142995280572) (cit. on p. 55).
- [107] A. Castro, M. A. L. Marques, and A. Rubio, *Propagators for the time-dependent Kohn-Sham equations*, *J. Chem. Phys.* **121**, 8, 3425–3433 (2004), DOI: [10.1063/1.1774980](https://doi.org/10.1063/1.1774980) (cit. on pp. 55, 73).
- [108] W. H. Press, S. A. Teukolsky, W. T. Vetterling, and B. P. Flannery, *Numerical Recipes 3rd Edition: The Art of Scientific Computing*, 3rd ed., New York, NY, USA: Cambridge University Press, 2007, ISBN: 0521880688, 9780521880688 (cit. on pp. 55, 58).
- [109] P. Linz, *Numerical methods for Volterra integral equations of the first kind*, *Comput. J.* **12**, 4, 393–397 (1969), DOI: [10.1093/comjnl/12.4.393](https://doi.org/10.1093/comjnl/12.4.393) (cit. on pp. 56, 112).

- [110] S. E. B. Nielsen, M. Ruggenthaler, and R. van Leeuwen, *Many-body quantum dynamics from the density*, EPL **101**, 3, 33001 (2013), DOI: [10.1209/0295-5075/101/33001](#) (cit. on p. [57](#), [91](#)).
- [111] M. Ruggenthaler and R. van Leeuwen, *Global fixed-point proof of time-dependent density-functional theory*, EPL **95**, 1, 13001 (2011), DOI: [10.1209/0295-5075/95/13001](#) (cit. on p. [57](#)).
- [112] S. E. B. Nielsen, M. Ruggenthaler, and R. van Leeuwen, *Quantum Control of Many-Body Systems by the Density* arXiv: [1412.3794](#) (quant-ph) (2014) (cit. on p. [58](#)).
- [113] M. Ruggenthaler, M. Penz, and R. van Leeuwen, *Existence, uniqueness, and construction of the density-potential mapping in time-dependent density-functional theory*, J. Phys.: Condens. Matter **27**, 20, 203202 (2015), DOI: [10.1088/0953-8984/27/20/203202](#) (cit. on p. [58](#)).
- [114] P. Pulay, *Convergence acceleration of iterative sequences. the case of scf iteration*, Chem. Phys. Lett. **73**, 2, 393–398 (1980), DOI: [10.1016/0009-2614\(80\)80396-4](#) (cit. on p. [58](#)).
- [115] A. J. Garza and G. E. Scuseria, *Comparison of self-consistent field convergence acceleration techniques*, J. Chem. Phys. **137**, 5, 054110 (2012), DOI: [10.1063/1.4740249](#) (cit. on p. [58](#)).
- [116] A Pietzsch, A Föhlisch, M Beye, M Deppe, F Hennies, M Nagasono, E Suljoti, W Wurth, C Gahl, K Döbrich, and A Melnikov, *Towards time resolved core level photoelectron spectroscopy with femtosecond x-ray free-electron lasers*, New J. Phys. **10**, 3, 033004 (2008), DOI: [10.1088/1367-2630/10/3/033004](#) (cit. on p. [63](#)).
- [117] M. Müller, A. Paarmann, and R. Ernstorfer, *Femtosecond electrons probing currents and atomic structure in nanomaterials*, Nat. Commun. **5**, 5292 (2014), DOI: [10.1038/ncomms6292](#) (cit. on p. [63](#)).
- [118] F. Buchner, A. Lubcke, N. Heine, and T. Schultz, *Time-resolved photoelectron spectroscopy of liquids*, Rev. Sci. Instrum. **81**, 11, 113107, 113107 (2010), DOI: [10.1063/1.3499240](#) (cit. on p. [63](#)).
- [119] S. Yamaguchi and H. Hamaguchi, *Ultrafast Electronic Relaxation and Hydrogen-Bond-Formation/Dissociation Dynamics of Photoexcited All-trans Retinal in Protic Solvents*, J. Phys. Chem. A **104**, 18, 4272–4279 (2000), DOI: [10.1021/jp993551o](#) (cit. on p. [63](#)).
- [120] M. Motzkus, S. Pedersen, and A. H. Zewail, *Femtosecond Real-Time Probing of Reactions. 19. Nonlinear (DFWM) Techniques for Probing Transition States of Uni- and Bimolecular Reactions*, J. Phys. Chem. **100**, 14, 5620–5633 (1996), DOI: [10.1021/jp960265t](#) (cit. on p. [63](#)).
- [121] J. Hauer, T. Buckup, and M. Motzkus, *Pump-Degenerate Four Wave Mixing as a Technique for Analyzing Structural and Electronic Evolution: Multidimensional Time-Resolved Dynamics near a Conical Intersection*, J. Phys. Chem. A **111**, 42, 10517–10529 (2007), DOI: [10.1021/jp073727j](#) (cit. on p. [63](#)).

- [122] A. Pohl, P.-G. Reinhard, and E. Suraud, *Towards Single-Particle Spectroscopy of Small Metal Clusters*, Phys. Rev. Lett. **84**, 22, 5090–5093 (2000), DOI: [10.1103/PhysRevLett.84.5090](#) (cit. on p. [63](#)).
- [123] A. D. Dutoi, K. Gokhberg, and L. S. Cederbaum, *Time-resolved pump-probe spectroscopy to follow valence electronic motion in molecules: Theory*, Phys. Rev. A **88**, 1, 013419 (2013), DOI: [10.1103/PhysRevA.88.013419](#) (cit. on p. [63](#)).
- [124] L. Koziol, V. A. Mozhayskiy, B. J. Braams, J. M. Bowman, and A. I. Krylov, *Ab Initio Calculation of the Photoelectron Spectra of the Hydroxycarbene Diradicals*, J. Phys. Chem. A **113**, 27, 7802–7809 (2009), DOI: [10.1021/jp903476w](#) (cit. on p. [63](#)).
- [125] L. S. Cederbaum and W. Domcke, *On the vibrational structure in photoelectron spectra by the method of Green's functions*, J. Chem. Phys. **60**, 7, 2878–2889 (1974), DOI: [10.1063/1.1681457](#) (cit. on p. [63](#)).
- [126] C. Ko, M. V. Pak, C. Swalina, and S. Hammes-Schiffer, *Alternative wave-function ansatz for including explicit electron-proton correlation in the nuclear-electronic orbital approach*, J. Chem. Phys. **135**, 5, 054106 (2011), DOI: [10.1063/1.3611054](#) (cit. on pp. [70](#), [127](#)).
- [127] T. Kreibich, R. van Leeuwen, and E. K. U. Gross, *Multicomponent density-functional theory for electrons and nuclei*, Phys. Rev. A **78**, 2, 022501 (2008), DOI: [10.1103/PhysRevA.78.022501](#) (cit. on pp. [70](#), [76](#), [127](#)).
- [128] N. Säkkinen, Y. Peng, H. Appel, and R. van Leeuwen, *Many-body Green's function theory for electron-phonon interactions: Ground state properties of the Holstein dimer*, J. Chem. Phys. **143**, 23, 234101 (2015), DOI: [10.1063/1.4936142](#) (cit. on pp. [70](#), [127](#)).
- [129] N. Säkkinen, Y. Peng, H. Appel, and R. van Leeuwen, *Many-body Green's function theory for electron-phonon interactions: The Kadanoff-Baym approach to spectral properties of the Holstein dimer*, J. Chem. Phys. **143**, 23, 234102 (2015), DOI: [10.1063/1.4936143](#) (cit. on pp. [70](#), [127](#)).
- [130] A. K. Rajagopal, *Time-dependent functional theory of coupled electron and electromagnetic fields in condensed-matter systems*, Phys. Rev. A **50**, 5, 3759–3765 (1994), DOI: [10.1103/PhysRevA.50.3759](#) (cit. on p. [77](#)).
- [131] A. Vukics, T. Grieser, and P. Domokos, *Elimination of the A-Square Problem from Cavity QED*, Phys. Rev. Lett. **112**, 7, 073601 (2014), DOI: [10.1103/PhysRevLett.112.073601](#) (cit. on pp. [79](#), [131](#)).
- [132] M. Ruggenthaler, *Ground-State Quantum-Electrodynamical Density-Functional Theory* arXiv: [1509.01417](#) (quant-ph) (2015) (cit. on p. [81](#)).
- [133] J. I. Fuks, M. Farzanehpour, I. V. Tokatly, H. Appel, S. Kurth, and A. Rubio, *Time-dependent exchange-correlation functional for a Hubbard dimer: Quantifying nonadiabatic effects*, Phys. Rev. A **88**, 6, 062512 (2013), DOI: [10.1103/PhysRevA.88.062512](#) (cit. on p. [87](#)).
- [134] Y. Li and C. A. Ullrich, *Time-dependent V-representability on lattice systems*, J. Chem. Phys. **129**, 4, 044105 (2008), DOI: [10.1063/1.2955733](#) (cit. on p. [87](#)).



- [135] M. Farzanehpour and I. V. Tokatly, *Time-dependent density functional theory on a lattice*, Phys. Rev. B **86**, 12, 125130 (2012), DOI: [10.1103/PhysRevB.86.125130](#) (cit. on p. [87](#)).
- [136] R. J. Glauber, *The Quantum Theory of Optical Coherence*, Phys. Rev. **130**, 6, 2529–2539 (1963), DOI: [10.1103/PhysRev.130.2529](#) (cit. on p. [89](#)).
- [137] R. J. Glauber, *Coherent and Incoherent States of the Radiation Field*, Phys. Rev. **131**, 6, 2766–2788 (1963), DOI: [10.1103/PhysRev.131.2766](#) (cit. on p. [89](#)).
- [138] N. T. Maitra and K. Burke, *Demonstration of initial-state dependence in time-dependent density-functional theory*, Phys. Rev. A **63**, 4, 042501 (2001), DOI: [10.1103/PhysRevA.63.042501](#) (cit. on p. [90](#)).
- [139] N. T. Maitra, K. Burke, and C. Woodward, *Memory in Time-Dependent Density Functional Theory*, Phys. Rev. Lett. **89**, 2, 023002 (2002), DOI: [10.1103/PhysRevLett.89.023002](#) (cit. on p. [90](#)).
- [140] J. Flick, M. Ruggenthaler, H. Appel, and A. Rubio, *Kohn-Sham approach to quantum electrodynamical density-functional theory: Exact time-dependent effective potentials in real space*, Proc. Natl. Acad. Sci. USA **112**, 50, 15285–15290 (2015), DOI: [10.1073/pnas.1518224112](#) (cit. on pp. [91](#), [119](#), [123](#)).
- [141] P. Elliott, J. I. Fuks, A. Rubio, and N. T. Maitra, *Universal Dynamical Steps in the Exact Time-Dependent Exchange-Correlation Potential*, Phys. Rev. Lett. **109**, 26, 266404 (2012), DOI: [10.1103/PhysRevLett.109.266404](#) (cit. on pp. [91](#), [100](#)).
- [142] J. I. Fuks, P. Elliott, A. Rubio, and N. T. Maitra, *Dynamics of Charge-Transfer Processes with Time-Dependent Density Functional Theory*, J. Phys Chem. Lett. **4**, 5, 735–739 (2013), DOI: [10.1021/jz302099f](#) (cit. on pp. [91](#), [100](#)).
- [143] G. Jaeger, *Quantum Information: An Overview*, Springer New York, 2007, ISBN: 9780387369440 (cit. on p. [93](#)).
- [144] L. Mandel, *Sub-Poissonian photon statistics in resonance fluorescence*, Opt. Lett. **4**, 7, 205–207 (1979), DOI: [10.1364/OL.4.000205](#) (cit. on p. [94](#)).
- [145] O. V. Gritsenko, R. van Leeuwen, and E. J. Baerends, *Molecular exchange-correlation Kohn-Sham potential and energy density from ab initio first- and second-order density matrices: Examples for XH (X=Li, B, F)*, J. Chem. Phys. **104**, 21, 8535 (1996), DOI: [10.1063/1.471602](#) (cit. on p. [99](#)).
- [146] K. Luo, J. I. Fuks, E. D. Sandoval, P. Elliott, and N. T. Maitra, *Kinetic and interaction components of the exact time-dependent correlation potential*, J. Chem. Phys. **140**, 18, (2014), DOI: [10.1063/1.4867002](#) (cit. on p. [100](#)).
- [147] J. C. Tully, *Molecular dynamics with electronic transitions*, J. Chem. Phys. **93**, 2, 1061–1071 (1990), DOI: [10.1063/1.459170](#) (cit. on p. [105](#)).
- [148] C. Pellegrini, J. Flick, I. V. Tokatly, H. Appel, and A. Rubio, *Optimized Effective Potential for Quantum Electrodynamical Time-Dependent Density Functional Theory*, Phys. Rev. Lett. **115**, 9, 093001 (2015), DOI: [10.1103/PhysRevLett.115.093001](#) (cit. on pp. [107](#), [108](#), [119](#)).
- [149] A. Mitra, *Hans bethe, quantum mechanics, and the lamb shift*, Resonance **10**, 10, 33–48 (2005), DOI: [10.1007/BF02867166](#) (cit. on p. [109](#)).

- [150] F. Schwabl, *Quantenmechanik (QM I)*: Springer-Lehrbuch, Springer, 2002, ISBN: 9783540431060 (cit. on p. 114).
- [151] J. Flick, M. Ruggenthaler, H. Appel, and A. Rubio, *Atoms and Molecules in Cavities: Strong Coupling and Quantum Chemistry, to be submitted to PNAS* (cit. on p. 117).
- [152] E. Orgiu, J. George, J. A. Hutchison, E. Devaux, J. F. Dayen, B. Doudin, F. Stellacci, C. Genet, J. Schachenmayer, C. Genes, G. Pupillo, P. Samorì, and T. W. Ebbesen, *Conductivity in organic semiconductors hybridized with the vacuum field*, Nat. Mater. **14**, 11, 1123–1129 (2015), DOI: [10.1038/nmat4392](https://doi.org/10.1038/nmat4392) (cit. on pp. 117, 128).
- [153] A. Shalabney, J. George, J. Hutchison, G. Pupillo, C. Genet, and T. W. Ebbesen, *Coherent coupling of molecular resonators with a microcavity mode*, Nat. Commun. **6**, 5981 (2015), DOI: [10.1038/ncomms6981](https://doi.org/10.1038/ncomms6981) (cit. on pp. 117, 128).
- [154] J. A. Hutchison, A. Liscio, T. Schwartz, A. Canaguier-Durand, C. Genet, V. Palermo, P. Samorì, and T. W. Ebbesen, *Tuning the Work-Function Via Strong Coupling*, Adv. Mater. **25**, 17, 2481–2485 (2013), DOI: [10.1002/adma.201203682](https://doi.org/10.1002/adma.201203682) (cit. on p. 117).
- [155] A. Wallraff, D. I. Schuster, A. Blais, L. Frunzio, R.-S. Huang, J. Majer, S. Kumar, S. M. Girvin, and R. J. Schoelkopf, *Strong coupling of a single photon to a superconducting qubit using circuit quantum electrodynamics*, Nature **431**, 7005, 162–167 (2004), DOI: [10.1038/nature02851](https://doi.org/10.1038/nature02851) (cit. on p. 117).
- [156] A. Blais, R.-S. Huang, A. Wallraff, S. M. Girvin, and R. J. Schoelkopf, *Cavity quantum electrodynamics for superconducting electrical circuits: An architecture for quantum computation*, Phys. Rev. A **69**, 6, 062320 (2004), DOI: [10.1103/PhysRevA.69.062320](https://doi.org/10.1103/PhysRevA.69.062320) (cit. on p. 117).
- [157] O. Benson, *Assembly of hybrid photonic architectures from nanophotonic constituents*, Nature **480**, 7376, 193–199 (2011), DOI: [10.1038/nature10610](https://doi.org/10.1038/nature10610) (cit. on p. 117).
- [158] H. Ritsch, P. Domokos, F. Brennecke, and T. Esslinger, *Cold atoms in cavity-generated dynamical optical potentials*, Rev. Mod. Phys. **85**, 2, 553–601 (2013), DOI: [10.1103/RevModPhys.85.553](https://doi.org/10.1103/RevModPhys.85.553) (cit. on p. 117).
- [159] J. Galego, F. J. Garcia-Vidal, and J. Feist, *Cavity-Induced Modifications of Molecular Structure in the Strong-Coupling Regime*, Phys. Rev. X **5**, 4, 041022 (2015), DOI: [10.1103/PhysRevX.5.041022](https://doi.org/10.1103/PhysRevX.5.041022) (cit. on pp. 117, 120, 123).
- [160] R. Loudon, *One-Dimensional Hydrogen Atom*, Am. J. Phys. **27**, 9, 649–655 (1959), DOI: [10.1119/1.1934950](https://doi.org/10.1119/1.1934950) (cit. on p. 119).
- [161] A. Crawford-Uranga, D. J. Mowbray, and D. M. Cardamone, *Quantum-ionic features in the absorption spectra of homonuclear diatomic molecules*, Phys. Rev. A **91**, 3, 033410 (2015), DOI: [10.1103/PhysRevA.91.033410](https://doi.org/10.1103/PhysRevA.91.033410) (cit. on pp. 119, 141).
- [162] Y. Todorov, A. M. Andrews, R. Colombelli, S. De Liberato, C. Ciuti, P. Klang, G. Strasser, and C. Sirtori, *Ultrastrong Light-Matter Coupling Regime with Polariton Dots*, Phys. Rev. Lett. **105**, 19, 196402 (2010), DOI: [10.1103/PhysRevLett.105.196402](https://doi.org/10.1103/PhysRevLett.105.196402) (cit. on p. 120).

- [163] M. Bamba and T. Ogawa, *Laser under ultrastrong light-matter interaction: Qualitative aspects and quantitative influences by level and mode truncations*, Phys. Rev. A **93**, 3, 033811 (2016), DOI: [10.1103/PhysRevA.93.033811](#) (cit. on p. [120](#)).
- [164] P. Melo and A. Marini, *An unified theory of quantised electrons, phonons and photons out-of-equilibrium: a simplified ab-initio approach based on the Generalised Baym-Kadanoff ansatz* arXiv: [1512.07490](#) (cond-mat.mes-hall) (2015) (cit. on p. [127](#)).



## LIST OF FIGURES

Figure 1	Born-Oppenheimer potential-energy surfaces in an one-dimensional Hydrogen molecule . . . . .	12
Figure 2	Ground-state Hohenberg-Kohn theorem . . . . .	16
Figure 3	Kohn-Sham construction . . . . .	18
Figure 4	Runge-Gross proof . . . . .	23
Figure 5	Schematic view on the photoemission process and the description of the sudden approximation to photoemission. . .	37
Figure 6	Schematic view on Trans-Polyacetylene . . . . .	46
Figure 7	Schematic view on Jaynes-Cummings-Hubbard model . . .	47
Figure 8	Schematic view on GaAs quantum dot in an optical cavity .	49
Figure 9	Mapping of two-photon number states onto a two-dimensional two-photon wave function. . . . .	52
Figure 10	Block structure of the Hamiltonian imposed by the conserved number operator . . . . .	55
Figure 11	Exact BO surfaces vs. harmonic approximation . . . . .	65
Figure 12	Photoelectron spectra for Trans-Polyacetylene . . . . .	67
Figure 13	Nonadiabaticity in the BO ground state of the Trans-Polyacetylene chain . . . . .	68
Figure 14	SHA and exact spectra obtained from TP and SOS . . . . .	70
Figure 15	Excitation with Frank-Condon transition . . . . .	72
Figure 16	Time-dependent pump-probe photoelectron spectroscopy .	74
Figure 17	Kohn-Sham construction in QEDFT. . . . .	83
Figure 18	Exact results for the JCH Hamiltonian in the weak-coupling limit . . . . .	85
Figure 19	Exact potentials and densities compared to mean-field potentials and densities in the weak-coupling limit. . . . .	86
Figure 20	Exact potentials and densities compared to mean-field potentials and densities in the strong-coupling limit. . . . .	87
Figure 21	Exact results for the JCH Hamiltonian in the weak-coupling limit for a coherent initial state. . . . .	88
Figure 22	Exact and mean-field results for the JCH Hamiltonian in the weak-coupling limit for a coherent initial state. . . . .	89
Figure 23	Static results for the GaAs quantum dot in an optical cavity.	92
Figure 24	Static results for the GaAs quantum dot in an optical cavity. Exact eigenenergies. . . . .	94
Figure 25	Static results for the GaAs quantum dot in an optical cavity. Exact ground-state densities. . . . .	95
Figure 26	Dynamical results for the GaAs quantum dot in an optical cavity with coherent initial state (1). . . . .	96
Figure 27	Dynamical results for the GaAs quantum dot in an optical cavity with coherent initial state (2). . . . .	97

Figure 28	Dynamical results for the GaAs quantum dot in an optical cavity with superposition of two Fock states as initial state (1).	98
Figure 29	Dynamical results for the GaAs quantum dot in an optical cavity with superposition of two Fock states as initial state (2).	99
Figure 30	Dynamical results for the GaAs quantum dot in an optical cavity with correlated initial state (1).	100
Figure 31	Dynamical results for the GaAs quantum dot in an optical cavity with correlated initial state (2).	101
Figure 32	Validating the numerical fixed-point algorithm	102
Figure 33	The Born-Oppenheimer surfaces of the correlated electron-photon problem.	103
Figure 34	The occupation of the photon number states in the first PES and the third PES	104
Figure 35	Hartree and Fock diagram Feynman diagrams.	108
Figure 36	Static OEP results.	110
Figure 37	Time-dependent OEP results for $\lambda = 0.1$ for sudden switch example.	111
Figure 38	Time-dependent OEP results for $\lambda = 0.1$ for factorizable initial state.	112
Figure 39	Time-dependent OEP results for $\lambda = 0.5$ for sudden switch example.	113
Figure 40	Validation of the numerical implementation	114
Figure 41	Schematic view on optical cavity.	118
Figure 42	Eigenenergies and bond length for optical cavity.	120
Figure 43	CBOA surfaces and overlaps for optical cavity.	121
Figure 44	Absorption spectra for optical cavity.	122

## LIST OF TABLES

---

Table 1	Pascal's triangle . . . . .	54
Table 2	Comparison of exact/harmonic BO states to exact correlated states . . . . .	66
Table 3	Overview of different density-functional theories. . . . .	78
Table 4	Ground-state properties of the cavity-GaAs model . . . . .	93

## LIST OF ACRONYMS

---

ALDA	adiabatic local-density approximation
BO	Born-Oppenheimer
BOA	Born-Oppenheimer approximation
CBOA	cavity Born-Oppenheimer approximation
DFT	density-functional theory
DHA	double-harmonic approximation
DIIS	direct inversion in the iterative subspace
EOM	equation of motion
GaAs	gallium arsenide
GGA	generalized-gradient approximation
Hxc	Hartree-exchange-correlation
JCH	Jaynes-Cummings-Hubbard
KLI	Krieger-Li-Iafrate
KS	Kohn-Sham
LDA	local-density approximation
Mxc	meanfield-exchange-correlation
OEP	optimized effective potential
PES	potential-energy surface
PBE	Perdew-Burke-Ernzerhof
QED	quantum electrodynamics
QEDFT	quantum electrodynamical density-functional theory
RWA	rotating-wave approximation
SA	sudden approximation
SHA	single-harmonic approximation
SSH	Su-Schrieffer-Heeger
TDCDFT	time-dependent current density-functional theory
TDDFT	time-dependent density-functional theory



**TDOEP** time-dependent optimized effective potential

**xc** exchange-correlation



## LIST OF PUBLICATIONS

---

The following publications are part of this thesis:

- [1] J. Flick, H. Appel, and A. Rubio, *Nonadiabatic and Time-Resolved Photoelectron Spectroscopy for Molecular Systems*, J. Chem. Theory Comput. **10**, 4, 1665–1676 (2014), DOI: [10.1021/ct4010933](https://doi.org/10.1021/ct4010933).
- [2] M. Ruggenthaler, J. Flick, C. Pellegrini, H. Appel, I. V. Tokatly, and A. Rubio, *Quantum-electrodynamical density-functional theory: Bridging quantum optics and electronic-structure theory*, Phys. Rev. A **90**, 1, 012508 (2014), DOI: [10.1103/PhysRevA.90.012508](https://doi.org/10.1103/PhysRevA.90.012508).
- [3] C. Pellegrini, J. Flick, I. V. Tokatly, H. Appel, and A. Rubio, *Optimized Effective Potential for Quantum Electrodynamical Time-Dependent Density Functional Theory*, Phys. Rev. Lett. **115**, 9, 093001 (2015), DOI: [10.1103/PhysRevLett.115.093001](https://doi.org/10.1103/PhysRevLett.115.093001).
- [4] J. Flick, M. Ruggenthaler, H. Appel, and A. Rubio, *Kohn-Sham approach to quantum electrodynamical density-functional theory: Exact time-dependent effective potentials in real space*, Proc. Natl. Acad. Sci. USA **112**, 50, 15285–15290 (2015), DOI: [10.1073/pnas.1518224112](https://doi.org/10.1073/pnas.1518224112).
- [5] J. Flick, M. Ruggenthaler, H. Appel, and A. Rubio, *Atoms and Molecules in Cavities: Strong Coupling and Quantum Chemistry*, to be submitted to PNAS.
- [6] J. Flick, C. Pellegrini, I. V. Tokatly, H. Appel, and A. Rubio, *Spontaneous Emission and Ground-state Properties in QEDFT Using the Optimized Effective Potential*, in preparation.

The following publication is not part of this thesis:

- [7] J. Flick, F. Tristram, and W. Wenzel, *Modeling loop backbone flexibility in receptor-ligand docking simulations*, J. Comput. Chem. **33**, 31, 2504–2515 (2012), DOI: [10.1002/jcc.23087](https://doi.org/10.1002/jcc.23087).



## LIST OF TALKS AND POSTERS AT CONFERENCES

---

List of talks presented at conferences:

- [1]  $\Psi_k$  2015 conference  
San Sebastian, Spain, September 2015.
- [2] *Frühjahrstagung der DPG*  
Berlin, Germany, March 2015.
- [3] *APS Spring meeting*  
San Antonio, USA, March 2015.
- [4] *Group Seminar AG Prof. Draxl*  
Humboldt University Berlin, Germany, Oktober 2014.
- [5] *White nights of material science: From physics and chemistry to data analysis, and back*  
Saint Petersburg, Russia, June 2014.
- [6] *Frühjahrstagung der DPG*  
Dresden, Germany, April 2014.
- [7] *DinL Winterschool*  
Winkelmoos, Germany, March 2014.
- [8] *Group Seminar AG Prof. Knorr*  
Technical University Berlin, Germany, January 2014.
- [9] *6th Time-Dependent Density-Functional Theory: Prospects and Applications*  
Benasque, Spain, January 2014.
- [10] *Frühjahrstagung der DPG*  
Regensburg, Germany, March 2013.

List of posters presented at conferences:

- [1] *6th Time-Dependent Density-Functional Theory: Prospects and Applications*  
Benasque, Spain, January 2014 (awarded with **Poster Prize**).
- [2] *Density-functional theory: learning from the past, looking to the future*  
Berlin, Germany, July 2013.
- [3] *Vibrational coupling: most important, often ignored, and a challenge for ab-initio theory*  
Lausanne, Switzerland, November 2012.
- [4] *9th ETSF Young Researchers Meeting*  
Brussels, Belgium, May 2012.



## ACKNOWLEDGMENTS

---

This thesis would have not been possible without the help of many people.

I thank Angel Rubio for his encouragement, his constant support and his countless new ideas on all the projects.

I also thank Matthias Scheffler for giving me the great opportunity to work on the PhD in the Fritz-Haber institute in Berlin. I very much enjoyed the last years working in the theory department of the Fritz-Haber, which is a truly amazing scientific environment.

Then, I want to thank my supervisor Heiko Appel. I appreciate all your help and the many scientific discussions we had. I learned not only many interesting physics from you, but also many of the numerical aspects on how to realize all that on a computer.

I would also like to acknowledge my supervisor at the Humboldt university, Claudia Draxl for accepting me as a PhD student at the Humboldt university. I further thank Dieter Bauer for accepting the role of the third reviewer of this thesis.

Many aspects of this work would not have been possible without Michael Ruggenthaler. Thank you for our very fruitful collaboration and especially for the many Skype sessions we had, which helped me enormously.

Then I also want to thank Camilla Pellegrini and Ilya Tokatly from San Sebastian for our collaboration and Ignacio Franco for all our discussions.

I met many friends during my time at the Fritz-Haber institute, you all made me feel very welcome and helped me a lot. Thanks to Karsten Rasim, Björn, René, Wael, Fabio, Guillem, Jessica, Franz, Sebastian, Arvid, Lydia, Markus and all the other current members and alumnis of the FHI in Berlin and the Max-Planck Institute for Structure and Dynamics of Matter (MPSD) in Hamburg.

I am truly grateful to all my proofreaders (in alphabetic order) Christian, Heiko, Michael, Tanja, and Teresa.

A big thanks goes to my family, Georg for joining me in Berlin, Bärbel, Klemens, Detlef, Christin, Karola, Franz, Liesel, Alfons, and also Petra and Toni.

And thank you Tanja, for all your love and your support.





## DECLARATION

---

Hiermit erkläre ich, die Dissertation selbstständig und nur unter Verwendung der angegebenen Hilfen und Hilfsmittel angefertigt zu haben. Ich habe mich anderwärts nicht um einen Doktorgrad beworben und besitze keinen entsprechenden Doktorgrad.

Ich erkläre die Kenntnisnahme der dem Verfahren zugrunde liegenden Promotionsordnung der Mathematisch-Naturwissenschaftlichen Fakultät der Humboldt Universität zu Berlin.

*Berlin, den 23.2.2016*

---

Johannes Flick



## COLOPHON

This document was typeset using  $\text{\LaTeX}$  and `classicthesis`.  
The plots have been created using python 2.7.9. with matplotlib and SciPy,  
Inkscape, GIMP, and JaxoDraw.

*Final Version* as of August, 2016.